ASPECTS OF THE CALCIUM CARBONATE-WATER INTERFACE

A Thesis submitted for the Degree of

Doctor of Philosophy in the

University of Oxford

by

Christopher A. Brown

St. John's College

Hilary Term 1992

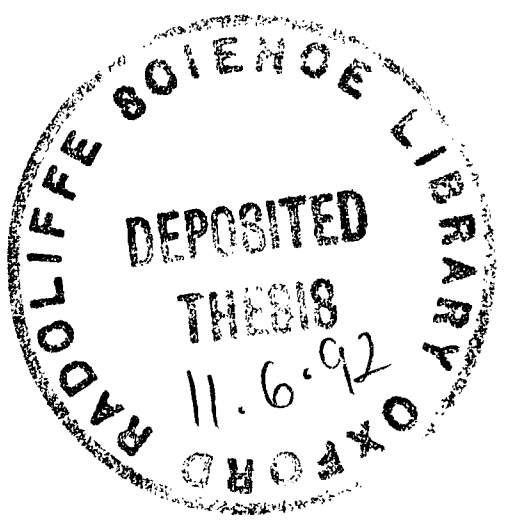

ASPECTS OF THE CALCIUM CARBONATE-WATER INTERFACE

Abstract of a thesis submitted for the degree of Doctor of Philosophy
Christopher A. Brown
St. John's College, Oxford
Hilary Term 1992

The channel flow method has established the net dissolution kinetics of calcite single crystals at high pH (7.7-9.7) and varying bulk Ca^{2+} concentrations (0-10 mM), using wide ranges of solution flow rates (10^{-3}-0.3 $cm^3\ s^{-1}$). Literature rate equations were in poor agreement with experiment. Modelling with the following mechanism, where Ca^{2+} and CO_3^{2-} undergo Langmuirian adsorption:

$$Ca^{2+}_{(aq)} \rightleftharpoons Ca^{2+}_{(ads)}$$

$$CO_3^{2-}{}_{(aq)} \rightleftharpoons CO_3^{2-}{}_{(ads)}$$

$$Ca^{2+}_{(ads)} + CO_3^{2-}{}_{(ads)} \rightleftharpoons CaCO_{3\ (ads)}$$

$$CaCO_{3\ (ads)} \longrightarrow CaCO_{3\ (lattice)}$$

and the consequent rate law

$$J_{net}/\text{mol cm}^{-2}\text{s}^{-1} = k_p K_{Ca} K_{CO_3} \left\{ \frac{K_{sp} - [Ca^{2+}]_o[CO_3^{2-}]_o}{(1 + K_{Ca}[Ca^{2+}]_o)(1 + K_{CO_3}[CO_3^{2-}]_o)} \right\}$$

gave excellent agreement with experiment under all conditions studied. This mechanism is shown to explain all literature streaming potential, electrophoresis and kinetic salt effect data.

Dissolution of calcite under the above conditions was strongly inhibited by Mg^{2+} and fully deprotonated forms of succinic acid, 2-sulphobutanedioic acid, phthalic acid and maleic acid. Mechanisms were established; for the maleate dianion, the inhibition was due to the blocking of the dissolution sites at which $CaCO_3$ units are incorporated into the crystal lattice. For the other ions, inhibition arose from competitive Langmuirian adsorption either between CO_3^{2-} and the anions, or between Ca^{2+} and Mg^{2+}.

A new method to quantify the inhibited dissolution of *particulate* $CaCO_3$ ($\approx$10 μm) via enhanced mass transport of solution to the rotating disc electrode, due to the rotation of the particles in the diffusion layer, has been established. Good agreement was found with that measured independently using the channel flow cell.

A.c. impedance spectroscopy has been used to characterise scaled ($CaCO_3$) steel tubes. Results provide scope for (i) monitoring scale growth, and (ii) use in safety control devices for alerting to the scaling of pipe-work.

ACKNOWLEDGEMENTS

First of all I would like to thank Richard Compton for all his help and supervision during the course of this work. I am also grateful to Barry Coles for his helpful advice about SPICE and the late Norsk computer.

It has been very enjoyable working with all the present members of the Electrochemistry Group. They are far too many to mention individually, but I hope they will forgive me for picking out a few names; thanks to Adrian Fisher for his friendship over the last 3+ years and for, at times, keeping me sane, Tony Spackman for his helpful discussions, and Christine Narramore, without whom the BCN equation would never be quite the same. To mention a few names from the past, I would also like to thank Tony Barwise and Colette Walker for their companionship in the late evenings of calcite dissolution.

Thanks are also due to SERC and Ciba-Geigy Industrial Chemicals (which became Ciba-Geigy Additives and is now, I believe, owned by FMC) for the funding of this project. At Ciba-Geigy I am grateful to Michael Lees for useful discussions and to Garry Grigg, who was always more than willing to help me with the microscopy.

Finally, in the preparation of this thesis I would like to thank Alexandra for all her support, Mark Harding for proof-reading part of the thesis and Martin Booth for his help in photocopying the figures.

Oxford
January 1992

C.A.B.

For my parents

CONTENTS

LIST OF SYMBOLS

Listed below are the symbols used throughout this thesis with the usual units in parentheses. Wherever possible the IUPAC convention [1] set out by Mills *et al.* has been followed unless another form is in common usage.

a particle radius (cm)

or crystallographic axis

a_i activity of species i (dimensionless)

a_j matrix element (BIFD)

A electrode area (RDE) (cm^2)

or Debye-Hückel constant

A_p effective cross-sectional area of particle (cm^2)

b crystallographic axis

b_j matrix element (BIFD)

B coefficient of Levich equation for RDE (see equation (7.19)) (A $s^{1/2}$ $rad^{-1/2}$)

c concentration (mol cm^{-3})

or crystallographic axis

c_{bulk} bulk solution concentration (mol cm^{-3})

c_j matrix element (BIFD)

c_o surface concentration (mol cm^{-3})

C capacitance (F)

$C^\dagger$ transmission line capacitance per unit length (F cm^{-1})

C_{dl} capacitance of double layer (F cm^{-1})

C_i interfacial capacitance used in non-distributed circuit, see Figure 6.20, and terminated transmission line, see Figure 6.22a (F)

C_s capacitance of scale used in non-distributed circuit, see Figure 6.20, and terminated transmission line, see Figure 6.22a (F)

d channel width (cm)

or local decrease in the diffusion layer thickness at a particle

d_j matrix element (BIFD)

D diffusion coefficient ($cm^2\ s^{-1}$)

E potential (V)

$\underline{E}$ voltage phasor (V)

E_o amplitude of alternating voltage (V)

f frequency of a.c. signal (Hz)

or revolutions per second of RDE (Hz)

F Faraday ($C\ mol^{-1}$)

$g^A_{j,k}$ concentration of species A (usually Ca^{2+}) at point (k,j) on finite difference grid (BIFD) ($mol\ cm^{-3}$)

$g^C_{j,k}$ concentration of species CO_3^{2-} at point (k,j) on finite difference grid (BIFD) ($mol\ cm^{-3}$)

h channel half-height (cm)

I current (A)

or ionic strength

$\underline{I}$ current phasor

I_{lim} transport limited current (A)

I_o alternating current amplitude (A)

j $\sqrt{-1}$

j grid line in y-direction (BIFD) (dimensionless)

J flux (mol cm^{-2} s^{-1})

or total number of grid points in y-direction (BIFD) (dimensionless)

J_d flux of calcite dissolution reaction (equation (4.39)) (mol cm^{-2} s^{-1})

J_{lim} transport limited flux (mol cm^{-2} s^{-1})

J_{net} net dissolution flux of calcite (mol cm^{-2} s^{-1})

J_p flux of calcite preciptitation reaction (equation (4.40)) (mol cm^{-2} s^{-1})

k rate constant

or grid line in x direction (BIFD) (dimensionless)

k_d calcite dissolution rate constant (equation (4.39)) (mol cm^{-2} s^{-1})

k_p calcite precipitation rate constant (equation (4.40)) (mol cm^{-2} s^{-1})

K total number of grid points in x direction (BIFD) (dimensionless)

K_{a2} (mixed) second acid dissociation constant of carbonic acid (mol cm^{-3})

K_{Ca} Equilibrium constant for the Langmuirian adsorption of Ca^{2+} on calcite (cm^3 mol^{-1})

K_{CO3} Equilibrium constant for the Langmuirian adsorption of CO_3^{2-} on calcite (cm^3 mol^{-1})

K_I Equilibrium constant for the Langmuirian adsorption of an inhibitor species I on calcite (cm^3 mol^{-1})

K_{sp} solubility product of calcite (mol^2 cm^{-6})

K_w dissociation constant of water (mol^2 cm^{-6})

l length of transmission line (cm)

or length of reactive surface (cm)

l_{so} length of "scale only" section of bipartite transmission line (cm)

l_{ss} length of "scale and solution" section of bipartite transmission line (cm)

L inductance (H)

m_δ total mass of particles in the diffusion layer (g)

m_p mass of one particle (g)

M molar mass (g mol^{-1})

n number of electrons involved in reaction (dimensionless)

or amount of substance (mol)

or reaction order (dimensionless)

N total number of particles

N_δ number of particles in the diffusion layer

P pressure (N m^{-2})

P_{CO2} partial pressure of CO_2 (atm)

q charge (C)

r distance from particle z-axis

or cylindrical axes coordinate

r_E radius of rotating disc electrode (cm)

r_o radius of domain with active film transport in particulate experiments (cm)

R resistance (Ω)

or gas constant (J K^{-1} mol^{-1})

$R^\dagger$ transmission line resistance per unit length (Ω cm^{-1})

R_{ct} charge transfer resistance (Ω)

R_s resistance of scale used in non-distributed circuit, see Figure 6.20, and terminated transmission line, see Figure 6.22a (Ω)

$R^\dagger_{so}$ resistance per unit length of "scale only" section in bipartite transmission line (Ω cm^{-1})

$R^{\dagger}_{ss}$ resistance per unit length of "scale and solution" section in bipartite transmission line (Ω cm^{-1})

R_{tml} total transmission line resistance (Ω)

R_u uncompensated solution resistance (Ω)

Re Reynolds number (dimensionless)

t time (s)

T temperature (K)

u ionic mobility (cm^2 s^{-1} V^{-1})

or see equation (6.34)

u_j matrix element (BIFD)

v_o velocity of solution in x-direction at centre of the channel (cm s^{-1})

v_x velocity of solution in x-direction in the channel (cm s^{-1})

V_f volume flow rate of solution (cm^{3}s^{-1})

V_p total volume of particles (cm^3)

V_s volume of solution (cm^3)

V_δ volume of diffusion layer (cm^3)

w channel electrode width (cm)

x Cartesian coordinate

x_c crystal length (cm)

x_e electrode length (cm)

Δx distance between grid points on x-axis (BIFD) (cm)

X_C capacitative reactance (Ω)

X_L inductive reactance (Ω)

y Cartesian coordinate

Δy distance between grid points on y-axis (BIFD) (cm)

z Cartesian coordinate

or cylindrical axes coordinate

or charge number of ion

Z impedance (Ω)

$\underline{Z}$ impedance vector

Z' real impedance (Ω)

Z'' imaginary impedance (Ω)

$Z^{\dagger}$ transmission line impedance per unit length (Ω cm^{-1})

Z_{tml} transmission line impedance (Ω)

Z_W Warburg impedance (Ω)

α bipartite transmission line parameter (see equation (A6.24))

or crystallographic interaxial angle

α_j (BIFD)

β bipartite transmission line parameter (see equation (A6.25)

β_j (BIFD)

γ bipartite transmission line parameter (see equation (A6.26))

γ_i activity coefficient of species i on molar scale (dimensionless)

$\gamma_{\pm}$ mean ion activity coefficient (dimensionless)

δ diffusion layer thickness (cm)

or bipartite transmission line parameter (see equation (A6.27))

$\Delta\delta$ decrease in diffusion layer thickness (cm)

ε permittivity (C^2 J^{-1} cm^{-1})

$\zeta_{\cos 1}$ bipartite transmission line parameter (see equation (A6.30))

$\zeta_{\cos 2}$ bipartite transmission line parameter (see equation (A6.31))

$\zeta_{\text{sin 1}}$ bipartite transmission line parameter (see equation (A6.32))

$\zeta_{\text{sin 2}}$ bipartite transmission line parameter (see equation (A6.33))

η absolute viscosity (g cm^{-1} s^{-1})

θ cylindrical axes coordinate

θ_i surface coverage of species i (dimensionless)

Λ molar conductivity (S cm^2 mol^{-1})

λ_j see equation (2.22) (BIFD)

ν kinematic viscosity (cm^2 s^{-1})

ρ density (g cm^{-3})

σ Warburg coefficient (Ω s^{-})

ϕ phase angle (rad)

or volume fraction (vol %)

or electric potential (V)

ω angular frequency of a.c. signal (rad s^{-1})

or angular velocity of RDE (rad s^{-1})

ω_p angular velocity of rotating particle (rad s^{-1})

Ω saturation ratio of calcite = $a_{Ca}a_{CO3}/K_{sp}$ (dimensionless)

∇ grad $\{scalar\} = \left(\boldsymbol{i}\frac{\partial}{\partial x} + \boldsymbol{j}\frac{\partial}{\partial y} + \boldsymbol{k}\frac{\partial}{\partial z}\right)\{\boldsymbol{scalar}\}$

$\nabla.$ div . $\{vector\} = \left(\boldsymbol{i}\frac{\partial}{\partial x} + \boldsymbol{j}\frac{\partial}{\partial y} + \boldsymbol{k}\frac{\partial}{\partial z}\right).\{\boldsymbol{vector}\}$

∇^2 Laplacian operator

[i] molar concentration of species i (mol cm^{-3})

$[i]_{bulk}$ bulk molar concentration of species i (mol cm^{-3})

$[i]_o$ surface molar concentration of species i (mol cm^{-3})

$[i]_{eq}$ molar concentration of species i at equilibrium (mol cm^{-3})

(hkl) crystal plane with Miller indices h,k,l

$\{hkl\}$ symmetrical set of crystal planes with equivalent symmetry to (hkl) plane

$[hkl]$ crystallographic direction represented by a vector with $a = h$, $b = k$, $c = l$

$<hkl>$ symmetrical set of crystallographic vectors with equivalent symmetry to $[hkl]$

ABBREVIATIONS

BI backwards implicit [finite difference method]

BIFD backwards implicit finite difference [method]

CE counter electrode

DIC differential interference-contrast [microscopy]

ECI electrochemical interface

FRA frequency response analyser

$HMal^-$ mono-anion of maleic acid

Mal^{2-} di-anion of maleic acid

RDE rotating disc electrode

RE reference electrode

SCE saturated calomel electrode

TMPD N,N,N',N'-tetramethyl-p-phenylenediamine

WE working electrode

CHAPTER 1

INTRODUCTION

1.1 Outline of Thesis

The work in this thesis involves the study of several aspects of the calcium carbonate-water interface. The dissolution kinetics of calcium carbonate at neutral and high pH will be investigated over a wide range of conditions using a system with well-defined hydrodynamic flow. It is to be hoped that the resulting rate law governing the reaction between water and calcium carbonate will provide a better understanding of the mechanism of calcium carbonate dissolution and precipitation. The inhibition of the dissolution process by certain foreign species will also be investigated.

The effect of calcium carbonate scale on the impedance of an electrode will be explored using a.c. techniques and the response will be described by an equivalent circuit.

1.2 Reasons for Study

Calcium carbonate is one of the most reactive common minerals, the dissolution and precipitation reactions of which are important in controlling its abundance and composition. Knowledge of the reaction kinetics of calcium carbonate has important applications in a wide variety of fields. Concern over the "greenhouse effect" due to global carbon dioxide accumulation and the effects of "acid rain" on karst systems, lakes and stream water, together with the counter-measures of "lake-liming", are all environmental aspects of the calcium carbonate system. Calcium carbonate dissolution and precipitation is also fundamental to the study of soil science, freshwater and marine environments. Industrially the

crystallisation of calcium carbonate is important in heat-exchanger systems such as in desalination plants or power stations due to the formation of scale on heat transfer surfaces. Knowledge of the precipitation mechanism and study of the effects of additives on the reaction kinetics would facilitate the better design of industrial scale inhibitors. Despite the huge interest in the calcium carbonate system the mechanism of the dissolution and precipitation of calcium carbonate is poorly understood and therefore an aim of this thesis is to provide a better understanding of reactions at the calcium carbonate-water interface.

Before reviewing previous studies on the dissolution and precipitation of calcium carbonate, a brief summary will be presented of key aspects of reactions at the solid-liquid interface.

1.3 Reactions at the Solid-Liquid Interface

Reactions which occur between a liquid and a solid surface involve a number of elementary steps, summarised in Figure 1.1, in which reactants are

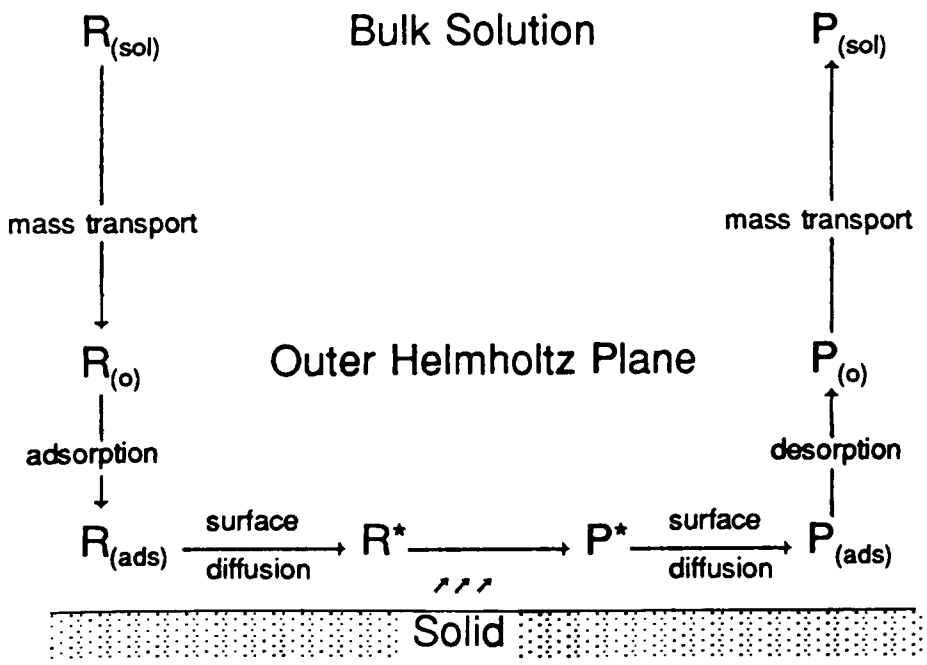

Figure 1.1. Elementary steps that occur in reactions at the solid-liquid interface, where R *represents the reactant species and* P *the products. The asterisked species represent those adsorbed at reaction sites.*

brought to the reaction site and products are removed. Reactant species are conveyed to the Outer Helmholtz plane by one or more of the mass transport processes to be detailed in Section 1.4. Once there, the reactant can be adsorbed onto the reactive surface with a possible reduction in solvation. This adsorbed species may then undergo surface diffusion to a reaction site where it is converted to products. The product species can then follow the reverse process of desorption followed by mass transport away into bulk solution. For the particular solid-liquid interface under investigation any one of these elementary steps may be the rate determining process. A heterogeneous rate law can be written for this, which will have the general form

$$J\ /\mathrm{mol\,cm^{-2}s^{-1}} = k[\mathrm{R}]_o^n \tag{1.1}$$

where J is the flux of reactant reaching the reactive surface, the subscript o denotes a surface concentration, k is a rate constant and n is the reaction order. In the case where the reaction is occurring at a metal-solution interface the flux can be directly measured from the electrode current, I, since

$$I = nFAJ \tag{1.2}$$

where n is the number of electrons transferred, F is the Faraday constant and A is the area of the electrode. However, when the reaction is occurring at an insulator-liquid interface a much more challenging situation is encountered since no direct analogue of the electrode current exists. To measure the flux, J, the concentration of a reactant or product species must be monitored as close to the reaction site as possible. This criterion is vital to obtain a high degree of mechanistic sensitivity. Measurement of bulk concentrations, on the other hand, provides less information on the surface reaction mechanism because of the remote nature of the detection.

1.4 Mass Transport

The amount of a species transported through a surface of unit area in a unit time is the flux, J, with units mol cm^{-2} s^{-1}. This can be related to an average velocity, v, of the species in the direction normal to this surface and its concentration, c

$$J(x,t) = vc(x,t) \tag{1.3}$$

There are three mechanisms by which reactants can be brought from bulk solution to the solid-liquid interface or, conversely, by which products may be removed from it into bulk solution. These are convection, diffusion and migration.

Migration is the movement of charged particles in an electric field. The force on the particle is proportional to the electric field, i.e. the electrical potential gradient, and its charge. Diffusion is the process by which particles move from a region of high concentration to one of lower concentration so as to maximise entropy. Convection is a process in which solution as a whole is transported and not solely the solute species, as is the case with migration and diffusion.

1.4.1 Migration

The existence of a potential gradient causes the migration of charged species. If the local potential ϕ varies along the x-axis then there is an electrostatic force acting on the ions in the x-direction which is opposed by viscous forces. This results [2] in the ions having a velocity v

$$v = -\frac{zu}{|z|}\frac{\partial \phi}{\partial x} \tag{1.4}$$

where u is the mobility of the ions with charge number z. Utilizing the identity (1.3) this can be transformed into the migratory flux.

$$J(x,t) = -\frac{zuc(x,t)}{|z|}\frac{\partial\phi}{\partial x} \tag{1.5}$$

1.4.2 Diffusion

Diffusion is the movement of species "down" a concentration gradient and was shown by Fick [3,4] to be proportional to this gradient

$$J(x,t) = -D\frac{\partial c(x,t)}{\partial x} \tag{1.6}$$

where D is the diffusion coefficient, and is known as Fick's first law. Diffusion alters the concentration gradient with time. Conserving mass with planar diffusion gives Fick's second law [3,4]

$$\frac{\partial c(x,t)}{\partial t} = D\frac{\partial^2 c(x,t)}{\partial x^2} \tag{1.7}$$

1.4.3 Convection

Convection is movement which arises as a result of a pressure gradient which exists in the fluid. Two forms can be distinguished: forced convection and natural convection. Forced convection results from motion deliberately introduced into the system by stirring or pumping, for example. This is usually irreproducible unless care is taken to set up the forced convection in a controlled and quantifiable way. Natural convection results from reactions at the solid-liquid interface. A reaction which increases the amount of solute will increase the density of the solution slightly in the locality of the reaction site. Such regions of solution will tend to fall under gravity, whereas regions of depleted solute will tend to rise, setting up natural convection.

The flux of a species *i* due to all three modes of transport can be summarised by a general mass transport equation [5] where

$$\underline{J}_i = c_i\underline{v} - D_i\underline{\nabla}c_i - \frac{z_i u_i c_i}{|z_i|}\underline{\nabla}\phi \qquad (1.8)$$

convection *diffusion* *migration*

To be able to investigate the kinetics at the solid-liquid interface it is therefore necessary to have well defined and quantifiable mass transport for each of these processes. Transport due to migration can be made negligible by the addition of an excess of an inert supporting electrolyte.

1.4.4 Supporting Electrolyte

The effect that supporting or background electrolyte has can be illustrated by the electrolysis between two parallel plates with the cathode above the anode to reduce any natural convection. At the anode the electrode is dissolving

$$M_{(s)} - ne^-_{(M)} \longrightarrow M^{n+}_{(sol)} \qquad (1.9)$$

and at the cathode

$$M^{n+}_{(sol)} + ne^-_{(M)} \longrightarrow M_{(s)} \qquad (1.10)$$

When the only ions in solution are the electroactive cation and its associated anion the concentration profile for the two ions is as shown in Figure 1.2. When both

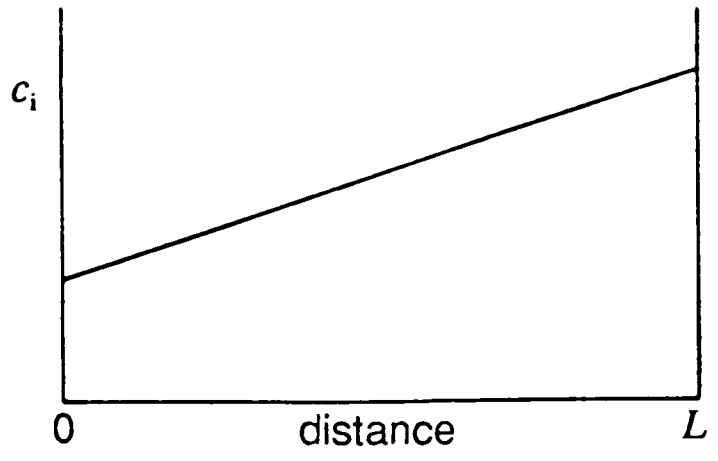

Figure 1.2. Concentration of ions as a function of distance between two electrodes, a distance L apart. Only the electroactive cation and its anion are present.

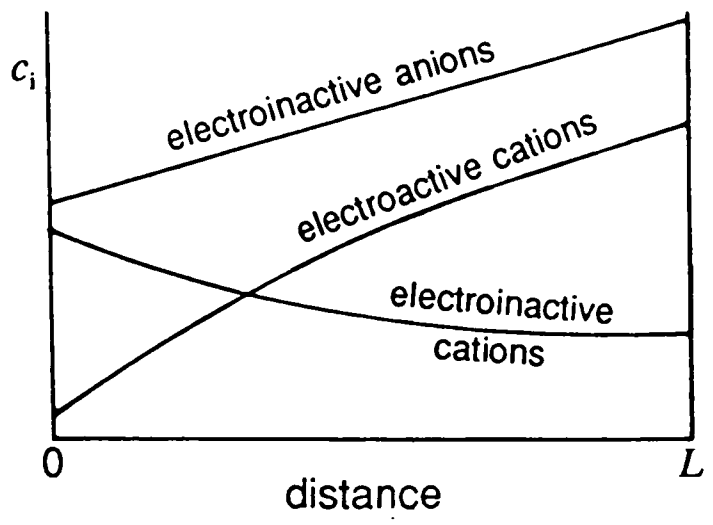

Figure 1.3. As for Figure 1.2 but with the addition of supporting electrolyte.

ions have the same magnitude of charge, it can be shown [6] that exactly half of the transport is due to diffusion and half is due to migration. Thus, in this case, half the potential difference between the electrodes is used to set up the Nernstian speciation at both electrodes and the other half is used to drive the current through the solution, i.e. the so-called ohmic drop.

The situation is altered on the addition of an inert "supporting" electrolyte. The total cation and anion concentration profile is still the same linear function of distance as in Figure 1.2, but this is no longer the case for concentration profiles of the individual cationic species, as shown in Figure 1.3. The addition of supporting electrolyte reduces the migration of the electroactive species. The limiting current in the totally unsupported case is exactly twice that when the supporting electrolyte is in an infinite excess. This is because in the former case, the flux due to migration is as big as the diffusion flux, whereas with an infinite amount of supporting electrolyte present only the mass transport due to diffusion remains. To reduce the migratory component to 1% of the diffusive component, a 33-fold excess of the supporting electrolyte is required [7], at least in the homovalent case. It is often stated that migration is negligible with supporting electrolyte present because "the current is largely carried by the supporting ions" [8]. However this is

not the case; the electroactive ions carry all the current and the other ions are effectively immobile at steady state. A more accurate explanation is that the electroinactive ions redistribute themselves in the solution so that there is no potential gradient within the solution. This absence of a potential gradient to drive the migration therefore makes diffusion dominant.

Clearly migration is only important when dealing with ionic species and with charged surfaces or electrodes. By the addition of an excess of supporting electrolyte, it can be regarded as a negligible transport process.

1.4.5 Convective-Diffusion Equation

The use of diffusion alone to transport the reactants to the solid-liquid interface gives poor reproducibility due to natural convection, requiring forced convection to be used. However, the introduction of convective processes into the mass transport of species to and from the reactive surface requires knowledge of the velocity profile of the system for the mass transport to be quantifiable.

For solutions containing an excess of supporting electrolyte migration can be neglected so that the general mass transport equation (1.8) becomes

$$\underline{J}_i = c_i\underline{v} - D_i\underline{\nabla}c_i \tag{1.11}$$

The variation of c with time is given by

$$\frac{\partial c_i}{\partial t} = -\underline{\nabla}.\underline{J}_i = -\underline{div}\,\underline{J}_i \tag{1.12}$$

Combining equations (1.11) and (1.12) yields the general convective-diffusion equation

$$\frac{\partial c_i}{\partial t} = D_i\nabla^2 c_i - \underline{v}.\underline{\nabla}c_i \tag{1.13}$$

assuming D is not a function of spacial position and in the absence of migration. In three-dimensional Cartesian coordinates, substituting for the Laplacian operator, ∇^2, and for the scalar product of the velocity and grad c, this can be written as

$$\frac{\partial c_i}{\partial t} = D_i\left(\frac{\partial^2 c_i}{\partial x^2} + \frac{\partial^2 c_i}{\partial y^2} + \frac{\partial^2 c_i}{\partial z^2}\right) - \left(v_x\frac{\partial c_i}{\partial x} + v_y\frac{\partial c_i}{\partial y} + v_z\frac{\partial c_i}{\partial z}\right) \tag{1.14}$$

Before the convective-diffusion equation can be solved for the concentration profile, $c(x,y,z)$, expressions are required for the velocity profile, $\underline{v}(x,y,z)$.

The velocity profile for an incompressible fluid is calculated from the solution of two equations: the continuity equation

$$\frac{\partial \rho}{\partial t} = -\underline{\nabla}.(\rho \underline{v}) = 0 \tag{1.15}$$

and the Navier-Stokes equation [9]

$$\rho\frac{\partial \underline{v}}{\partial t} = -\underline{\nabla}P + \eta\nabla^2\underline{v} + f \tag{1.16}$$

which is Newton's second law applied to fluids with the left-hand side representing the rate of change of momentum of a volume element, and where P is the pressure, ρ is the density, η is the viscosity and f is the gravitational force acting on a unit volume of fluid. The Navier-Stokes equation is normally rewritten in terms of kinematic viscosity $\nu = \eta/\rho$

$$\frac{\partial \underline{v}}{\partial t} = -\frac{1}{\rho}\underline{\nabla}P + \nu\nabla^2\underline{v} + \frac{f}{\rho} \tag{1.17}$$

The first term represents the change in velocity due to the pressure acting on the fluid, the second represents the frictional forces and the final term represents the effect of natural convection due to density gradients. For most cases the forced convection is constant and $\partial\underline{v}/\partial t$ is zero.

Provided the Navier-Stokes equation can be solved, the mass transport of species in a hydrodynamic system can be calculated from the convective-diffusion equation (1.13).

1.5 Previous Studies

The dissolution and precipitation of calcium carbonate have been studied for over a century [10-13]. In CO_2-free systems the dissolution kinetics can be divided into two regimes; one at low pH where the reaction is with H^+, and one at high pH where the reaction is with H_2O. The kinetics of low pH dissolution has been covered elsewhere [14,15]. Most early studies concluded that the kinetics were controlled by the rate of mass transport of H^+ to the surface. Using a controlled hydrodynamic technique (*vide infra*), however, Compton and Unwin [14,15] demonstrated that at high rates of mass transport the reaction was in fact chemically controlled with the following heterogeneous rate law

$$J_{Ca^{2+}} / \mathrm{mol\,cm^{-2}\,s^{-1}} = 0.043[H^+]_o \qquad (1.18)$$

where $[H^+]_o$ is the surface H^+ concentration (mol cm^{-3}).

The kinetics of the high pH dissolution and precipitation of calcite has been reviewed elsewhere [16-18]. Most work has been carried out on calcium carbonate powders, using either "free-drift" or constant composition techniques. The former involves monitoring the variation of the solution composition with time. The latter, often referred to as "pH-stat" or "chemo-stat" methods, keep the solution composition constant by the addition of the appropriate ions to the solution as required. The more recent studies are outlined below.

1.5.1 Dissolution

Dorange and Guetchidjian [19] investigated the dissolution of marble in the presence of a CO_2-N_2 atmosphere for initial bulk pHs 4.5 - 6.7 and concluded the following rate law

$$\frac{d[Ca^{2+}]}{dt} = k([Ca^{2+}]_{eq} - [Ca^{2+}]) \qquad (1.19)$$

where $[Ca^{2+}]_{eq}$ represents the Ca^{2+} concentration at equilibrium for the pH concerned.

Morse and colleagues [20-24] have published a series of papers concerning the dissolution of calcium carbonate in sea water. Using a pH-stat technique, with the pH held constant at 7.17 and P_{CO2} at $10^{-2.58}$ atm by bubbling a CO_2-air mixture through the solution, the dissolution rate in a NaCl-$CaCl_2$ solution of similar composition to sea water was measured as $6x10^{-13}$ mol cm^{-2} s^{-1} with a reproducibility of ±10% [20]. Further experiments were carried out with this system and it was found that for pHs above 4 the rates of dissolution were much less than those predicted by diffusion control [21].

Early work by Plummer [25] investigated the dissolution of crushed Iceland spar in CO_2-saturated solutions (pH 3.91) by monitoring the solution pH with time. It was concluded that the dissolution was controlled by the kinetics of a surface reaction. From the pH response and solution equilibria, the Ca^{2+} ion concentration was calculated. The dissolution process was found to fit an empirical second order relation with respect to Ca^{2+} and H^+ until pH 5.9 was reached, after which higher reaction orders were observed.

Further experiments were carried out by Plummer *et al.* [26] on stirred Iceland spar powders over a range of CO_2 partial pressures (P_{CO2} 0 - 1 atm), pHs (2

- 7) and temperatures (5 - 60°C) using both pH-stat and free-drift methods. The former method was used for conditions far from equilibrium, whilst free-drift was used near equilibrium. From the variation of dissolution rate with pH three regions were identified. (i) At low pH (pH < 4.5 for $P_{CO2} \approx 0$, pH < 3.5 for $P_{CO2} \approx 1$ atm) the dissolution rate was independent of CO_2 partial pressure but proportional to the bulk H^+ activity. (ii) At intermediate pHs the dissolution was dependent on both P_{CO2} and a_{H+}. (iii) At high pH (pH > 6.5 for $P_{CO2} \approx 0$, pH > 5.5 for $P_{CO2} \approx 1$ atm) the dissolution rate was independent of pH and, for low P_{CO2} (< 1 - 3%), the forward rate was independent of P_{CO2}. Analysis of the data led to the empirical equation [16,26]

$$rate\ /\mathrm{mmol\,cm^{-2}s^{-1}} = k_1 a_{H^+} + k_2 a_{H_2CO_3^*} + k_3 a_{H_2O} - k_4 a_{Ca^{2+}} a_{HCO_3^-} \qquad (1.20)$$

at constant temperature and P_{CO2}, where a_i refer to bulk ion activities. The rate constant k_1 was found to be a function of stirring rate, whereas k_2 and k_3 were not significantly dependent on stirring. The values of the rate constants at 25°C were k_1 = 0.051 cm s^{-1} (1800 - 2300 rpm), $k_2 = 3.5 \times 10^{-5}$ cm s^{-1} and $k_3 = 1.2 \times 10^{-7}$ cm s^{-1}.

Plummer *et al.* [16,26] proposed a mechanistic model to rationalise equation (1.20) and to derive a theoretical expression for k_4. This was developed from the adsorption layer heterogeneous reaction model of Mullin [27]. They assumed the existence of a thin adsorption or surface layer, in which the species were loosely bound to the surface with relatively low mobility. The reaction sites on the crystal surface were assumed to be at discontinuities. The mechanism proposed consisted of three simultaneous surface reactions [16]

$$CaCO_3 + H^+_{(o)} \rightleftharpoons Ca^{2+}_{(s)} + HCO^-_{3\,(s)} \tag{1.21}$$

$$CaCO_3 + H_2CO_{3\,(o)} \rightleftharpoons Ca^{2+}_{(s)} + 2HCO^-_{3\,(s)} \tag{1.22}$$

$$CaCO_3 + H_2O_{(o)} \longrightarrow Ca^{2+}_{(s)} + HCO^-_{3\,(s)} + OH^-_{(s)} \tag{1.23}$$

with associated back reactions

$$\left|Ca^{2+} + HCO^-_3\right|^+_{(o)} + CO^{2-}_{3\,(s)} \longrightarrow CaCO_3 + H^+_{(s)} + CO^{2-}_{3\,(s)} \tag{1.24}$$

$$\left|Ca^{2+} + HCO^-_3\right|^+_{(o)} + HCO^-_{3\,(s)} \longrightarrow CaCO_3 + H_2CO_{3\,(s)} \tag{1.25}$$

$$\left|Ca^{2+} + HCO^-_3\right|^+_{(o)} + OH^-_{(s)} \longrightarrow CaCO_3 + H_2O_{(s)} \tag{1.26}$$

where the subscripts (o) and (s) represent the base of the boundary layer and the adsorbed layer, respectively. Distinction between free Ca^{2+} and HCO_3^- ions and the ion pair $CaHCO_3^+$ was not made, hence the $|Ca^{2+} + HCO_3^-|^+$ terms in the above reaction scheme. This mechanism assumed the interaction of reactants in the boundary layer with species adsorbed at reaction sites. Furthermore, it was assumed that the surface species were in equilibrium with calcite and that the boundary layer activities were equal to the bulk activities, for all species other than H^+ [25]. Reaction (1.21) was also assumed to be mass transport controlled. Given these assumptions, the mechanism agreed with the empirical rate law (1.20) and defined k_4 as

$$k_4 = \frac{K_{a2}}{K_{sp}}\left\{k_1 + \frac{1}{a_{H^+_{(s)}}}\left(k_2 a_{H_2CO^*_{3(s)}} + k_3 a_{H_2O_{(s)}}\right)\right\} \tag{1.27}$$

where K_{a2} is the second acid dissociation constant of carbonic acid and K_{sp} the solubility product of calcite. Plummer *et al.* [16] compared their rate equation with previous studies. Most dissolution rates were within a factor of 10 and many within

a factor of 2. The larger discrepancies, however, were thought to be significant. The model predicted that adding Ca^{2+} to the system in CO_2-free conditions should have little effect on the dissolution rate. However, a dissolution rate decrease had been observed on adding $CaCl_2$ [28,29]. Worse agreement was found with calcite precipitation data, with the calculated rates of growth being 4 - 68 times greater than observed, though usually 10 - 20 times faster. This led to the identification of problem areas, namely the need for the quantification of the mass transport to the calcite surface, the uncertainty in the surface area and reaction site density and the difficulty in defining the surface pH.

It has been reported [18] that Busenburg and Plummer refined their model. For saturations of $\Omega < 0.6$, where Ω is the saturation ratio defined as $a_{Ca}a_{CO3}/K_{sp}$, the back (precipitation) reaction could be described by the Langmuirian adsorption of the participating ions. Nearer equilibrium the dissolution kinetics could be described by a term similar to the Freundlich adsorption isotherm.

The dissolution of both calcite powders and crystals have been extensively studied by Sjöberg and Rickard. Early work by Sjöberg [28] involved measuring the dissolution rate of $CaCO_3$ powder under free-drift conditions by monitoring the bulk pH. Experiments were carried out at an ionic strength of 0.7 M (KCl) and an initial pH of 8 under an atmosphere of O_2-free N_2, though the solutions were not degassed of CO_2. In the presence of added $CaCl_2$ the following empirical dissolution rate law was concluded

$$\frac{\partial[Ca^{2+}]}{\partial t} = kA\left(\sqrt{K_{sp}} - \sqrt{[Ca^{2+}][CO_3^{2-}]}\right) \qquad (1.28)$$

where k is a constant, A the surface area and K_{sp} the calcite solubility product. The final, equilibrium pH was 10.08 at 20 ± 1°C which gave the solubility product as 6.05×10^{-14} mol^2 cm^{-6}. However, the dissolution rate was found to be dependent on the stirring rate used.

Further work was carried out by Sjöberg [29] on powders and calcite single crystals using both the free-drift and pH-stat methods. The dissolution reaction was found to be pH independent above pH 4, with an apparent activation energy of 35 kJ mol^{-1} for single crystals, implying some chemical control. The addition of Ca^{2+} ions decreased the dissolution rate, due to the increasing importance of a back reaction. The effect of Ca^{2+} was thought to fit the Langmuir adsorption isotherm.

A major improvement in experimental design was made by Sjöberg and Rickard [30,31] by incorporating a calcite crystal in a rotating disc apparatus. This gave well-defined hydrodynamics and therefore calculable mass transport of reactants to the calcite surface, which none of the powder experiments had. However the dissolution rate was still measured by monitoring changes to the bulk solution pH, and therefore was insensitive to the surface processes.

It was argued that in neutral and alkaline solutions the dissolution was controlled by mixed kinetics, i.e. interdependent chemical and transport processes. Transport across the diffusion layer thickness was given by

$$\frac{\partial c}{\partial t} = \frac{k_T A (c_o - c_{bulk})}{V} \qquad (1.29)$$

where k_T was a transport rate constant, V the volume of solution and c_o and c_{bulk} the concentrations of the dissolving species at the surface and in the bulk respectively.

Implicit in equation (1.29) are the assumptions that the species concerned is not involved in homogeneous reactions in the boundary layer or bulk solution [25]. The rate of the chemical reaction was said to be proportional to a function of the chemical potential difference between the concentration of the dissolving $CaCO_3$ at the surface and the concentration at equilibrium, c_{eq}

$$\left.\frac{\partial c}{\partial t}\right|_C = \frac{k_C A(c_{eq} - c_o)^n}{V} \tag{1.30}$$

where k_C was a chemical reaction rate constant. Equating equations (1.29) and (1.30), which assumes that the species is not involved in homogeneous reactions within the boundary layer [25], gave the following rate law for $n = 1$

$$\frac{\partial c}{\partial t} = \frac{k_T k_C}{(k_T + k_C)} \frac{A(c_{eq} - c_{bulk})}{V} \tag{1.31}$$

The empirical rate equation (1.28) was shown to be equivalent to this rate law [31]. Using this model the initial dissolution rate was written in terms of the diffusion layer thickness for a rotating disc and this gave [31]

$$\frac{1}{rate} = \frac{1.61\,\nu^{1/6}}{D^{2/3} c_{eq}\,\omega^{1/2}} + \frac{1}{c_{eq} k_C} \tag{1.32}$$

where ν was the kinematic viscosity of the solution, D the diffusion coefficient and ω the rotational velocity of the rotating disc. Experiments [31] gave linear plots of $1/rate$ against $1/\sqrt{\omega}$ from which it was concluded that equation (1.31) gave an accurate description of the kinetics and that calcite dissolution was first order with respect to H_2O.

In this high pH region (pH > 5.5) using the rotating disc apparatus in a pH-stat mode Sjöberg and Rickard found [32] that the dissolution rate was independent of pH but was dependent on the nature of the calcium carbonate; Carrara marble

dissolving faster than Iceland spar. In their model they proposed that only Ca^{2+}, CO_3^{2-} and H_2O were present in the "diffusion layer" and rapid protonation of the carbonate ion occurred at the diffusion layer boundary. The onset of H^+-dependent kinetics was argued to occur when "H^+ penetrated the diffusion layer and reached the calcite surface". Their chemical step rate constant, k_c, was shown [33] to be independent of added bulk calcium ion concentrations up to 0.2 mM. It was concluded that the reduction in dissolution rate on adding Ca^{2+} ions was purely due to a reduction in diffusion rate and not due to inhibition of the chemical step, as concluded earlier [29]. The rotating disc method was also used to investigate the temperature dependence of the dissolution rate with an Arrhenius activation energy for k_c being 46 ± 4 kJ mol^{-1} for Iceland spar [34].

Compton and Daly also used the rotating disc method to study the dissolution of Iceland spar crystals [35-37]. In the pH range 3.0 - 6.2 the dissolution rate was monitored by a Ca^{2+} ion selective electrode, and was found to reasonably follow a Plummer type equation of the form [35]

$$J_{Ca^{2+}} = k_1[H^+] + k_2[H_2CO_3] + k_3 \qquad (1.33)$$

The value of k_3 was shown to be critically dependent on the surface morphology of the calcite [36]. For a well-polished crystal rinsed in 10^{-3} M HCl $k_3 = 1.4 \times 10^{-10}$ mol cm^{-2} s^{-1}, which was very similar to that of Plummer *et al.*, but on increasing the surface roughness k_3 was found to increase. Polishing the crystal at an angle to the {100} cleavage planes caused an enhanced dissolution rate, which was attributed to the increased number of kinks on higher index planes [36]. The kinetics at higher pHs were probed by allowing the dissolution to proceed to

saturation [37]. The experimental data was found to fit the rate equations of Sjöberg (equation (1.28)) and Plummer.

Schott *et al.* [38] used the pH-statted rotating disc technique to study the dissolution of strained calcite and found that for increasing the dislocation density from 10^6 to 10^9 cm^{-2} increased the dissolution rate by a factor of 2 or 3.

Buhmann and Dreybrodt [39-42] have considered calcite dissolution in karst formations for both open and closed systems. They derived a model for the turbulent and laminar flow of a solution film across the calcite surface, with the film in contact with the atmosphere in the open case. Three rate determining steps were treated simultaneously; the heterogeneous kinetics at the calcite-water interface, modelled using the Plummer equation (1.20); the slow conversion of CO_2 to H_2CO_3; and the mass transport of the dissolved species to and from the surface. Experiments were carried out with a stationary or stirred solution layer sitting over the calcite surface [39,40]. After a given time the solution was extracted and analysed for $[Ca^{2+}]$. In all cases the dissolution or precipitation rates could be described by an equation similar in form to that of Rickard and Sjöberg (1.31) and agreement was found within a factor of 2.

Chou *et al.* [43] studied the dissolution of calcite powder in a fluidized bed reactor [44], which created high turbulence, supposedly providing better mixing than conventional stirring. The forward dissolution rate was of the same form as the Plummer equation but the backward precipitation rate decreased rapidly with increasing $a_{Ca}a_{HCO3}$, in contradiction to Plummer *et al.*. Instead the activity product of Ca^{2+} and CO_3^{2-} was proportional to the precipitation rate, so it was concluded that the net dissolution rate was given by

$$J_{net} = k_1 a_{H^+} + k_2 a_{H_2CO_3^*} + k_3 a_{H_2O} - k_4 a_{Ca^{2+}} a_{CO_3^{2-}} \quad (1.34)$$

with k_1, k_2, k_3 being 0.089, 5.0×10^{-5}, 6.5×10^{-8} cm s^{-1} and k_4 being 0.015 cm^4 mol^{-1} s^{-1}.

1.5.2 Precipitation

The kinetics of calcite precipitation, especially in marine environments, have received much study. Nancollas and Reddy [45,46] used a free drift method with calcite seed crystals and the precipitation rate was measured by monitoring the pH and $[Ca^{2+}]$ by means of ^{45}Ca isotope exchange or atomic absorption spectroscopy. The precipitation rate, after an initial surge, was found to be independent of stirring rate and to follow a second order rate law

$$\frac{d[Ca^{2+}]}{dt} = -kA\left([Ca^{2+}][CO_3^{2-}] - \frac{K_{sp}}{\gamma_{\pm}^2}\right) \quad (1.35)$$

where $\gamma_{\pm}$ is the divalent ion activity coefficient. The activation energy was calculated as 46 ± 4 kJ mol^{-1} [46] which is in good agreement with later findings of Wiechers *et al.* [47] of 43.1 ± 3.8 kJ mol^{-1}, Kazmierczak *et al.* [48] of 39.2 ± 3.6 kJ mol^{-1} and Inskeep and Bloom [49] of 48.1 kJ mol^{-1}. This activation energy was concluded to be supportive of a surface controlled mechanism for crystal growth.

Another rate law for calcite growth was proposed by Reddy [50,51] and Reddy and Nancollas [52] and this time was of the form

$$rate = kA\left([Ca^{2+}] - [Ca^{2+}]_{eq}\right)^2 \quad (1.36)$$

The maximum variation in the equilibrium calcium ion concentration, $[Ca^{2+}]_{eq}$, for the growth experiments for this equation was 10%, whereas that for equation (1.35) was much greater [52].

Plummer *et al.* [16] noted the similarity between the Nancollas and Reddy equation (1.35) and their equation (1.20), which under conditions of high pH and low P_{CO2} reduced to

$$rate = k_3 a_{H_2O}\left(1 - \frac{a_{H^+}}{a_{H^+_{(s)}}}\Omega\right) \tag{1.37}$$

where Ω is the saturation ratio defined as $a_{Ca}a_{CO3}/K_{sp}$. The additional term of the proton activity ratio, which was not present in equation (1.35), was calculated to be just below unity for low P_{CO2} [16]. It was suggested [26] that the Plummer model might be applicable to calcite precipitation. This was investigated by Reddy, Plummer and Busenburg [53]. From the analysis of $[Ca^{2+}]$ with time for seeded growth experiments at P_{CO2} between 0.03 and 0.3 atm they found that plots of log *rate* versus log Ω, log (Ω - 1) and log ($[Ca^{2+}]$ - $[Ca^{2+}]_{eq}$) were all non-linear. The rate was calculated by the Plummer equation, assuming that the surface P_{CO2} was the same as that of the bulk. The surface a_{H+} was calculated assuming equilibrium at the surface. Agreement within a factor of 3 was seen between observed and calculated rates for P_{CO2} at 0.029 and 0.096 atm. However marked discrepancies were observed at higher P_{CO2} and nearer equilibrium (Ω < 5) with the observed precipitation rate being less than expected.

A variation of the pH-stat method was used by Kazmierczak, Tomson and Nancollas [48] as an attempt to keep all solution species at the same concentration during crystallisation. They concluded that the precipitation rate was given by the following rate equation

$$\frac{d[Ca^{2+}]}{dt} = -kA\left(\sqrt{a_{Ca^{2+}}a_{CO_3^{2-}}} - \sqrt{K_{sp}}\right)^2 \tag{1.38}$$

where a_i are activities and K_{sp} is the thermodynamic solubility product of calcite. In this form, the rate constant k was found to be independent of the ionic strength of the supersaturated solution over a wide range (0.007 to 0.20 mol dm^{-3}).

Zhong and Mucci [54] carried out seeded calcite growth in seawater solutions of various salinities and fitted the data to an empirical rate law of the form

$$rate = k(\Omega - 1)^n \tag{1.39}$$

with the empirical reaction order, n, between 2.5 and 3.3 and found the precipitation rates to be "fairly" independent of the salinity. This empirical rate law has also been used by other investigators [49,55-58].

Another model, first developed by Davies and Jones [59,60] for the precipitation of silver chloride, assumes that (i) there is a monolayer of hydrated ions covering the surface and (ii) hydration or dehydration of the lattice ions at the surface sites precedes dissolution or precipitation. This was based on the double layer model with the surface concentrations given by the Boltzmann distribution

$$[Ca^{2+}]_{(s)} = [Ca^{2+}]\exp\left(-\frac{2F\phi}{RT}\right) \tag{1.40}$$

$$[CO_3^{2-}]_{(s)} = [CO_3^{2-}]\exp\left(\frac{2F\phi}{RT}\right) \tag{1.41}$$

It was assumed that the surface concentrations of Ca^{2+} and CO_3^{2-} were equal, thus

$$[Ca^{2+}]_{eq\,(s)} = \frac{K_{sp}^{1/2}}{\gamma_{\pm}} \tag{1.42}$$

and also from equations (1.40) and (1.41)

$$\exp\left(\frac{2F\phi}{RT}\right) = \left(\frac{[Ca^{2+}]}{[CO_3^{2-}]}\right)^{1/2} \tag{1.43}$$

The rate of growth was assumed to be proportional to the amount of Ca^{2+} and CO_3^{2-} available for growth, i.e.

$$rate = k\gamma_{\pm}^2\left\{[Ca^{2+}]_{(s)} - [Ca^{2+}]_{eq\,(s)}\right\}\left\{[CO_3^{2-}]_{(s)} - [CO_3^{2-}]_{eq\,(s)}\right\} \tag{1.44}$$

which on substitution gave

$$rate = k\gamma_{\pm}^2\left\{\sqrt{[Ca^{2+}][CO_3^{2-}]} - \sqrt{\frac{K_{sp}}{\gamma_{\pm}^2}}\right\}^2 \tag{1.45}$$

The assumption that the surface concentrations of the cation and anion are equal, however, has been shown to be invalid for calcite [61,62].

House [63] tested several of the proposed rate laws against data from seeded crystal growth experiments in supersaturated and metastable calcium bicarbonate solutions by monitoring solution pH and conductivity. He concluded that the rate equations proposed by Nancollas and Reddy (equation (1.35)), Reddy (equation (1.36)) and a screw dislocation model of Nielsen [64] gave poor agreement over the supersaturation range. The Davies and Jones (equation (1.45)) gave good agreement over a limited range, while that of Plummer *et al.* (equation (1.20)) was consistent with the data, though unique growth curves were not obtained. The temperature dependence of the rate constants of these two equations was also investigated [65].

Inskeep and Bloom [49] similarly investigated the validity of the rate laws for seeded growth using a pH-stat technique for pH 8.25 - 8.70, $P_{CO2} < 0.01$ atm and ionic strengths of 0.015 - 0.10 mol dm^{-3}. One form of the Davies-Jones model and the Reddy and Nancollas equation (1.36) were found not to fit the data. The Davies-Jones model written in terms of surface potential (equation (1.45)) was consistent with the data but was discarded because of the errors inherent in the

derivation. The Plummer equation (1.20) was consistent with most of their data but broke down when the ratio of initial $[Ca^{2+}]/[CO_3^{2-}]$ was varied. Best agreement was found with the Nancollas and Reddy equation (1.35) when modified to account for ionic strength effects.

Christoffersen and Christoffersen [66] performed calcite seeded growth experiments at constant pH and explained the kinetics in terms of a spiral growth mechanism proposed by Nielsen [64,67]. The overall rate of growth was given by

$$rate\ /\mathrm{mol\ s^{-1}} = \frac{0.1a\left(\frac{\nu_{in}}{\nu}\right)K_{ad}c_{eq}}{\left(\frac{\gamma}{k_B T}\right)\exp\left(\frac{\gamma}{k_B T}\right)}(S-1)S^{1/2}\ln S \qquad (1.46)$$

where a is the mean lattice ionic diameter, ν_{in} the frequency of a species entering a kink from a neighbouring site, ν the number of ions in a formula unit, K_{ad} an adsorption constant, c_{eq} the equilibrium concentration, γ the edge work and S the supersaturation expressed as $([Ca^{2+}][CO_3^{2-}]/K_{sp})^{1/\nu} = \Omega^{1/\nu}$.

1.5.3 Inhibition of Dissolution/Precipitation

The effect of various species on the reaction kinetics has also been widely investigated, as well as the study of sorption and coprecipitation, as summarised in Appendix 1. Such species may affect the nucleation of calcium carbonate, the rate of dissolution, aragonite to calcite transformations or coprecipitation of species with calcium carbonate. Magnesium has received the widest attention because of its occurrence in natural waters. The inhibition of calcite dissolution/precipitation kinetics by Mg^{2+} is reviewed in detail in Chapter 5. Phosphates have also received much attention because of their potency as inhibitors. Heavy metal cations have been studied due to the concern of the effects of pollution on aquatic environments.

Organic compounds have also received some study due to their potential as scale inhibitors.

A few models have been proposed to account for the dissolution and growth of crystals, and are discussed by House [68]. The Burton, Cabrera and Frank [69] model has been widely used and introduced the concept of steps on surfaces and kinks within steps, as shown in Figure 1.4. Such sites are more exposed and more reactive and, as such, are thought to be where dissolution, precipitation and inhibition by foreign species occur. In the case of crystal growth, once the growth unit has been transported near to the surface, adsorption of the growth unit may occur. Partial dehydration of the species is often believed to happen at this stage. This growth unit can then diffuse across the surface to a step, followed by incorporation of the growth unit into a kink on the step. This latter process may involve further dehydration.

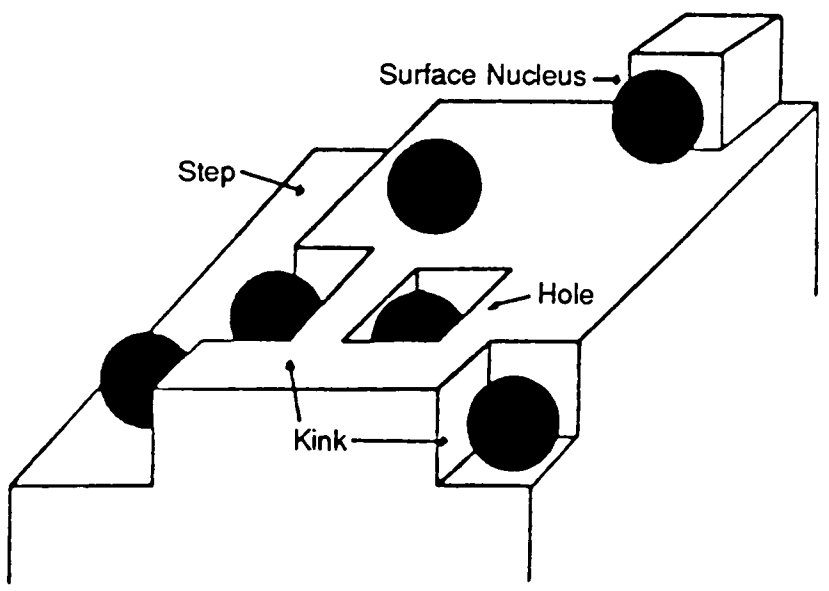

Figure 1.4. Schematic diagram of a crystal surface according to the Burton, Cabrera and Frank model showing terraces, steps and kinks, together with adsorbed ions shown in black.

1.6 Hydrodynamic Approach to the Study of Calcite Dissolution

In most of the studies into calcite kinetics cited above the hydrodynamics of the system were completely ill-defined. Where mechanisms were inferred from the

observed rate laws, gross assumptions had often to be made regarding the surface concentrations of the species concerned. Usually the surface concentrations were assumed to be the same as concentrations in bulk solution. As outlined in Section 1.3, in order to define the kinetics at the solid-liquid interface the surface concentrations of the reactive species must be known. To achieve this the mass transport of the reactants to the surface must be well-defined and quantifiable. Furthermore the mass transport of species to the detector, which is used to monitor the reaction rate, must also be known.

In many cases the solutions were stirred in a mathematically ill-defined fashion. The rotating disc studies did, however, have controlled mass transport of the reactants to the calcite surface but monitored the reaction rate by detecting changes in bulk solution. Such detection is insensitive to the surface processes. To allow much more sensitive probing of concentrations at the calcite surface, the channel flow cell methodology, as used by Compton *et al.* [15], was adapted for the study of calcite dissolution at high pH.

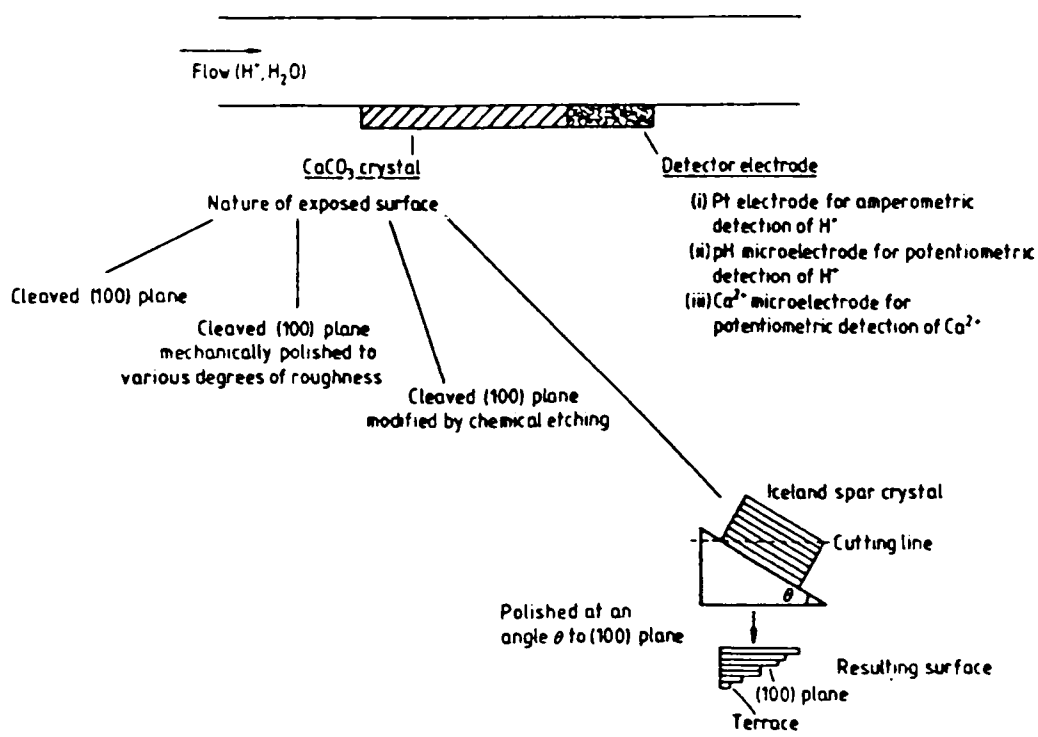

Figure 1.5. Flow cell strategy for the investigation of the dissolution kinetics of calcium carbonate.

The channel cell consisted of a rectangular duct through which solution flowed in a laminar fashion. Inset in one wall of the channel was a calcite crystal immediately downstream of which was a detector, as shown in Figure 1.5. One fundamental advantage of this technique over all the others reviewed in the literature was that the mass transport of the reactants to the calcite-solution interface and that from the interface to the detector was well defined. In fact the mass transport equation for the channel cell is known and can be solved. The second advantage of the technique was the ability to control accurately the surface pre-treatment of the calcite crystal, e.g. how finely the crystal is polished, whether or not it is first etched with mineral acids, or which crystal plane is used. Thirdly detection was adjacent to the reactive surface and therefore more accurately probed the surface reaction.

The hydrodynamics of the channel cell and the solution of the mass transport equations will be discussed further in the next chapter.

CHAPTER 2

MASS TRANSPORT IN THE CHANNEL CELL

2.1 Introduction

In this chapter the hydrodynamics of the channel flow cell are examined, together with the solution of the mass transport equation. The analytical solution to the convective-diffusion equation is given in the transport limited case for the associated channel electrode, where the reactive surface of the channel is an electrode. In addition, a powerful numerical method is described, which is used to solve the mass transport equation for the channel cell.

2.2 Hydrodynamic Flow Systems

In hydrodynamic flow systems the mass transport of reactants to, and transport of products away from, the reactive surfaces is controlled. Forced convection in such systems is advantageous in that the reactant is being supplied continuously, so a reaction can be studied at steady state.

2.2.1 Diffusion Layer

A useful concept in such systems is that of the diffusion layer. Its boundary marks the border between the region where a species has its bulk concentration and the region where the concentration has been altered due to the surface reaction, see Figure 2.1. Inside the diffusion layer there is no convection in the direction of interest and therefore a concentration gradient is set up, due to a depletion of reactants and formation of products. This concentration gradient gives rise to diffusion. It must be noted, however, that convection perpendicular to this diffusion can still be a significant process within the diffusion layer. If the

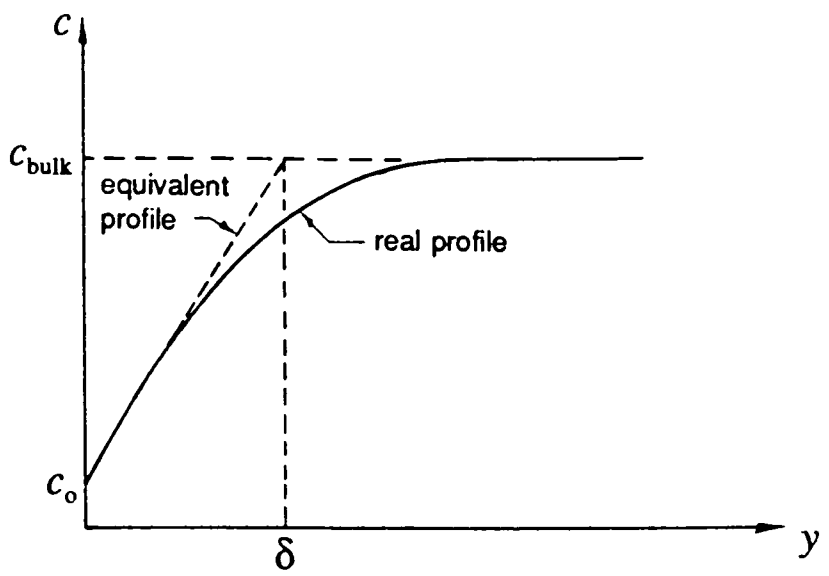

Figure 2.1. The variation of reactant concentration with distance away from the reactive surface giving rise to the concept of a diffusion layer.

concentration gradient is assumed to be linear then the flux, J, at the electrode is given by

$$J = D\frac{\partial c}{\partial y} = D\frac{(c_{bulk} - c_o)}{\delta} \qquad (2.1)$$

where δ is the thickness of the Nernst diffusion layer and c_o and c_{bulk} are the concentrations at the surface and in bulk solution, respectively. The diffusion limited flux occurs when all the reactant reaching the interface reacts, i.e. $c_o = 0$, in which case

$$J_{lim} = \frac{Dc_{bulk}}{\delta} \qquad (2.2)$$

At low rates of convection the diffusion layer is thicker, so the concentration gradient within the diffusion layer is smaller and thus diffusion of the species will be at a slower rate. Conversely with fast convection the diffusion layer is thin giving rise to faster diffusion.

The channel flow cell, which was used in this thesis to probe calcite dissolution, will now be examined in detail.

2.3 Hydrodynamics of the Channel Cell

The channel cell has the reactive surface embedded in one wall of a rectangular duct, along which solution flows. A detector electrode is located flush to the channel wall immediately downstream of the reactive interface, i.e. a calcite crystal. This is shown in Figure 2.2, along with the co-ordinate system used and some of the cell parameters.

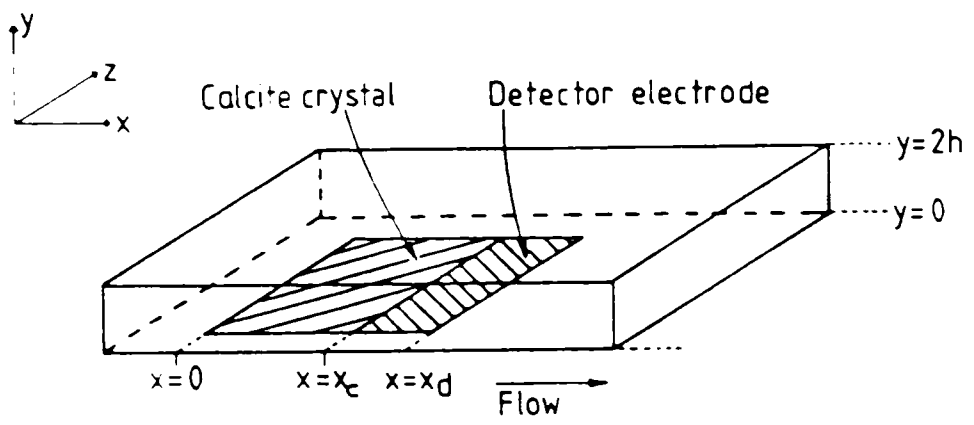

Figure 2.2. Schematic diagram of the channel cell.

The nature of the fluid flow is described by the Reynolds number [70]

$$Re = \frac{v_o h}{\nu} \tag{2.3}$$

where v_o is the solution velocity at the centre of the channel, h is the half-height of the channel and ν the kinematic viscosity of the solution. Below a critical value of Re = 2000 [70-72] the flow is laminar; above this, flow is turbulent. Under the practical conditions used in this thesis, flow was always laminar and therefore this will be assumed henceforth.

As solution flows through the channel, friction at the walls retards the flow at the edges of the channel. The boundary at which the flow rate is less than the initial value moves towards the centre of the channel as the flow proceeds, due to viscous forces, as shown in Figure 2.3. After an entry length, l_e, given

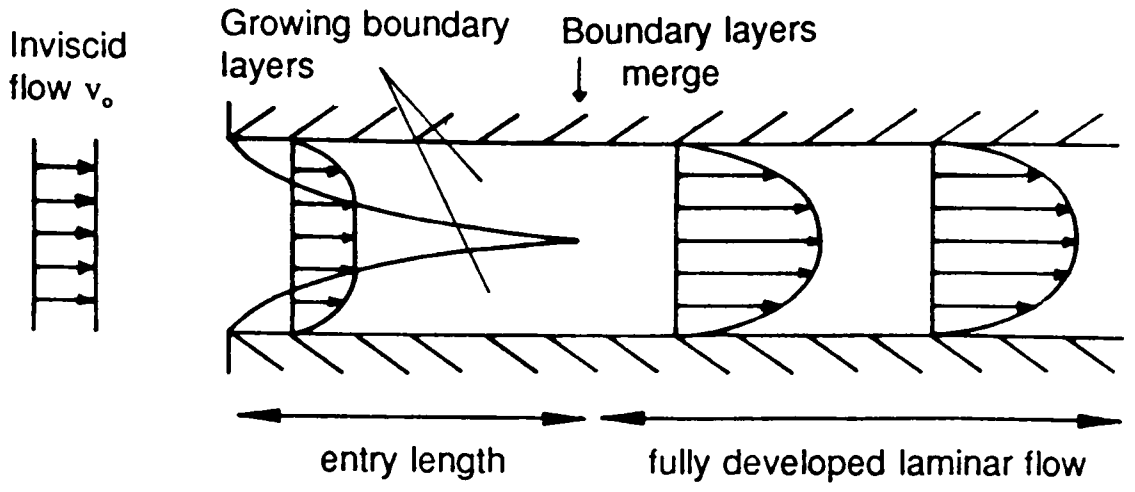

Figure 2.3. Hydrodynamic flow in the channel cell under laminar conditions. Parabolic Poiseuille flow is established after a lead-in length.

approximately by [73]

$$l_e = 0.1hRe \tag{2.4}$$

Poiseuille flow is established. In this regime the laminar flow is parabolic in shape and the velocities along the Cartesian axes are

$$v_x = v_o\left(1 - \frac{(h-y)^2}{h^2}\right) \tag{2.5}$$

and

$$v_y = 0 \; ; \quad v_z = 0 \tag{2.6}$$

Mass transport of species in a hydrodynamic system, as discussed in Chapter 1, are described by the following general differential equation containing diffusion and convection terms

$$\frac{\partial c_i}{\partial t} = D_i \nabla^2 c_i - \left(v_x \frac{\partial c_i}{\partial x} + v_y \frac{\partial c_i}{\partial y} + v_z \frac{\partial c_i}{\partial z}\right) \tag{2.7}$$

where c_i is the concentration of the ith species and D_i is its diffusion coefficient (and assuming no homogeneous chemical reactions).

The convective-diffusion equation (2.7) can be rewritten given equation (2.6), together with the assumption that axial diffusion will be small compared to axial convection and neglecting lateral diffusion.

$$\frac{\partial c}{\partial t} = D\frac{\partial^2 c}{\partial y^2} - v_x\frac{\partial c}{\partial x} \tag{2.8}$$

2.4 Analytical Solution of the Channel Cell Convective-Diffusion Equation

Equation (2.8) was solved by Levich [74] who applied the Lévêque approximation [75] which linearises the parabolic velocity profile.

$$v_x \approx 2v_o\left(1 - \frac{h-y}{h}\right) \tag{2.9}$$

This approximation is valid for $y \approx 0$ or $2h$, i.e. close to the channel walls. Under steady-state conditions, together with the Lévêque approximation, the convective-diffusion equation (2.8) becomes

$$D\frac{\partial^2 c}{\partial y^2} = \frac{2v_o y}{h}\frac{\partial c}{\partial x} \tag{2.10}$$

Applying the boundary conditions for a simple transport-limited heterogeneous reaction

$$\begin{aligned} &0 \le x \le l\,, \quad y = 0\,; \qquad c = 0 \\ &x < 0 \quad \text{or} \quad y \to \infty\,; \qquad c = c_{bulk} \end{aligned} \tag{2.11}$$

yields the transport-limited flux to the reactive surface, as given in equation (2.2) where the diffusion layer thickness, δ, is [74,76]

$$\delta = 0.982\left(\frac{Dhl}{v_o}\right)^{1/3} \tag{2.12}$$

Hence the total mass transport limited flux to the interface is

$$J_{\text{lim}} = 0.925 c_{bulk} \left(\frac{D^2 V_f}{h^2 l d} \right)^{1/3} \tag{2.13}$$

where c_{bulk} is the bulk concentration of the electroactive species (mol cm^{-3}), l the length of the reactive surface (cm) and V_f the volume flow rate (cm^3 s^{-1}).

In the specific case where the reactive surface is an electrode, equation (2.13) can be rewritten using equation (1.2) to give the transport limited current for a simple n electron reduction or oxidation reaction. This is the Levich equation for the channel electrode [74]

$$I_{\text{lim}} = 0.925 n F w c_{bulk} \left(\frac{x_e^2 D^2 V_f}{h^2 d} \right)^{1/3} \tag{2.14}$$

where I_{lim} is the transport-limited current (ampere), n is the number of electrons transferred, F is Faraday's constant (C mol^{-1}), w the electrode width (cm), x_e the electrode length (cm) and d the channel width (cm). The validity of the Levich equation with its associated assumptions will now be discussed.

First the Lévêque approximation, as stated above, only applies close to the electrode. This causes no problem when the diffusion layer thickness is small, but when it is comparable to the channel height this approximation breaks down. In this case (the so called "thin layer" limit) the limiting current is given by [77]

$$I_{\text{lim}} = n F V_f c_{\text{bulk}} \tag{2.15}$$

According to the expression for the diffusion layer thickness, equation (2.12), the thin layer limit only occurs with very low flow rates or long electrodes.

The second assumption is that axial diffusion is negligible compared to convection. Flanagan and Marcoux [78] solved equation (2.8) numerically using a

simple explicit method and demonstrated that this assumption was valid under the same conditions as the Lévêque approximation.

The assumption that lateral diffusion is negligible can break down giving rise to "edge effects" [79], which cause larger limiting currents than would otherwise be expected. Such phenomena only occur for short electrodes (< 10 μm) or very low flow rates and has been examined analytically by Oldham [79] and numerically by Amatore [80]. Deviations from the Levich equation observed [81-83] at slow flow rates are either attributable to this effect or to natural convection, as opposed to forced convection, becoming significant.

The diffusion layer thickness in the channel cell varies with distance along the x-axis. As x increases so does the diffusion layer (equation (2.12)), hence the channel electrode is "non-uniformly accessible". Non-uniform accessibility had been thought to be a major disadvantage in that it made it much more difficult to calculate kinetic parameters from limiting currents. However introduction of the Lévêque approximation greatly simplified the analytical solution of the mass transport equations, giving a linear velocity relationship at the electrode surface, unlike the parabolic terms at the surface of the rotating disc and wall-jet electrodes.

2.5 Numerical Solution of the Channel Cell Convective-Diffusion Equation

In Section 2.4 above the mass transport equation for the channel cell was solved analytically using the Lévêque approximation. Alternatively numerical methods can be used and are particularly useful under conditions where the assumptions made in the analytical solution are no longer valid or complex kinetic processes make analytical solution difficult.

Many different numerical approaches have been used to solve the mass transport equations [84]. All involve dividing up the solution with a grid of finite elements. Anderson and Moldoveanu [77] explored three such numerical methods applied to the channel electrode, namely the simple explicit (SE) method, the Crank-Nicolson implicit (CNI) method [85] and the backward implicit (BI) method, and found the BI finite difference (BIFD) method superior, with excellent agreement with theoretical [86] and semi-empirical [87] results. The BI method was first developed by Laasonen [88] and has been used to study mechanistic electrochemistry at the channel electrode [77,89,90].

The advantages of the BI approach are as follows:

(a) The upstream edge of the reactive surface is a point of discontinuity, since the surface concentration suddenly changes at this point. This causes uncertainty over what concentration value to use at this point in the boundary conditions. With the SE method the result depends on the value chosen for this point and on the size of the grid used. The CNI approach also requires knowledge of this but it would appear to have no influence on the computed results. Only the BI calculation does not need knowledge of the concentrations at this discontinuity point.

(b) The BI method required at least 100 times fewer grid points in the x-direction than for SE to obtain convergence, thus saving computing time.

(c) The CNI method offers no advantage over the BI approach, and is more complex.

2.5.1 Backwards Implicit Finite Difference Solution of the Channel Cell Convective-Diffusion Equation

The application of the BIFD approach to a simple heterogeneous reaction has been considered [89] where a species A undergoes a mass transport limited reaction at a reactive surface in the channel. The reaction in question could equally be a one electron redox reaction at a channel electrode or a heterogeneous reaction between species A and an insulator surface. This case is illustrated below.

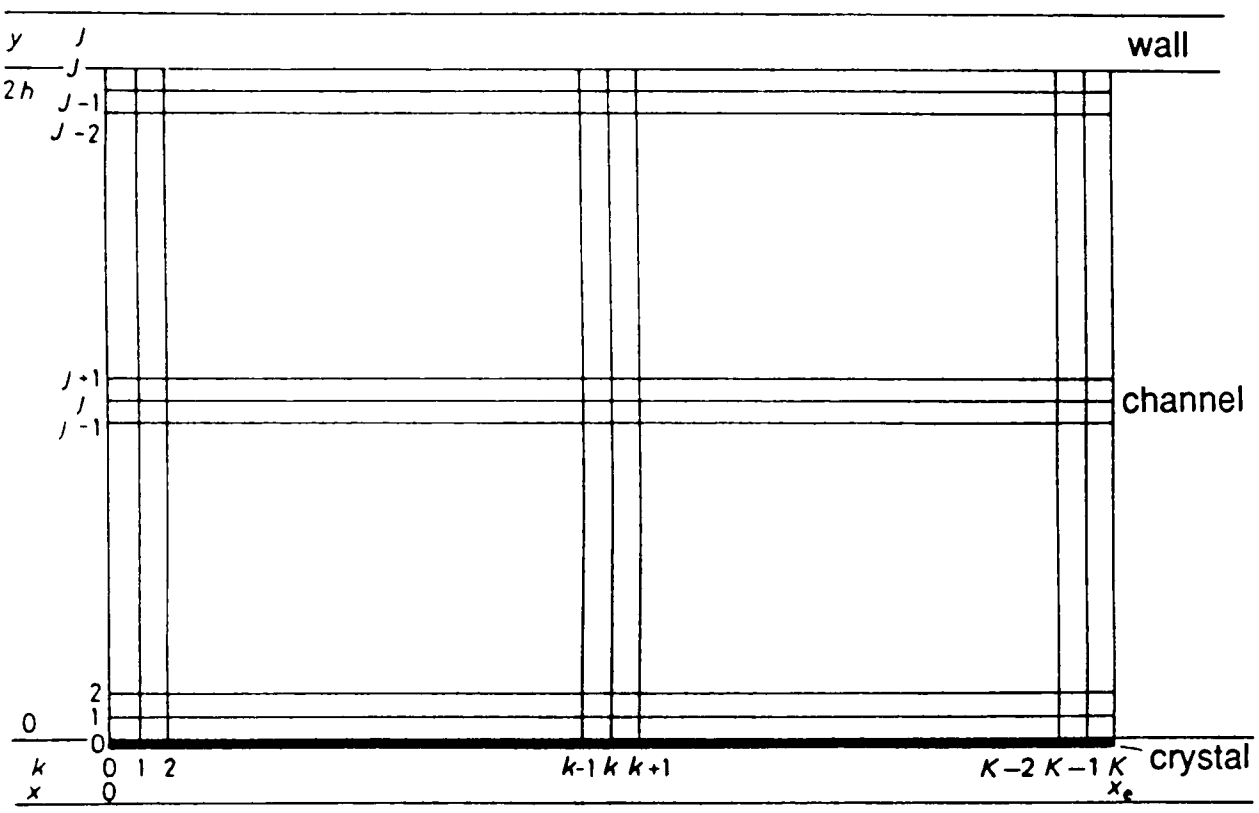

Figure 2.4. Finite difference grid.

The steady-state transport equation for species A is

$$D\frac{\partial^2[\mathrm{A}]}{\partial y^2} - v_o\left(1 - \frac{(y-h)^2}{h^2}\right)\frac{\partial[\mathrm{A}]}{\partial x} \qquad (2.16)$$

In order to apply the BIFD method the xy-plane is covered with a two-dimensional finite-difference grid, (Figure 2.4). Increments in the x-direction are Δx

and in the y-direction, Δy. The co-ordinates of a general point (x_k, y_j) in the channel are given by

$$y_j = j\Delta y \quad j = 0, 1.... J \quad \text{where} \quad \Delta y = \frac{2h}{J} \tag{2.17}$$

$$x_k = k\Delta x \quad k = 0, 1... K \quad \text{where} \quad \Delta x = \frac{x_e}{K} \tag{2.18}$$

The derivatives in equation (2.16) are approximated to

$$\frac{\partial g^{\mathbf{A}}}{\partial x} = \frac{g^{\mathbf{A}}_{j,k+1} - g^{\mathbf{A}}_{j,k}}{\Delta x} \tag{2.19}$$

where g^{A} is the concentration of species A and

$$\frac{\partial^2 g^{\mathbf{A}}}{\partial y^2} = \frac{g^{\mathbf{A}}_{j-1,k+1} - 2g^{\mathbf{A}}_{j,k+1} + g^{\mathbf{A}}_{j+1,k+1}}{(\Delta y)^2} \tag{2.20}$$

Combining equations (2.16), (2.19) and (2.20) results in

$$\left(\frac{D}{(\Delta y)^2}\right)\left\{g^{\mathbf{A}}_{j-1,k+1} - 2g^{\mathbf{A}}_{j,k+1} + g^{\mathbf{A}}_{j+1,k+1}\right\} = \left\{g^{\mathbf{A}}_{j,k+1} - g^{\mathbf{A}}_{j,k}\right\}\left(\frac{D}{\lambda_j(\Delta y)^2}\right) \tag{2.21}$$

where

$$\lambda_j = \frac{D\Delta x(2h)^3 d}{6V_{\mathrm{f}} j(\Delta y)^3(2h - j\Delta y)} \tag{2.22}$$

In this equation, V_{f} is the volume flow rate, where

$$V_{\mathrm{f}} = \frac{4}{3}\mathrm{v}_{\mathrm{o}} hd \tag{2.23}$$

The appropriate boundary conditions for the calculation of the speciation for the transport-limited regime are

$$x = 0\ ; \quad [\mathrm{A}]_{\mathrm{o}} = [\mathrm{A}]_{\mathrm{bulk}}\ ; \quad g^{\mathbf{A}}_{j,0} = [\mathrm{A}]_{\mathrm{bulk}} \tag{2.24}$$

$$y = 0\ ; \quad [\mathrm{A}]_{\mathrm{o}} = 0\ ; \quad g^{\mathbf{A}}_{0,k} = 0 \tag{2.25}$$

$$y = 2h\ ; \quad \frac{\partial[\mathrm{A}]}{\partial y} = 0\ ; \quad g^{\mathbf{A}}_{J,k} = g^{\mathbf{A}}_{J-1,k} \tag{2.26}$$

Thus equation (2.21) simplifies to

$$g^{\mathbf{A}}_{1,k} = (2\lambda_1 + 1)g^{\mathbf{A}}_{1,k+1} - \lambda_1 g^{\mathbf{A}}_{2,k+1} \tag{2.27}$$

$$g^{\mathbf{A}}_{j,k} = -\lambda_j g^{\mathbf{A}}_{j-1,k+1} + (2\lambda_j + 1)g^{\mathbf{A}}_{j,k+1} - \lambda_j g^{\mathbf{A}}_{j+1,k+1} \qquad j = 2,3\ldots J\text{-}2 \tag{2.28}$$

$$g^{\mathbf{A}}_{J-1,k} = -\lambda_{J-1} g^{\mathbf{A}}_{J-2,k+1} + (\lambda_{J-1} + 1)g^{\mathbf{A}}_{J-1,k+1} \tag{2.29}$$

These (J-1) simultaneous equations may be expressed as a (J-1) x (J-1) matrix equation

$$\{d\} = [T]\{u\} \tag{2.30}$$

i.e.

$$\begin{bmatrix} d_1 \\ d_2 \\ \vdots \\ \vdots \\ \vdots \\ d_j \\ \vdots \\ \vdots \\ \vdots \\ d_{J-2} \\ d_{J-1} \end{bmatrix} = \begin{bmatrix} b_1 & c_1 & 0 & & & & & & \\ a_2 & b_2 & c_2 & 0 & & & & & \\ & \ddots & \ddots & \ddots & & & & & \\ & & \ddots & \ddots & \ddots & & & & \\ & & & 0 & a_j & b_j & c_j & 0 & \\ & & & & \ddots & \ddots & \ddots & & \\ & & & & & \ddots & \ddots & \ddots & \\ & & & & & & a_{J-2} & b_{J-2} & c_{J-2} \\ & & & & & & 0 & a_{J-1} & b_{J-1} \end{bmatrix} \begin{bmatrix} u_1 \\ u_2 \\ \vdots \\ \vdots \\ \vdots \\ u_j \\ \vdots \\ \vdots \\ \vdots \\ u_{J-2} \\ u_{J-1} \end{bmatrix} \tag{2.31}$$

where

$$d_j = g^{\mathbf{A}}_{j,k} \qquad j = 1,2\ldots J\text{-}1 \tag{2.32}$$

$$u_j = g^{\mathbf{A}}_{j,k+1} \qquad j = 1,2\ldots J\text{-}1 \tag{2.33}$$

$$a_j = -\lambda_j \qquad j = 2,3\ldots J\text{-}1 \tag{2.34}$$

$$b_j = 2\lambda_j + 1 \qquad j = 1,2\ldots J\text{-}2 \tag{2.35}$$

$$b_{J-1} = \lambda_{J-1} + 1 \tag{2.36}$$

$$c_j = -\lambda_j \qquad j = 1,2\ldots J\text{-}2 \tag{2.37}$$

The matrix $[T]$ being of tridiagonal form allows the use of the Thomas algorithm [91] (see Appendix 2), to calculate $\{u\}_k$ from $\{d\}_k$. The boundary condition $g^{A}_{j,0} = [A]_{bulk}$ supplies the vector $\{d\}_0$ from which $\{u\}_0$ is calculated. In the absence of homogeneous chemical complications, $\{d\}_{k+1} = \{u\}_k$, so $\{u\}_1$ is calculated from $\{d\}_1$ ($= \{u\}_0$) and so on until $\{u\}_K$ is obtained. Thus all the values $g^{A}_{j,k}$ (j = 1,2... J-1, k = 1,2... K) are evaluated.

Using the theory outlined, concentration profiles can be calculated for the species of interest using FORTRAN 77 programs on a VAX/VMS mainframe computer or Sun Sparc IPC workstation.

In the case where the reactive surface is an electrode the redox current at the electrode can be calculated using Fick's first law.

$$I = FwD\sum_{k=1}^{K}\left(\frac{g^{A}_{1,k} - g^{A}_{0,k}}{\Delta y}\right)\Delta x \qquad (2.38)$$

Under mass transport limiting conditions this reduces to the numerical equivalent to the Levich equation (2.14).

$$I_{lim} = \frac{FDw\Delta x}{\Delta y}\sum_{k=1}^{K} g^{A}_{1,k} \qquad (2.39)$$

Clearly for cases where the reactive surface is not an electrode equations (2.38) and (2.39) are not applicable. For such cases the solution to the matrix equation (2.31) has already given the concentration profile of species A for the region of the channel over the reactive interface. The BI calculations are continued "downstream" over the detector electrode but with modified boundary conditions. Equation (2.25) is now replaced by

$$y = 0 ; \quad \frac{\partial[A]}{\partial y} = 0 ; \quad g^{A}_{0,k} = g^{A}_{1,k} \tag{2.40}$$

thus equation (2.27) is replaced by

$$g^{A}_{1,k} = (\lambda_1 + 1)g^{A}_{1,k+1} - \lambda_1 g^{A}_{2,k+1} \tag{2.41}$$

Solution of the modified matrix equation produces the concentrations at the surface of the detector electrode, from which the detector response can be calculated.

The application of the channel technique and BIFD method to the study of calcite dissolution, where the reactive surface in the channel is a calcite crystal, is discussed further in Chapter 4.

CHAPTER 3

EXPERIMENTAL DETAILS

3.1 Introduction

This chapter deals with experimental aspects common to more than one of the areas of this thesis. Specific details relating to each method of investigation are discussed in detail in the chapters concerned.

3.2 Potentiostat

The potentiostat is a device which actively maintains the potential difference between the working (WE) and reference (RE) electrodes at a given value by altering the voltage between the working and counter (CE) electrodes as necessary. In other words it forces whatever current is necessary through the WE so that the required potential is achieved. The potentiostats used were either an Oxford Electrodes Potentiostat (Oxford, Oxon.) or a Solartron Instruments 1286 Electrochemical Interface (Schlumberger Electronics Ltd., Farnborough, Hants.). The circuit designs of the potentiostats are given in Appendix 3.

3.3 pH Measurement

Apart from the *in-situ* channel pH measurements (see Chapter 4) the pH of solutions was measured using a combination glass pH electrode connected to a Jenway 3030 pH meter which had an accuracy of ±0.002pH and had automatic temperature compensation accurate to 0.5°C.

3.4 Chemicals

The source and purity of the chemicals used are summarised in Table 3.1. The calcite single crystals were semi-optical grade Iceland Spar crystals which originated from Chihuahua, Mexico. Chemical analysis of this was carried out by

Ciba-Geigy and the results are shown in Table 3.2. Water was purified using an Elgastat UHQ II (Elga Ltd., High Wycombe, Bucks.) which employs reverse osmosis, adsorption, deionisation, microfiltration and photo-oxidation and results in water with a resistivity of 18 MΩ cm.

Table 3.1. Source and Purity of Chemicals used.

Chemical	Purity	Supplier
DL-Aspartic Acid	98%	Aldrich Chemical Co. Ltd., Gillingham, Dorset
Iceland spar (single crystals)	semi-optical (see Table 3.2)	Roger Tayler minerals, Cobham, Surrey
Calcium Carbonate	AnalaR	BDH Ltd., Poole, Dorset
Calcium Chloride	AnalaR	BDH Ltd., Poole, Dorset
Calcium Nitrate tetrahydrate	AnalaR	BDH Ltd., Poole, Dorset
Colourkey Buffer Solutions: pH4.00, pH7.00 & pH10.00	Laboratory Reagent	BDH Ltd., Poole, Dorset
Hydrochloric Acid	AnalaR	BDH Ltd., Poole, Dorset
Maleic Acid	AnalaR	BDH Ltd., Poole, Dorset
Magnesium Sulphate	99%	Aldrich Chemical Co. Ltd., Gillingham, Dorset
Phthalic Acid	puriss	Fluka
Potassium Carbonate	AnalaR	Hopkin & Williams Ltd., Chadwell Heath, Essex
Potassium Chloride	AnalaR, Aristar	BDH Ltd., Poole, Dorset
Potassium Ferricyanide	AnalaR	BDH Ltd., Poole, Dorset
Potassium Hydroxide	AnalaR	East Anglia Chemicals, Ipswich
Potassium Nitrate	AnalaR	BDH Ltd., Poole, Dorset
Potassium Sulphate	AnalaR	BDH Ltd., Poole, Dorset
Succinic Acid	99%	Aldrich Chemical Co. Ltd., Gillingham, Dorset
2-Sulphobutane-1,4-dioic Acid, trisodium salt, dihydrate	-	Ciba-Geigy Additives, Manchester

Table 3.2. Chemical analysis of Iceland Spar

Element	Concentration /ppm
Cd	< 5
Cu	< 5
Fe	< 10
Mn	< 5
Na	< 10
P	< 50
Sb	< 20
Zn	< 5

3.5 Computing

Computer programs for the Backwards Implicit calculations were written in FORTRAN 77 and executed either on the Oxford University VAX/VMS cluster or the Physical Chemistry Laboratory, Oxford, Sun Sparc workstations.

3.6 DIC Microscopy

Optical interference microscopy is a very powerful tool for examining very shallow surface features. In this thesis Nomarski differential interference-contrast (DIC) microscopy was used. Calcite samples were observed using a Zeiss Universal R-Pol microscope in reflective mode. The image could either be viewed through an eyepiece of magnification x10 or projected onto the film plane of a 35 mm SLR camera. The objective lenses used were Zeiss Nomarski DIC objectives of x16 and x40 magnification.

Figure 3.1 shows a schematic representation of the DIC microscope in reflective mode. Polarised white light passes through a Nomarski-modified Wollaston prism [93], which splits the light up into two perpendicularly polarised

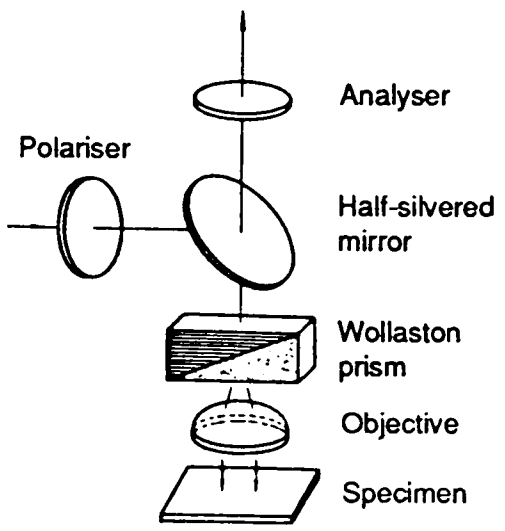

Figure 3.1 A schematic diagram of the differential interference-contrast microscope.

beams a few microns apart. These beams are reflected off the sample, recombined by the Wollaston prism and pass through a second polariser (the analyser) to the image plane. Any path differences between the two light paths, due to different surface heights, causes interference effects at the image plane.

CHAPTER 4

CALCITE DISSOLUTION KINETICS AT HIGH pH

4.1 Introduction

This chapter describes the investigation of the dissolution kinetics of calcite single crystals using the channel cell technique. Comparison of different kinetic rate laws and possible mechanisms are discussed. None of the rate laws existing in the literature were found to adequately describe the dissolution kinetics over the very wide range of experimental conditions used and therefore a new rate law with a sound mechanistic rationale has been developed which accurately describes all observed experimental data.

4.2 Experimental

4.2.1 Flow Cell

The channel flow cell was made up of two parts - the channel and coverplate, as shown in Figure 4.1. The channel was a rectangular groove cut into

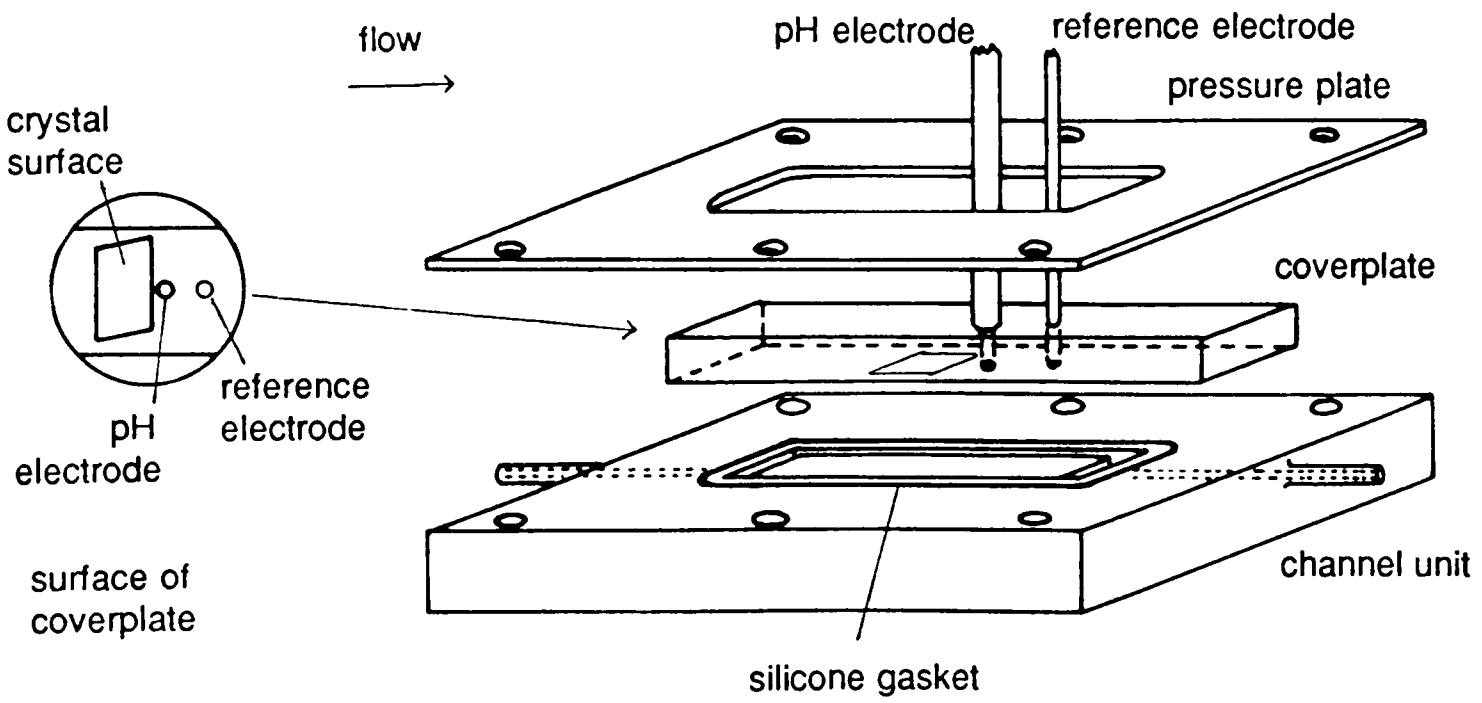

Figure 4.1. Channel cell configured to study dissolution of calcite at high pH.

a block of Perspex. The inlet and outlet pipes fed into a deeper duct at either end of the groove so as to even out the flow of the solution into the channel. The coverplate formed the fourth side of the channel and consisted of a cleaved calcite crystal (Roger Tayler Minerals, Cobham, Surrey) set into a block of Araldite (Resin CY219, Hardener HY219, Accelerator DY219; Ciba-Geigy, Duxford, Cambs.) and polished down to 1μm using diamond lapping compounds (Hyprez Sprays; Engis, Maidstone, Kent).

A gasket of silicone rubber (Nº555-588; R.S. Components, Corby, Northants.) between the Perspex block and the coverplate formed an airtight seal when pressure was applied to the coverplate by means of a pressure plate and six bolts. The coverplate was positioned in such a way that the crystal was a distance greater than the necessary lead-in length away from the beginning of the channel to ensure Poiseuille flow had been obtained. For the typical channel dimensions used this was less than a few millimetres at all flow rates used (equation (2.4)).

A flat membrane glass pH electrode (MI-404; Microelectrodes Inc., Londonderry, New Hampshire, USA) was inserted in a hole 2.5 mm in diameter which was drilled in the coverplate immediately downstream of the crystal so that it lay in the centre of the channel (width-wise), in order to minimise any "edge effects" (see Chapter 2). Care was taken to ensure that the glass electrode lay absolutely flush with the coverplate surface. The Ag/AgCl reference electrode (Microelectrodes Inc. MI-401) was inserted into another hole in the coverplate further downstream. Electrodes were held in place by PTFE tape and wax (Wax-a-Way; Vychem Ltd, Poole, Dorset) which ensured an airtight seal of the cell. The flow cell was mounted in a thermostatted air bath held at 25 ± 0.5°C.

The solution under investigation was held in a 500 cm^3 reservoir. Argon gas (British Oxygen Company Limited, Guildford, Surrey) was bubbled through the solution to remove dissolved CO_2. From the reservoir the solution flowed through a 1.5 mm bore PTFE tube (Altex; Anachem, Luton), which was jacketed in argon to prevent the ingress of CO_2, through the channel cell, then through a capillary to waste. At least 1 m of the PTFE tubing upstream of the channel was situated in the thermostatted box to ensure that the solution was at constant temperature. The capillaries were also held inside the box to maintain constant flow. The rate of flow of solution through the channel was varied by changing the bore of the capillary and by altering the height of the reservoir relative to the outlet tube.

4.2.2 Surface Preparation

Two forms of calcite surface preparation were used. In both cases a cleaved calcite crystal was set into the Araldite coverplate and polished to 1 μm with diamond grits, as described above, and thoroughly rinsed with ultra high purity water. In the case of the "polished" surface the only further treatment was to rinse the surface with millimolar hydrochloric acid for a minute to remove any organic species. For the "etched" surface the procedure was identical to this except that the crystal was etched by flowing 0.5 M KCl (pH > 7) over the surface in the channel for at least 100 minutes to achieve an equilibrated surface morphology.

4.2.3 Operation

Having constructed the channel cell as described above and degassed the solutions under investigation, the Microelectrode pH and reference electrodes were connected to a Radiometer PHM84 Research pH meter (Radiometer, Copenhagen, Denmark) which had an accuracy of ±0.2 mV (±0.002 pH). This was interfaced

with a BBC Master microcomputer using a purpose built circuit to adjust the output voltage range to between 0 and 1.8 V required by the microcomputer's analogue to digital input.

Solution was passed through the channel at a variety of flow rates, V_f, and the steady-state surface pH immediately downstream of the crystal was recorded for each on the microcomputer.

4.2.4 Calibration

4.2.4.1 *Capillary*

Each capillary used was calibrated by measuring the amount of water flowing through to waste in a given time. For each capillary the mass of water collected over a known time was measured for several "solution heights". Using the density of water (ρ = 0.99707 g cm^{-3} at 25°C, ρ = 0.99823 g cm^{-3} at 20°C [93]) a mean capillary constant of flow rate per unit height of solution (cm^3 s^{-1} cm^{-1}) was determined for each capillary. During an experiment the flow rate was simply calculated from the product of this capillary constant and the solution height.

4.2.4.2 *Channel Dimensions*

The channel width d, crystal length x_c, crystal to pH sensor separation and pH electrode diameter were all measured using a travelling microscope (Unicam Instruments, Cambridge) capable of measuring to 10^{-3} cm.

The final cell dimension required to interpret results was the channel half-height h. This was determined by measuring the transport limiting current for a simple one electron reduction or oxidation of a species with a known diffusion coefficient over a range of solution flow rates. To observe this the flow cell had to be modified from potentiometric operation to an amperometric mode. This required

the three electrode system (see Appendix 3) - working, reference and counter electrodes. For this a Perspex coverplate was used on which was attached a ≈ 2 mm strip of 25 μm thick silver foil (Goodfellow, Cambridge) with Evo-stik (Evode Ltd, Stafford). A coating of AgCl was formed on this by making the foil the anode in 0.1 M HCl and passing 0.4 mA cm^{-2} for 30 minutes [94]. This Ag/AgCl electrode acted as the reference electrode. Downstream of the reference electrode a ≈ 1 mm strip of 12.5 μm thick platinum foil (Goodfellow, Cambridge) was attached in a similar manner to act as the working electrode. The edges of the platinum foil were masked off using thin PTFE tape in such a way that approximately 1 mm of the coverplate between the channel edge wall and the working electrode was covered. This was to minimise any edge effects. The counter electrode was a piece of platinum gauze (whose area was much larger than that of the working electrode) which was coiled and inserted into a glass tube. This was plumbed into the flow system immediately downstream of the channel flow cell. The three electrodes were connected to an Oxford Electrode Potentiostat, which controlled the potential applied to the working electrode relative to the reference electrode (see Appendix 3).

The electroactive species used was the ferricyanide anion which undergoes a one electron reduction to the ferrocyanide anion and has a diffusion coefficient of 7.6×10^{-6} cm^2 s^{-1} [95]. The solution used was 1mM $K_3Fe(CN)_6$ at pH 13 with 0.5 M KCl as background electrolyte. By ramping the potentiostat from +0.5 V to 0 V, with respect to Ag/AgCl, and measuring the limiting current, a Levich plot of I_{lim} versus $V_f^{1/3}$ could be drawn. The gradient of this yielded the channel half-height h according to the Levich equation (2.14) for the channel.

Typical dimensions of the cell parameters were as follows,

Channel height, $2h$	0.114 ± 0.006 cm
Channel width, d	0.600 ± 0.003 cm
Crystal length, x_c	0.674 - 0.783 cm
Crystal - sensor separation	0.049 - 0.200 cm
"Active" pH electrode diameter	0.134 - 0.214 cm

4.2.4.3 *pH Electrodes*

The pH of solutions was measured using a glass combination pH electrode connected to a Jenway 3030 pH meter. This was calibrated using BDH Colourkey buffer solutions of pH 4.00 (±0.02) and pH 7.00 or pH 7.00 and pH 10.00 depending on the range to be used. The small Microelectrode pH electrode with its associated reference connected to the Radiometer pH meter and BBC interface was calibrated against this using a range of alkaline solutions and a least squares fitting computer program. This calibration was carried out *ex-situ* just before and/or immediately after the channel experiment.

4.3 Theory

In this section theory is derived which relates the potentiometric response of a pH electrode in the flow system to the mechanism of the dissolution/precipitation reaction taking place at the calcite surface at high pH (pH > 7), and which predicts the influence of solution flow rate and flow cell geometry. The problem was complicated by the need to take into account the solution equilibria (4.2) and (4.3) in addition to the heterogeneous reaction (4.1).

$$CaCO_3 + H_2O \longrightarrow Ca^{2+} + CO_3^{2-} \qquad (4.1)$$

$$CO_3^{2-} + H_2O \rightleftharpoons HCO_3^- + OH^- \qquad (4.2)$$

$$H^+ + OH^- \rightleftharpoons H_2O \tag{4.3}$$

The steady-state convective-diffusion equation describing the distribution of Ca^{2+} ions in the flow cell was [15]:

$$\frac{\partial[Ca^{2+}]}{\partial t} = 0 = D\frac{\partial^2[Ca^{2+}]}{\partial y^2} - v_x\frac{\partial[Ca^{2+}]}{\partial x} \tag{4.4}$$

where D is the diffusion coefficient of Ca^{2+}, x and y are coordinates defined in Figure 2.2, and v_x is the solution velocity in the x-direction. The latter is given by:

$$v_x = v_o\left\{1 - \frac{(h-y)^2}{h^2}\right\} \tag{4.5}$$

where v_o is the solution velocity in the centre of the channel and h is the channel half-height.

The boundary conditions were as follows:

(i) *Upstream of the Crystal*

The Ca^{2+} concentration was that present in the bulk solution entering the flow cell:

$$x = 0, \quad 0 < y < 2h, \quad [Ca^{2+}] = [Ca^{2+}]_{bulk} \quad \& \quad [CO_3^{2-}] = 0 \tag{4.6}$$

(ii) *Zone of the Crystal*

At the surface of the crystal the flux of Ca^{2+} entering the solution was given by the appropriate rate law for the dissolution/precipitation reaction. The exact form of this is the subject of discussion below. It suffices at present to indicate that the net dissolution flux was some function, f, of the concentrations of Ca^{2+} and CO_3^{2-} at the Outer Helmholtz Plane:

$$0 < x < x_c\,, \quad y = 0\,, \quad D\frac{\partial[Ca^{2+}]}{\partial y} = f\{[Ca^{2+}]_o, [CO_3^{2-}]_o, K_{sp}\} \tag{4.7}$$

where K_{sp} is the solubility product of $CaCO_3$. There was an additional no-flux condition at the channel wall opposite the crystal:

$$0 < x < x_c \,, \quad y = 2h \,, \quad D\frac{\partial[Ca^{2+}]}{\partial y} = 0 \tag{4.8}$$

where x_c is the length of the crystal.

(iii) *Downstream of the Crystal*

Over the surface of the pH electrode and over the gap between the crystal and the detector a no-flux condition operated:

$$x > x_c \,, \quad y = 0 \,, \quad D\frac{\partial[Ca^{2+}]}{\partial y} = 0 \tag{4.9}$$

and again at the channel wall:

$$x > x_c \,, \quad y = 2h \,, \quad D\frac{\partial[Ca^{2+}]}{\partial y} = 0 \tag{4.10}$$

As outlined in Chapter 2, the Backwards Implicit Finite Difference method [89] can be used to solve transport problems in channel electrodes. The method involved only vector calculations where the vectors describe concentrations in the y-direction for different values of x. The calculation proceeded "downstream", each vector enabling the calculation of the next, starting from the vector defining the boundary conditions specified for upstream of the crystal. It can be seen that the computation of $[Ca^{2+}]$ as a function of x and y throughout the flow cell could be readily achieved in this way if the quantities $[Ca^{2+}]_o$ and $[CO_3^{2-}]_o$ in equation (4.7) were known. However as this was not the case, the following procedure was followed:

(i) In the zone of the crystal the values of $[Ca^{2+}]_o$ and $[CO_3^{2-}]_o$ from the "preceding" vector were used as an initial guess to enable the calculation of Ca^{2+} along the vector of interest.

(ii) Next reactions (4.2) and (4.3) were assumed to be at equilibrium so that

$$a_{H^+} a_{OH^-} = K_w \tag{4.11}$$

and

$$\frac{a_{H^+}[CO_3^{2-}]}{[HCO_3^-]} = K_{a2} \tag{4.12}$$

where K_{a2} is the (mixed) second dissociation constant of carbonic acid [96]. The equilibrium assumption was justified by the values of pH measured close to the electrode surface (*vide infra*) together with the known [97] rate constant for the reaction

$$OH^- + HCO_3^- \xrightarrow{k=6\times10^9 M^{-1}s^{-1}} H_2O + CO_3^{2-} \tag{4.13}$$

Moreover if it is assumed that Ca^{2+}, HCO_3^- and CO_3^{2-} have similar diffusion coefficients then stoichiometric dissolution of $CaCO_3$ implied that at each point in space,

$$[Ca^{2+}] - [Ca^{2+}]_{bulk} = [CO_3^{2-}] + [HCO_3^-] \tag{4.14}$$

Also since dissolution must preserve electro-neutrality,

$$2[Ca^{2+}] - 2[Ca^{2+}]_{bulk} = 2[CO_3^{2-}] + [HCO_3^-] + [OH^-] - [OH^-]_{bulk} \tag{4.15}$$

where $[\ ]_{bulk}$ denotes bulk concentrations and assuming that $[OH^-] \gg [H^+]$.

Equations (4.11), (4.12), (4.14) & (4.15) could be combined to give

$$\left([Ca^{2+}] - [Ca^{2+}]_{bulk} + \frac{K_w}{\gamma_{OH^-} a_{H^+,bulk}}\right)\frac{a_{H^+}^2}{K_2} + \left(a_{H^+,bulk}^{-1} - K_2^{-1}\right)\frac{K_w a_{H^+}}{\gamma_{OH^-}} - \frac{K_w}{\gamma_{OH^-}} = 0 \quad (4.16)$$

where γ_{OH^-} is the activity coefficient of OH^-. This is a quadratic equation in a_{H+} which, knowing $[Ca^{2+}]$ from (i), was solved to give a_{H+} along the vector of interest. This then, in combination with equations (4.12) and (4.14) permitted the deduction of $[HCO_3^-]$ and $[CO_3^{2-}]$ along the same vector.

(iii) The new values of $[HCO_3^-]_o$ and $[CO_3^{2-}]_o$ thus generated were used to provide improved values for equation (4.7) and the steps in (i) and (ii) were repeated until all concentrations had converged. Typically this required about five iterations to give concentrations correct to six significant figures.

(iv) Having used the above procedure to find the concentration profiles in the zone of the crystal, the vector describing the $[Ca^{2+}]$ profile along the downstream edge of the crystal was used to provide a "starting" vector for the zone downstream of the crystal. The calculation in this zone proceeded without the need for iteration; a_{H+} was calculated from $[Ca^{2+}]$ via equation (4.16) and hence the other concentrations were deduced.

Having calculated the speciation throughout the channel cell in the above manner the H^+ activity was averaged over the surface of the pH sensor and thus the dependence of the measured pH on the proposed rate law (equation (4.7)) and flow rate for a defined channel geometry was deduced. The following thermodynamic quantities, pertaining to 25°C, were assumed in this modelling:

(a) K_w = 1.008x10^{-14} mol^2 dm^{-6} [98].

(b) K_{a2} = 1.409x10^{-10} mol dm^{-3}. This was deduced using the value of Harned and Scholes at infinite dilution [99] corrected with the activity coefficients for CO_3^{2-} and HCO_3^- as measured by Walker *et al.* [100] for the ionic strength at which the experiments described below were conducted (0.5 mol dm^{-3}). These activity coefficient values agree almost exactly with those predicted by the Davies equation [101]

$$\log\gamma = -Az^2\left(\frac{I^{1/2}}{1+I^{1/2}} - 0.2I\right) \qquad (4.17)$$

where z is the charge on the ion, I is the ionic strength of the solution and A is a constant dependent on temperature and dielectric constant of the solvent, which for water at 25°C is 0.509.

(c) γ_{OH^-} = 0.69. This was predicted by the Davies equation (4.17) for an ionic strength of 0.5 M.

(d) K_{sp} = 6.26x10^{-8} mol^2 dm^{-6}. This was deduced from the experimental value of Inskeep and Bloom [49] corrected for the activity coefficients of Ca^{2+} and CO_3^{2-} at 0.5 mol dm^{-3}. The activity coefficient of Ca^{2+} was calculated from the Davies equation and that of CO_3^{2-} was an experimental value [100]. The value of K_{sp}

Table 4.1. Solubility Product of Calcite

Reference	$K_{sp} = [Ca^{2+}][CO_3^{2-}]$ /mol^{2}dm^{-6}	Ionic Strength /mol dm^{-3}	Temperature /°C
Inskeep & Bloom [49]	3.35 ± 0.15x10^{-9}	0	25
Jacobson & Langmuir [102]	3.80x10^{-9}	0	25

Reference	$K_{sp} = [Ca^{2+}][CO_3^{2-}]$ /mol^{2}dm^{-6}	Ionic Strength /mol dm^{-3}	Temperature /°C
Plummer & Busenburg [103]	$3.31 \pm 0.15 \times 10^{-9}$	0	25
Sjöberg [28]	6.05×10^{-8}	0.7	20
Compton & Daly [37]	2.7×10^{-8}	0.3	25
Martynova *et al.* [104]	3.6×10^{-9}	0	25
Ghiringhelli & Bianucci [105]	2.9×10^{-9}	0	25
Krauskopf [101]	4.47×10^{-9}	0	25
Akin & Lagerwerff [106]	5.0×10^{-9}	0	25
Grèzes & Basset [107]	4.4×10^{-9}	0	25
Larson & Buswell [108]	4.55×10^{-9}	0	25
Millero *et al.* [109]	$3.47 \pm 0.24 \times 10^{-9}$	0	25
Nancollas & Reddy [46]	$4.7 \pm 0.3 \times 10^{-9}$	0	25
Frear & Johnston [110]	4.8×10^{-9}	0	25
Wolf *et al.* [111]	$3.4 \pm 0.7 \times 10^{-9}$	0	25
Langmuir [112]	$3.98 \pm 0.19 \times 10^{-9}$	0	25
Miller [112,113]	3.5×10^{-9}	0	25
Christ *et al.* [114]	$3.3 \pm 0.4 \times 10^{-9}$	0	20

closely agrees with that measured by Sjöberg [28]. Table 4.1 lists other literature values of the calcium carbonate solubility product.

(e) The diffusion coefficient of Ca^{2+} ions D = 7.93x10^{-6} cm^2 s^{-1}. This was calculated from the ionic conductivity of Ca^{2+} [115] using the Einstein relation [116] after converting into ionic mobility. This was in good agreement with the value of 7.4x10^{-6} cm^2 s^{-1} obtained from rotating disc experiments on Iceland spar in 0.7 M KCl solutions [34]. Other work in the literature assumed an arbitrary value of 1x10^{-5} cm^2 s^{-1} [21,32].

Numerous equations, both empirical and mechanistic, for calcite dissolution/precipitation appear in the literature, as discussed in Chapter 1, and these are summarised in Table 4.2. Each of these rate laws was incorporated into the surface boundary condition in turn. To illustrate this the matrix elements for the Nancollas-Reddy equation are derived below.

4.3.1 Derivation of Matrix Elements

The Nancollas-Reddy rate law was incorporated into the surface boundary condition of the Backwards Implicit calculation as follows. According to Fick's first law the flux of calcium ions entering solution at the solid-liquid interface was given by

$$flux = D\left.\frac{\partial g^{A}}{\partial y}\right|_{j=0} = -k_{NR} + \frac{k_{NR}}{K_{sp}} g^{A}_{0,k+1} g^{C}_{0,k+1} \qquad (4.18)$$

where D is the diffusion coefficient of calcium ions, k_{NR} is a rate constant, K_{sp} is the solubility product of calcite and $g^{A}_{j,k}$ is the concentration of Ca^{2+} ions and $g^{C}_{j,k}$ is the

Table 4.2. Literature Rate Laws for Calcite Dissolution/Precipitation

Reference	Net Dissolution Flux, J_{net}
Dorange and Guetchidjian [19][1]	$k_{DG}\left\{[Ca^{2+}]_{eq} - [Ca^{2+}]_o\right\}$
Sjöberg [28]	$k_S\left\{\sqrt{K_{sp}} - \sqrt{[Ca^{2+}]_o[CO_3^{2-}]_o}\right\}$
Plummer [16,26]	$k_P - k_P' a_{Ca^{2+}} a_{HCO_3^-}$
Nancollas and Reddy [46]; Inskeep and Bloom [49]	$k_{NR}\left\{1 - \frac{[Ca^{2+}]_o[CO_3^{2-}]_o}{K_{sp}}\right\}$
Davies and Jones [59,60]; Kazmierczak *et al.* [48]	$k_{DJ}\left\{\sqrt{K_{sp}} - \sqrt{\gamma_\pm^2[Ca^{2+}]_o[CO_3^{2-}]_o}\right\}^2$
Chiang and Donohue [117]; Reddy [50,51] & Reddy and Nancollas [52][2]	$k_{CD}\left\{[Ca^{2+}]_{eq}^2 - [Ca^{2+}]_o^2\right\}$

[1] $[Ca^{2+}]_{eq}$ is the equilibrium calcium ion concentration in a saturated solution of calcite [19].

[2] $\gamma_\pm$ is the mean ionic activity coefficient.

concentration of CO_3^{2-} ions at the point $x = k$, $y = j$. At the surface the differential term was linearised as follows

$$\left.\frac{\partial g^{A}}{\partial y}\right|_{j=0} = \frac{g^{A}_{1,k+1} - g^{A}_{0,k+1}}{\Delta y} \tag{4.19}$$

Equations (4.18) and (4.19) were combined to give

$$g^{A}_{0,k+1} = \frac{D g^{A}_{1,k+1} + \Delta y k_{NR}}{D + \Delta y \dfrac{k_{NR}}{K_{sp}} g^{C}_{0,k+1}} \tag{4.20}$$

At the crystal surface equation (2.21) became

$$g^{A}_{1,k} = -\lambda_1 g^{A}_{0,k+1} + (2\lambda_1 + 1) g^{A}_{1,k+1} - \lambda_1 g^{A}_{2,k+1} \tag{4.21}$$

Substituting the surface concentration term (4.20) in equation (4.21) this became

$$d_1 = b_1 g^{A}_{1,k+1} + c_1 g^{A}_{2,k+1} \tag{4.22}$$

where

$$d_1 = g^{A}_{1,k} + \frac{\lambda_1 k_{NR} \Delta y}{D + \dfrac{k_{NR}}{K_{sp}} \Delta y g^{C}_{0,k+1}} \tag{4.23}$$

$$b_1 = \left(2 - \frac{D}{D + \dfrac{k_{NR}}{K_{sp}} \Delta y g^{C}_{0,k+1}}\right) \lambda_1 + 1 \tag{4.24}$$

$$c_1 = -\lambda_1 \tag{4.25}$$

Thus equation (4.22) incorporated the Nancollas-Reddy rate equation into the BI calculation which proceeded as described in Chapter 2.

The other equations cited in Table 4.2 were converted into the surface boundary condition in a similar fashion. Plummer *et al.* [16] demonstrated that the Plummer equation was similar to the Nancollas-Reddy equation at high pH (see equation (1.37)). When written in terms of surface concentrations these two equations are identical, therefore only one need be considered.

There was a slight modification to the approach for rate laws with non-unity powers of calcium ion concentration (ie Sjöberg, Davies-Jones, Chiang-Donohue). To obtain an equivalent expression to equation (4.20) for $g^{A}_{0,k+1}$ would have involved solving a polynomial. This was avoided by using the (known) previous vector's surface concentration for the first calculation on a particular vector. Subsequent iterations used updated concentration values. Thus for the Sjöberg rate equation at the crystal surface the flux was

$$J = D\left(\frac{g^{A}_{1,k+1} - g^{A}_{0,k+1}}{\Delta y}\right) = -k_S\sqrt{K_{sp}} + k_S\sqrt{g^{A}_{0,k}\,g^{C}_{0,k}} \tag{4.26}$$

which rearranged to

$$g^{A}_{0,k+1} = g^{A}_{1,k+1} + \frac{\Delta y k_S\left\{\sqrt{K_{sp}} - \sqrt{g^{A}_{0,k}\,g^{C}_{0,k}}\right\}}{D} \tag{4.27}$$

Substitution of equation (4.27) into equation (4.21) yielded equation (4.22) but with

$$b_1 = \lambda_1 + 1 \tag{4.28}$$

$$c_1 = -\lambda_1 \tag{4.29}$$

and, for the first iteration

$$d_1 = g^{A}_{1,k} + \frac{\lambda_1 \Delta y k_S\left\{\sqrt{K_{sp}} - \sqrt{g^{A}_{0,k}\,g^{C}_{0,k}}\right\}}{D} \tag{4.30}$$

but for subsequent iterations

$$d_1 = g^{A}_{1,k} + \frac{\lambda_1 \Delta y k_S \left\{ \sqrt{K_{sp}} - \sqrt{g^{A}_{0,k+1} g^{C}_{0,k+1}} \right\}}{D} \tag{4.31}$$

Both the Dorange-Guetchidjian and Chiang-Donohue equations contain an equilibrium calcium ion concentration, $[Ca^{2+}]_{eq}$. This could be calculated for a given bulk calcium ion concentration since at equilibrium

$$K_{sp} = [Ca^{2+}]_{eq}[CO_3^{2-}]_{eq} \tag{4.32}$$

This together with equations (4.11), (4.12), (4.14) and (4.15) yielded the following quartic equation in $[CO_3^{2-}]_{eq}$

$$[CO_3^{2-}]_{eq}^{4} + \left(2[Ca^{2+}]_{bulk} - \frac{K_w}{\gamma_{OH^-} a_{H^+,bulk}} - \frac{K_w}{\gamma_{OH^-} K_{a2}} \right) [CO_3^{2-}]_{eq}^{3}$$

$$+ \left([Ca^{2+}]^2_{bulk} - 2K_{sp} - \frac{K_w}{\gamma_{OH^-} a_{H^+,bulk}} \right) [CO_3^{2-}]_{eq}^{2} \tag{4.33}$$

$$+ \left(\frac{K_w}{\gamma_{OH^-} a_{H^+,bulk}} - 2[Ca^{2+}]_{bulk} \right) K_{sp}[CO_3^{2-}] + (K_{sp})^2 = 0$$

Equation (4.33) was solved using the method of Grant and Hitchins as used in the NAG Library routine C02AEF. The solution so obtained combined with equation (4.32) generated $[Ca^{2+}]_{eq}$.

The matrix elements for each rate law derived as described above are summarised in Tables 4.3 and 4.4.

Table 4.3. Matrix Elements for the Channel Cell

		d_j	a_j	b_j	c_j	u_j
j=1	crystal	see Table 4.4 & 4.5	-	see Table 4.4 & 4.5	$-\lambda_1$	$g^{A}_{1,k+1}$
	downstream	$g^{A}_{1,k}$	-	$\lambda_1 + 1$	$-\lambda_1$	$g^{A}_{1,k+1}$
$j = 2, .., J\text{-}2$		$g^{A}_{j,k}$	$-\lambda_j$	$2\lambda_j + 1$	$-\lambda_j$	$g^{A}_{j,k+1}$
$j = J\text{-}1$		$g^{A}_{J-1,k}$	$-\lambda_{J-1}$	$\lambda_{J-1} + 1$	-	$g^{A}_{J-1,k+1}$

Table 4.4. Surface Boundary Matrix Elements for Literature Rate Laws

Rate Equation	$g^{A}_{0,k+1}$	d_1	b_1
Dorange-Guetchidjan	$\dfrac{D g^{A}_{1,k+1} + \Delta y k_{DG} g^{A}_{sat}}{D + \Delta y k_{DG}}$	$g^{A}_{1,k} + \dfrac{\lambda_1 \Delta y k_{DG} g^{A}_{sat}}{D + \Delta y k_{DG}}$	$\left(2 - \dfrac{D}{D + \Delta y k_{DG}}\right)\lambda_1 + 1$
Sjöberg	$g^{A}_{1,k+1} + \dfrac{\Delta y k_S\left(\sqrt{K_{sp}} - \sqrt{g^{A}_{0,k} g^{C}_{0,k}}\right)}{D}$	$g^{A}_{1,k} + \dfrac{\lambda_1 \Delta y k_S\left(\sqrt{K_{sp}} - \sqrt{g^{A}_{0,k+1} g^{C}_{0,k+1}}\right)}{D}$	$\lambda_1 + 1$
Nancollas-Reddy	$\dfrac{D g^{A}_{1,k+1} + \Delta y k_{NR}}{D + \Delta y \dfrac{k_{NR}}{K_{sp}} g^{C}_{0,k+1}}$	$g^{A}_{1,k} + \dfrac{\lambda_1 k_{NR} \Delta y}{D + \dfrac{k_{NR}}{K_{sp}} \Delta y g^{C}_{0,k+1}}$	$\left(2 - \dfrac{D}{D + \dfrac{k_{NR}}{K_{sp}} \Delta y g^{C}_{0,k+1}}\right)\lambda_1 + 1$
Davies-Jones	$g^{A}_{1,k+1} + \dfrac{\Delta y k_S\left(\sqrt{K_{sp}} - \sqrt{g^{A}_{0,k} g^{C}_{0,k}}\right)^2}{D}$	$g^{A}_{1,k} + \dfrac{\lambda_1 \Delta y k_{DJ}\left(\sqrt{K_{sp}} - \sqrt{g^{A}_{0,k+1} g^{C}_{0,k+1}}\right)^2}{D}$	$\lambda_1 + 1$
Chiang-Donohue	$g^{A}_{1,k+1} + \dfrac{\Delta y k_{CD}\left\{\left(g^{A}_{sat}\right)^2 - \left(g^{A}_{0,k}\right)^2\right\}}{D}$	$g^{A}_{1,k} + \dfrac{\lambda_1 \Delta y k_{DG}\left\{\left(g^{A}_{sat}\right)^2 - \left(g^{A}_{0,k+1}\right)^2\right\}}{D}$	$\lambda_1 + 1$

4.4 Results

4.4.1 Heavily Etched Surface

Experiments were conducted on solutions containing 0.5 mol dm^{-3} KCl and of varying bulk calcium ion concentrations of between 0 and 10^{-2} mol dm^{-3}. Figures 4.2 and 4.3 show some typical results in the form of plots of $[H^+]$, as deduced from the detector pH electrode, as a function of solution flow rate. Clearly the solution pH decreased with flow rate. This was attributable to the fact that less surface reaction can take place for a given volume element of solution the faster it flows and the quicker its transit time over the crystal surface. Also at faster rates of flow the perturbation of the solution concentrations from their bulk values is diluted more and this will again have the effect of lowering the pH.

The data in plots such as Figures 4.2 and 4.3 were modelled using the theory presented above and with each of the rate laws in Table 4.2 in turn for equation (4.7) as a boundary condition. The fitting procedure involved varying the rate constant in each rate law for a given data set until the closest fit between model and experiment was achieved across the flow rate range. Examples of "best fits" achieved with these rate laws are shown in Figures 4.2 and 4.3. Of the literature rate laws the Davies-Jones equation gave the best flow rate response. However this did not have a sound mechanistic basis since the model assumed that the positive and negative surface ion concentrations were equal (see Chapter 1) [68], which has been shown experimentally not to be the case on calcite [61,62]. None of the existing rate equations considered were found to give a satisfactory fit across the entire flow rate range for all of our sets of data, for different values of pH_{bulk} and $[Ca^{2+}]_{bulk}$ and to have a viable mechanistic rational. The contradiction of

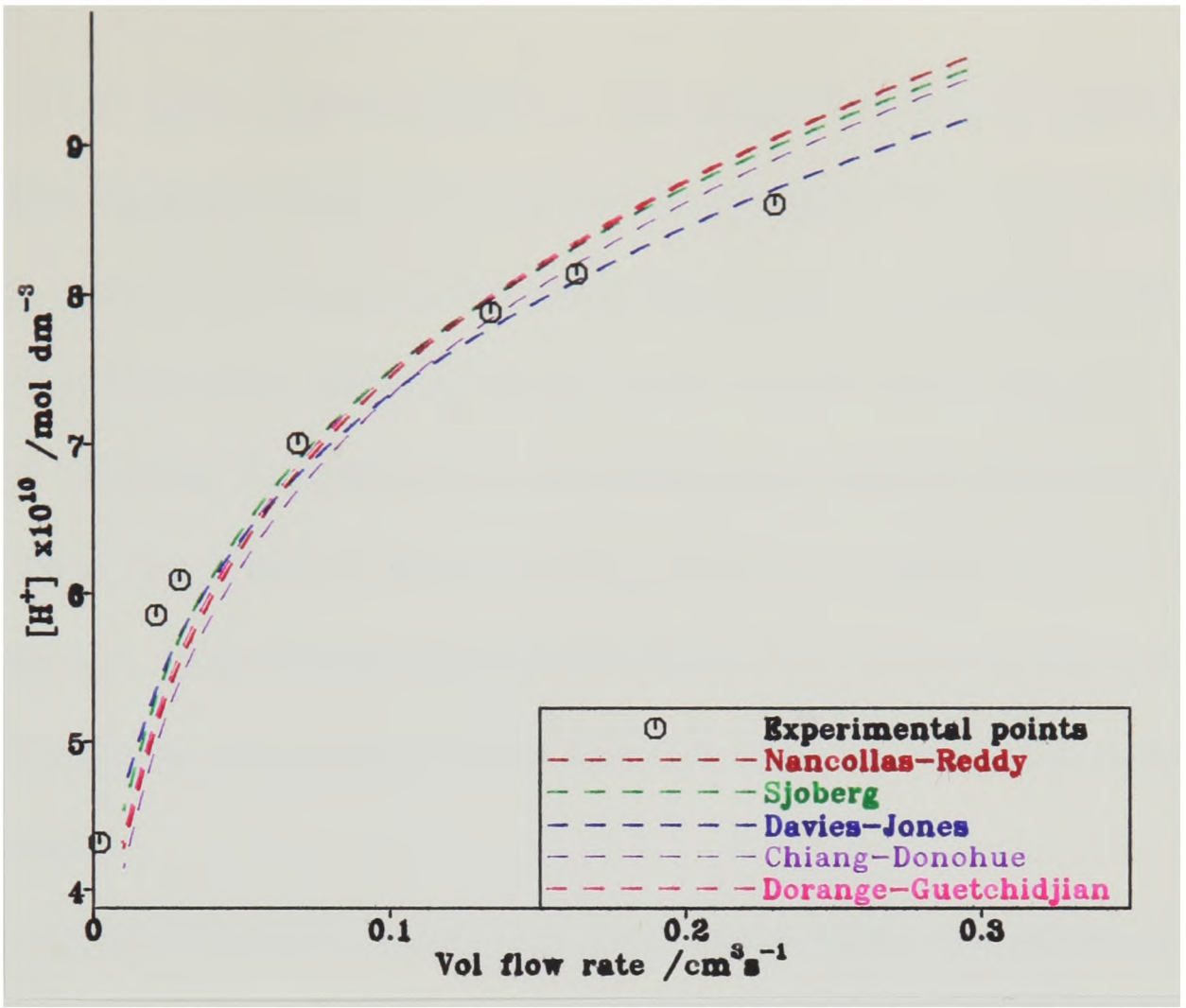

Figure 4.2. The flow rate depedence of the channel cell $[H^+]$ *sensor for* pH_{bulk} = 8.44 *and* $[Ca^{2+}]_{bulk}$ = 0. *The dashed lines show the theoretical behavior predicted using the literature rate laws listed in Table 4.2.*

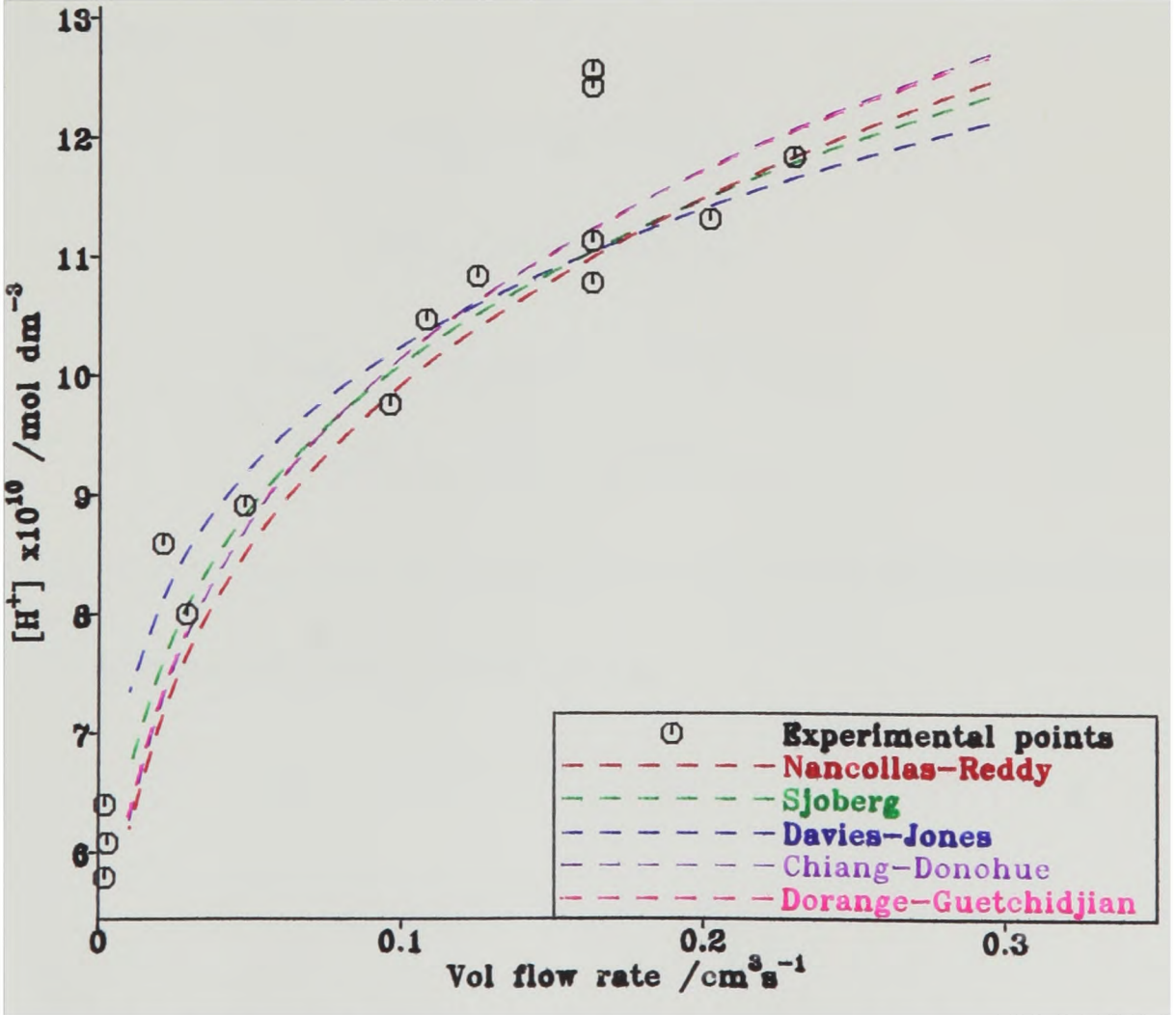

Figure 4.3. The flow rate depedence of the channel cell $[H^+]$ *sensor for* pH_{bulk} = 8.38 *and* $[Ca^{2+}]_{bulk}$ = 1.01 mM. *The dashed lines show the theoretical behavior predicted using the literature rate laws listed in Table 4.2.*

these previous rate laws arose first from the wide range of conditions, especially of the rate of mass transport, used in our flow cell experiments. Also the pH detector electrode was positioned adjacent to the dissolving crystal, as opposed to the more remote, and thus insensitive, sensing typically used in other work. This, on account of the controlled hydrodynamics and theory given above, enabled the inference of the surface concentrations and thus the discrimination between candidate rate laws. It should be noted that the curvature of the experimental pH sensor plots was quite unique and differed from the response predicted by the existing rate laws.

Given the unsatisfactory assessment of the existing literature rate laws for calcite dissolution/precipitation a new, mechanistically rational approach was developed by adapting the surface reaction/molecule integration mechanism of Chiang and Donohue [117]:

$$Ca^{2+}_{(aq)} \rightleftharpoons Ca^{2+}_{(ads)} \tag{4.34}$$

$$CO_3^{2-}{}_{(aq)} \rightleftharpoons CO_3^{2-}{}_{(ads)} \tag{4.35}$$

$$Ca^{2+}_{(ads)} + CO_3^{2-}{}_{(ads)} \rightleftharpoons CaCO_{3\ (ads)} \tag{4.36}$$

$$CaCO_{3\ (ads)} \rightleftharpoons CaCO_{3\ (lattice)} \tag{4.37}$$

The net dissolution rate can then be written as the balance between a forward dissolution term and a back precipitation term:

$$J_{net} = J_d - J_p \tag{4.38}$$

where,

$$J_d = k_d\left(1 - \theta_{Ca}\right)\left(1 - \theta_{CO_3}\right) \tag{4.39}$$

and

$$J_p = k_p \theta_{Ca} \theta_{CO_3} \tag{4.40}$$

where θ_A indicates the surface coverage of adsorbed A (A = Ca^{2+} or CO_3^{2-}) and k_d and k_p are rate constants for the dissolution and precipitation processes respectively. These rate terms make no distinction over whether steps (4.36) or (4.37) are rate determining. The transition state of the rate determining step is, however, a neutral species and steps (4.34) and (4.35) are at equilibrium.

In the surface reaction/molecule integration mechanism proposed by Chiang and Donohue [117] for crystal growth the dissolution flux was given by

$$J_d = k' \theta_{Ca,eq} \theta_{CO_3,eq} \tag{4.41}$$

instead of equation (4.39) i.e., the dissolution flux was thought to be proportional to the adsorbed ion surface coverage at equilibrium. However, the mechanism outlined above proposes that step (4.36) or (4.37) is rate determining and therefore the dissolution flux will be proportional to the number of unoccupied adsorption sites. Thus equation (4.39) is correct, not (4.41).

Assuming that the adsorption follows the Langmuir isotherm:

$$\theta_A = \frac{K_A [A]_o}{1 + K_A [A]_o} \tag{4.42}$$

If additionally it is assumed that at equilibrium, $J_d = J_p$, and that under that condition $[Ca^{2+}]_o[CO_3^{2-}]_o = K_{sp}$, it can be deduced that

$$J_{net}/\text{mol cm}^{-2}\text{s}^{-1} = k_p K_{Ca} K_{CO_3} \left\{ \frac{K_{sp} - [Ca^{2+}]_o [CO_3^{2-}]_o}{(1 + K_{Ca}[Ca^{2+}]_o)(1 + K_{CO_3}[CO_3^{2-}]_o)} \right\} \tag{4.43}$$

where $k_d = k_p K_{Ca} K_{CO3} K_{sp}$. Equation (4.43) was used to interpret the experiments described above. The surface boundary matrix elements for this equation are shown in Table 4.5. As with the Sjöberg equation, combining equations (4.19) and (4.43) yielded a quadratic equation in $g^A_{0,k+1}$, i.e.

Table 4.5. Surface Boundary Matrix Elements for Equation (4.43)

	Approach 1	Approach 2
$g^{A}_{0,}$	$g^{A}_{1,k+1} + \dfrac{\Delta y k_b K_{Ca} K_{CO_3}}{D}\left\{\dfrac{K_{sp} - g^{A}_{0,k} g^{C}_{0,k}}{\left(1 + K_{Ca} g^{A}_{0,k}\right)\left(1 + K_{CO_3} g^{C}_{0,k}\right)}\right\}$	$\dfrac{\left\{D g^{A}_{1,k+1} + \dfrac{\Delta y k_b K_{Ca} K_{CO_3} K_{sp}}{\left(1 + K_{Ca} g^{A}_{0,k}\right)\left(1 + K_{CO_3} g^{C}_{0,k}\right)}\right\}}{\left\{D + \dfrac{\Delta y k_b K_{Ca} K_{CO_3} g^{C}_{0,k+1}}{\left(1 + K_{Ca} g^{A}_{0,k}\right)\left(1 + K_{CO_3} g^{C}_{0,k}\right)}\right\}}$
d_1	$g^{A}_{1,k} + \dfrac{\lambda_1 \Delta y k_b K_{Ca} K_{CO_3}}{D}\left\{\dfrac{K_{sp} - g^{A}_{0,k} g^{C}_{0,k}}{\left(1 + K_{Ca} g^{A}_{0,k}\right)\left(1 + K_{CO_3} g^{C}_{0,k}\right)}\right\}$	$g^{A}_{1,k} - \dfrac{\left\{\dfrac{\lambda_1 \Delta y k_b K_{Ca} K_{CO_3} K_{sp}}{\left(1 + K_{Ca} g^{A}_{0,k}\right)\left(1 + K_{CO_3} g^{C}_{0,k}\right)}\right\}}{\left\{D + \dfrac{\Delta y k_b K_{Ca} K_{CO_3} g^{C}_{0,k+1}}{\left(1 + K_{Ca} g^{A}_{0,k}\right)\left(1 + K_{CO_3} g^{C}_{0,k}\right)}\right\}}$
b_1	$\lambda_1 + 1$	$1 + \lambda_1\left\{2 - \dfrac{D}{\left\{D + \dfrac{\Delta y k_b K_{Ca} K_{CO_3} g^{C}_{0,k+1}}{\left(1 + K_{Ca} g^{A}_{0,k}\right)\left(1 + K_{CO_3} g^{C}_{0,k}\right)}\right\}}\right\}$

All $g_{0,k}$ values are replaced by $g_{0,k+1}$ values on second and subsequent iterations.

See Table 4.3 for other matrix elements.

$$DK_{Ca}\left(g^{A}_{0,k+1}\right)^2 + \left\{D - DK_{Ca}g^{A}_{1,k+1} + \frac{\Delta y k_p K_{Ca} K_{CO_3} g^{C}_{0,k+1}}{1 + K_{CO_3} g^{C}_{0,k+1}}\right\} g^{A}_{0,k+1} - \left\{Dg^{A}_{1,k+1} + \frac{\Delta y k_p K_{Ca} K_{CO_3} g^{C}_{0,k+1}}{1 + K_{CO_3} g^{C}_{0,k+1}}\right\} = 0 \quad (4.44)$$

thus complicating further substitutions. Two methods of approach have been adopted to obtain an expression for $g^{A}_{0,k+1}$. The first was to approximate all the concentration terms in equation (4.43) to be the same as the previous vector's concentrations in the first iteration and then update these on subsequent iterations. The second was to approximate just the numerator concentration terms to be the same as the previous vector's in the first iteration. Both approaches yielded identical numerical values for the calculated concentration profiles in the channel cell. The computer program used to solve the convective-diffusion equation with equation (4.43) as the surface boundary condition is listed in Appendix 4. The same fitting procedure used for the literature rate laws was used to fit equation (4.43) to the experimental data.

The level of agreement between theory and experiment can be seen from Figures 4.4-4.6 which are typical: excellent agreement was seen over the entire flow rate range for all the experiments described above. Preliminary estimates of the three parameters in equation (4.43) were obtained by the examination of a data subset, including rate data measured for high bulk calcium levels. Under these latter conditions ($[Ca^{2+}]_{bulk} \approx 10^{-3}$ mol dm^{-3}) the surface calcium concentration was effectively fixed, as dissolution added relatively few Ca^{2+} ions and this enabled K_{CO3} to be estimated as 3×10^7 cm^3 mol^{-1}. Examination of the data measured with low

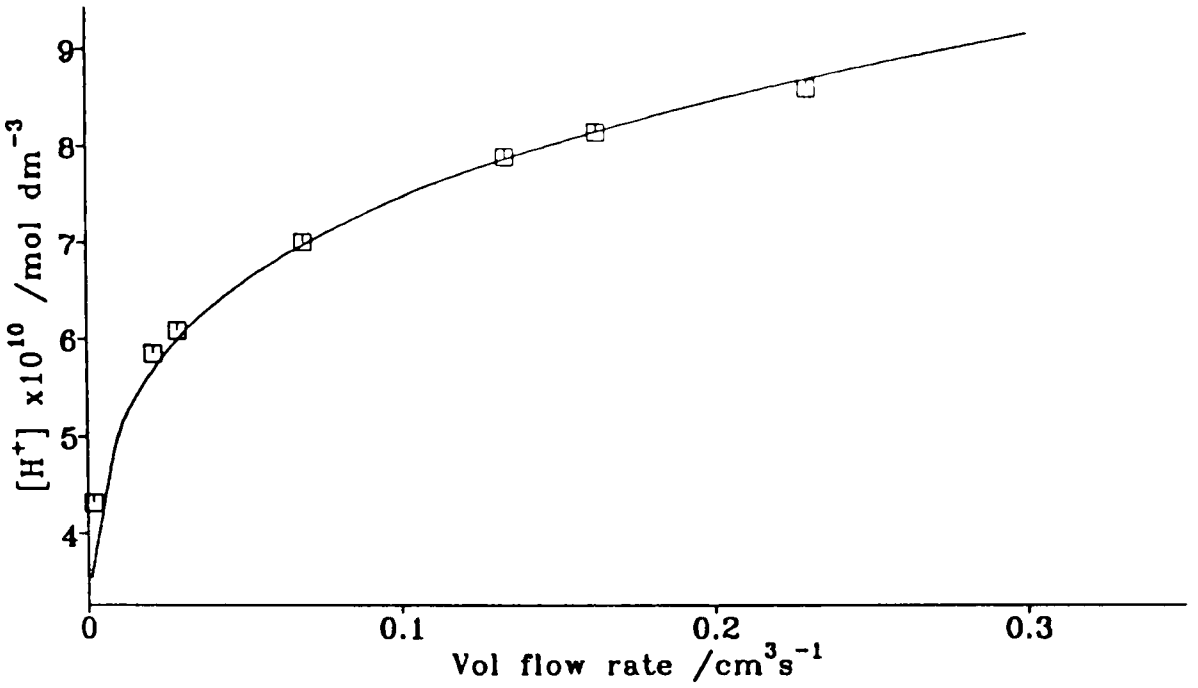

Figure 4.4. Flow behaviour of the detector pH electrode for pH_{bulk}=8.44 & $[Ca^{2+}]_{bulk}$=0. *The line shows the behaviour predicted using equation (4.43) and parameters in Table 4.7 (Run C4).*

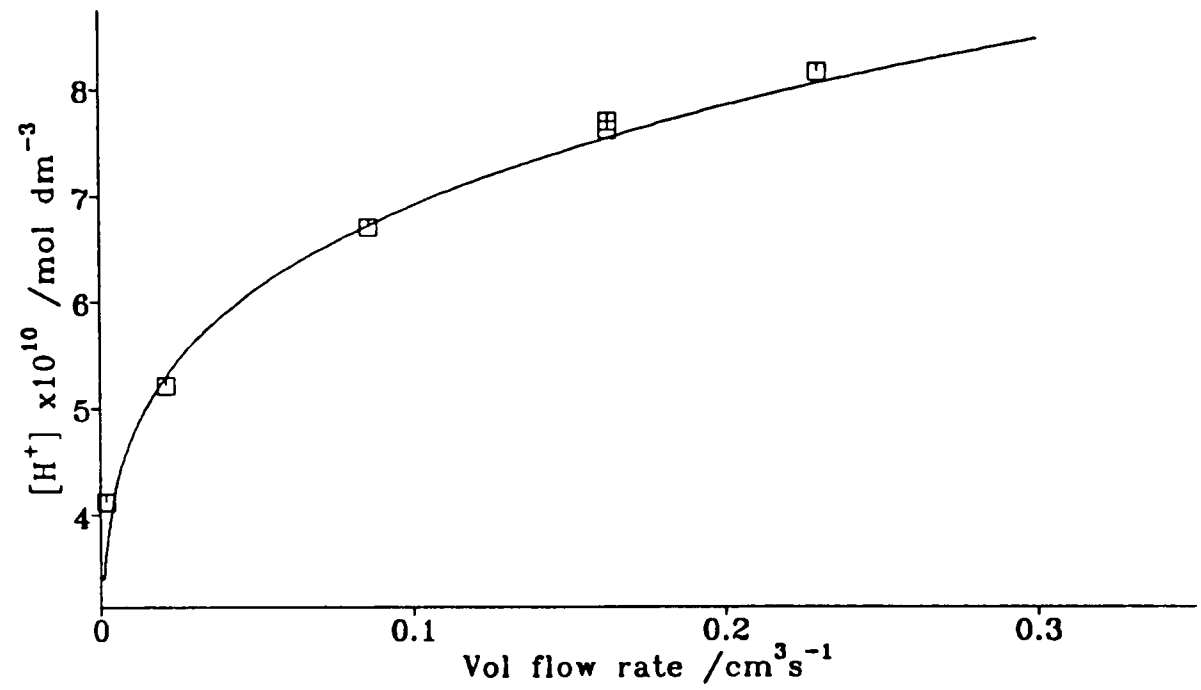

Figure 4.5. Flow behaviour of the detector pH electrode for pH_{bulk}=8.34 & $[Ca^{2+}]_{bulk}$=0.102 mM. *The line shows the behaviour predicted using equation (4.43) & parameters in Table 4.7 (Run C10).*

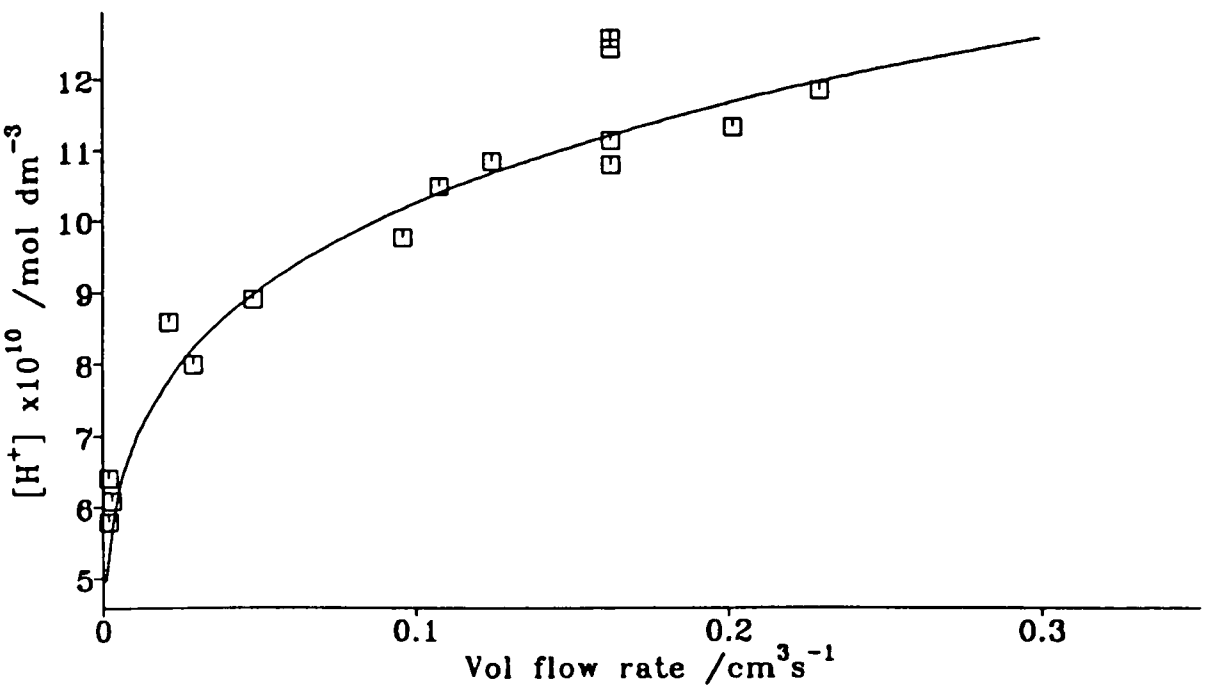

Figure 4.6. Flow behaviour of the detector pH electrode for pH_{bulk}=8.38 & $[Ca^{2+}]_{bulk}$=1.01 mM. *The line shows the behaviour predicted using equation (4.43) & parameters in Table 4.7 (Run C12).*

Table 4.6. Experimental Parameters for the Surface Reaction/Molecule Integration Model

Run	$[Ca^{2+}]_{bulk}/\mu M$	pH_{bulk}	K_{CO3}/cm^3mol^{-1}	$k_p K_{Ca} K_{CO3}$ /$cm^4mol^{-1}s^{-1}$	
				$K_{Ca} = 0$	$K_{Ca} = 10^6$ cm^3mol^{-1}
D1	0	8.30	$1.5x10^7$	930	950
C1	0	8.45	$3x10^7$	800	820
C2	0	8.70	$4.5x10^7$	675	685
C3	0	8.46	$3x10^7$	750	760
C4	0	8.44	$3x10^7$	930	950
C5	0	8.43	$4.5x10^7$	1710	1770
C6	1.02	8.34	$1.5x10^7$	495	505
C7	10.2	8.50	$1.5x10^7$	1238	1290
C8	50.8	8.12	$3x10^7$	720	770
C9	102	8.62	$3x10^7$	1440	1650
C10	102	8.34	$3x10^7$	1140	1300
C11	204	8.57	$3x10^7$	990	1250
C12	1011	8.38	$3x10^7$	600	1200
C13	1065	8.53	$4.5x10^7$	720	1500
D3	5013	8.38	$3x10^7$	200	1200
D4	10000	8.69	$3x10^7$	40	450
E1	10000	8.48	$3x10^7$	120	1400

levels of calcium present in bulk then revealed K_{Ca} to be no greater than 10^6 cm^3 mol^{-1}, i.e. the value of the product $K_{Ca}[Ca^{2+}]_o$ in the denominator of equation (4.43) was found to be small compared to unity for these cases. Table 4.6 shows the best fits for the parameters k_p and K_{CO3} deduced from this subset of data with K_{Ca} = 0 in the denominator. It can be seen that on moving to yet higher bulk calcium concentrations ($[Ca^{2+}]_{bulk} \approx 10$ mM) the value of k_p obtained with K_{Ca} = 0 was significantly smaller than for the other experiments. By contrast, with the data subset fitted with $K_{Ca} = 10^6$ cm^3 mol^{-1}, as also given in Table 4.6, there was much less variation in the value of $k_pK_{Ca}K_{CO3}$ required to fit the data. This implied that K_{Ca} was at the maximum of its range determined by low bulk $[Ca^{2+}]$ experiments since less variation in the constant term $k_pK_{Ca}K_{CO3}$ was achieved with $K_{Ca} = 10^6$ cm^3 mol^{-1}. K_{Ca} cannot be larger than 10^6 cm^3 mol^{-1} without distorting the shape of the sensor-flow rate response at low bulk calcium concentrations.

The reason for the decrease in $k_pK_{Ca}K_{CO3}$ when K_{Ca} = 0 was used to fit the experimental data was because the apparent value of k_pK_{Ca} in the case where $[Ca^{2+}]_o$ is large was in fact given by

$$\frac{k_pK_{Ca}}{1 + K_{Ca}[Ca^{2+}]_o} \approx \frac{k_p}{[Ca^{2+}]_o} \qquad (4.45)$$

and thus decreased as the surface calcium ion concentration increased.

The rate information from the 40 separate experiments detailed in Table 4.7 were modelled using these mean values of $K_{CO3} = 3\times10^7$ cm^3 mol^{-1} and $K_{Ca} = 10^6$ cm^3 mol^{-1}. A mean value of $k_pK_{Ca}K_{CO3}$ = 990 cm^4 mol^{-1} s^{-1} (standard deviation 580) was deduced from this complete set of data. This corresponded to an average precipitation rate constant $k_p = 3.3\times10^{-11}$ mol cm^{-2} s^{-1} (standard deviation

Table 4.7. Analysis of the Full Set of Experimental Rate Data for Etched Surface with $K_{Ca} = 10^6$ cm^3 mol^{-1} and $K_{CO3} = 3 \times 10^7$ cm^3 mol^{-1}

Run	$[Ca^{2+}]_{bulk}$ /μM	pH_{bulk}	$k_p K_{Ca} K_{CO3}$ /cm^4 mol^{-1} s^{-1}
A1[1]	0	8.47	1980
A2	0	8.47	1550
A3	0	8.54	2090
A4	0	8.75	1030
A5	0	8.53	1760
A6	0	8.49	2620
A7	0	8.12	1230
B1[2]	0	8.74	380
B2	0	8.17	560
B3[2]	0	8.44	550
B4	0	8.22	820
B5[2]	0	8.71	390
B6[2]	0	8.80	270
B7[2]	0	8.30	150
B8	0	8.37	710
B9[2]	10	8.51	780
B10[2]	20	8.77	130
B11[2]	50	8.34	1250
B12[2]	103	8.66	330

[1] The letters A - E refer to five separate crystals.

[2] Experiments by C.A.Narramore

Run	$[Ca^{2+}]_{bulk}$ /μM	pH_{bulk}	$k_p K_{Ca} K_{CO3}$ /cm^4 mol^{-1} s^{-1}
B13[2]	103	8.42	510
B14[2]	206	8.61	180
B15	0	8.45	1240
C1	0	8.45	820
C2	0	8.70	670
C3	0	8.46	760
C4	0	8.44	950
C5	0	8.43	1600
C6	1	8.34	520
C7	10	8.50	1500
C8	51	8.12	770
C9	102	8.62	1650
C10	102	8.34	1300
C11	204	8.57	1250
C12	1010	8.38	1200
C13	1070	8.53	1450
D1	0	8.30	1045
D2[2]	0	8.60	610
D3	5010	8.38	1200
D4	10000	8.69	450
E1	10000	8.48	1400

$1.9x10^{-11}$) and a dissolution rate constant $k_d = 6.2x10^{-11}$ mol cm^{-2} s^{-1} (standard deviation $3.6x10^{-11}$). In addition, good agreement was seen between different calcite crystals: the runs given in Table 4.7 were based on five separate crystals. It may be concluded that equation (4.43) can adequately describe the kinetics of calcite dissolution/precipitation over a wide range of conditions and the merits of approaching the problem using the channel cell is evident. In particular, the existence of a well-defined and calculable hydrodynamic regime permitted the sensitive interrogation of the dissolving interface using variable mass transport as a probe. This should be evident from Figures 4.7-4.13 which show the computed concentration profiles within the flow cell for all the kinetically significant species deduced using the mean parameters specified above and for a flow rate of 10^{-2} cm^3 s^{-1}.

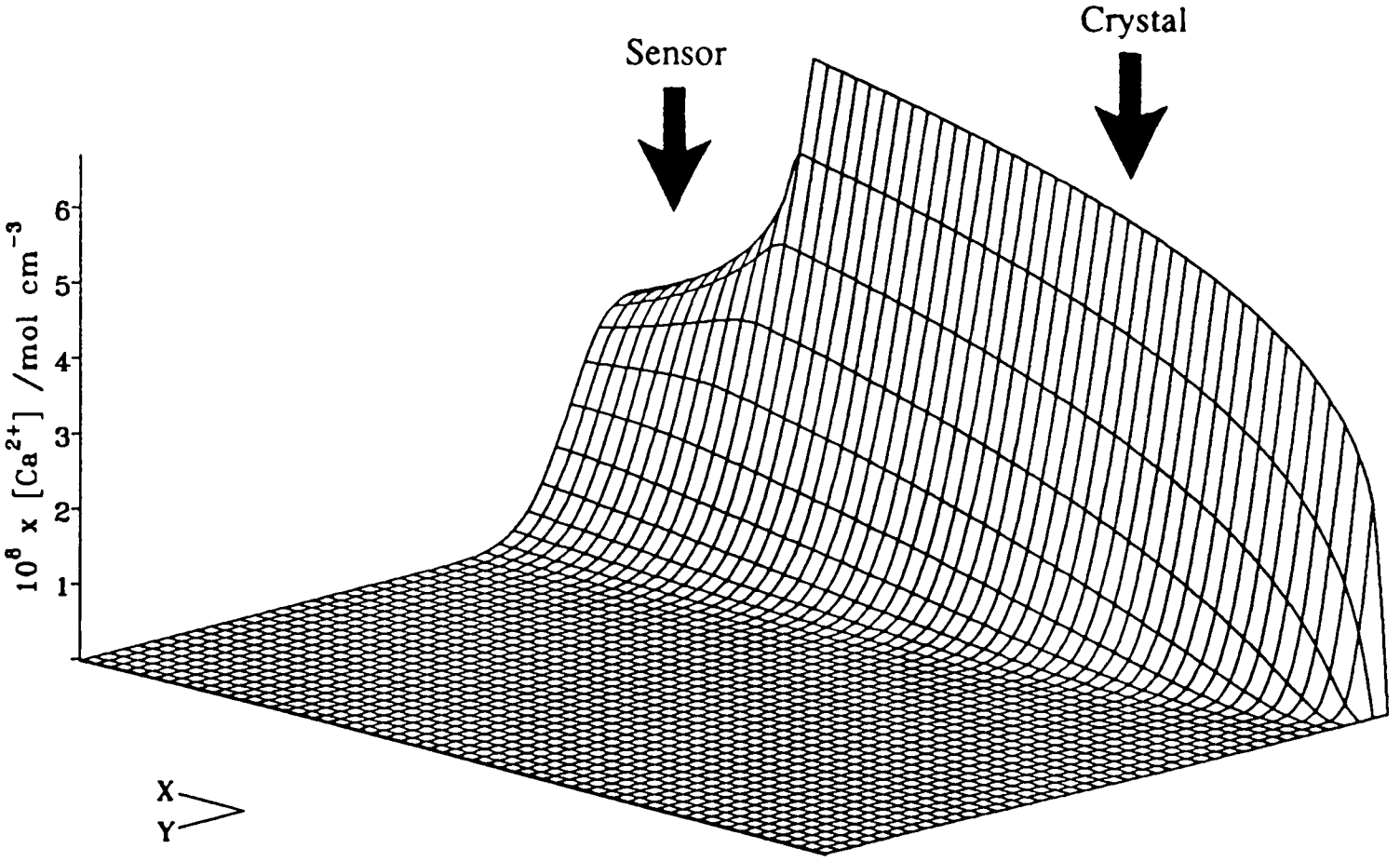

Figure 4.7. Computed concentration profile of Ca^{2+} *in the channel cell calculated using the theoretical model and mean parameters described in the text together with the values of flow rate =* 10^{-2} cm^3 s^{-1} *and* pH_{bulk} = 8.5.

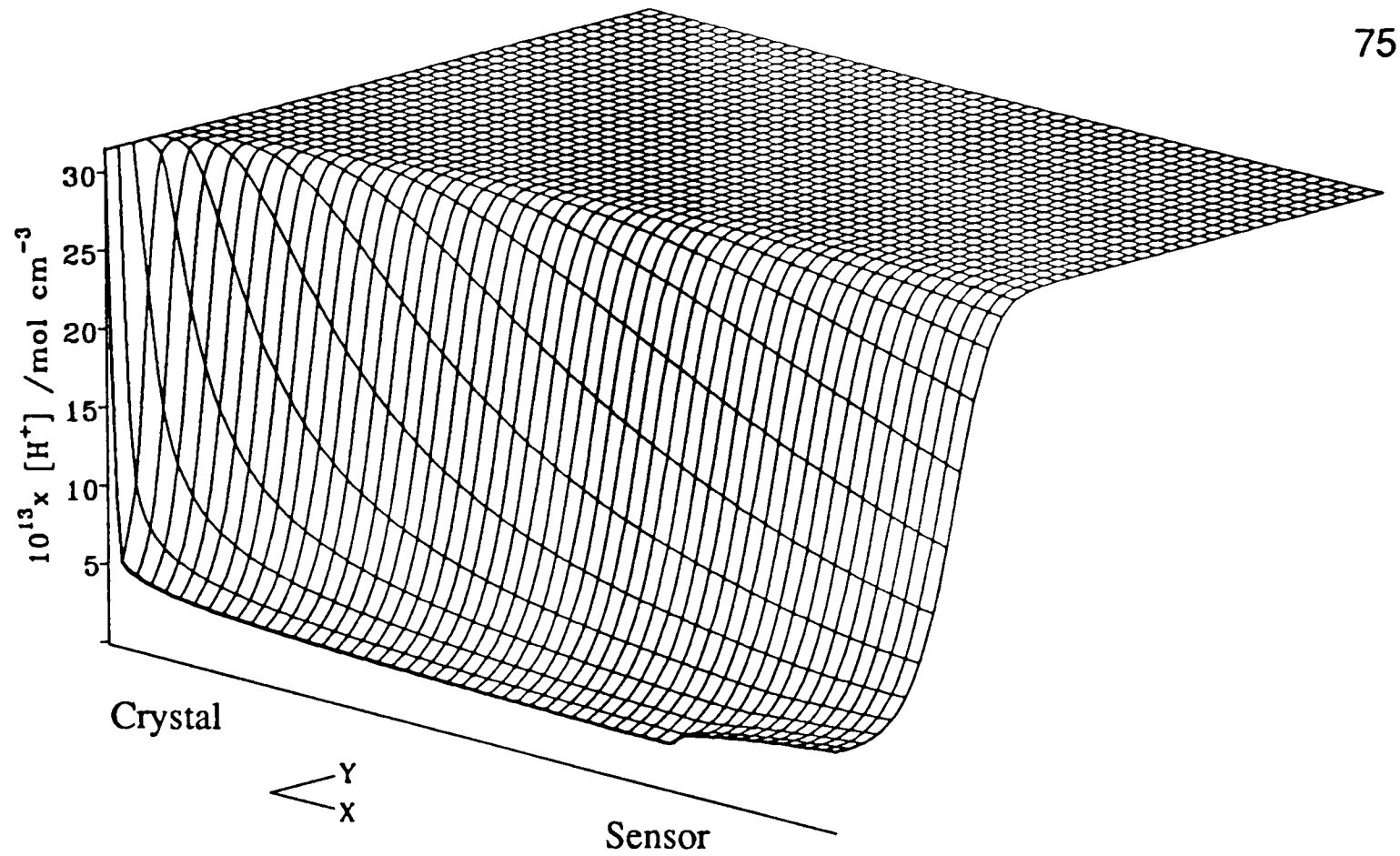

Figure 4.8. Computed concentration profile of H^+ *in the channel cell calculated using the theoretical model and mean parameters described in the text together with the values of flow rate =* 10^{-2} cm^3 s^{-1} *and* pH_{bulk} = 8.5.

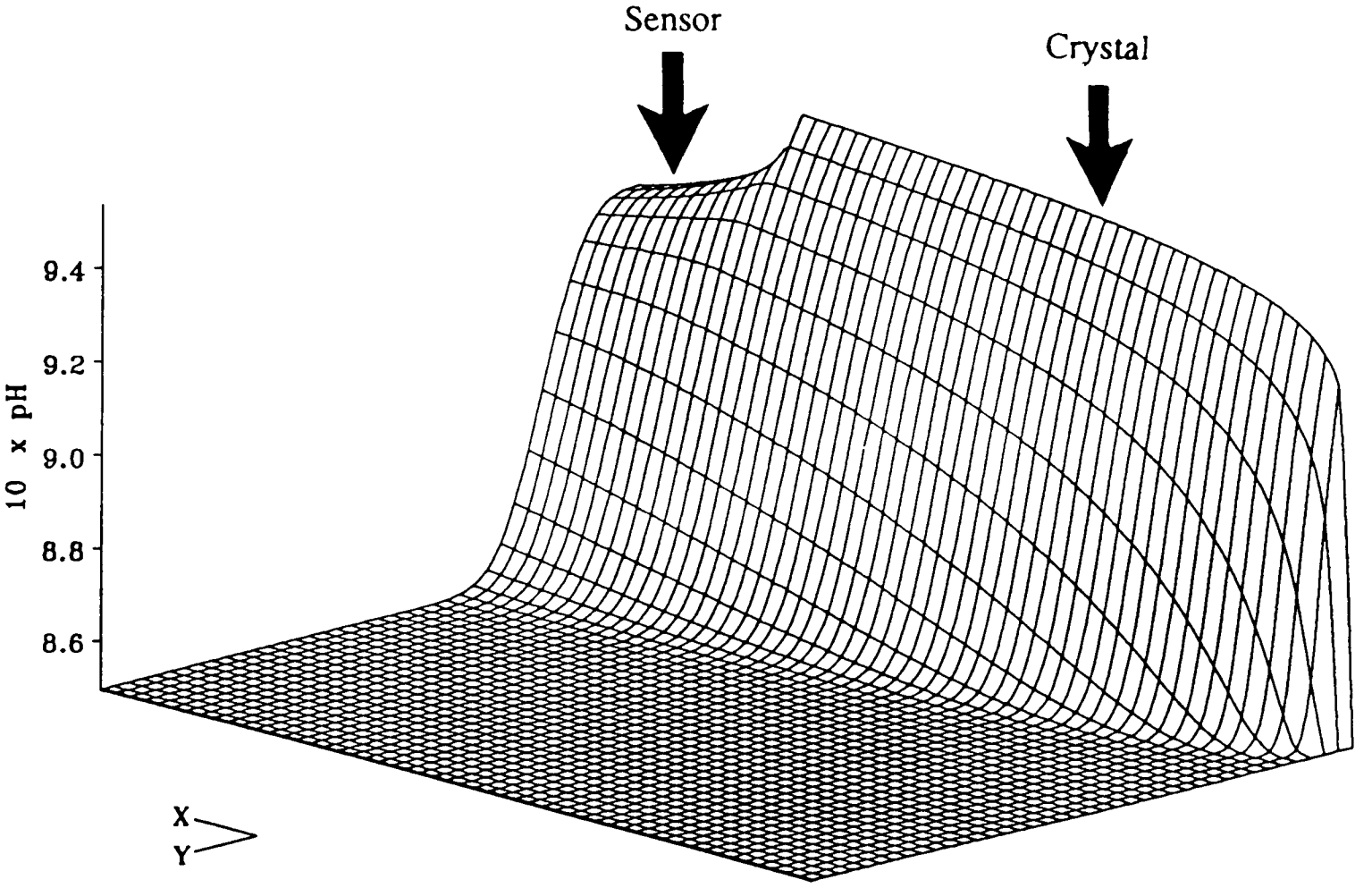

Figure 4.9. Computed pH*-profile in the channel cell calculated using the theoretical model and mean parameters described in the text together with the values of flow rate =* 10^{-2} cm^3 s^{-1} *and* pH_{bulk} = 8.5.

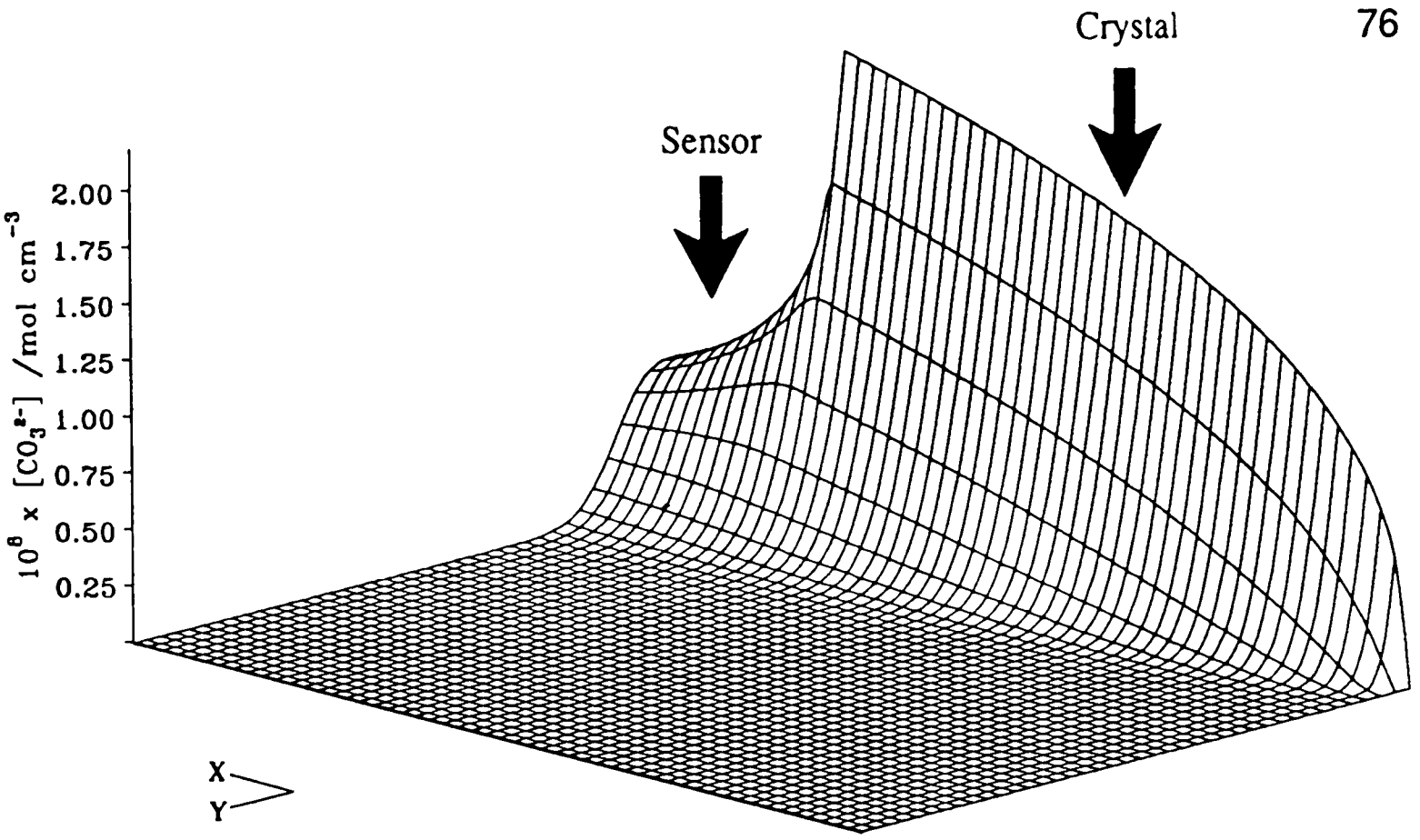

Figure 4.10. Computed concentration profile of CO_3^{2-} *in the channel cell calculated using the theoretical model and mean parameters described in the text together with the values of flow rate =* 10^{-2} cm^3 s^{-1} *and* pH_{bulk} = 8.5.

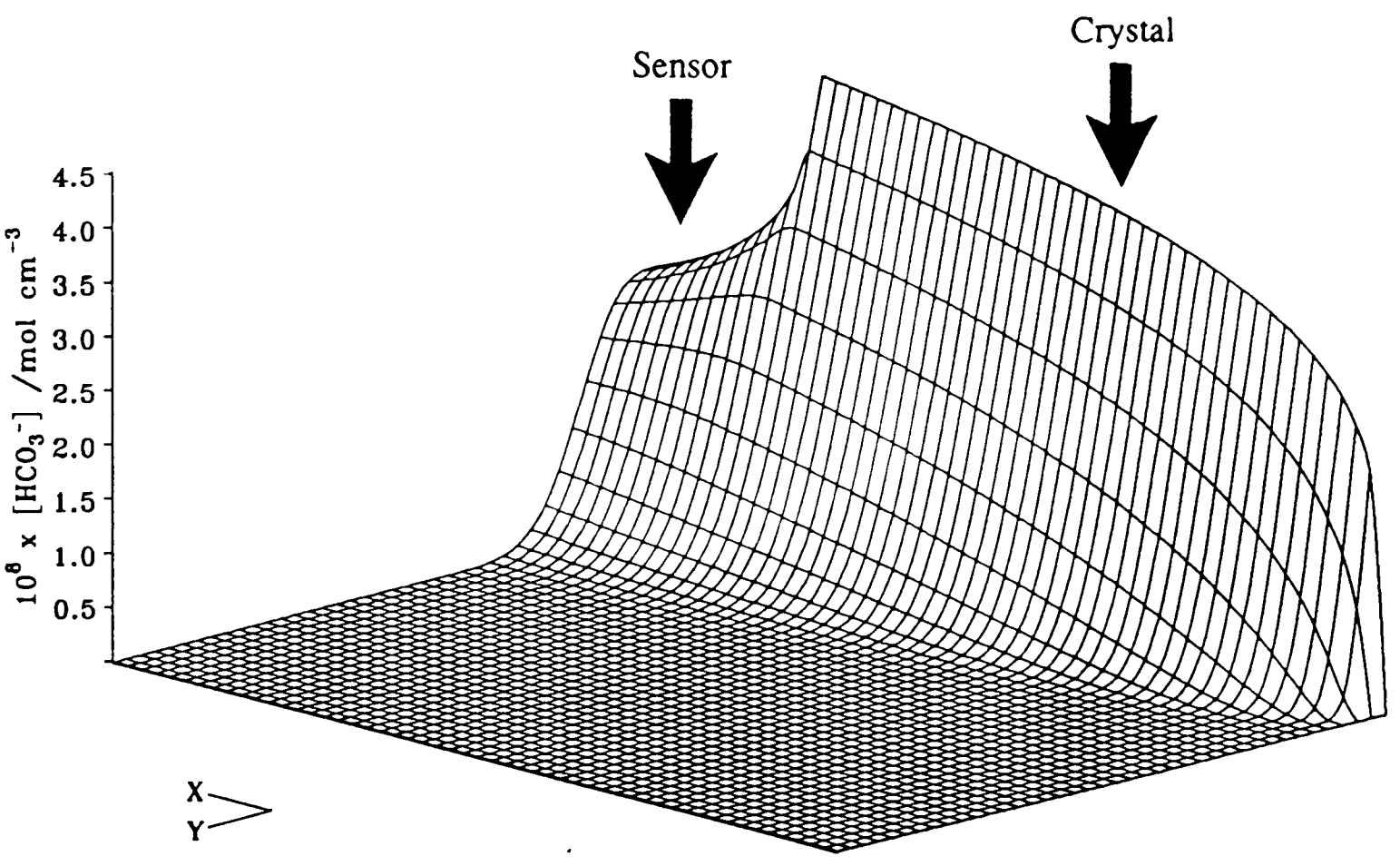

Figure 4.11. Computed concentration profile of HCO_3^- *in the channel cell calculated using the theoretical model and mean parameters described in the text together with the values of flow rate =* 10^{-2} cm^3 s^{-1} *and* pH_{bulk} = 8.5.

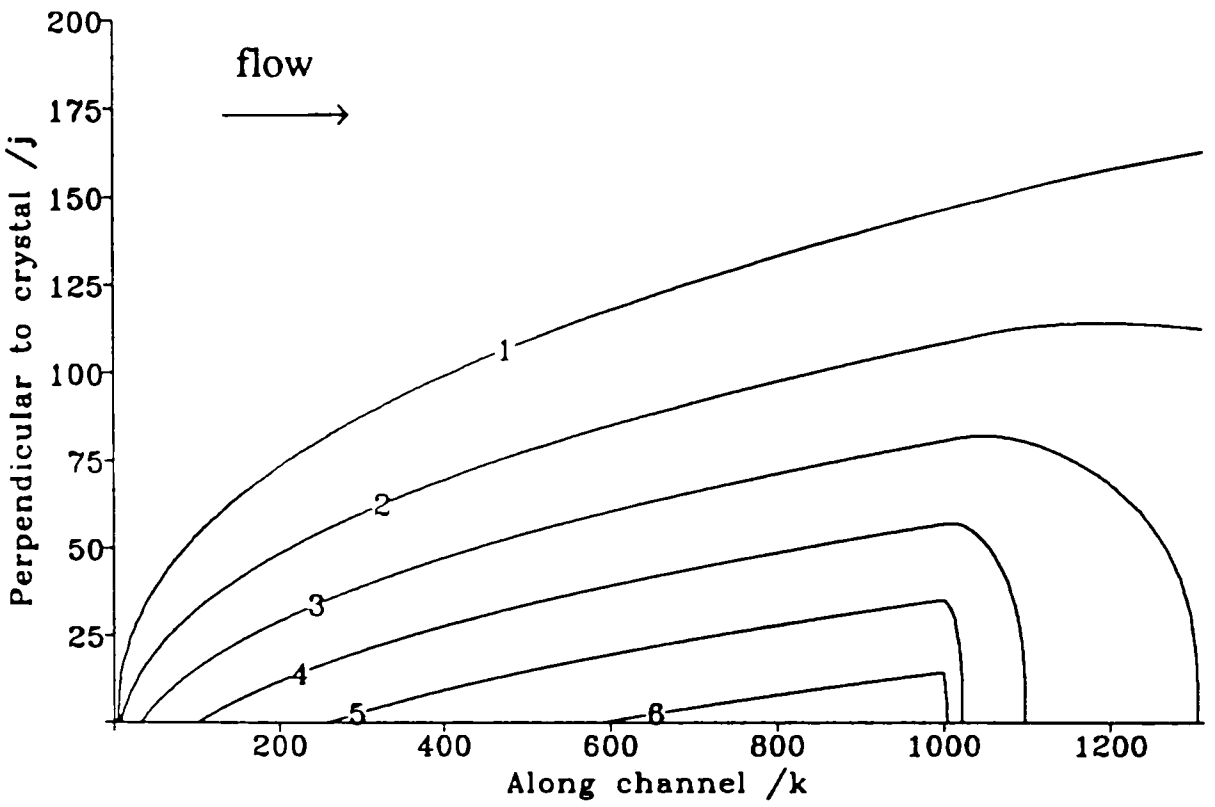

Figure 4.12. Computed contour plot of the Ca^{2+} *concentration profile in the channel cell calculated using the same parameters as Figure 4.7. Contours are in units of* $[Ca^{2+}]x10^{8}$ mol cm^{-3}. *Scales are in BI coordinates, where the crystal is situated between* $k = 0$ *and* 1000, *with the crystal surface at* $j = 0$ *and the channel wall at* $j = 1000$.

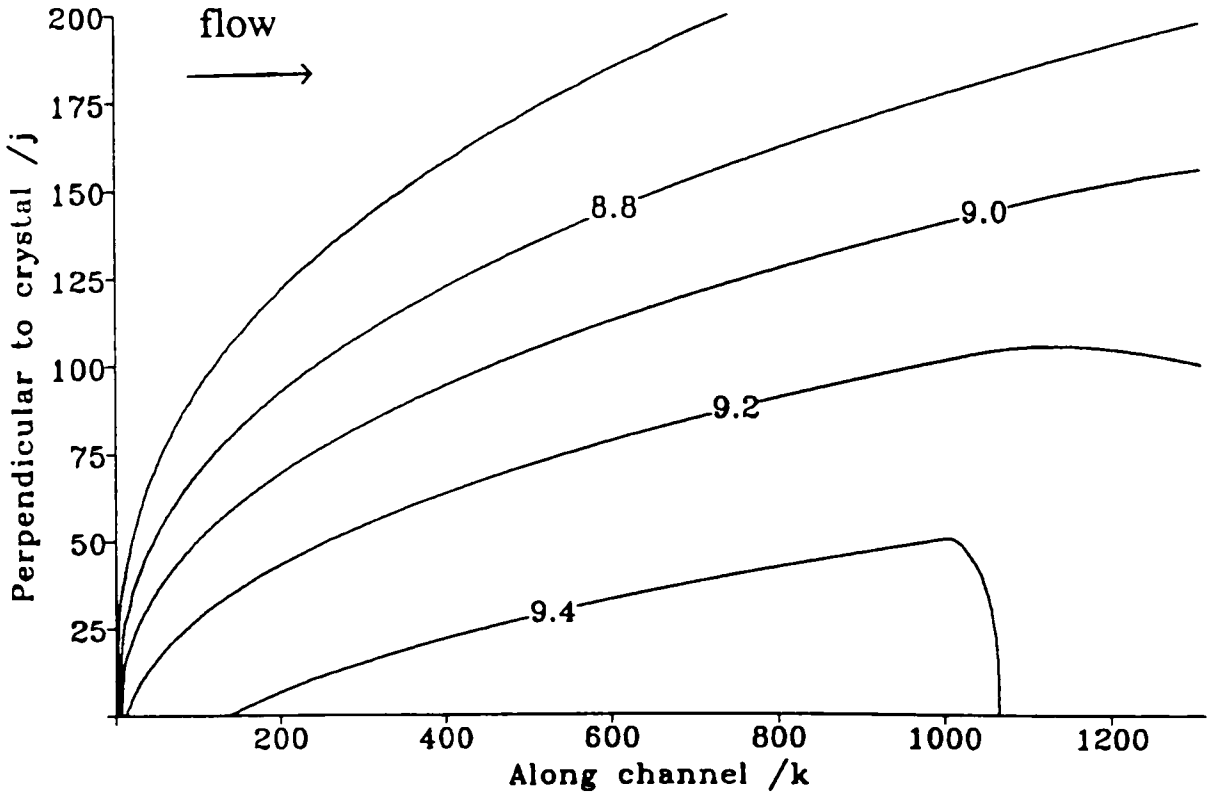

Figure 4.13. Computed contour plot of the pH-*profile in the channel cell calculated using the same parameters as Figure 4.9. Scales are in BI coordinates, where the crystal is situated between* $k = 0$ *and* 1000, *with the crystal surface at* $j = 0$ *and the channel wall at* $j = 1000$.

4.4.2 Polished Surface

Experiments were also carried out using cleaved calcite crystals which had only been polished using 1 μm diamond lapping compound and rinsed in millimolar HCl for one minute. Equation (4.43) was again found to give an excellent fit across the wide flow rate and wide pH range (pH 7.70 to 9.74) used. Experiments at higher pHs were precluded by the precision of the potentiometric detection under these conditions. The parameters used to model these experiments are listed in Table 4.8. The lack of variable bulk calcium ion concentration data prevented the accurate determination of K_{Ca} and K_{CO3} on this surface and they were assumed to be unchanged from the "heavily etched" case. The mean value of $k_p K_{Ca} K_{CO3}$ = 6730 $cm^4\ mol^{-1}\ s^{-1}$ (standard deviation 3770 $cm^4\ mol^{-1}\ s^{-1}$) thus obtained, corresponds to the values k_p = 2.2x10^{-10} mol $cm^{-2}\ s^{-1}$ and k_d = 4.2x10^{-10} mol $cm^{-2}\ s^{-1}$.

This demonstrated that the polished surface dissolved at a faster rate than the etched surface. A similar trend was observed by House and colleagues [36,65], who found that the initial dissolution flux for BDH calcite powder was 1.35x10^{-10} mol $cm^{-2}\ s^{-1}$, whereas that for Calopake F calcite powder was 3.61x10^{-11} mol $cm^{-2}\ s^{-1}$. Microscopy showed that whilst the BDH powder consisted of small regular rhombohedral particles of area 0.22 $m^2\ g^{-1}$ the Calopake F was composed of elliptically shaped particles (5.65 $m^2\ g^{-1}$). Though not directly comparable, because House used the Plummer rate equation, the trend in dissolution flux observed by House on increasing the surface area of the particles was the same as the variation in k_d.

Table 4.8. Analysis of the Experimental Rate Data for Polished Calcite with $K_{Ca} = 10^6$ cm^3 mol^{-1} and $K_{CO3} = 3 \times 10^7$ cm^3 mol^{-1}

Run	pH_{bulk}	$k_p K_{Ca} K_{CO3}$ /cm^4 mol^{-1} s^{-1}
A10[1]	8.41	2800
A11	8.46	3200
A12	8.54	5200
A13	8.71	3000
E10	7.70	6550
E11	8.17	8250
E12	8.30	10500
E13	8.44	8250
E14	8.75	4280
E15	8.83	4000
E16	9.04	3950
E17	9.47	14600
E18	9.74	12000
E19	8.50	3700
E20	8.43	3500
F10	8.45	8400
F11	8.62	12300

[1] The letters A, E and F refer to three separate crystals.

4.4.3 Microscopy

The surfaces of the calcite crystals, set in the coverplates, were examined using differential interference-contrast light microscopy, as described in Chapter 3. The polished surface after rinsing in millimolar HCl for one minute showed small (< 1 μm wide) scratches and etch pits just beginning to form. After flowing 0.5 M KCl (pH > 7) over this polished surface at V_f = 0.2 cm^3 s^{-1} for 30 minutes, which was typically the time taken for an experimental run, the surface scratches had been etched to form lines of deeper pits. The pits at the upstream edge of the crystal were about 5 μm across, but downstream were 1 - 2 μm in size.

The heavily etched surface, however, showed little evidence of scratches and the etch pits had grown into each other. After flowing electrolyte over the crystal for 7 - 8 hours at V_f = 0.004 cm^3 s^{-1}, the pits upstream were ≈ 50 μm across; downstream they were ≈ 20 μm across (Plates 1 and 2). Similarly at V_f = 0.27 cm^3 s^{-1}, the upstream edge pits were much larger (≈ 60 μm) than those further downstream (≈ 20 μm) as shown in Plates 3 and 4. The smaller pits downstream were due to the build up of surface Ca^{2+} concentration and hence a reduction in the net dissolution rate. The pit densities on these surfaces were typically 3x10^4 cm^{-2} and are believed to nucleate at emergent screw dislocations [118].

The rhombohedral shape of the etch pits reflected the ionic geometry of the {100} cleavage planes (Figure 4.14). This was because the size of the observable etch pit was much larger than that of the stress field associated with the emergent dislocation [119] and therefore the latter did not influence the pit shape. The growth of the etch pits involved two processes [120]: nucleation at the emergent dislocation and the recession of steps away from the dislocation site.

Plate 1. DIC micrograph of the upstream edge of a calcite crystal etched in the channel cell at V_f = 0.004 $cm^3\ s^{-1}$ *for* 7 - 8 hours. *Magnification is approximately* x200.

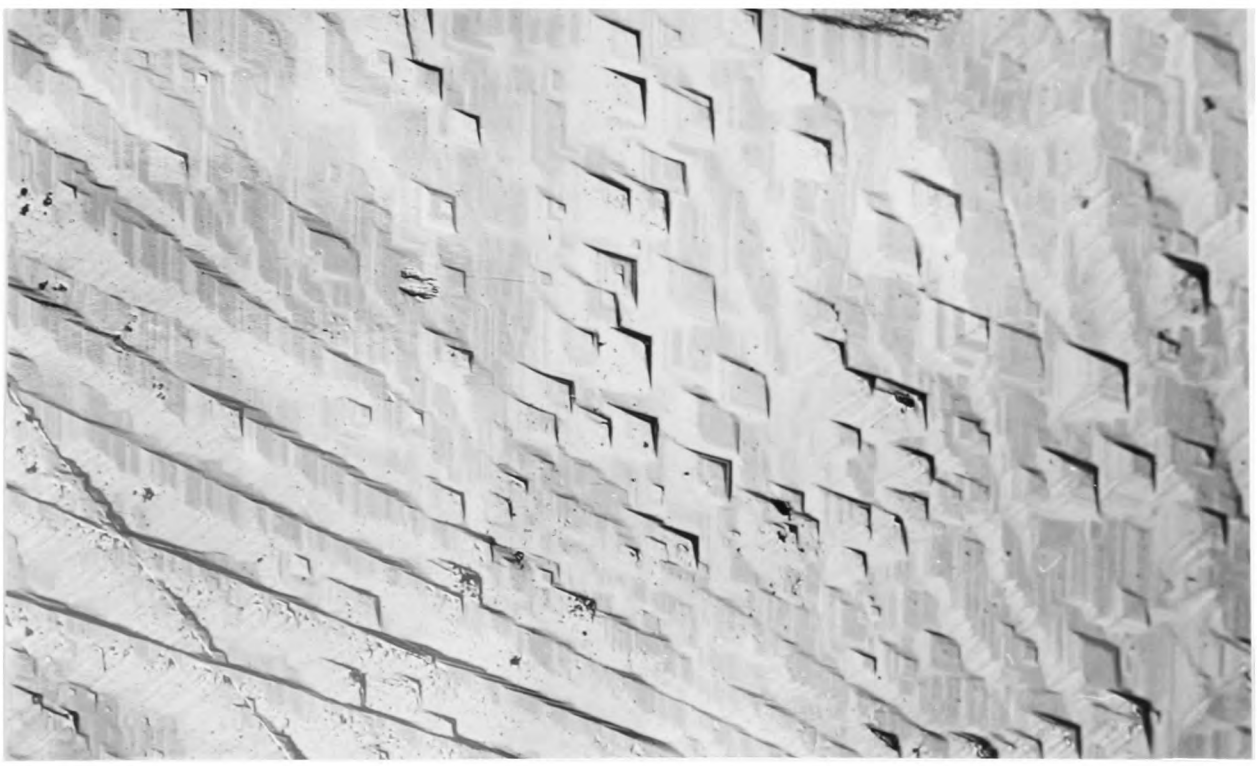

Plate 2. DIC micrograph of the downstream edge of a calcite crystal etched in the channel cell at V_f = 0.004 $cm^3\ s^{-1}$ *for* 7 - 8 hours. *Magnification is approximately* x200.

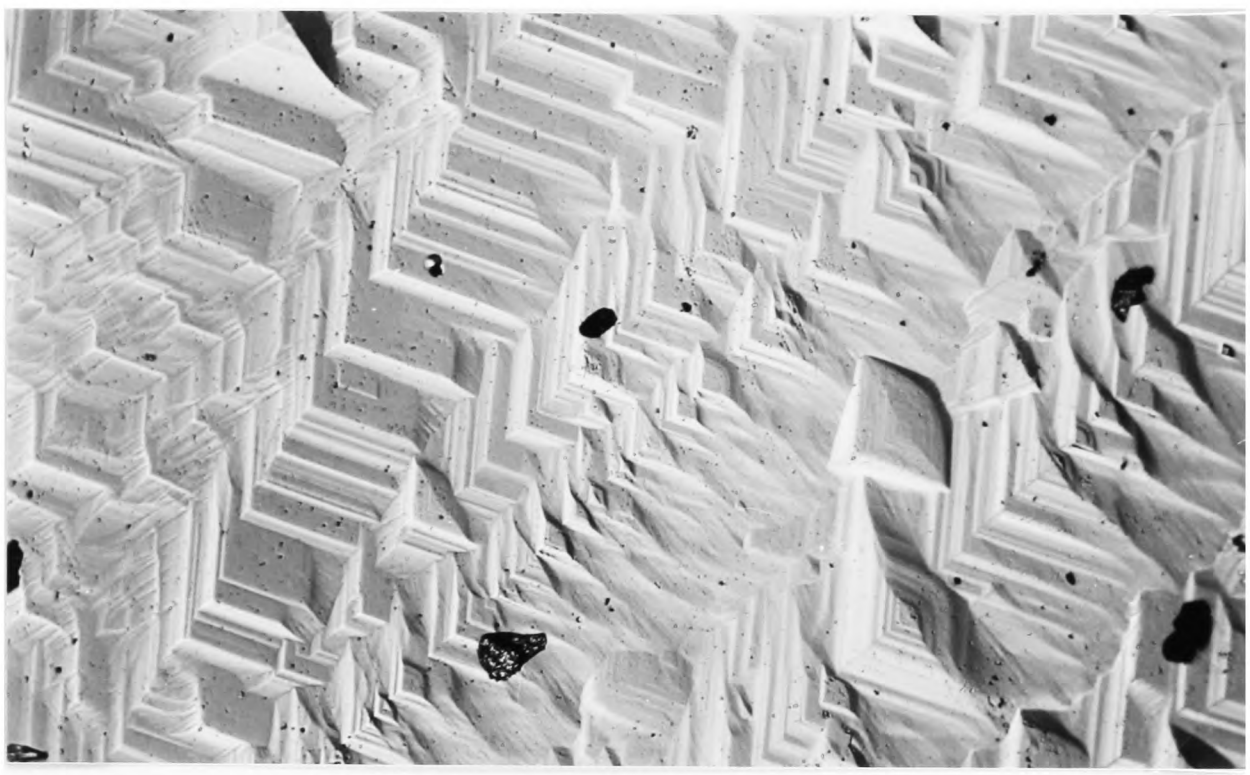

Plate 3. DIC micrograph of the upstream edge of a calcite crystal etched in the channel cell at V_t = 0.004 $cm^3\ s^{-1}$ *for* 7 - 8 hours. *Magnification is approximately* x200.

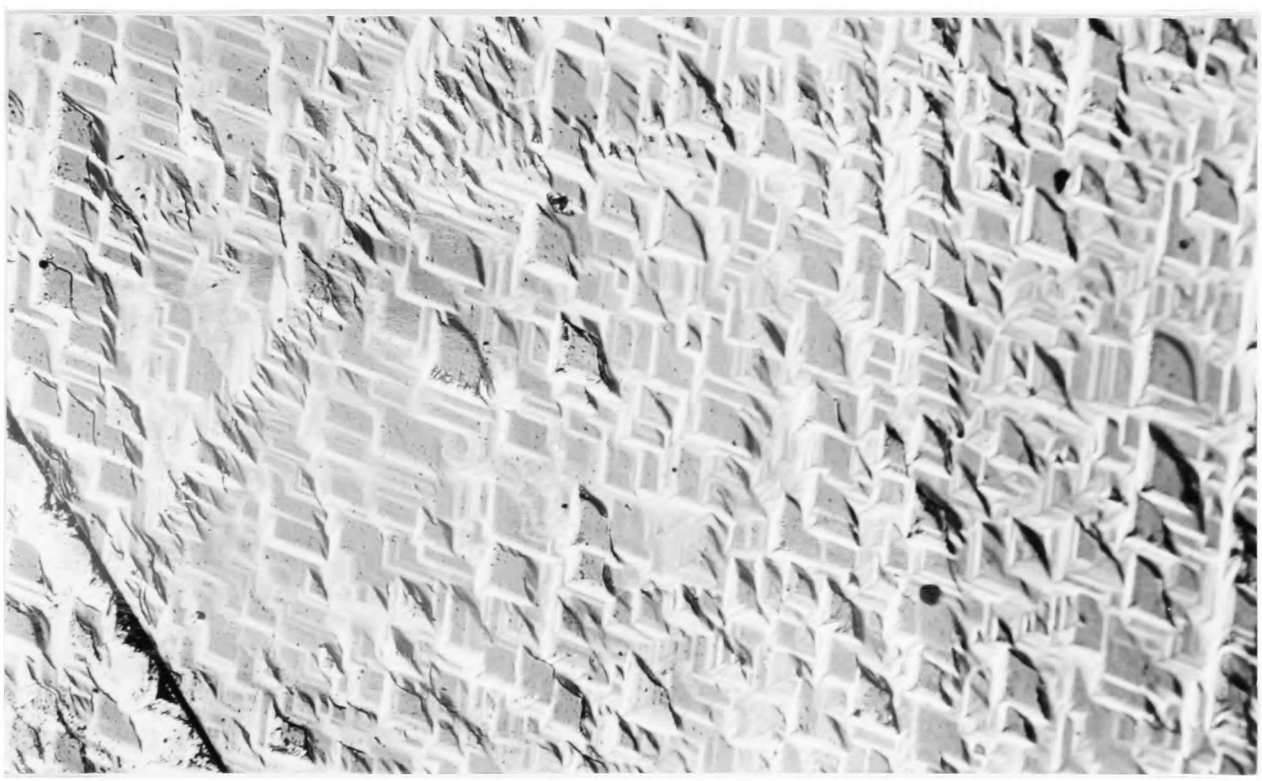

Plate 4. DIC micrograph of the downstream edge of a calcite crystal etched in the channel cell at V_t = 0.004 $cm^3\ s^{-1}$ *for* 7 - 8 hours. *Magnification is approximately* x200.

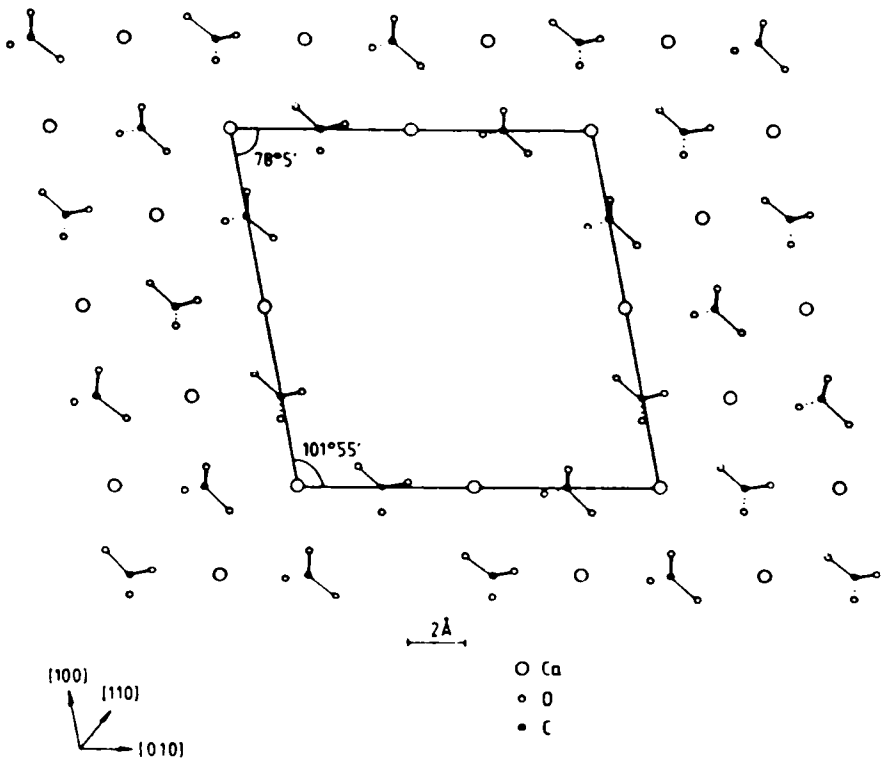

Figure 4.14. A schematic representation of the shape of the etch pits relative to the geometry of the (001) crystal plane. The [001] direction is into the paper (see Appendix 5 for details of crystallographic notation).

4.5 Discussion

The success of equation (4.43) in describing the calcite dissolution reaction under the widely differing conditions described in this chapter, suggested that the surface reaction/ molecule integration mechanism is likely to be a correct description of the process under study. It is interesting to consider some previous observations in the light of this probable mechanism. First Christoffersen and Christoffersen have pointed out that the rate of calcite growth/dissolution, as described by a Davies and Jones type rate equation, is strikingly independent of the saturated solution's ionic strength (from 0.01 M to 0.20 M) if the equation is written in terms of the activities of the solution species [48,66]. This is consistent with the electroneutral transition state predicted by the surface reaction/molecule integration mechanism. Second, streaming potential measurements of Thompson have shown that CO_3^{2-} and Ca^{2+}, but not HCO_3^-, are surface active on calcite [62]. This again supports the proposed mechanism. Also the observation that $K_{Ca} < K_{CO3}$

is consistent with the data of Thompson, as are the electrophoresis measurements of Smith [61,121], which show calcite surfaces to bear a negative charge, except at high pCa values where they become positive. Moreover, it should be noted that equation (4.43) fitted the observed rate data over a wide range of conditions, including pCa. The fact that the surface charge is known to vary over these conditions [61,62,121] is additional evidence in favour of a neutral transition state. Very recently Huang *et al.* [122] have demonstrated, using calcite powder and Ca^{2+} ion selective electrodes, that the adsorption of Ca^{2+} ions fits the Langmuir isotherm with an adsorption constant of 1.80×10^6 cm^3 mol^{-1}. Sjöberg [29] also concluded that the effect of Ca^{2+} ions on single crystal dissolution rates was due to Langmuirian adsorption with an adsorption constant of 1.32×10^6 cm^3 mol^{-1}. Both of these values of K_{Ca} are in excellent agreement with the value deduced from the fitting procedure described above. Zachara *et al.* [123] studied the adsorption of divalent metal ions (M^{2+}) on calcite and concluded that M^{2+}-Ca^{2+} exchange occurred on cation specific surface sites. The nature of the adsorbed species was uncertain, though the data suggested that some ions (Mn, Cd) dehydrate rapidly after adsorption to produce a surface co-precipitate, whereas others (Co, Ni, Zn) remain adsorbed as hydrated complexes until incorporated into the crystal lattice. Möller and colleagues concluded that equilibrium between the solid and solution only occurred at the surface layers [124] and that no more than a monolayer of the calcite surface participated in Ca^{2+}-Ca^{2+} exchange [125]. Finally House [63] has found previously used rate expressions to be inadequate and concluded that there is no unique experimental growth curve. This points to the need to consider surface coverages of adsorbed ions in describing the calcite-water interface.

In conclusion, the channel flow cell has been successfully used to deduce the fundamental rate law - equation (4.43) - describing the dissolution/precipitation kinetics at high pH.

CHAPTER 5

INHIBITION OF CALCITE DISSOLUTION

5.1 Introduction

In Chapter 4 dissolution/precipitation processes at the calcite-water interface were investigated. A new rate law was developed which accurately described the kinetics over the full range of conditions. In this chapter, the results are reported of the effects of some possible inhibitor species on the dissolution of calcite single crystals, investigated using the channel cell. The species investigated for their inhibitory effect were substituted 1,2-dicarboxylic acids and magnesium ions. The theory developed in Chapter 4 to account for the dissolution/precipitation processes was extended to include the adsorption of inhibitor species on the calcite surface. DIC microscopy was used to monitor any observable the effect of the inhibitor on the morphology of the dissolution etch pits.

5.2 Previous Studies

Chemical etchants have been used to investigate the dislocation structures of calcite crystals [118,126-128] and the shapes of the etch pits formed were found to be specific to the chemicals used and their concentrations. A wide variety of chemical etchants have been used, as summarised in Table 5.1; carboxylic acids having received wide attention. Their morphological effect on the growth of calcite has also been studied [129].

5.2.1 1,2-Dicarboxylic Acids

The influence of 1,2-dicarboxylic acids on the kinetics of calcite dissolution and precipitation has received much less research. The inhibition of calcite growth by benzene-polycarboxylic acids at pH 8.50 has been investigated [130] using the

Table 5.1. Previous Studies of Etch Pit Morphology on Calcite

Etchant	Reference
Hydrochloric acid	[131]
Nitric acid	[128]
Nitric acid (1:100 ethanol)	[126]
Formic acid HCO_2H	[126]
Acetic acid CH_3CO_2H	[126]
Propionic acid $CH_3CH_2CO_2H$	[126]
Lactic acid $CH_3CH(OH)CO_2H$	[126]
Malic acid $HO_2CCH_2CH(OH)CO_2H$	[118]
Maleic acid *cis* $HO_2CCH=CHCO_2H$	[126,131]
Fumaric acid *trans* $HO_2CCH=CHCO_2H$	[131]
Tartaric acid $HO_2CCH(OH)CH(OH)CO_2H$	[118,126,132]
Citric acid $HO_2CCH_2C(OH)(CO_2H)CH_2CO_2H$	[126,128]
Ethylene diamine tetra-acetic acid $(HO_2CCH_2)_2NCH_2CH_2N(CH_2CO_2H)_2$	[126]
Sodium dihydrogen phosphate NaH_2PO_4	[128]

chemo-stat technique. It was shown [130] that benzenehexacarboxylic acid followed the Langmuirian adsorption isotherm, but benzene-1,3,5-tricarboxylic acid caused little inhibition.

The channel cell technique has been used to investigate the inhibition of the low pH dissolution kinetics of calcite in the presence of maleic [131], tartaric [132] and polymaleic [133] acids. Langmuirian adsorption of all three species was found. The potency of the inhibitors, and the resultant etch pit morphology, could be related to the similarity between the interatomic Ca^{2+}-Ca^{2+} distance on the calcite surface and the intramolecular separation of the carboxyl groups of the acid. For this reason maleic acid was found [131] to be a potent inhibitor, while its isomer,

fumaric acid, which had a larger carboxyl group separation, had little influence on the kinetics.

5.2.2 Magnesium Ions

The effect of Mg^{2+} ions on the dissolution and growth of calcium carbonate has been widely studied because of its relevance to marine chemistry. The dissolution of calcium carbonate in the presence of Mg^{2+} was investigated by Buhmann and Dreybrodt [134], who monitored the conductivity of the solution in contact with Carrara marble over time. They concluded that foreign ions displaced the calcite solution equilibria by altering the ionic strength, ion pairing and common ion effect. However they found an unexpected initial decrease in dissolution rate on additions of small amounts of $MgCO_3$ and assumed that the Mg^{2+} ions adsorbed on the surface, causing inhibition. Kaushansky and Yariv [135] passed $MgCl_2$ solutions over calcite particles and equilibrated such solutions with the powder. In both cases no new phase was detected and the dissolution of calcite was very small. In all cases more Mg^{2+} ions were lost from solution than the Ca^{2+} ions gained and it was thought that the surface adsorption of Mg^{2+} was more important than topochemical substitution. Sjöberg [29] demonstrated that magnesium ions inhibited the dissolution rate of calcite powder and single crystals. In the case of the latter, the Mg^{2+} inhibition could be described by a Langmuir adsorption isotherm with an adsorption constant of 1.68×10^5 cm^3 mol^{-1}.

Most work in the literature, however, focuses on the deposition processes, especially those under marine conditions. It has been stated [18] that no area of carbonate reaction kinetics has been more controversial than the precipitation of calcite from Mg^{2+} containing solutions. The composition of the surface layers of

calcium carbonate precipitated from such solutions have been studied by a variety of methods. Mucci and Morse [136-138] have used Auger spectroscopy to determine the composition of the surface layers (≈ 10 Å) of calcite after exposure to saturated synthetic seawater. Thin (30 - 300 Å) magnesian calcite overgrowths were precipitated by exposing polished Iceland spar crystals to various slightly supersaturated ($\Omega \approx 1.2$) synthetic seawater solutions with $[Mg^{2+}]/[Ca^{2+}]$ ranging from 0.5 to 20.0 at constant ionic strength (I = 0.697 M) [137]. Auger spectroscopy permitted the determination of $[Mg^{2+}]/[Ca^{2+}]$ ratios with a resolution of 10 Å. This, together with ion sputtering, was used to investigate the variation of this ratio with depth into the overgrowth. The outer-most layer (≈ 10 Å) of the calcite had high magnesium levels, with $([Mg^{2+}]/[Ca^{2+}])_{surface} = 1.3 \pm 0.3$ at the seawater value of $([Mg^{2+}]/[Ca^{2+}])_{solution} = 5.13$. Further into the sample the magnesium concentration decreased rapidly over 30 to 60 Å, followed by a slightly slower decrease over the next 80 to 150 Å, after which constant $[Mg^{2+}]$ and $[Ca^{2+}]$ were reached. This was believed to be representative of the magnesian calcite overgrowth containing 8 ± 1 mol % $MgCO_3$. The amount of magnesium incorporated into the magnesian calcite overgrowth was found to be independent of the level of the solution supersaturation ($1.2 \leq \Omega \leq 17$) for constant $[Mg^{2+}]/[Ca^{2+}]$. The dependence of the surface magnesium to calcium ion ratio on that of the solution followed a Langmuirian adsorption isotherm with the surface magnesium to calcium ion ratio reaching a constant value for $([Mg^{2+}]/[Ca^{2+}])_{solution} \geq 5$. Auger spectroscopy was also used to examine dolomite and magnesite surfaces [138]. A major disadvantage of the technique was the requirement to transfer the calcite to the vacuum, thus reducing the reliability in determining the surface composition. Titration methods [55] also

demonstrated that the amount of $MgCO_3$ incorporated in calcite overgrowths was independent of the solution saturation state (3 - 17) or precipitation rate, but was dependent on the $([Mg^{2+}]/[Ca^{2+}])_{solution}$ ratio.

Concurrent Ca-^{45}Ca isotope and Ca^{2+}-Mg^{2+} ion exchange was used by Möller and colleagues [124,125,139-143] to determine the composition of the adsorbed layers on calcite exposed to solutions of varying magnesium ion concentration. Möller and Sastri [125] demonstrated that not more than a monolayer of the calcite surface was involved in the Ca-^{45}Ca exchange process. It was shown [139] that Na^+, Cl^- and SO_4^{2-} ions did not interfere with the Ca^{2+}-Mg^{2+} exchange process. Experiments on calcite powders [124,140,141] showed that $([Mg^{2+}]/[Ca^{2+}])_{surface}$ remained constant at unity for $([Mg^{2+}]/[Ca^{2+}])_{solution} \approx 2 - 6$ and similarly on single crystals [142] for $([Mg^{2+}]/[Ca^{2+}])_{solution} \approx 10 - 15$. The latter high value was believed to be due to exchange inhibition by trace phosphate ions [139]. Using the tracer techniques to follow the precipitation kinetics, it was concluded [143] that both the nucleation and precipitation rate of calcite decrease with increasing magnesium ion concentration in solution.

De Groot and Duyvis [144] measured the streaming potentials across compressed calcite and aragonite powders in $CaCl_2$ and $MgCl_2$ solutions. Zeta potentials were determined from the streaming potential measurements and were found to increase with increasing $[Ca^{2+}]$ or $[Mg^{2+}]$. This was attributed to the specific adsorption of Ca^{2+} and Mg^{2+} ions, which occurred to a similar extent on calcite, but Mg^{2+} adsorption occurred to a much smaller extent than Ca^{2+} on aragonite.

Controversy exists over whether magnesium incorporation is a kinetic phenomenon or is in exchange equilibrium. Lafon [145] and Garrels and Wollast [146] have proposed that naturally occurring magnesian calcites with up to 12 - 15 mol % $MgCO_3$ may be in equilibrium with the solutions. Conversely it has been proposed by Berner [147,148] and Thorstenson and Plummer [149,150] that the degree of magnesium incorporation in magnesian calcites grown in seawater is dependent on the kinetics of precipitation and does not represent the simple exchange equilibrium of calcium and magnesium between seawater and calcite. Berner [148] pointed to the fact that the magnesium content of the calcites precipitated in the laboratory from constant $[Mg^{2+}]/[Ca^{2+}]$ seawater varied considerably and did not reflect exchange equilibrium with seawater. However, Morse and Bender [151] pointed out that for many of these experiments the conditions changed dramatically during precipitation, thus invalidating the evidence. Commenting on this data set, they noted that the only cases where magnesian calcites of > 10 mol % $MgCO_3$ were precipitated were those which started with a calcium carbonate ion activity product greater than 120 times that of the calcite solubility product. High magnesian calcites were, therefore, only produced at extremely high precipitation rates. Surface seawater is, however, only 7 times supersaturated with respect to calcite. Mackenzie *et al.* [152] demonstrated that there was strong correlation between the magnesium content of the precipitate and the solution $[Mg^{2+}]/[Ca^{2+}]$. Also Mucci and Morse [55] and Mucci *et al.* [137] showed that the partition coefficient of magnesium in calcite was independent of the reaction rate even when the rate was varied by nearly 12 orders of magnitude.

Burton and Walter [153] showed that the temperature and partial pressure of CO_2 significantly influenced the incorporation of Mg^{2+} into calcite overgrowths.

Reddy and Nancollas [154] used X-ray powder diffraction, chemical analysis and scanning electron microscopy to examine calcium carbonate precipitated from solutions containing magnesium and sulphate ions. The sulphate ions were found not to interact with the calcite surfaces sufficiently to inhibit their growth rate or alter their morphology. However, in the presence of Mg^{2+} ions above 10^{-3} mol dm^{-3}, the initial precipitate contained amorphous calcium carbonate which eventually recrystallised to give aragonite and a low magnesian calcite with distorted morphology. This was attributed to the incorporation of magnesium ions in specific high-index calcite faces with resultant inhibition of nucleation and modification of the subsequent crystal growth. As relatively little Mg^{2+} was incorporated into the solid phase it was concluded that it is a phenomenon of the crystal-solution interface.

Meyer [155] investigated the influence of numerous impurities on the growth rate of calcite and in one experiment with Mg^{2+} much more than $5x10^{-5}$ mol dm^{-3} Mg^{2+} was required to reduce the rate by 20%. Magnesium ions have also been shown to inhibit the aragonite to calcite transformation; total inhibition being at $5.6x10^{-4}$ mol dm^{-3} at 50°C [156] and $1x10^{-4}$ mol dm^{-3} at 108°C [157]. Other work which showed the inhibition of calcite growth by Mg^{2+} included that by Pytkowicz [158], Koß and Möller [159] and Reddy and Wang [160].

5.3 Theory

The surface reaction/molecule integration model proposed in Chapter 4 and outlined below provides a basis for explaining the mode of action of species known

to inhibit the growth and/or dissolution of calcite.

$$Ca^{2+}_{(aq)} \rightleftharpoons Ca^{2+}_{(ads)} \tag{5.1}$$

$$CO_3^{2-}{}_{(aq)} \rightleftharpoons CO_3^{2-}{}_{(ads)} \tag{5.2}$$

$$Ca^{2+}_{(ads)} + CO_3^{2-}{}_{(ads)} \rightleftharpoons CaCO_3{}_{(ads)} \tag{5.3}$$

$$CaCO_3{}_{(ads)} \rightleftharpoons CaCO_3{}_{(lattice)} \tag{5.4}$$

In particular, two modes of action can be envisaged. First the inhibitor might specifically adsorb at a growth site and thus prevent the incorporation of $CaCO_3$ units into the crystal lattice (reaction (5.4)). This would cause a reduction in rate constants k_p and k_d. Second general adsorption of the inhibitor on the crystal surface might occur, so that the adsorbed inhibitor competes with the adsorption of Ca^{2+} or CO_3^{2-} (reactions (5.1) and (5.2)). This would not only reduce the amount of Ca^{2+} or CO_3^{2-} on the surface and hence slow down the rate of growth, but would also reduce the number of empty adsorption sites free to receive calcium or carbonate ions dissolving from the lattice (reaction (5.3)).

In the latter case of general adsorption, the dissolution rate law would be modified depending on whether the inhibitor was negatively charged, and thus competed with CO_3^{2-} for adsorption sites, or whether it was positive and so competed with Ca^{2+}. Thus, in the case of a negatively charged inhibitor, the surface coverage of adsorbed CO_3^{2-} ions is given by

$$\theta_{CO_3} = \frac{K_{CO_3}[CO_3^{2-}]_o}{1 + K_{CO_3}[CO_3^{2-}]_o + K_I[I^-]_o} \tag{5.5}$$

where K_I is the adsorption equilibrium constant for the inhibitor. This replaces equation (4.42) in the surface reaction/molecule integration scheme outlined in

Chapter 4. From this, equation (4.43) was modified so that the net dissolution flux, in the presence of negative inhibitors displaying Langmuirian adsorption, was given by

$$J_{net}/\text{mol cm}^{-2}\text{s}^{-1} = k_p K_{Ca} K_{CO_3} \left\{ \frac{K_{sp} - [Ca^{2+}]_o [CO_3^{2-}]_o}{(1 + K_{Ca}[Ca^{2+}]_o)(1 + K_{CO_3}[CO_3^{2-}]_o + K_I[I^-]_o)} \right\} \quad (5.6)$$

An expression for the Langmuirian adsorption of a positive inhibitor was derived similarly

$$J_{net}/\text{mol cm}^{-2}\text{s}^{-1} = k_p K_{Ca} K_{CO_3} \left\{ \frac{K_{sp} - [Ca^{2+}]_o [CO_3^{2-}]_o}{(1 + K_{Ca}[Ca^{2+}]_o + K_I[I^+]_o)(1 + K_{CO_3}[CO_3^{2-}]_o)} \right\} \quad (5.7)$$

5.4 Experimental

The experimental procedure used for the investigation of the effects of inhibitors on the rate of calcite dissolution was the same as for the calcite single crystal channel dissolution experiments detailed in Chapter 4. The solutions used contained the inhibitor species in concentrations up to ≈ 80 mM and, where necessary, potassium hydroxide or hydrochloric acid was added to obtain the chosen speciation, together with sufficient potassium chloride to produce a total ionic strength of 0.5 M. The dissociation constants of the organic acids investigated were found in the literature or determined by potentiometric titration at an ionic strength of 0.5 M and are listed in Table 5.2. Their structures are shown in Figure 5.1. In the case of the magnesium ion, however, potassium sulphate was used as background electrolyte to give an ionic strength of 0.3 M. Both forms of crystal surface preparation techniques were used, i.e. a heavily etched surface and a polished surface rinsed briefly in acid.

Table 5.2 Dissociation Constants of Carboxylic Acids Used

Species	Ionic strength /mol dm^{-3}	pK_1	pK_2	Reference
Aspartic Acid	0.5	3.84±0.05	9.73±0.05	this work
Phthalic Acid	0.002-0.04[1]	2.95	5.41	[161]
Succinic Acid	0.02-0.15[1] & 0.06-0.7[1]	4.21	5.64	[162] [163]
2-Sulphobutanedioic Acid	0.5	pK_3 = 4.7 ± 0.1		this work
Maleic Acid	0.0	1.83	6.07	[93]

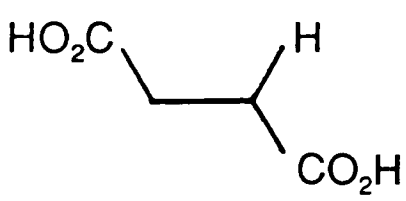

Succinic Acid

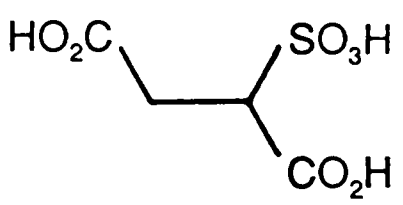

2-Sulphobutanedioic Acid

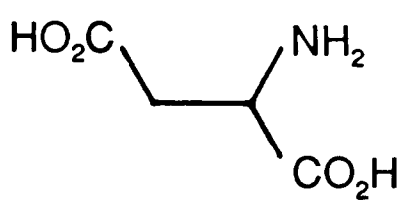

Aspartic Acid

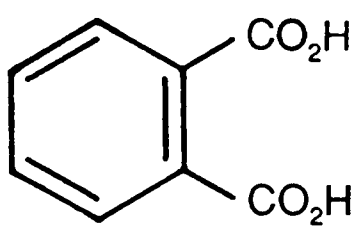

Phthalic Acid

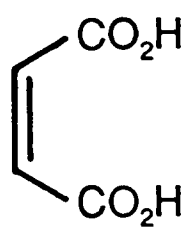

Maleic Acid

Figure 5.1. Structures of the dicarboxylic acid inhibitors used.

[1] Extrapolated to zero ionic strength.

For a given inhibitor concentration the response of the downstream pH electrode was recorded as a function of flow rate. The data thus obtained were analysed using equation (5.6) or (5.7) (as appropriate) incorporated into a BI calculation. Using the values for k_p, K_{Ca} and K_{CO3} determined for the uninhibited calcite dissolution (Chapter 4), a value of K_I was found. The concentration of each potential inhibitor was varied and equation (5.6) or (5.7) fitted for each.

The surface morphology of the calcite {100} planes, which had been etched in the presence of the inhibitors, was examined using DIC microscopy (Chapter 3). Microscopy samples were prepared by suspending a freshly cleaved calcite crystal in a stirred solution of appropriate composition, which included the background electrolyte used in the channel experiments. Wherever possible the pits are shown on the (001) plane, with the [010] direction from left to right, [100] direction towards the top of the page and [001] into the page (see Appendix 5).

5.5 Results and Discussion

5.5.1 Succinic Acid Dianion

5.5.1.1 *Kinetic Measurements*

Experiments in the presence of the succinic acid dianion were conducted on a heavily etched calcite crystal. The data obtained could be fitted to equation (5.6) in two ways:

(i) a "blank" run was performed without any inhibitor present using 0.5 M KCl to determine the value of $k_p K_{Ca} K_{CO3}$ immediately before each inhibitor run. This value was used in equation (5.6) to model the subsequent dissolution experiment in the presence of the inhibitor. K_I was altered until a good fit was obtained with the data from the inhibitor run;

(ii) the value of $k_pK_{Ca}K_{CO3}$ was fixed at the mean value of 990 $cm^4\ mol^{-1}\ s^{-1}$, obtained in Chapter 4, and K_I was altered until a good fit was achieved across the flow rate range.

Good agreement was achieved with equation (5.6) giving a mean Langmuirian adsorption constant, K_I, of $2.2x10^4$ or $2.6x10^4$ $cm^3\ mol^{-1}$, depending on which of the fitting methods were used (Table 5.3). A typical fit between experiment and theory is shown in Figure 5.2. This implied that succinate ions inhibited calcite dissolution by competing with CO_3^{2-} ions for adsorption sites, so reducing the number of empty sites available to receive the dissolving lattice CO_3^{2-} ions.

Table 5.3 Experimental Parameters for Succinic Acid Dianion Inhibition

Succinate concentration /mM	pH	$k_pK_{Ca}K_{CO3}$ of associated blank run /$cm^4mol^{-1}s^{-1}$	K_I /cm^3mol^{-1}	
			$k_pK_{Ca}K_{CO3}$ from blank run (method (i))	$k_pK_{Ca}K_{CO3}$=990 $cm^4mol^{-1}s^{-1}$ (method (ii))
20.0	8.53	1240	$4.5x10^4$	$2.5x10^4$
30.0	8.90	1030	$1.0x10^4$	$8.0x10^3$
40.0	8.83	820	$1.7x10^4$	$2.6x10^4$
50.0	8.43	560	$1.7x10^4$	$4.6x10^4$

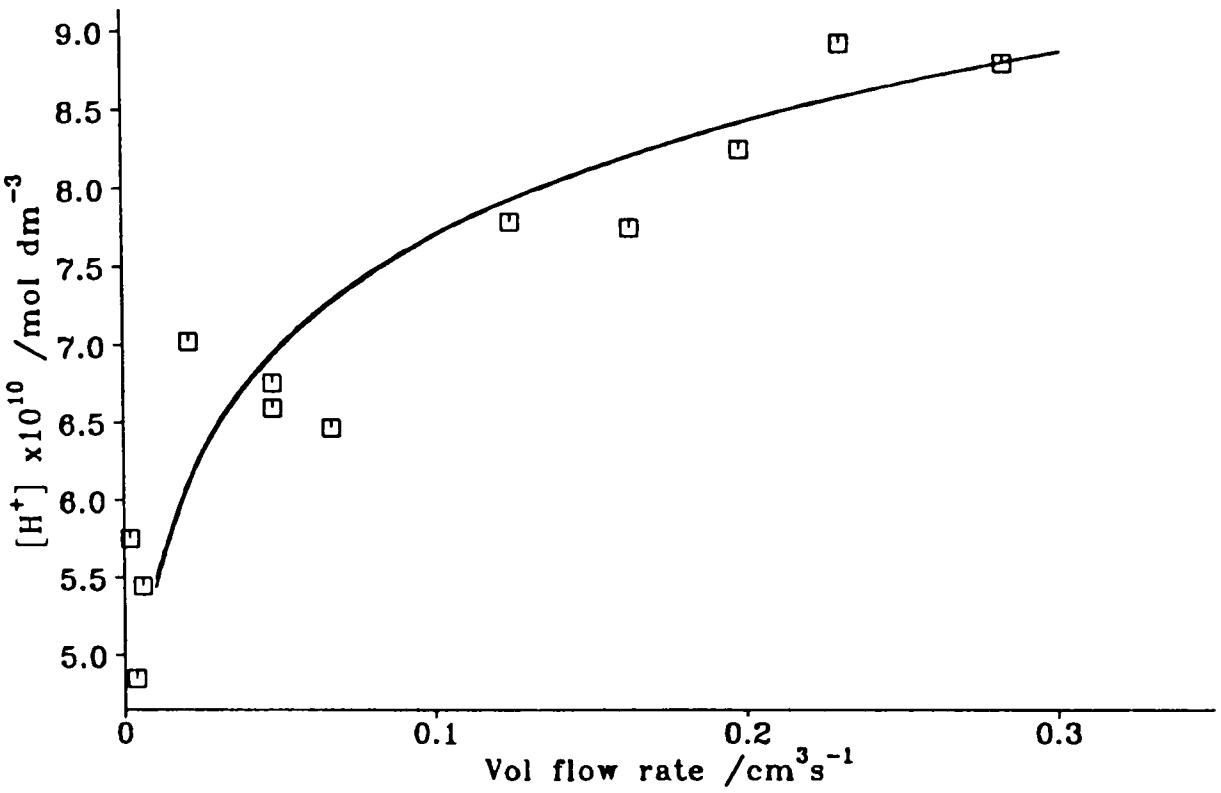

Figure 5.2. The flow rate dependence of the channel flow cell $[H^+]$ *sensor for a solution containing* 40.0 mM *succinic acid dianion* (□) *fitted to equation (5.6) with* $K_1 = 2.6\times10^4$ cm^3 mol^{-1}, $k_pK_{Cs}K_{CO3}$ = 990 cm^4 mol^{-1} s^{-1} *and with* $K_1 = 1.7\times10^4$ cm^3 mol^{-1}, $k_pK_{Cs}K_{CO3}$ = 820 cm^4 mol^{-1} s^{-1}.

5.5.1.2 *Etch Pit Morphology*

DIC microscopy of a calcite crystal etched in a solution containing 50 mM succinic acid dianions (pH 9.14 - 8.81) for 10 hours showed that the etch pits had a distorted lenticular shape with most of the dissolution occurring on the axis lying between the 78°5′ corners of the cleavage rhomb (Plate 5). For comparison the etch pits formed under similar conditions but in the absence of any inhibitor (i.e. only 0.5 M KCl) are shown in Plate 6. The etch pits in the absence of any inhibitor were rhombohedral in shape with the pit geometry mirroring the structure of the "perfect" calcite surface, as shown in Figure 5.3. The pyramidal apex of the pit often did not coincide with the geometrical centre of the etch pit. This is thought to indicate that the dislocations did not necessarily run perpendicular to the cleavage plane [118,131].

Plate 5. DIC micrograph of a calcite crystal etched in a solution containing 50 mM *succinic acid* (pH 9.14 - 8.81) *and* 0.35 M *KCl for* 10 hours (*magnification approximately* x200).

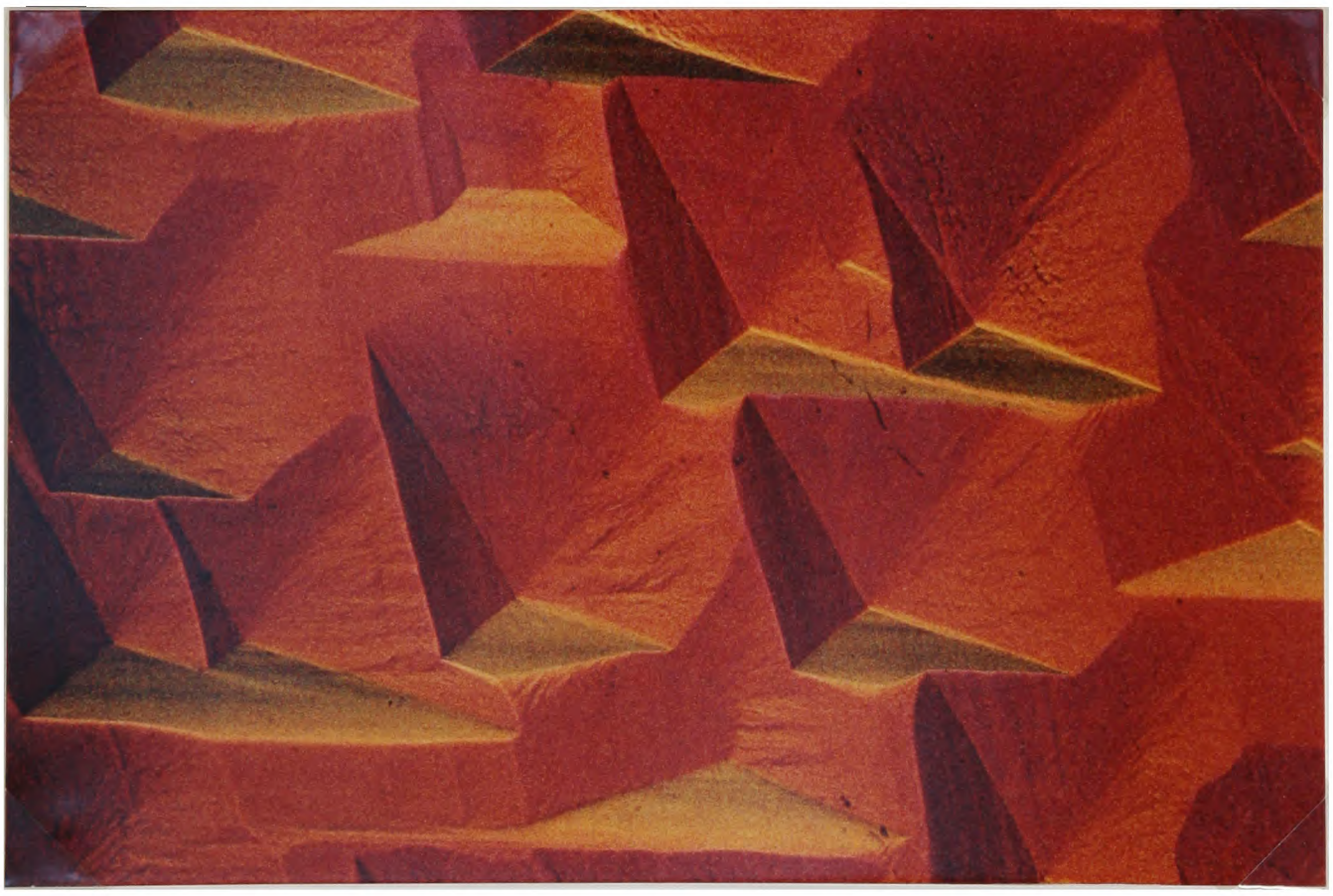

Plate 6. DIC micrograph of a calcite crystal etched in the absence of inhibitor species in a solution of 0.5 M KCl (pH 9.26 - 7.89) *for* 12 hours (*magnification approximately* x200).

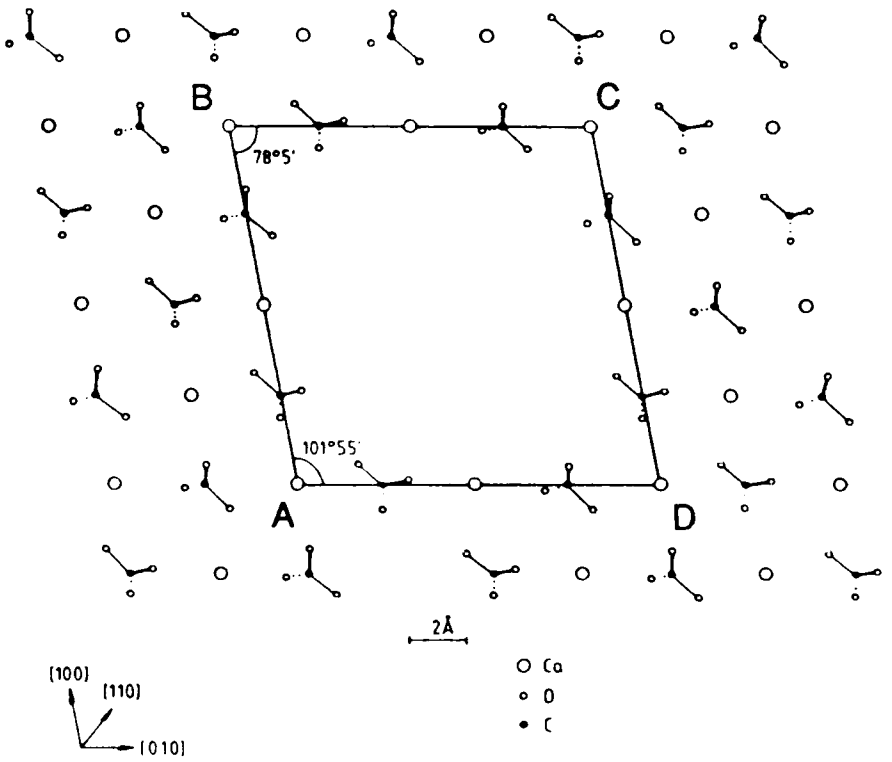

Figure 5.3. A schematic representation of the shape of the etch pits obtained without inhibitor relative to the geometry of the (001) *crystal plane. The* [001] *direction is into the paper.*

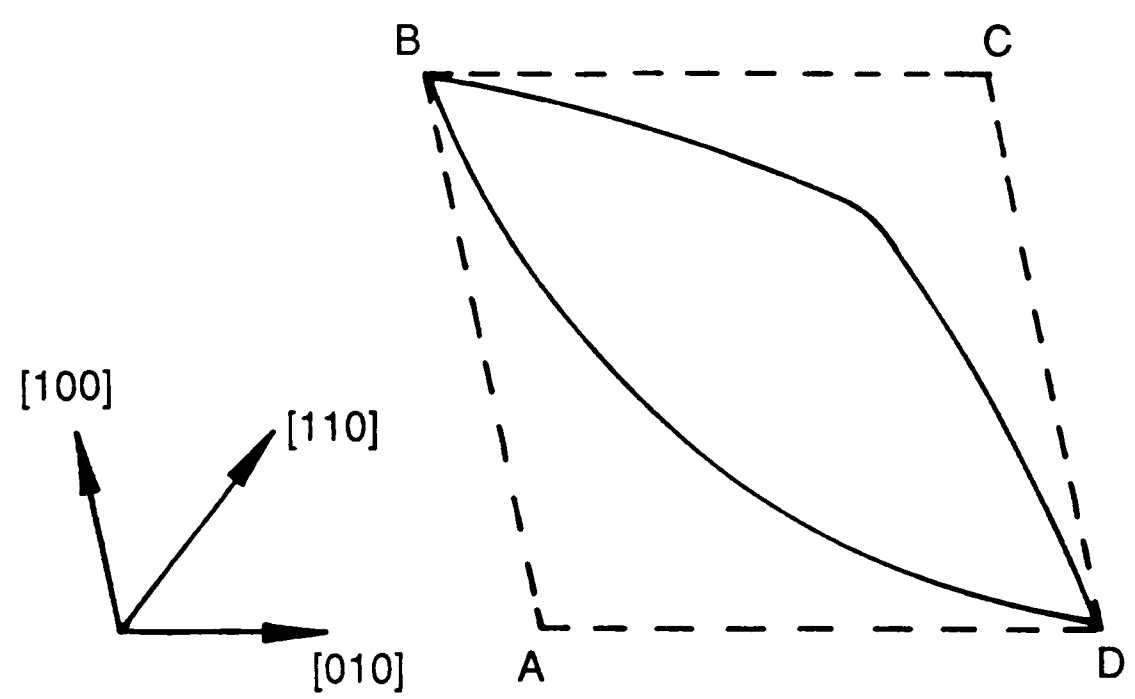

Figure 5.4. Schematic representation of the etch pit morphology on the calcite (001) *plane resulting from the dissolution in 50* mM *succinic acid at* pH ≈ *9. The etch pit characteristic of uninhibited dissolution is shown in dashed lines. The* [001] *direction is into the paper.*

The pits formed in the presence of succinate ions, as shown schematically in Figure 5.4, implied that the rate of growth of the etch pits in the [110] and [$\bar{1}\bar{1}$0] directions had been reduced considerably compared to that in the [1$\bar{1}$0] and [$\bar{1}$10]

directions. In addition pit growth in the [$\bar{1}\bar{1}$0] was retarded more than in the [110] direction. Using interatomic data for succinic acid [164] the distance between the carboxyl groups (taking the mid-point between the two oxygen atoms of each carboxyl group) was calculated to be 3.04 Å in the eclipsed conformation and 4.92 Å in the staggered conformation. As the dissolution process involves the propagation of kink sites, an inhibitor might operate by adsorption at such kink sites. Three types of kink site can be identified in the calcite structure and are shown schematically in Figure 5.5. The rhombohedral etch pits obtained in the absence of any inhibitor consisted of two "type 1" kinks (corners B and D in Figures 5.3 and 5.5) where the nearest Ca^{2+}-Ca^{2+} or CO_3^{2-}-CO_3^{2-} in-plane (a-a) separations are 4.04 Å, whereas cross-plane (b-c) separations are both 4.04 Å and 4.99 Å; a "type 2" kink (corner C) where the in-plane (a-a) separation is 4.99 Å and cross-plane (b-c) separation is 4.04 Å; and a "type 3" kink (corner A) where both the in-plane (a-a) separation and cross-plane (b-c) are 4.99 Å. Presumably the

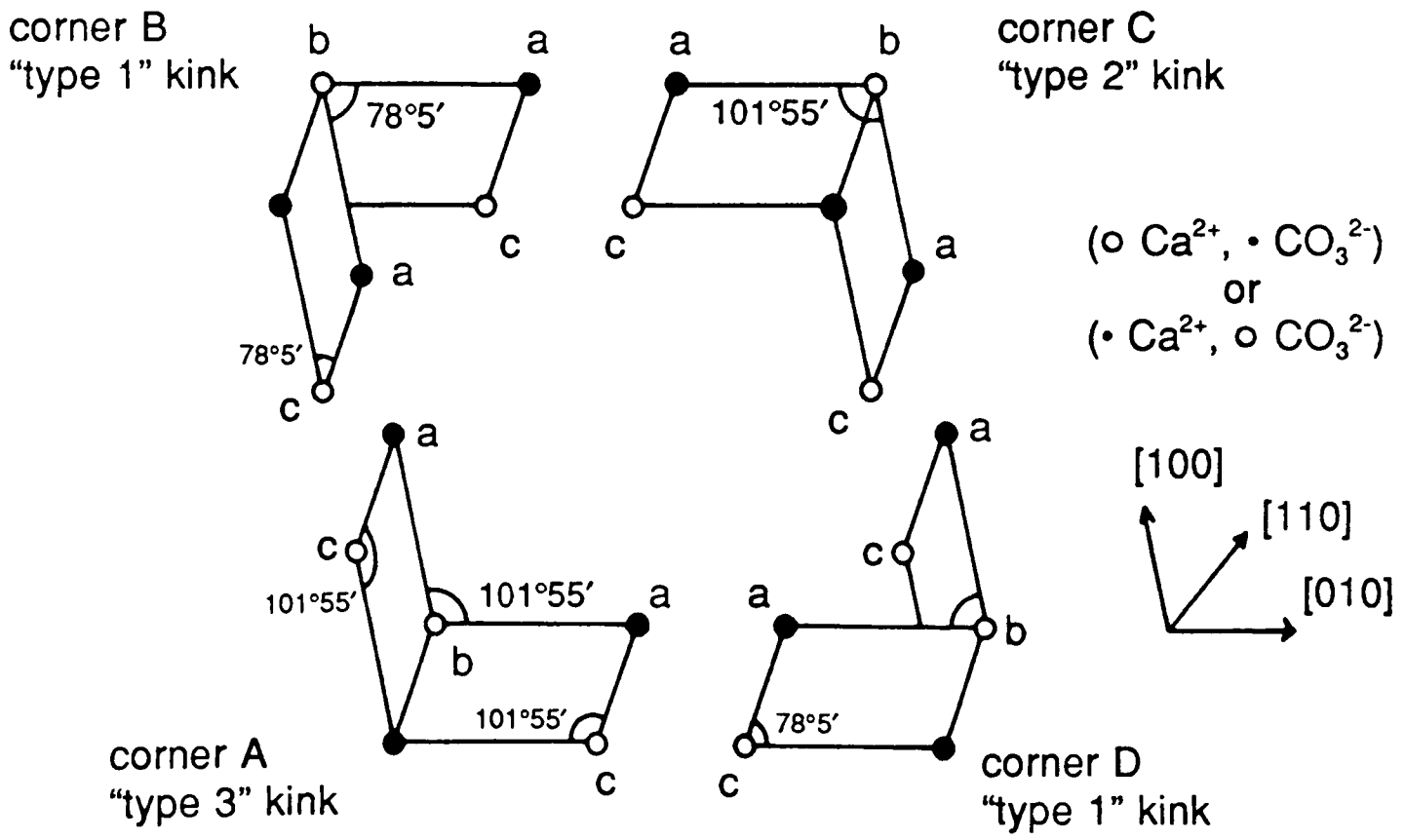

Figure 5.5. Schematic representation of the three kink sites characteristic of the calcite (001) *plane. The* [001] *direction is into the paper.*

succinic acid dianion could orientate itself to "bond" in a bidentate fashion at either of the two closest Ca^{2+}-Ca^{2+} distances. However, clamping across the 4.99 Å Ca^{2+}-Ca^{2+} separation would have the succinate ion in its lowest energy staggered conformation. Bidentate clamping across the shortest Ca^{2+}-Ca^{2+} would have an unfavourable energy associated with the required reorientation of the succinate ion away from its preferred configuration in solution. As a result all the etch pits observed were consistent with no inhibition having occurred across the 78°5′ corners, some inhibition having occurred at corner C due to in-plane adsorption and most inhibition having occurred at corner A due to in-plane and/or cross-plane adsorption.

5.5.2 Phthalic Acid Dianion

5.5.2.1 *Kinetic Measurements*

The experiments carried out in the presence of the phthalic acid dianion were also performed on a well etched calcite crystal and the analysis was carried out in an identical fashion to the succinic acid dianion. Again equation (5.6) was found to give satisfactory agreement with the experimental data across the range of flow rates used. The values of K_I thus obtained are shown in Table 5.4, which have a mean value of 3.1×10^4 cm^3 mol^{-1} by method (i) described above. The agreement with equation (5.6) implied that phthalate, like succinate, decreased the rate of calcite dissolution by adsorbing on the surface in competition with carbonate ions.

Table 5.4. Experimental Parameters for Phthalic Acid Dianion Inhibition

Phthalate concentration /mM	pH	$k_pK_{Ca}K_{CO3}$ of associated blank run /cm^{4}mol^{-1}s^{-1}	K_I /cm^{3}mol^{-1}	
			$k_pK_{Ca}K_{CO3}$ from blank run	$k_pK_{Ca}K_{CO3}$=990
9.99	8.82	1340	3.0x10^4	-
20.0	8.55	700	1.5x10^4	4.3x10^4
26.5	8.72	1230	4.7x10^4	3.0x10^4

5.5.2.2 *Etch Pit Morphology*

The shape of the etch pits formed in the presence of 50 mM phthalate ions after 13 hours at pH 9.91 - 9.42 is shown in Plate 7. All the etch pits formed in the presence of the phthalic acid dianions had the same distorted lenticular shape as those formed in succinate ion solutions. This again implied that the growth of the etch pits had been inhibited in the [110] and [$\bar{1}\bar{1}$0] directions compared with the [1$\bar{1}$0] and [$\bar{1}$10] directions and with more inhibition in the [$\bar{1}\bar{1}$0] direction. Using crystallographic data [165] the distance between the carboxyl groups of phthalic acid was calculated to be 3.74 Å, taking the mid-point between the oxygen atoms in each carboxyl group. Although the intramolecular carboxyl group separation in the phthalate ion was closer to the shorter Ca^{2+}-Ca^{2+} distance, adsorption had not occurred across the 78°5′ etch pit corner, as was evident from the microscopy. Presumably adsorption did not occur across this 4.04 Å Ca^{2+}-Ca^{2+} separation because of the stearic hindrance resulting from the ≈ 5 Å diameter benzene ring on

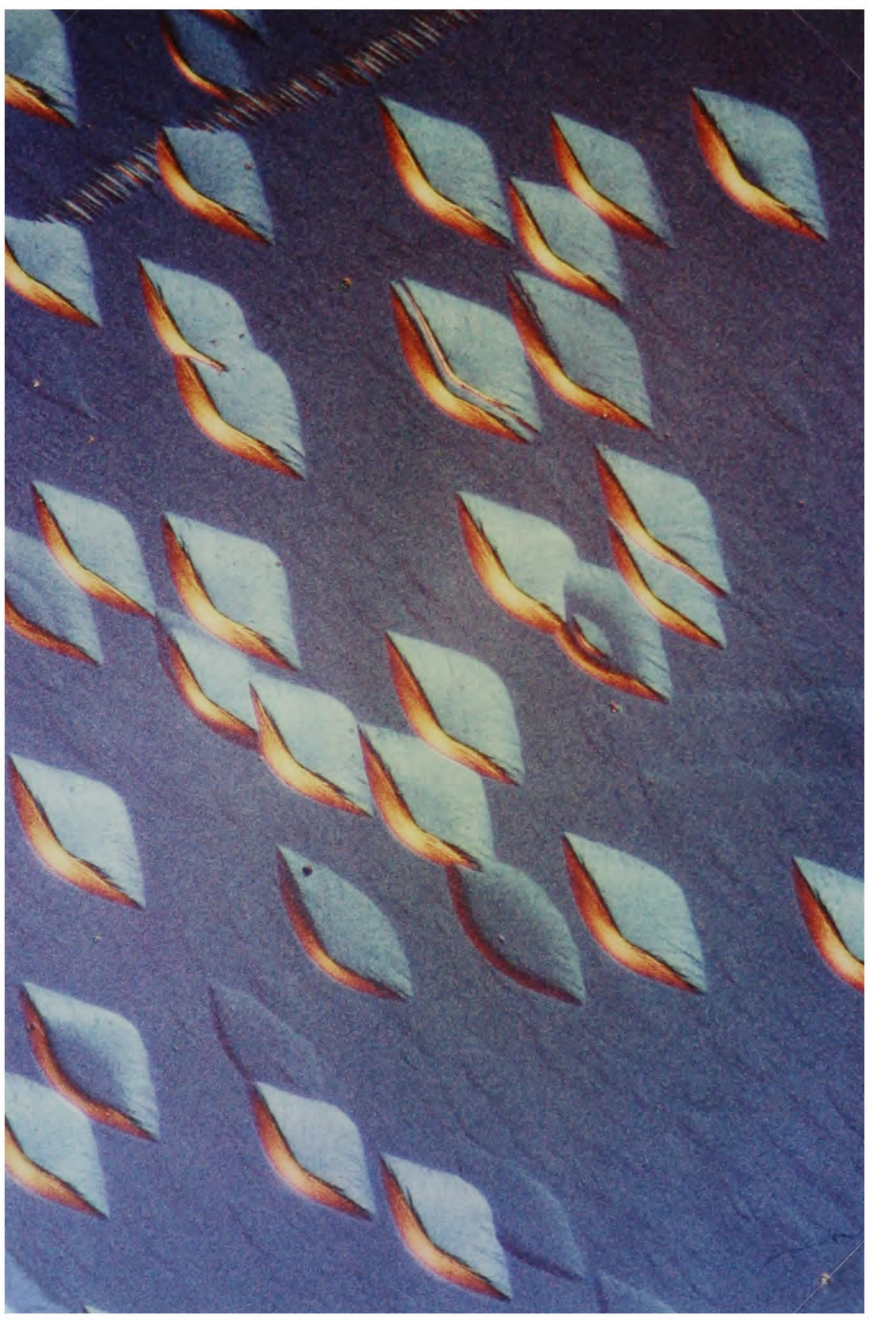

Plate 7. DIC micrograph of a calcite crystal etched in a solution containing 50 mM *phthalic acid* (pH 9.91 - 9.42) *and* 0.35 M *KCl for* 13 hours (*magnification approximately* x200).

the phthalate ion. Instead, adsorption occurred at type 2 and type 3 kinks, probably in a monodentate fashion, though it is unclear why the dissolution rate at the former was greater.

5.5.3 2-Sulphobutanedioic Acid Trianion

5.5.3.1 *Kinetic Measurements*

The inhibitory effect of the sulphonate derivative of succinic acid was carried out on a polished calcite crystal and therefore the value of $k_p K_{Ca} K_{CO3}$ used in equation (5.6) was 6730 $cm^4\ mol^{-1}\ s^{-1}$ as determined in Chapter 4. Good agreement with equation (5.6) was obtained and the parameters used to fit the experimental data are given in Table 5.5. The mean value for K_I thus obtained was $5.3 \times 10^5\ cm^3\ s^{-1}$.

Table 5.5. Experimental Parameters for 2-Sulphobutanedioic Acid Trianion Inhibition

2-Sulphobutanedioic ion concentration /mM	pH	K_I /$cm^3 mol^{-1}$ ($k_p K_{Ca} K_{CO3}$ = 6730 $cm^4 mol^{-1} s^{-1}$)
5.01	8.76	9.0×10^5
10.0	8.90	2.5×10^5
20.0	8.55	4.0×10^5
50.0	8.82	5.5×10^5

5.5.3.2 *Etch Pit Morphology*

DIC microscopy of a calcite crystal etched in the presence of 11 mM sulphobutanedioate ions for 12 hours (pH 9.72 - 8.89) showed no alteration of the etch pits away from their uninhibited rhombohedral shape. Whether the same result would be obtained at higher sulphobutanedioate ion concentrations could not be ascertained due to the limited availability of the specially prepared material.

5.5.4 Maleic Acid Dianion

5.5.4.1 *Kinetic Measurements*

Dissolution experiments with maleic acid present in its fully dissociated form were carried out on an etched calcite crystal. Using the value of $k_p K_{Ca} K_{CO3}$ obtained from dissolution experiments in the absence of the maleic acid dianion (Mal^{2-}) immediately before the inhibitor run, the fitting of equation (5.6) to the data was attempted by varying K_I. The correct order of magnitude of sensor H^+

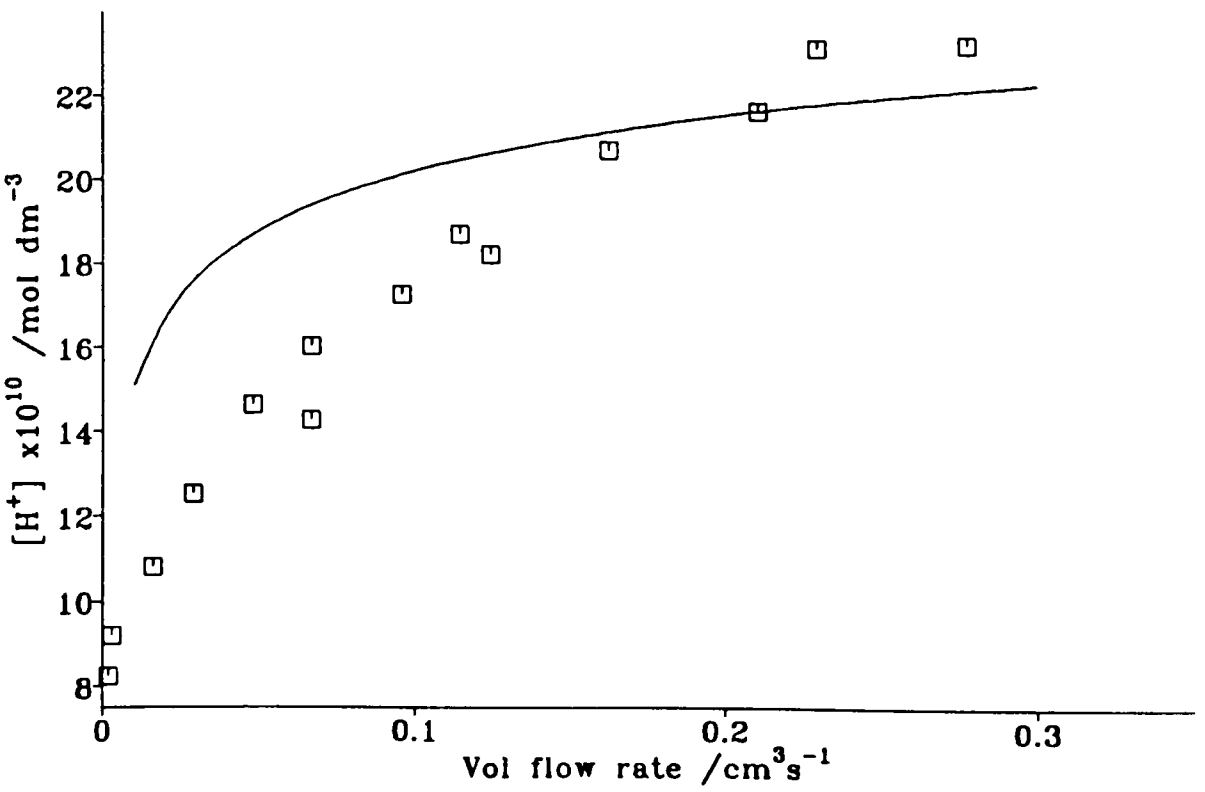

Figure 5.6. The flow rate dependence of the channel cell $[H^+]$ *sensor for a solution containing* 30.00 mM *maleic acid dianion* (□), *showing poor agreement with equation (5.6) for* $K_I = 5 \times 10^5$ $cm^3\ mol^{-1}$.

concentration was obtained with $K_I \approx 5x10^5$ cm^3 mol^{-1}. However quantitative agreement between equation (5.6) and experiment was unsatisfactory over the flow rate range used, as shown in Figure 5.6. This was despite the fact that general Langmuirian adsorption of Mal^{2-}, with the adsorption constant $K_{Mal} = 4.8x10^6$ cm^3 mol^{-1}, had been inferred from work at low pH [131] where dissolution is controlled by the reaction of H^+ with the exposed CO_3^{2-} ions on the surface. The poor agreement of the data at high pH with equation (5.6) suggested that the inhibition seen with maleate at high pH may proceed with the other inhibitor mechanism proposed in Section 5.3, namely the influence of the uptake/release of $CaCO_3$ species at specific growth sites, which would appear kinetically as a modification of k_p and k_d. Accordingly the high pH maleate inhibitor kinetic data was modelled with equation (5.6) and with K_I at the value obtained at low pH [131] and so deduced the apparent product $\{k_p K_{Ca} K_{CO3}\}_{app}$ over a range of flow rates, as shown in Table 5.6, for three maleate concentrations. In order to seek a mechanistic rationale for the apparent variation in k_p the average surface (Outer Helmholtz plane) Ca^{2+} and CO_3^{2-} ion concentrations were computed and summarised in Table 5.6. It can be seen that k_p appears to decrease with increasing flow rate and hence with decreasing mean surface calcium and carbonate concentrations. Closer inspection revealed that k_p approximated to a unique function of mean $[Ca^{2+}]_o$ and plotting $\{k_p K_{Ca} K_{CO3}\}_{app}^{-1}$ against $\{[Ca^{2+}]_o\}^{-1}$, as shown in Figure 5.7, gave an excellent straight line. This supports the tentative interpretation in terms of an altered k_p. A possible mechanistic explanation of this behaviour is that the rate k_p of reaction (5.4) is catalysed by enhanced calcium levels in the presence of maleate ions. This may arise from maleate co-adsorbed with calcium at growth

Table 5.6. Surface Ion Concentrations in the Presence of the Maleate Dianion

$[Mal^{2-}]$ /mM	V_f /$cm^3 s^{-1}$	$k_p K_{Ca} K_{CO3}$ /$cm^4 mol^{-1} s^{-1}$	$[H^+]_{sensor}$ x10^9 /mol dm^{-3}	Mean $[Ca^{2+}]_o$ x10^6/mol dm^{-3}	Mean $[CO_3^{2-}]_o$ x10^6/mol dm^{-3}
30.0	0.300	1.0×10^4	2.4	1.8	0.11
	0.200	1.5×10^4	2.2	3.1	0.22
	0.100	2.25×10^4	1.8	5.8	0.54
	0.050	2.7×10^4	1.5	8.7	1.0
	0.025	3.0×10^4	1.3	12	1.7
	0.010	3.15×10^4	1.0	10	2.9
19.99	0.300	1.3×10^4	2.7	3.5	0.22
	0.200	1.9×10^4	2.2	5.8	0.47
	0.100	2.7×10^4	1.6	10	1.2
	0.050	3.3×10^4	1.2	16	2.4
	0.025	3.5×10^4	1.0	21	3.7
	0.010	3.7×10^4	0.79	30	6.5
10.00	0.300	3.35×10^4	1.2	17	2.7
	0.200	3.65×10^4	1.0	22	3.8
	0.100	4.1×10^4	0.81	30	6.5
	0.050	4.2×10^4	0.67	39	9.5
	0.025	4.3×10^4	0.56	49	14
	0.010	4.3×10^4	0.46	65	21

sites. If this adsorption occurs at every growth site and is Langmuirian then

$$\{k_p\}_{app} = k_p + \frac{k_p' K' [Ca^{2+}]_o}{\left(1 + K' [Ca^{2+}]_o\right)} \qquad (5.8)$$

where K' is a Langmuirian adsorption constant. Provided $k_p' \gg k_p$ then equation (5.8) predicts the observed behaviour in Figure 5.7, with $k_p' = 1.5 \times 10^{-9}$ mol cm^{-2} s^{-1}

(i.e. $k_p'K_{Ca}K_{CO3}$ = 46000 $cm^4\ mol^{-1}\ s^{-1}$, as compared with $k_pK_{Ca}K_{CO3}$ = 990 $cm^4\ mol^{-1}\ s^{-1}$).

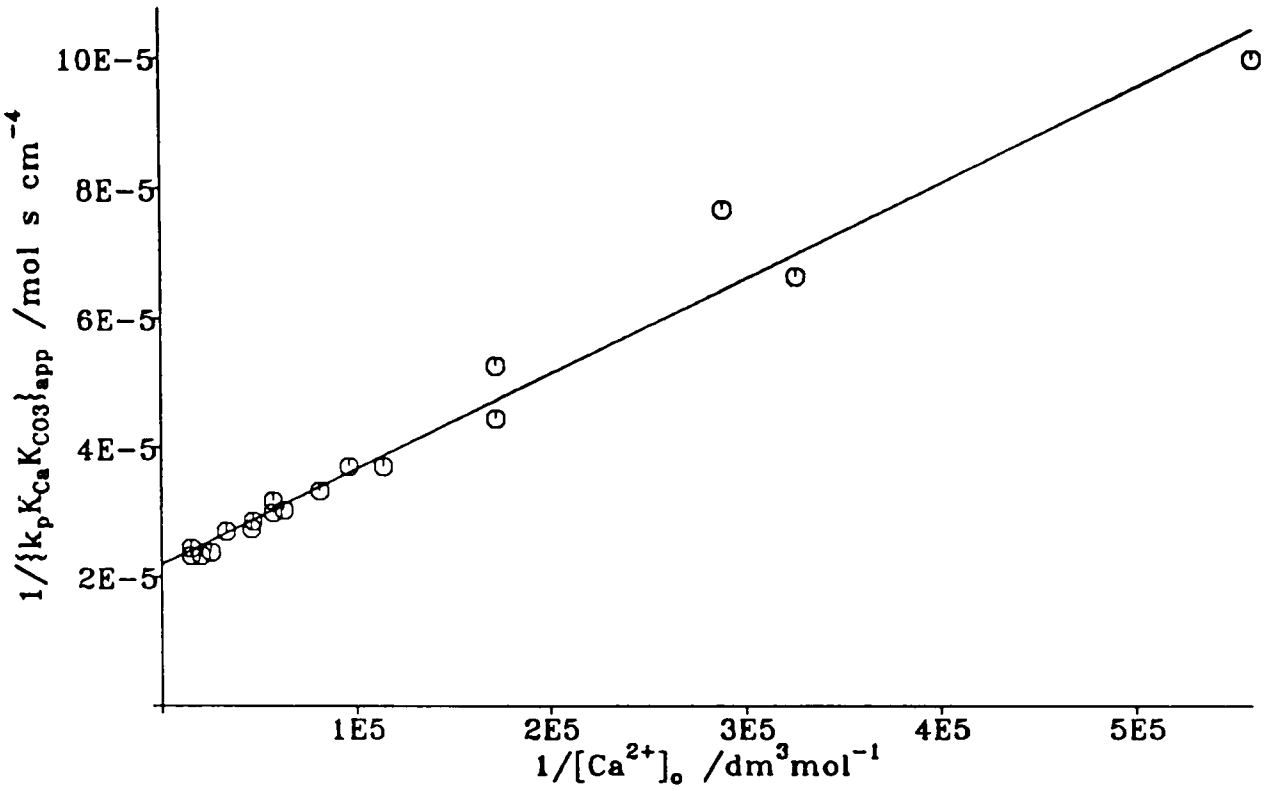

Figure 5.7. A plot of $\{k_pK_{Ca}K_{CO3}\}_{app}^{-1}$ *against* $\{[Ca^{2+}]_o\}^{-1}$ *using data from Table 5.6. The form of the graph is suggested by equation (5.8).*

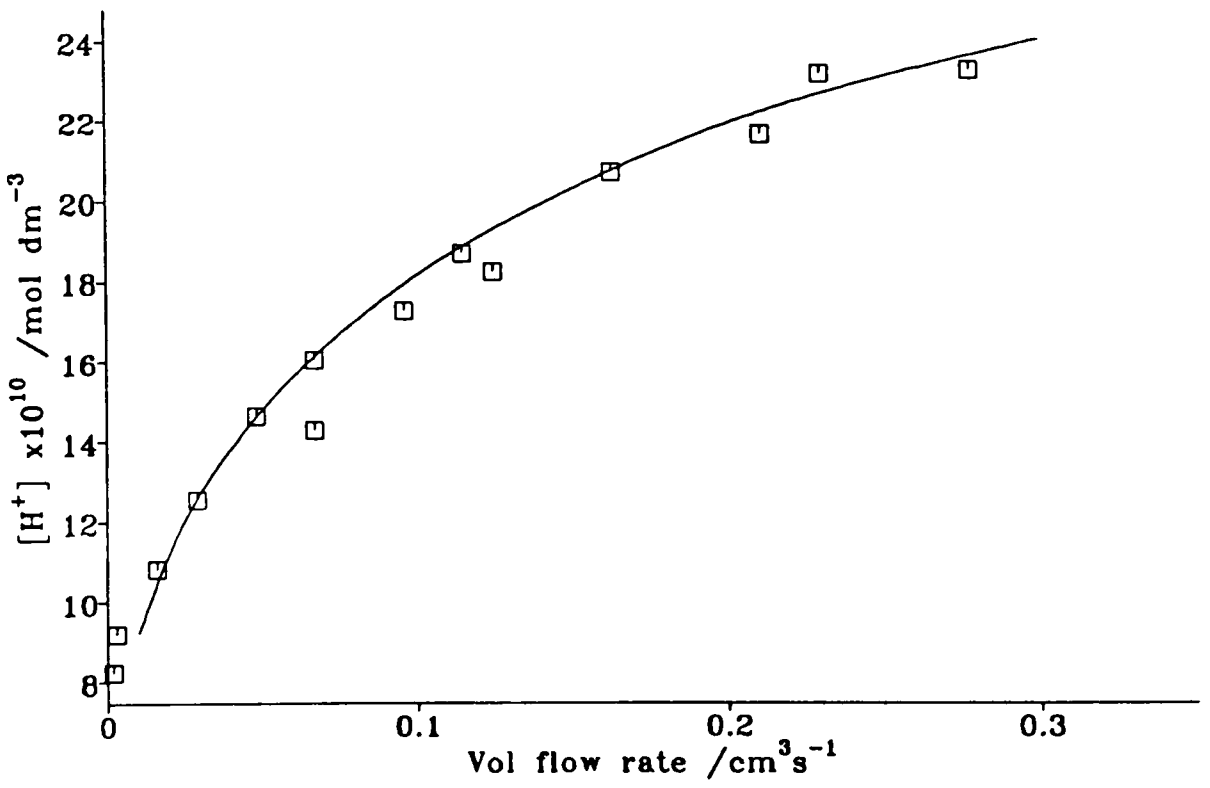

Figure 5.8. The flow rate behaviour of the channel cell $[H^+]$ *sensor for the* 30.0 mM *maleate data, shown in Figure 5.6, demonstrating good agreement with equation (5.9), which has a modified* k_p *term.*

Figure 5.8 shows the now good agreement between the high pH maleate data and the modified kinetic rate law with k_p altered to that of equation (5.8) such that

$$J_{net}/\text{mol cm}^{-2}\text{s}^{-1} = \frac{k_p' K_{Ca} K_{CO_3} K' [Ca^{2+}]_o}{1 + K'[Ca^{2+}]_o} \left\{ \frac{K_{sp} - [Ca^{2+}]_o [CO_3^{2-}]_o}{(1 + K_{Ca}[Ca^{2+}]_o)(1 + K_{CO_3}[CO_3^{2-}]_o)} \right\} \quad (5.9)$$

The possibility of calcium maleate ion pair formation was investigated by modelling using the stability constant for CaMal [166]. However, the effect of this on the shape of the sensor - flow rate response was negligible. Another hypothesis was that the neutral calcium maleate ion pairs adsorbed at growth sites on the calcite surface, in which case

$$\{k_p K_{Ca} K_{CO_3}\}_{app} = \frac{k_p' K_{Ca} K_{CO_3} K_{CaMal} [CaMal]_o}{1 + K_{CaMal}[CaMal]_o} \quad (5.10)$$

$$= \frac{k_p' K_{Ca} K_{CO_3} K_{CaMal} K'_{CaMal} [Ca^{2+}]_o [Mal^{2-}]_o}{1 + K_{CaMal} K'_{CaMal} [Ca^{2+}]_o [Mal^{2-}]_o}$$

where $\{k_p K_{Ca} K_{CO3}\}_{app}$ is the apparent value of $k_p K_{Ca} K_{CO3}$ from Table 5.6, K_{CaMal} is the calcium maleate Langmuir adsorption constant and K'_{CaMal} is the calcium maleate stability constant. Plotting $1/\{k_p K_{Ca} K_{CO3}\}_{app}$ against $1/[Ca^{2+}]_o[Mal^{2-}]_o$, as shown in Figure 5.9, gave a linear response which implied agreement with the Langmuir isotherm. The intercept gave $k_p' K_{Ca} K_{CO3}$ = 59600 cm^4 mol^{-1} s^{-1}, which together with the gradient yielded K_{CaMal} = 3.9x10^{12} cm^6 mol^{-2}.

These results suggest that maleate ions interact with specific growth site, implying that the more potent inhibitors, such as maleic acid, do not simply compete for the carbonate adsorption sites on the calcite surface but interact in a more complex fashion, probably involving adsorption at lattice dissolution sites.

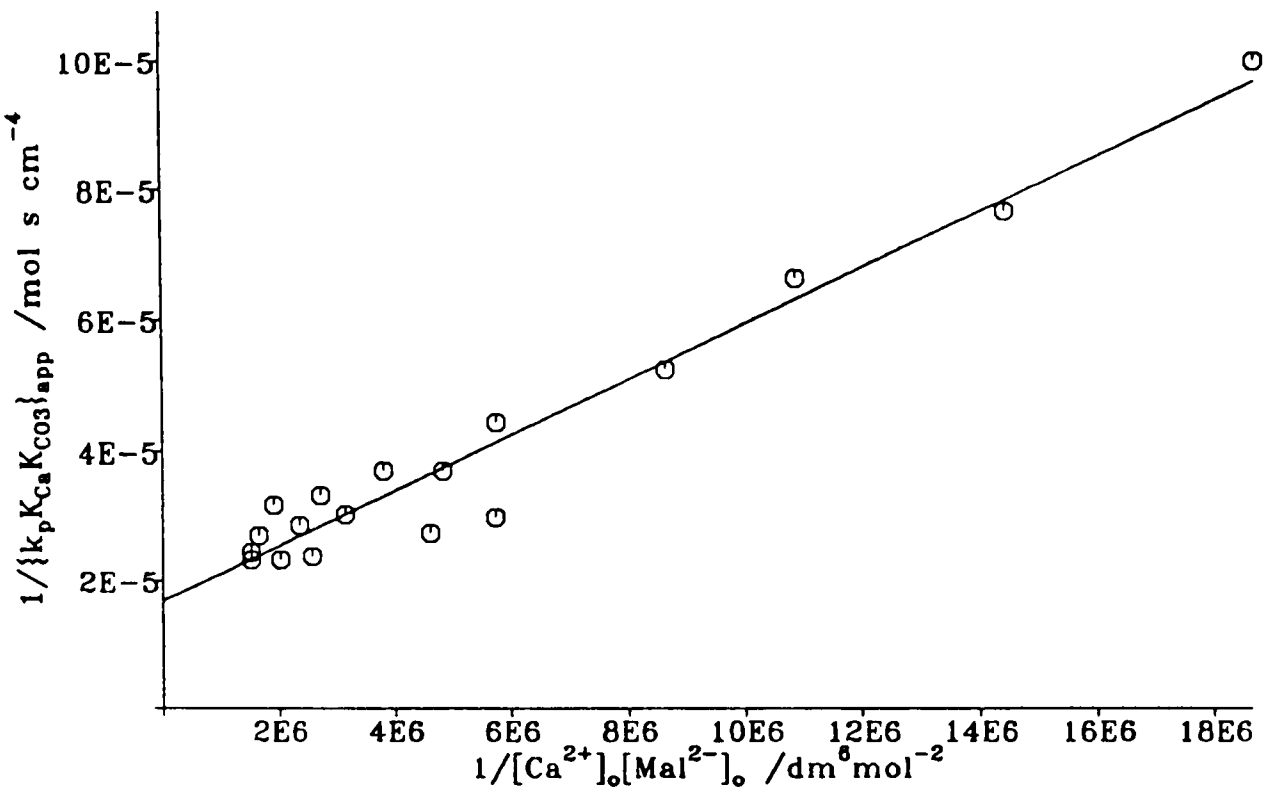

Figure 5.9. Plot of data in Table 5.6 showing agreement with the Langmuir isotherm for the adsorption of CaMal *at the growth sites, according to equation (5.10).*

5.5.4.2 *Etch Pit Morphology*

Typical etch pits formed on a freshly cleaved calcite crystal which had been suspended in a solution containing 50 mM maleic acid dianions at pH 8.77 - 8.79 for 12 hours are shown in Plate 8. These pits were rhombohedral in shape and appeared to be very similar to the pits formed in the absence of inhibitors. This result was in marked contrast to the behaviour of the phthalic and succinic acid dianions. This may reflect the difference in the kinetic behaviour of the maleate dianions compared with both the phthalic and succinic acid dianions.

This was in contrast with the etch pits formed in the presence of the maleate mono-anion, $HMal^-$ [131]. These pits were lenticular in shape, with the reduction in pit growth in the $[1\bar{1}0]$ and $[\bar{1}10]$ directions (on the (001) cleavage plane) due to the bidentate adsorption of Mal^{2-} across what would have been the 78°5′ corners of the etch rhomb (i.e. corners B and D of Figures 5.3 and 5.5).

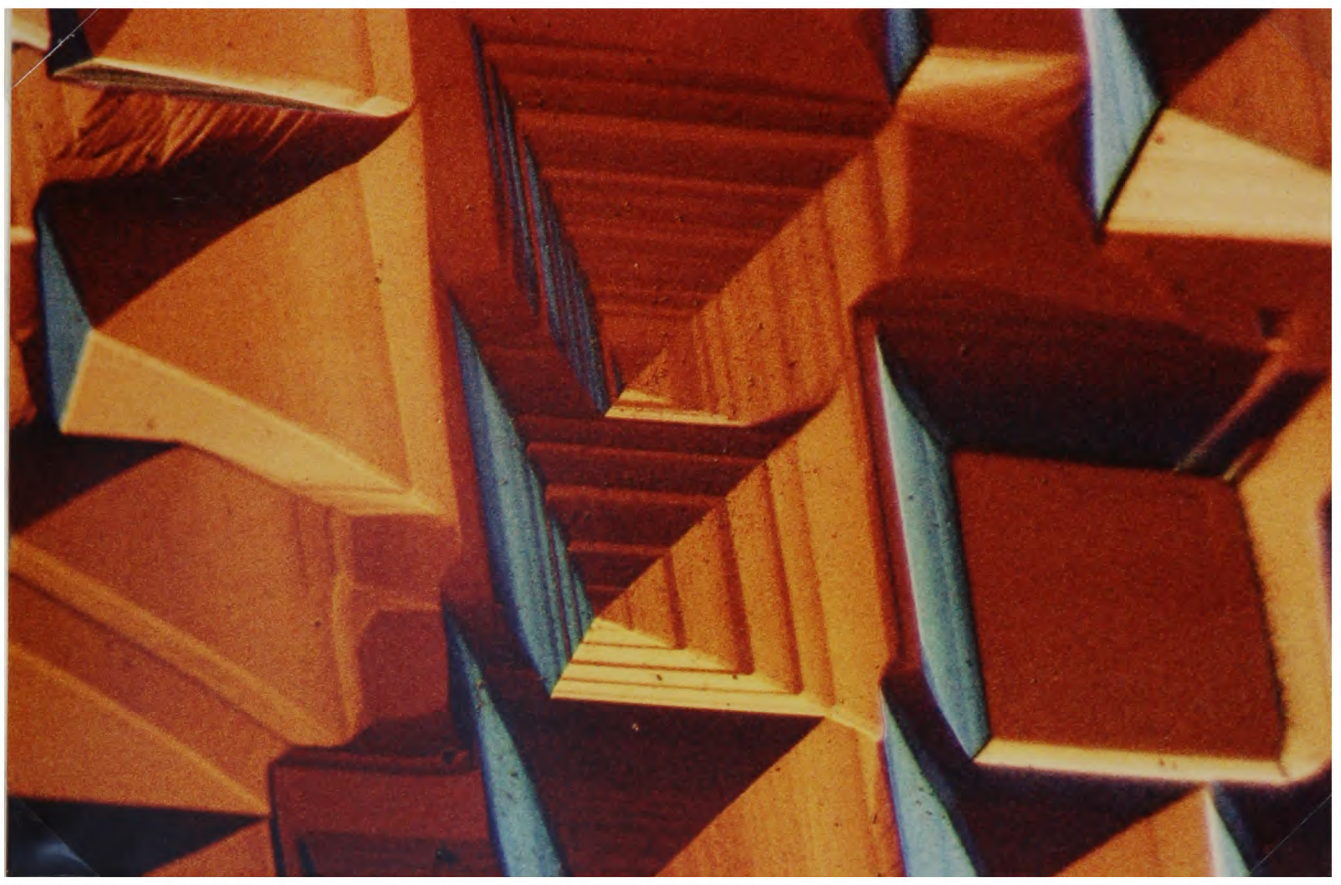

Plate 8. DIC micrograph of a calcite crystal etched in a solution containing 50 mM *maleic acid* (pH 8.77 - 8.79) *and* 0.35 M *KCl for* 12 hours (*magnification approximately* x200).

5.5.5 Aspartic Ions

Kinetic measurements of the rate of calcite dissolution in the presence of aspartic acid ions were carried out for bulk solution pHs around pH 8.5 where the mono-anion of aspartic acid predominated and around pH 9.7 where the mono- and dianions were of similar concentrations. Due to the value of the second dissociation constant of aspartic acid, the acid buffered the system making the extraction of kinetic information difficult.

5.5.6 Magnesium Ion

5.5.6.1 *Kinetic Measurements*

Unlike other experiments the investigation of the role of magnesium ions as a potential inhibitor were carried out with potassium sulphate as background electrolyte and with an ionic strength of 0.3 mol dm^{-3}. Under these conditions those parameters dependent on the ionic strength had to be recalculated. Using the activity coefficients given in Table 5.7, K_{a2} = 1.223x10^{-10} mol dm^{-3} as the second (mixed) acid dissociation constant of carbonic acid and K_{sp} = 4.76x10^{-8} mol^2 dm^{-6} as the (concentration) solubility product of calcite.

Table 5.7. Activity Coefficients for an Ionic Strength of 0.3 M

Species	γ	Source	Species	γ	Source
Ca^{2+}	0.25	Davies equ.[101]	SO_4^{2-}	0.25	Davies equ. [101]
CO_3^{2-}	0.278	Walker *et al.* [100]	$CaSO_4$	0.80	Yeatts & Marshall [167]
HCO_3	0.725	Walker *et al.* [100]			

Table 5.8 lists the relevant ion pair association constants both at infinite dilution (K) and corrected for the ionic strength (K') using the activity coefficients in Table 5.7. Under the conditions used the $CaSO_4$ ion pair was the most significant and was accounted for in the modelling, but its effect was minimal.

Table 5.8. Ion Pair Association Constants at Ionic Strengths of 0.0 and 0.3 M

Ion Pair	log K	K	K' /dm^{3}mol^{-1}	Reference
$CaSO_4$	2.31	204	16	Garrels & Thompson [168]
$MgCO_3$	2.88	760	66	Reardon & Langmuir [169]
$MgSO_4$	2.36	230	18	Garrels & Thompson [168]

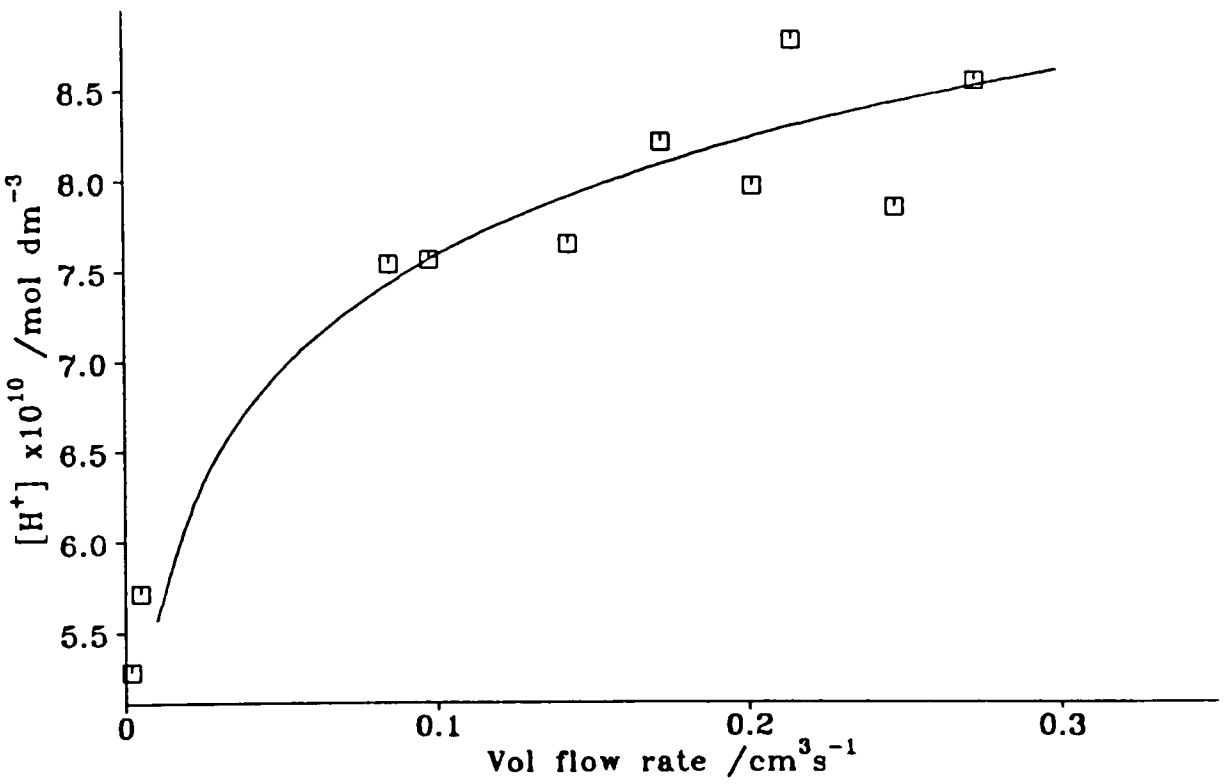

Figure 5.10. The flow rate dependence of the channel flow cell [H^+] *sensor for a solution containing 40* mM Mg^{2+} *ions fitted to equation (5.7) with* $K_1 = 2.5 \times 10^5$ cm^3 mol^{-1}.

Using these parameters, together with equation (4.43), gave a value of $k_p K_{Ca} K_{CO3}$ = 6200 $cm^4\ mol^{-1}\ s^{-1}$ for dissolution experiments on a polished calcite crystal in the absence of magnesium ions. This value was in good agreement with the value of $k_p K_{Ca} K_{CO3}$ = 6730 $cm^4\ mol^{-1}\ s^{-1}$ for the dissolution of a polished calcite crystal in the presence of 0.5 mol dm^{-3} KCl, implying negligible inhibition by the SO_4^{2-} ion. On the addition of $MgSO_4$, a marked inhibition of the dissolution process was observed and gave excellent agreement with the $[H^+]$ detector response predicted by equation (5.7) (see Figure 5.10). The values of the Langmuir adsorption equilibrium constant, K_I, obtained are listed in Table 5.9 with a mean value of 2.3×10^5 $cm^3\ mol^{-1}$ (standard deviation 0.6×10^5).

Table 5.9. Experimental Parameters for Magnesium Ion Inhibition

Magnesium ion concentration /mM	pH	K_I /$cm^3 mol^{-1}$ ($k_p K_{Ca} K_{CO3}$ = 6200 $cm^4 mol^{-1} s^{-1}$)
10	8.38	2.25×10^5
10	8.06	1.75×10^5
10	8.48	1.75×10^5
20	8.56	2.25×10^5
40	8.88	2.5×10^5
80	8.45	3.4×10^5

These results indicate that magnesium cations slow the rate of calcite growth/dissolution by adsorbing on the mineral surface in competition with Ca^{2+}

ions, so reducing the number of empty sites to receive dissolving lattice Ca^{2+} ions, or for net precipitation, the coverage of Ca^{2+} available for incorporation into the crystal lattice.

The value of K_{Mg} deduced has important implications to marine chemistry. Typical seawater concentrations are 0.0544 mol dm^{-3} in Mg^{2+} and 0.0105 mol dm^{-3} in Ca^{2+} [96] which, together with the values of K_{Mg} and K_{Ca} obtained, implies a surface coverage of 52% with Mg^{2+} and 44% with Ca^{2+}, i.e. a ratio of $([Mg^{2+}]/[Ca^{2+}])_{surface} = 1.2$.

Langmuirian adsorption of Mg^{2+} has been inferred from other kinetic studies of calcite dissolution, though using empirical rate laws. Sjöberg [29] concluded that both Ca^{2+} and Mg^{2+} adsorb on calcite in a Langmuirian fashion with $K_{Ca} = 1.32 \times 10^6$ cm^3 mol^{-1} and $K_{Mg} = 1.68 \times 10^5$ cm^3 mol^{-1} at pH 8.3 on a single crystal, which is in excellent quantitative agreement with the values deduced in this thesis. Buhmann and Dreybrodt [134] speculated that Ca^{2+} and Mg^{2+} ions adsorb on the surface of calcite causing inhibition, but with the former being more pronounced. In addition Mucci and Morse [138] have shown using Auger spectroscopy that the surface layers (≈ 10 Å) of a calcite crystal exposed to a supersaturated synthetic seawater have a surface Mg^{2+} to Ca^{2+} concentration ratio of near 1 (0.83 at a saturation of 1.2 and 1.34 at a saturation of 8). This is also in agreement with work by Möller and colleagues [124,125,139-143], who showed that for a solution Mg^{2+}/Ca^{2+} molar ratio of between 2 and 10, the calcite surface has a $[Mg^{2+}]/[Ca^{2+}]$ ratio of about 1.

5.5.6.2 *Etch Pit Morphology*

Plate 9 shows a DIC micrograph of the surface of calcite etched in a solution containing 50 mM Mg^{2+} ions for 12 hours at pH 8.97 - 8.15. The etch pits so

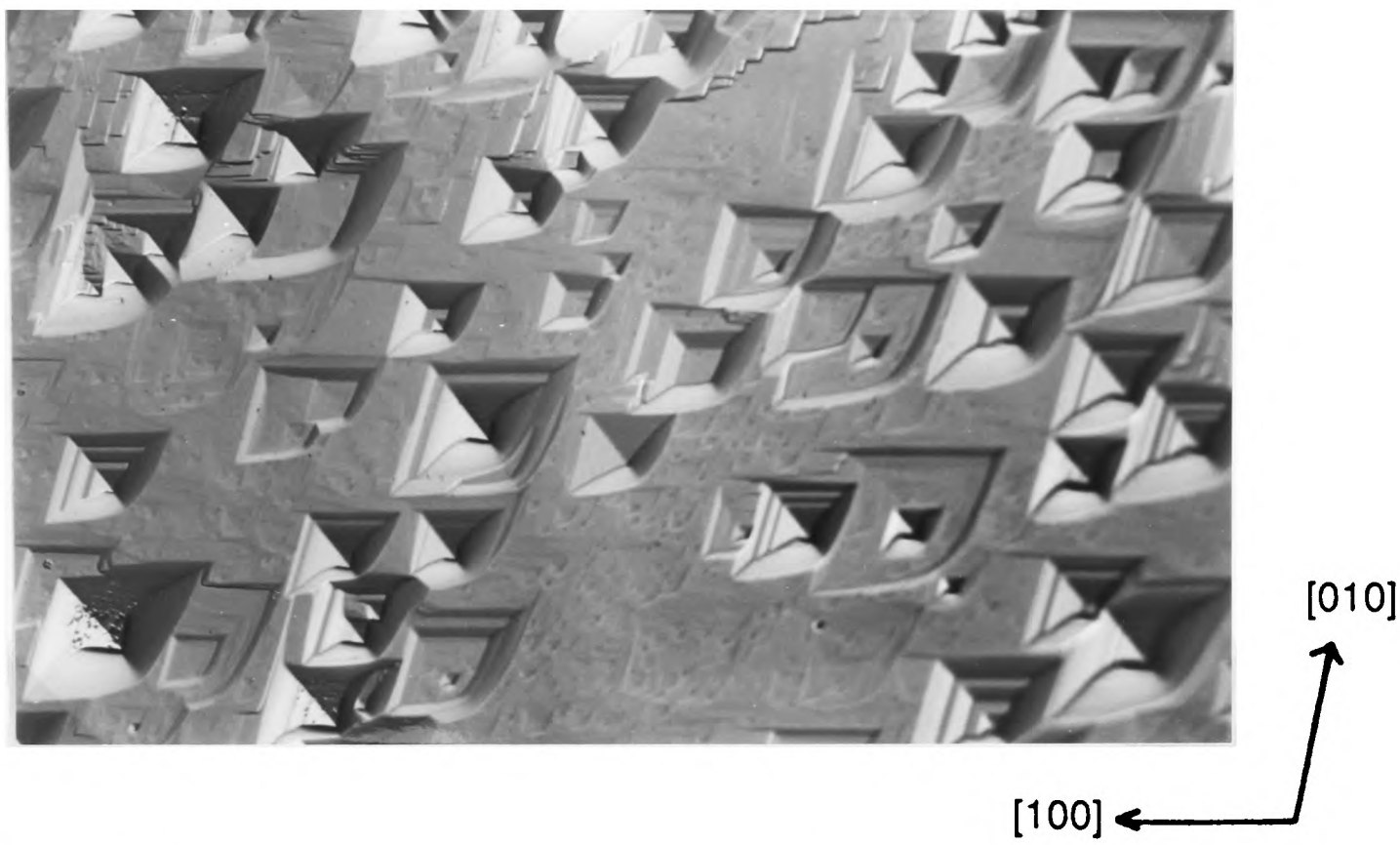

Plate 9. DIC micrograph of a calcite crystal etched in a solution containing 50 mM $MgSO_4$ *and* 0.1 M K_2SO_4 (pH 8.97 - 8.15) *for* 12 hours (*magnification approximately* x200).

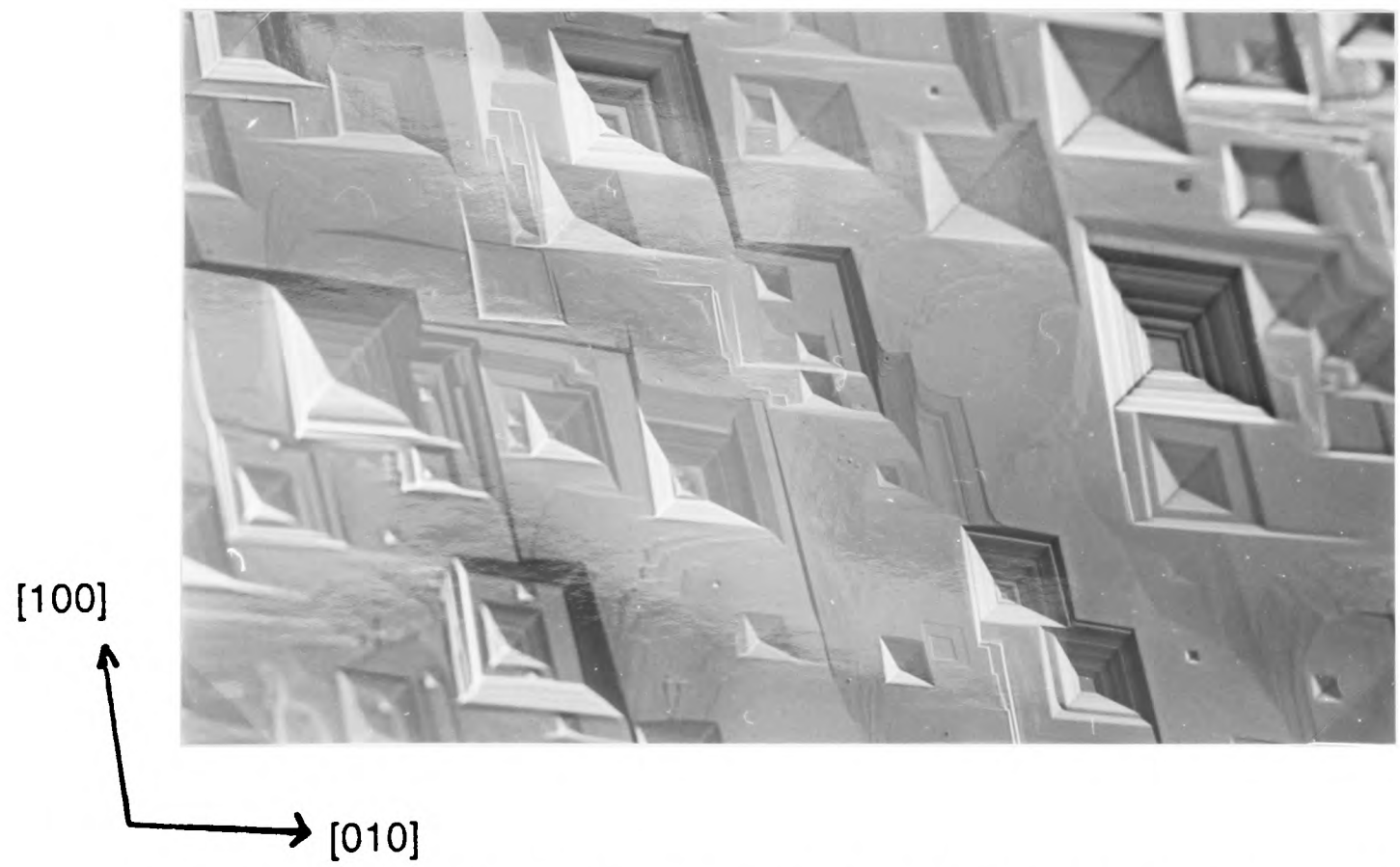

Plate 10. DIC micrograph of a calcite crystal etched in a solution containing 0.1 M K_2SO_4 (pH 8.86 - 9.29) *for* 12 hours (*magnification approximately* x200).

formed were distorted from the rhombohedral pits produced in potassium sulphate solutions (Plate 10), due to the apparent inhibition of pit growth at just one of the 101°55′ corners (corresponding to corner A in Figure 5.3). In all cases it was the same corner at which growth had been blocked, i.e. in the [$\bar{1}\bar{1}$0] direction. Examination of the crystal structure of calcite showed that the two 101°55′ corners are distinguishable. This was because the carbonate ions in the calcite lattice lie in planes which are orientated at approximately 45° [170] to the {100} cleavage planes, as shown in Figure 5.11. From the relative orientation of the etch pits and the crystal, it was clear that the Mg^{2+} ions were sited at the corner at which the carbonate plane was ≈ 135° to the surface, as opposed to the opposite corner where the CO_3^{2-} - {100} angle was acute. The occupancy of this site by the Mg^{2+} ions was somewhat unsurprising since at this corner of the etch pit the CO_3^{2-} ions are more "exposed" to the incoming cation.

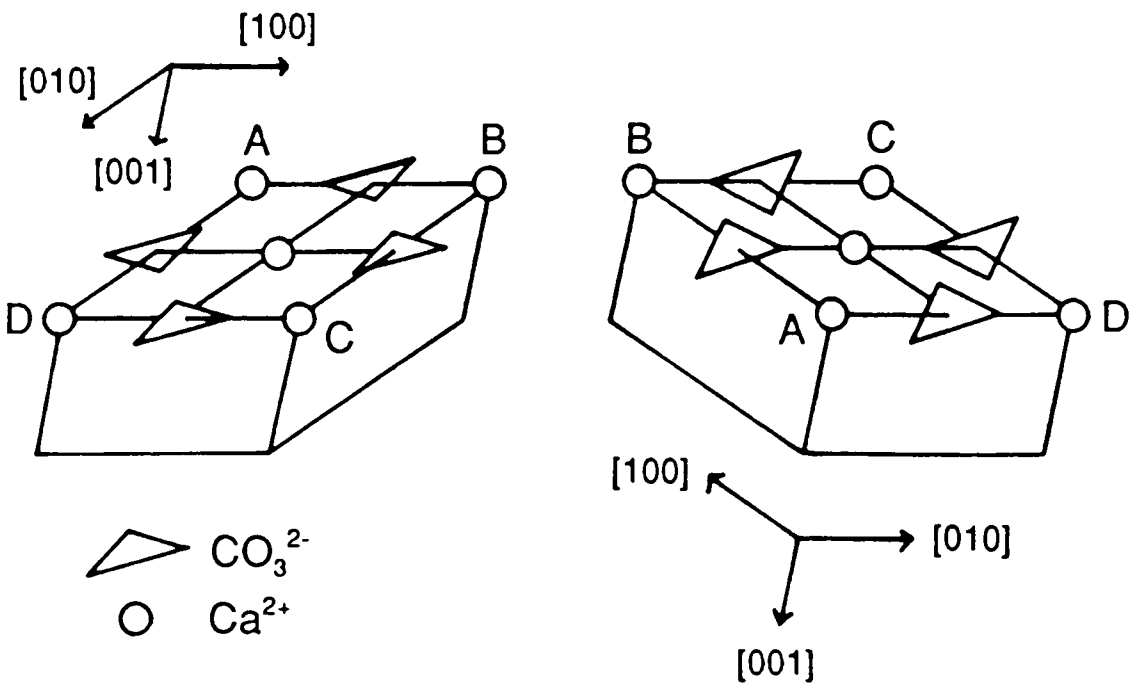

Figure 5.11. Schematic representation of the orientation of carbonate ions on matched (001) *cleavage surfaces.*

5.6 Conclusions

All the inhibitor species examined, with the exception of the maleic anion, agree with the model proposed where the inhibitor molecule competes with CO_3^{2-} ions, in the case of negatively charged inhibitors, or Ca^{2+} in the case of positive inhibitors, for adsorption sites on the calcite surface (reactions (5.1) and (5.2)). This implies that the inhibitors slow the rate of calcite growth/dissolution by reducing the number of empty sites to receive dissolving lattice ions, or for net precipitation, the coverage of Ca^{2+} or CO_3^{2-} available for incorporation into the crystal lattice. The adsorption constants for both phthalic and succinic dianions were a factor of 10^3 less than that for CO_3^{2-}. Both species also altered the shape of the etch pits formed during the dissolution. Introducing an $-SO_3^-$ on to the succinic dianion increased its potency as a dissolution inhibitor by a factor of 20, though this was measured using a different surface preparation.

The maleic acid dianion exhibited a much more complex interaction with the calcite surface, indicating that it did not just compete for carbonate ion adsorption sites on the surface but for specific surface sites, probably involving adsorption at lattice growth/dissolution sites.

The presence of Mg^{2+} ions showed a very marked inhibitory effect, with the adsorption constant only 5 times less than that for Ca^{2+}. As discussed above this result has important consequences for marine geochemistry where the concentrations of Ca^{2+} and Mg^{2+} are such that calcite in seawater has approximately equal numbers of Ca^{2+} and Mg^{2+} ions adsorbed on the surface, which is in agreement with independent surface science data. Microscopy has

shown that the Mg^{2+} ions interact with the CO_3^{2-} ions and inhibit dissolution in one direction.

Calcium ions are more readily competitively displaced than carbonate ions, since $K_{Ca} \ll K_{CO3}$. This implies that cationic dissolution inhibitors, which proceed via competitive general adsorption, will be more potent than anionic inhibitors with the same adsorption constant. The existence of cation and anion specific adsorption sites on the calcite surface has also been inferred by other studies. Cowan *et al.* [171] found using radioisotope tracer methods that SeO_3^{2-} exchanged with CO_3^{2-}. The presence of phosphate ions decreased the amount of selenite adsorbed, due to competition but was unaffected by Mg^{2+}, implying anion specific adsorption sites. Zachara *et al.* [123,172] investigated the metal ion - Ca^{2+} exchange for a number of divalent metal cations and concluded that exchange occurred at cation specific surface sites. This agreed with the findings of Kornicker *et al.* [173] where Ca^{2+}, Mg^{2+} and Co^{2+} all competed for adsorption sites.

CHAPTER 6

AC IMPEDANCE SPECTROSCOPY OF CALCIUM CARBONATE SCALES

6.1 Introduction

In this chapter the resistivity and capacitance of calcium carbonate scale will be investigated. The impedance of a heavily scaled tube was probed using a.c. impedance spectroscopy [174], which involves monitoring the amplitude and phase of the current on application of an alternating voltage at different frequencies. An equivalent electronic circuit was developed to model the a.c. response of the scaled tube. Following on from this work, the technique could be used to monitor the build up of calcium carbonate scales in pipe-work *in situ* and therefore clearly has useful industrial applications.

In the next section the conventions used in dealing with alternating signals will be discussed and the theoretical responses of some basic electronic circuits explained. The use of these as equivalent circuits to model the behaviour of electrochemical systems will be introduced. The experimental details and results of the investigations carried out into the response of a scaled tube to an a.c. signal will then be discussed and an equivalent circuit for the system developed.

6.2 A.C. Theory

A sinusoidal voltage can be represented by a rotating vector, or phasor, $\underline{E}$ whose magnitude at any given time t is simply the projection of the phasor onto a given axis, as shown in the polar diagram, Figure 6.1. Thus

$$|\underline{E}| = E = E_o \sin \omega t \qquad (6.1)$$

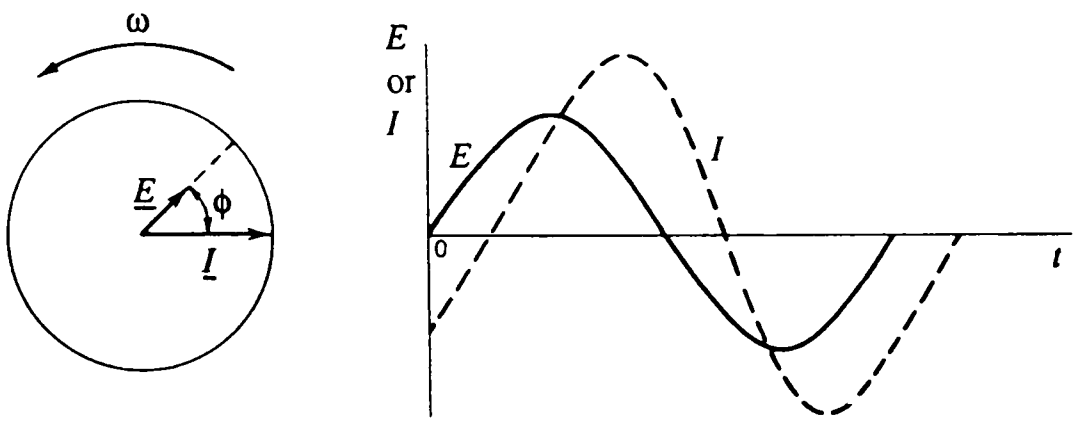

Figure 6.1. Phasor diagram for an alternating voltage $\underline{E}$ and the related alternating current, both at frequency ω.

where ω is the angular frequency ($\omega = 2\pi f$, where f is the frequency in hertz) and E_o is the amplitude of the alternating voltage. The current can be described by a second phasor $\underline{I}$ which in most cases has the same frequency as $\underline{E}$ but usually a different magnitude and phase. This is shown in the polar diagram Figure 6.1 and has a magnitude given by

$$|\underline{I}| = I = I_o \sin(\omega t + \phi) \tag{6.2}$$

where ϕ is the phase angle with respect to $\underline{E}$. The voltage and current phasors are related by the equation

$$\underline{E} = \underline{I}\underline{Z} \tag{6.3}$$

where $\underline{Z}$ is the impedance.

Phasors can also be represented mathematically using complex notation and hence displayed on an Argand diagram. Thus the voltage phasor can be split into two components, one of which is parallel to the current phasor, the other perpendicular, see Figure 6.2. Complex notation is used to distinguish between these components. The "real" component is that which is in phase with the current. The component which is 90° out of phase is assigned as "imaginary" and is multiplied by $j = \sqrt{-1}$. Thus the impedance can be written as

$$\underline{Z} = Z' + jZ'' \tag{6.4}$$

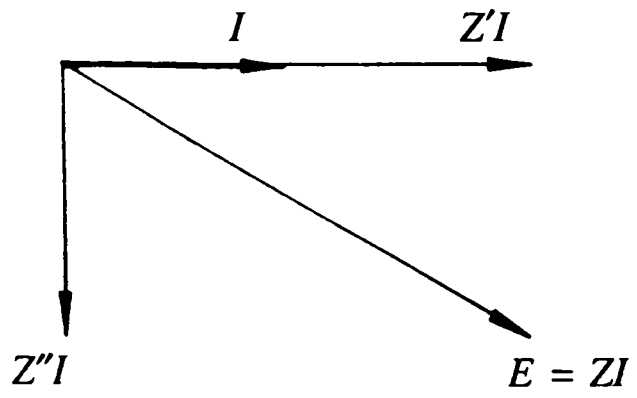

Figure 6.2. Phasor diagram showing the relationship between voltage and current phasors and the impedance.

It is important to note that the terms real and imaginary impedances are purely for "book keeping" purposes. Both are, in fact, real values and can be measured. The Argand diagram is used to display the impedance with the real component on the abscissa and imaginary impedance on the ordinate. It is usual to invert the ordinate axis (i.e. plot $-Z''$ versus Z') so that the axis tends to $-\infty$ as the phase angle is usually positive.

Other forms of notation are also used [175], such as the polar form

$$\underline{Z} = Ze^{j\phi} \tag{6.5}$$

and also admittance, which is the reciprocal of impedance.

The impedance of some basic electronic components and their combinations will now be investigated.

6.2.1 Resistor

The relationship between the voltage and current phasors for a pure resistor of value R is given by Ohm's Law

$$\underline{E} = \underline{I}R \tag{6.6}$$

$$\therefore \quad Z = R \tag{6.7}$$

Thus for a pure resistor R the phase angle ϕ is zero and the impedance plot is a single point on the real axis at $Z' = R$.

6.2.2 Capacitor

The charge q stored on a capacitor of value C farads is

$$q = CE \tag{6.8}$$

The current "flowing" through the capacitor is

$$I = \frac{dq}{dt} = C\frac{dE}{dt} \tag{6.9}$$

substituting equation (6.1) gives

$$I = \omega C E_o \cos\omega t \tag{6.10}$$

$$I = \omega C E_o \sin\left(\omega t + \frac{\pi}{2}\right) \tag{6.11}$$

Comparison between equations (6.1) and (6.11) yields

$$E = -j\frac{I}{\omega C} = -jX_C I \tag{6.12}$$

and hence

$$Z = -\frac{j}{\omega C} = -jX_C \tag{6.13}$$

where X_C is known as the capacitative reactance and has units of ohms. In impedance plots it is usual to plot the current phasor along the abscissa even though the current's phase angle is measured with respect to the voltage, hence the inclusion of the minus sign in equation (6.12). Thus a pure capacitor of value C has the current leading the voltage by 90° and has an impedance plot shown in Figure 6.3.

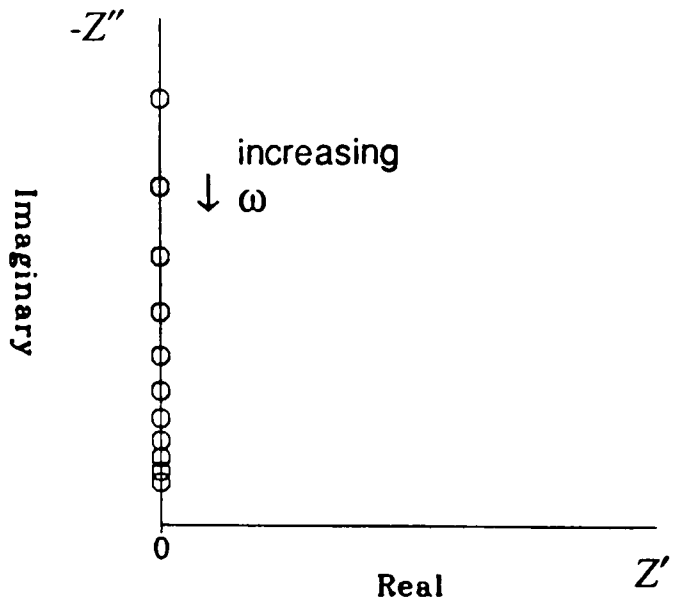

Figure 6.3. Impedance plot produced on applying an alternating voltage across a pure capacitor.

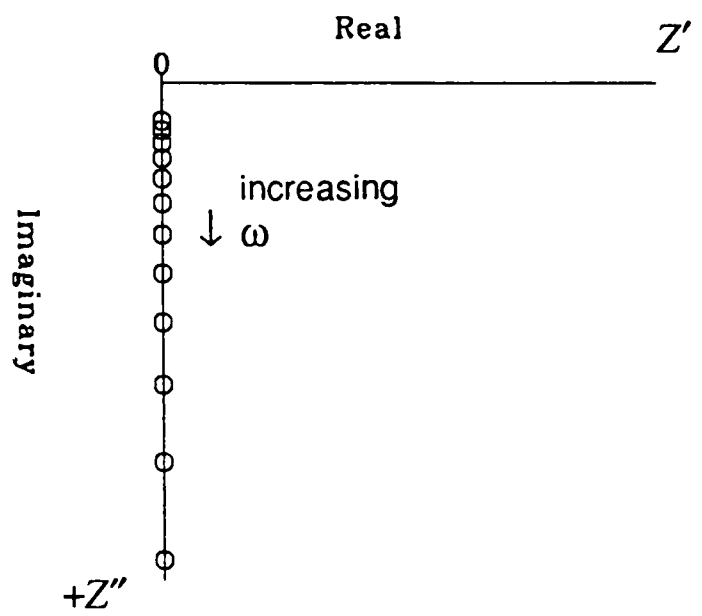

Figure 6.4. Impedance plot produced on applying an alternating voltage across a pure inductor.

6.2.3 Inductor

The voltage across a pure inductor of value L is given by

$$E = L\frac{dI}{dt} = E_o \sin\omega t \tag{6.14}$$

integrating

$$LI = -\frac{E_o}{\omega}\cos\omega t = \frac{E_o}{\omega}\sin\left(\omega t - \frac{\pi}{2}\right) \tag{6.15}$$

$$E = j\omega LI = jX_L I \tag{6.16}$$

where X_L is the inductive reactance. Thus with a pure inductor the current lags behind the voltage by 90° and has an impedance plot as shown in Figure 6.4.

6.2.4 RC in Series

The voltage applied across a resistor and capacitor in series is equal to the sum of the voltages dropped across each component, thus

$$\underline{E} = \underline{E}_R + \underline{E}_C \tag{6.17}$$

$$E = I(R - jX_C) = IZ \tag{6.18}$$

The magnitude of the impedance Z is $\sqrt{(R^2 + X_C^2)}$ and the phase angle is given by

$$\tan\phi = \frac{X_C}{R} \tag{6.19}$$

The shape of the impedance plot is shown in Figure 6.5.

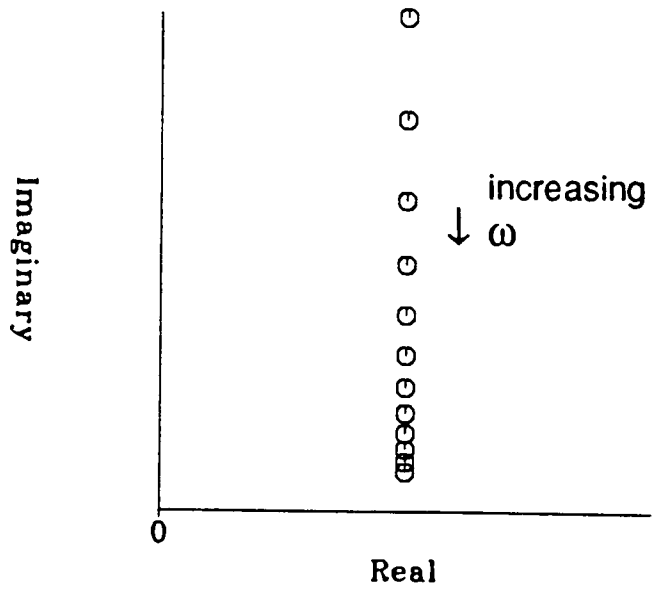

Figure 6.5. Impedance plot produced on applying an alternating voltage across a resistor and capacitor in series.

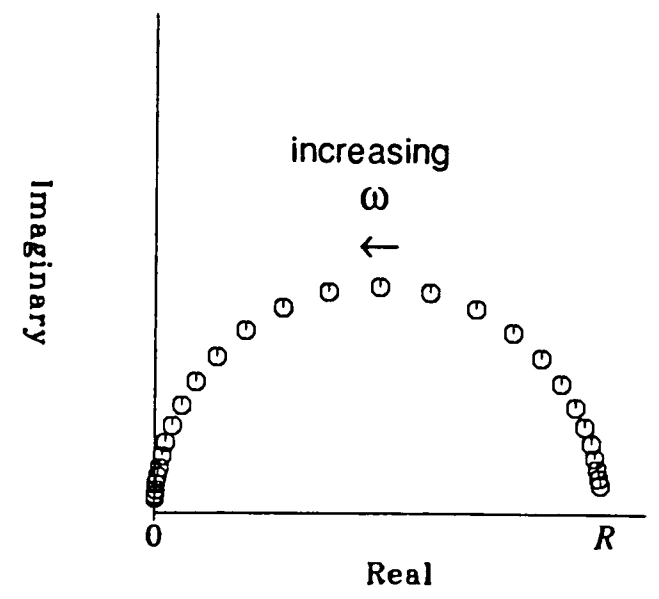

Figure 6.6. Impedance plot produced on applying an alternating voltage across a resistor and capacitor in parallel.

6.2.5 RC in Parallel

Impedances in parallel sum in the same fashion as resistances, thus for a resistor and capacitor in parallel the impedance is given by

$$\frac{1}{Z} = \frac{1}{Z_R} + \frac{1}{Z_C} = \frac{1}{R} - \frac{1}{jX_C} \tag{6.20}$$

$$Z = \frac{RX_C(X_C - jR)}{X_C^2 + R^2} = \frac{R - jR^2\omega C}{1 + R^2\omega^2 C^2} \tag{6.21}$$

This function is a semi-circle, as shown in Figure 6.6, with diameter R. At low frequencies the reactance of the capacitor is large so all the current passes through the resistor. Conversely, at high frequencies the reactance of the capacitor is small, so all the current "passes through" the capacitor.

6.2.6 Simple Transmission Line

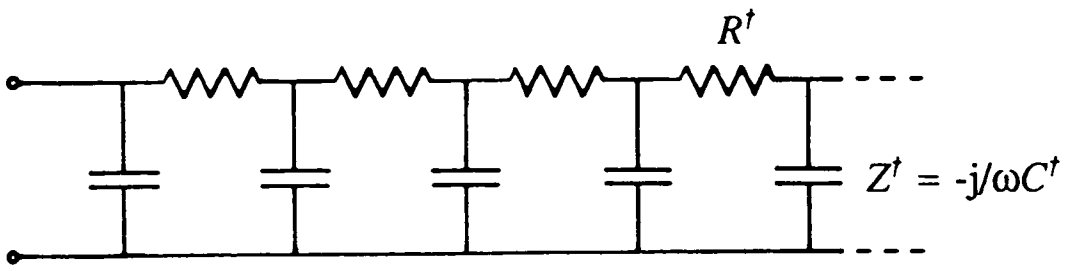

Figure 6.7. Circuit diagram of a semi-infinite transmission line.

A more complex circuit is the semi-infinite transmission line of resistors and capacitors, as shown in Figure 6.7. In order to derive an expression for the transmission line impedance consider a general case where R^t is the resistance per unit length, Z^t is the interfacial impedance per unit length and x is the direction along the transmission line, as shown in Figure 6.8.

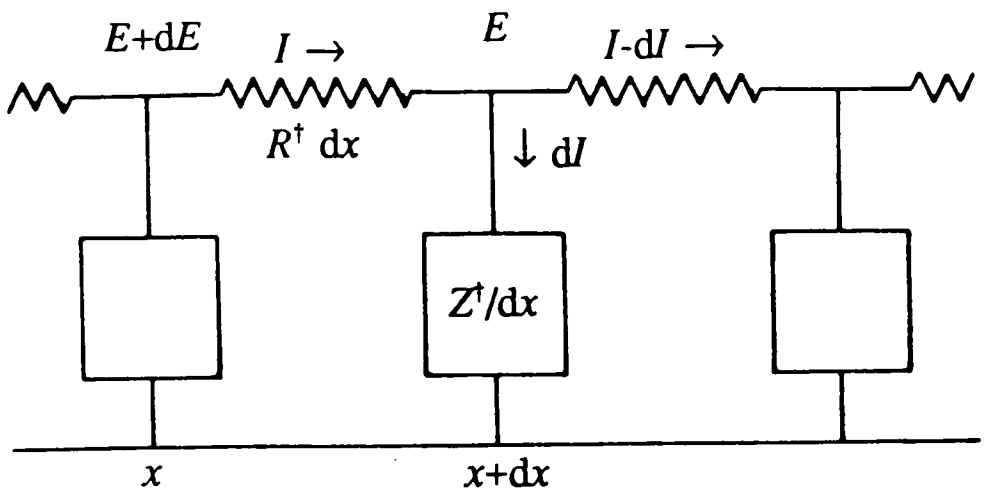

Figure 6.8. Circuit diagram showing an infinitely small section of a semi-finite transmission line.

For an infinitesimally small section dx and for small amplitudes, so that $Z^\dagger$ is only a function of ω,

$$dE = -IR^\dagger dx \quad \Rightarrow \quad \frac{dE}{dx} + IR^\dagger = 0 \tag{6.22}$$

$$dI = -\frac{E}{Z^\dagger}dx \quad \Rightarrow \quad \frac{dI}{dx} + \frac{E}{Z^\dagger} = 0 \tag{6.23}$$

Combining equations (6.22) and (6.23)

$$\frac{d^2I}{dx^2} - \frac{R^\dagger}{Z^\dagger}I = 0 \tag{6.24}$$

$$\frac{d^2E}{dx^2} - \frac{R^\dagger}{Z^\dagger}E = 0 \tag{6.25}$$

For a semi-infinite transmission line the boundary conditions are

$$E(\infty) = 0; \quad E(0) = E_o \tag{6.26}$$

Integrating equation (6.25) with these limits

$$E(x) = E_o \exp\left(-x\sqrt{\frac{R^\dagger}{Z^\dagger}}\right) \tag{6.27}$$

From equations (6.22) and (6.27)

$$I(x) = -\frac{1}{R^\dagger}\frac{dE}{dx} = \frac{E}{\sqrt{Z^\dagger R^\dagger}}\exp\left(-x\sqrt{\frac{R^\dagger}{Z^\dagger}}\right) \tag{6.28}$$

thus

$$I(0) = \frac{E}{\sqrt{Z^{\dagger}R^{\dagger}}} \tag{6.29}$$

The transmission line, therefore, has an impedance $\sqrt{(Z^{\dagger}R^{\dagger})}$. In the impedance plane, the impedance vector has magnitude $\sqrt{|Z^{\dagger}R^{\dagger}|}$ and phase angle $\phi/2$ (since $\sqrt{(\exp(j\phi))} = \exp(j\phi/2)$). In the specific case where the impedance $Z^{\dagger}$ per unit length is a pure capacitance $C^{\dagger}$ per unit length, substituting $Z^{\dagger} = -j/\omega C^{\dagger}$ in equation (6.29) yields

$$Z_{tml} = \sqrt{\frac{R^{\dagger}}{2\omega C^{\dagger}}}\,(1-j) \tag{6.30}$$

for the transmission line impedance Z_{tml}. This function is plotted in Figure 6.9.

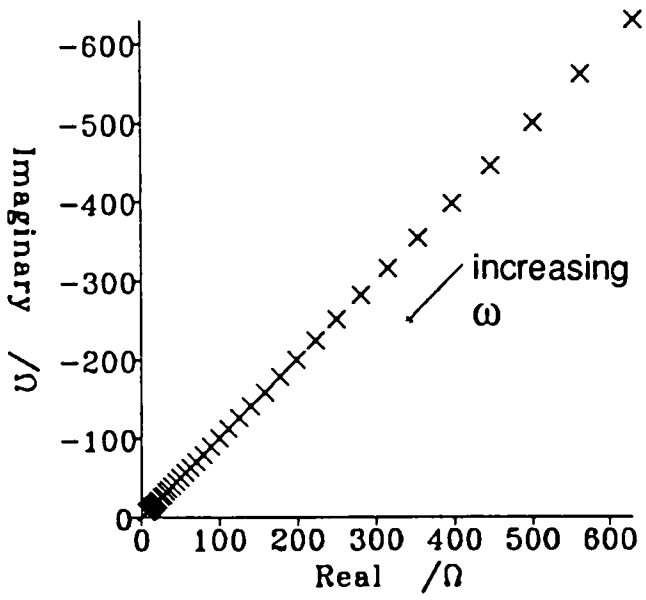

Figure 6.9. Impedance plot produced on applying an alternating voltage across a semi-infinite transmission line.

For a finite length transmission line terminating with an open circuit (i.e. reflective case) the boundary conditions are

$$E(0) = E_o; \quad \left.\frac{dE}{dx}\right|_{x=l} = 0 \tag{6.31}$$

Using equations (6.25) and (6.31) the transmission line impedance is [174,176]

$$Z_{tml} = \sqrt{Z^{\dagger}R^{\dagger}}\coth\frac{lR^{\dagger}}{\sqrt{Z^{\dagger}R^{\dagger}}} \tag{6.32}$$

In the case where the interface impedance is purely capacitative, i.e. $Z^{\dagger} = -j/\omega C^{\dagger}$, equation (6.32) becomes

$$Z_{tml} = \left(\frac{R^{\dagger}}{2\omega C^{\dagger}}\right)^{1/2}\left(\frac{\sinh u - \sin u - j(\sinh u + \sin u)}{\cosh u - \cos u}\right) \tag{6.33}$$

where

$$u = l(2R^{\dagger}C^{\dagger}\omega)^{1/2} \tag{6.34}$$

This function is plotted in Figure 6.10 and shows that at low frequency the transmission line becomes capacitative.

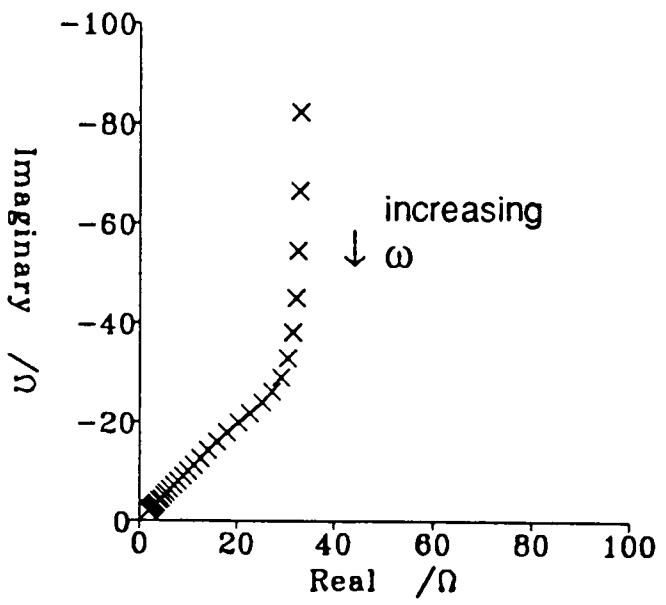

Figure 6.10. Impedance plot produced on applying an alternating voltage across a finite transmission line terminated with a capacitor.

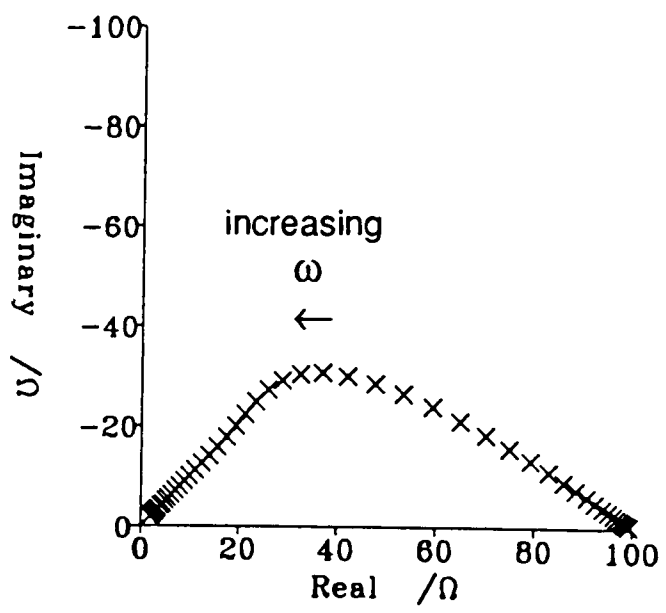

Figure 6.11. Impedance plot produced on applying an alternating voltage across a finite transmission line terminated with a resistor.

Alternatively if the transmission line is terminated in a resistance, i.e. the potential at $x = l$ is a non-zero constant value, then the transmission line impedance is [174]

$$Z_{tml} = \sqrt{Z^{\dagger}R^{\dagger}}\tanh\frac{lR^{\dagger}}{\sqrt{Z^{\dagger}R^{\dagger}}} \tag{6.35}$$

For a purely capacitative interface this becomes

$$Z_{tml} = \left(\frac{R^{\dagger}}{2\omega C^{\dagger}}\right)^{1/2}\left(\frac{\sinh u + \sin u - j(\sinh u - \sin u)}{\cosh u + \cos u}\right) \tag{6.36}$$

which is plotted in Figure 6.11. In this case, at low frequencies, the transmission line tends towards a pure resistance.

6.2.7 Equivalent Circuits

It is often possible to model the a.c. response of an electrochemical system using an equivalent electronic circuit. In the absence of any electroactive species at the potentials applied, an electrode's response can be simply modelled by a double-layer capacitance, C_{dl}, in series with an uncompensated solution resistance, R_u. Thus the electrode's response to an alternating signal would be as in Section 6.2.4.

The equivalent circuit becomes more complex in the presence of an electroactive species. In addition to a current due to the double-layer charging there will also be a current due to the faradaic process, so a faradaic impedance Z_f is placed in parallel to the double-layer capacitance, as shown in Figure 6.12. The components used to represent the faradaic impedance, however, are not ideal in that they alter with frequency. The faradaic impedance can be represented by a charge transfer resistance, R_{ct}, in series with the Warburg impedance, Z_W, which is

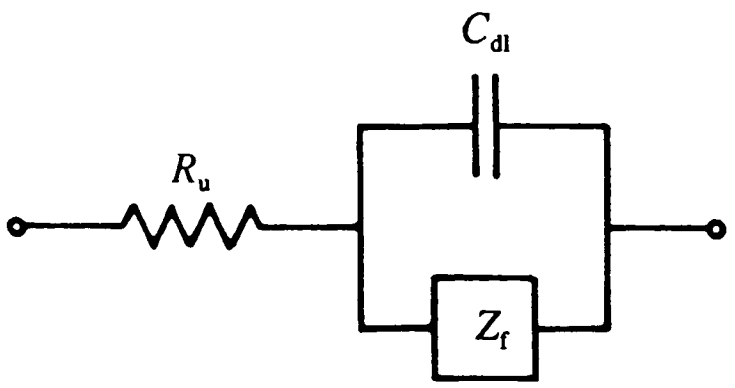

Figure 6.12. Equivalent circuit of an electrochemical cell.

a reactance that represents a resistance to mass transfer, i.e.

$$Z_f = R_{ct} + Z_W \tag{6.37}$$

where the Warburg impedance is given by

$$Z_W = \frac{\sigma}{\omega^{1/2}} - \frac{j\sigma}{\omega^{1/2}} \tag{6.38}$$

The Warburg coefficient, σ, is dependent on the diffusion parameters of the system. Figure 6.13 shows the overall behaviour of the faradaic impedance together with the double-layer capacitance and solution resistance.

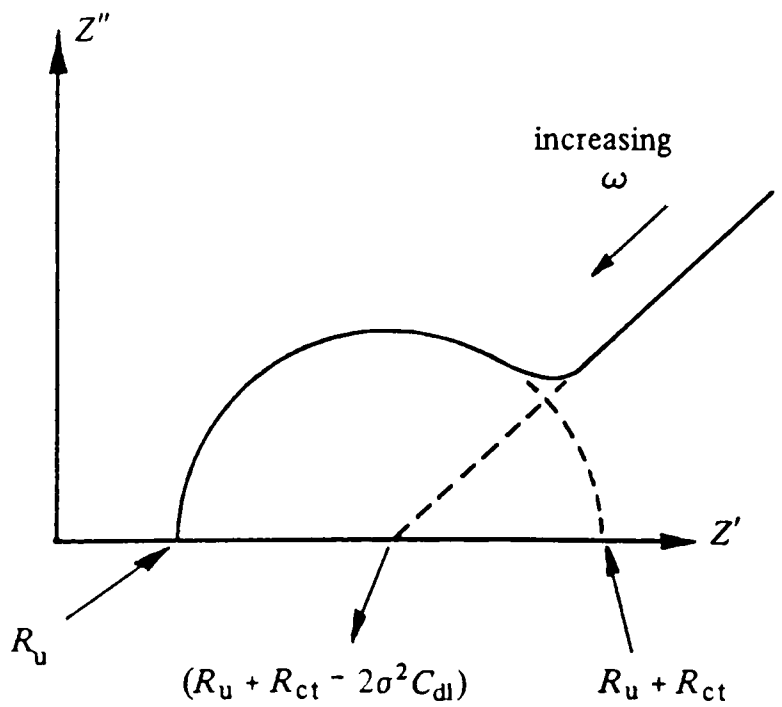

Figure 6.13. Impedance plot produced on applying an alternating voltage across the equivalent circuit shown in Figure 6.12 with the faradaic impedance, Z_f, represented by a charge transfer resistance, R_{ct}, in series with a Warburg impedance.

The transmission line circuits are used to mimic porous electrodes [176,177], where each pore is represented by a transmission line with $R^{\dagger}$ being the solution resistance of the pore per unit pore length and $Z^{\dagger}$ being the impedance of the electrolyte-electrode interface per unit pore length.

6.3 Instrumentation

In Section 6.2 it was stated that a sinusoidal voltage produced a sinusoidal current response at the same frequency. This assumes that the relationship between current and potential is linear, which is not strictly the case. For this approximation to be valid the amplitude of the excitation signal must be small, usually less than 10 mV peak-to-peak. Larger excitation voltages lead to a non-linear current response, which can be represented by a sum of sinusoidal harmonic components. Information can be extracted by tuning a lock-in amplifier to higher harmonic frequencies i.e. 2ω, 3ω etc.

The impedance of an electrochemical cell can be measured by a variety of different methods. One of the simplest methods is to use an a.c. Wheatstone bridge, which has a variable resistor and capacitor in one arm of the bridge and the electrochemical cell in the other. A more sophisticated approach is to use analogue a.c. analysers, which measure either the a.c. amplitude and phase angle of the alternating cell current, or the real and complex parts of the impedance. A different technique involves applying a multi-frequency potential and performing a Fourier transformation on the response signal to obtain the frequency dependent impedance.

6.4 Experimental

Equipment specific to the a.c. experiments is discussed here, unless already covered in Chapter 3.

6.4.1 A.C. Generation and Analysis

A Solartron Instruments 1250 Frequency Response Analyser (FRA) (Schlumberger Electronics Ltd., Farnborough, Hants.) was used to generate the alternating voltages and determine the gain and phase characteristics of the signal response. The alternating signal generated by the FRA was fed into the polarisation input of a Solartron Instruments 1286 Electrochemical Interface (ECI), which was used in its potentiostat mode. The ECI was in turn connected to the three electrode system under investigation (N.B. The second reference connector RE2 on the ECI was shorted to the working electrode WE). The voltage and current signals from the ECI were then fed back into the two analysers of the FRA which measured the phase angle and gain of the voltage with respect to the current, as shown in Figure 6.14. The FRA was controlled by a BBC Master

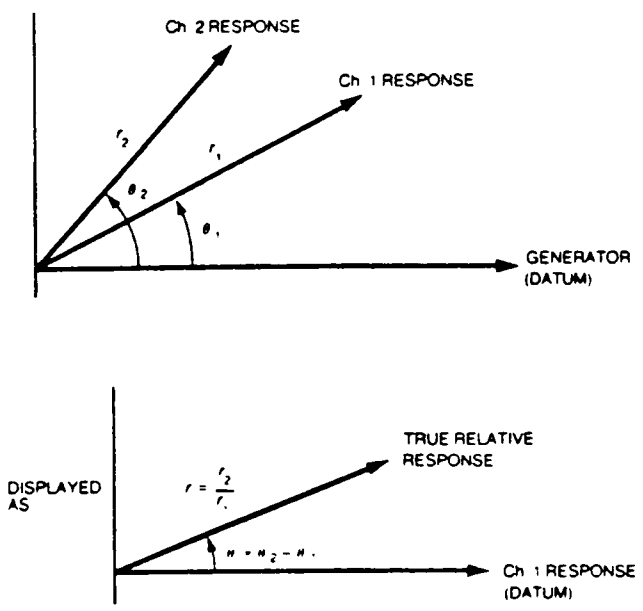

Figure 6.14. Operation of Schlumberger Solartron 1250 Frequency Response Analyser, with Channel 1 connected to the current output and Channel 2 connected to the voltage output of the potentiostat.

microcomputer. This also collected the data, which could be displayed as an imaginary versus real impedance plot using a Hewlett Packard 7470A plotter or transferred to the VAX mainframe for further analysis.

6.4.2 Scaled Electrodes

An internally scaled steel tube of internal diameter 0.540 cm was obtained from a hot beverage vending machine, which had cease to function due to the build up of calcium carbonate scales. The thickness of the scale layer, measured using a travelling microscope, is given in Table 6.1. The external surface of this tube, including the end annulus, was coated in a specially selected low melting cosmetic depilatory wax (Wax-a-Way), thus insulating the unscaled surfaces of the metal. This was immersed (see Figure 6.15) to varying depths in a solution of background electrolyte (usually 0.5 M) containing calcium and carbonate ions (≈3 mM in each) to prevent the dissolution of the scale. Potassium nitrate was used as the background electrolyte instead of the chloride because the latter may promote the corrosion of steel [178,179]. Another section of this steel tubing was descaled by

Table 6.1. Thickness of Scale Layer in Scaled Tube

Distance from bottom of tube /cm	Scale thickness (mean) at this height /cm	Mean scale thickness over tube length /cm
14.5	0.0635	0.083
7.0	0.0720	0.099
3.5	0.0955	0.115
0.0	0.1343	-

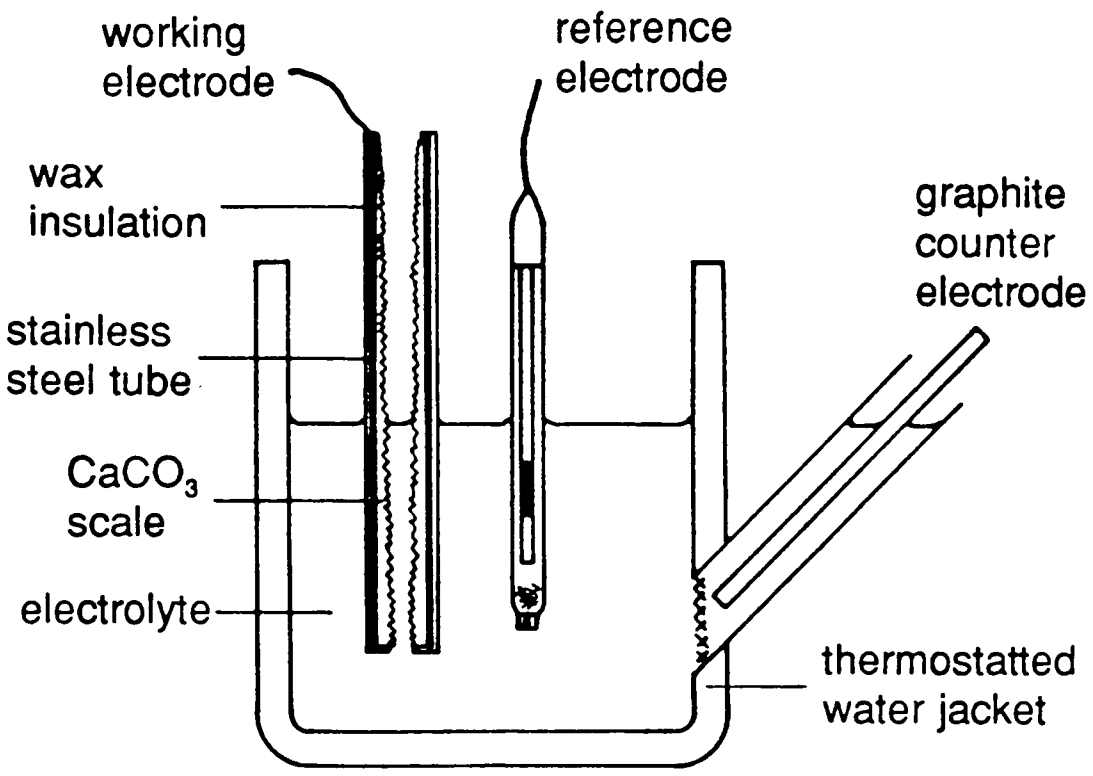

Figure 6.15. Schematic diagram of the apparatus used to investigate the impedance of scaled tubes. Here the scaled tube is shown partially immersed.

immersion in a solution of citric acid, so as to act as a control. The reference electrode used was usually a saturated calomel electrode (SCE) (401, Radiometer, Copenhagen), though a silver bromide coated silver wire was used at one stage, together with the addition of potassium bromide (≈1 mM) to the solution. The counter electrode was a graphite rod or platinum gauze sited behind a glass sinter. The d.c. potential applied to the tube was 0 V with respect to the reference electrode, where no net current flowed. The a.c. signal had amplitude 5 mV and had a frequency range of 0.01 Hz - 65 kHz. Solutions were degassed with argon and maintained at 25°C using a water bath.

6.4.3 Modelling

The frequency response of theoretical circuits was calculated using programs written in FORTRAN 77 on the VAX mainframe, in the cases where an analytical expression for the circuit impedance had been determined. Using the analytical expression, the real and imaginary impedances were calculated over the frequencies used experimentally and a $-Z''$ versus Z' plot drawn.

For other circuits, the SPICE program (version 2G.5) was used on the Norsk Data ND540 mainframe computer to calculate the impedance. SPICE is a general purpose circuit simulation program for nonlinear d.c., nonlinear transient and linear a.c. analyses and was developed at the University of California, Berkeley. Using SPICE, the required circuit was modelled by numbering the nodes where components were connected together and specifying which nodes each component was connected to, the type of component (e.g. resistor, capacitor) and the component's value. The node at which an alternating voltage was applied was also specified. The output of the program yielded the real and imaginary components, as well as magnitude, of the current at this node. Given that the voltage applied was set at zero phase, the real and imaginary components of the impedance were calculated as follows

$$Z' = -\frac{|\underline{E}|\,\Re(I)}{|\underline{I}|^2}, \quad Z'' = \frac{|\underline{E}|\,\Im(I)}{|\underline{I}|^2} \tag{6.39}$$

where $\Re(I)$ and $\Im(I)$ were the real and imaginary components of the current of magnitude $|\underline{I}|$, as calculated using SPICE.

For the modelling of transmission lines with SPICE, where the resistances and capacitances per unit length were continuous, the values of the components used were sufficiently small (i.e. enough components were used per unit length) to make the circuit appear continuous.

Whether SPICE or analytical modelling was used, the frequency dependence of the impedance of the given equivalent circuit was compared to that obtained from experiment by displaying the data on a $-Z''$ versus Z' plot. The magnitude of the circuit components were varied to obtain the optimal fit with experiment. The

optimal fits obtained from different equivalent circuits were then compared (see below).

6.5 Results and Discussion

6.5.1 Unscaled Tube

With the unscaled tube immersed similarly to the tube shown in Figure 6.15 and using the three electrode configuration, with the reference and counter electrodes outside the tube, the impedance plot obtained is shown in Figure 6.16. This shows a 45° line at high frequencies and a near vertical line at low frequencies. Such a response can be modelled with a simple open-ended (reflective) transmission line. Using the analytical equation (6.33) derived for this circuit, the best fit with experiment, shown in Figure 6.16, was found to be $R^{\dagger}$ = 90 Ω cm^{-1}, $C^{\dagger}$ = 21 μF cm^{-1}, R_u = 24.5 Ω and l = 2 cm. The solution contained

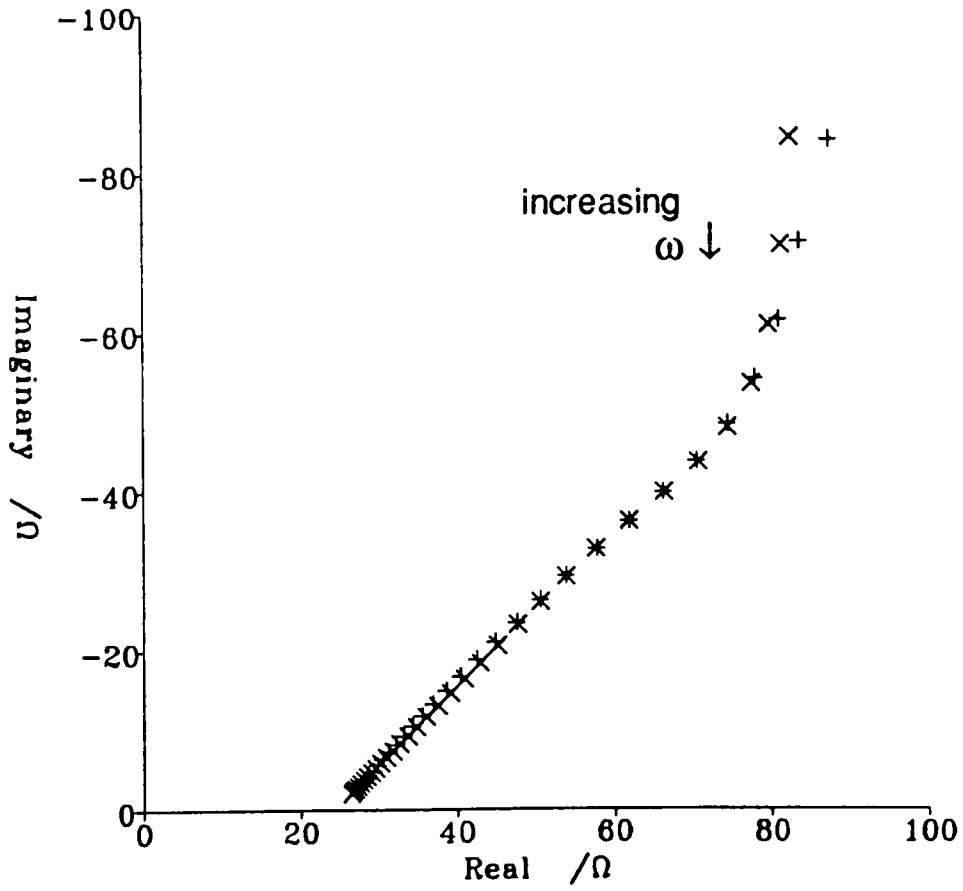

Figure 6.16. Impedance plot (+) obtained from the internal surface of the unscaled tube immersed to a depth of 2 cm. *This has been fitted* (×) *to the analytical equation for a simple reflective transmission line with* $R^{\dagger}$ = 90 Ω cm^{-1}, $C^{\dagger}$ = 21 μF cm^{-1} *and uncompensated solution resistance of* 24.5 Ω.

0.513 M KNO_3, which has a molar conductivity of 89.24 S cm^2 mol^{-1} at an ionic strength of 0.5 M and 18°C [180]. The internal diameter of the tube was 0.540 cm and so the resistance per unit length of the solution in the tube should have been $R^\dagger$ = 95 Ω cm^{-1}. The capacitance per unit length, $C^\dagger$ = 21 μF cm^{-1}, was equivalent to a capacitance per unit area of 12 μF cm^{-2}, which was typical of capacitances obtained on planar steel electrodes. This demonstrated an excellent agreement between expected and measured resistances and capacitances, thus giving support to the proposed equivalent model.

Experimentally the low frequency data did not produce a vertical line but had some slope (i.e. $\phi < 90°$). This has been attributed to surface roughness of electrodes [181-185] and can be modelled with a constant phase element for which

$$Z^{-1} = A(j\omega)^{\alpha}$$

where A is a frequency independent real constant. The exponent $\alpha = (D - 1)^{-1}$, where D ($2 < D < 3$) is the fractal dimension of the rough electrode. When $D = 2$ purely capacitative behaviour is obtained, corresponding to a perfectly smooth surface, whereas $D = 3$ gives $\alpha = 0.5$, which is the limiting case for a porous electrode [176,177].

For the reflective transmission line, the value of the real impedance where the impedance plot is vertical, is given by the limit of equation (6.33) where $\omega \rightarrow 0$. Substituting the Maclaurin expansions for the trigonometric and hyperbolic terms into this equation yields

$$Z'_{\lim \omega \to 0} = \left(\frac{R^\dagger}{2\omega C^\dagger}\right)^{1/2} \frac{u}{3} = \frac{R^\dagger l}{3} \qquad (6.41)$$

Thus at low frequencies the a.c. signal traverses the whole length of the transmission line.

The validity of this model was further tested by varying the extent to which the unscaled tube was immersed in the solution. If the tube were to be immersed deeper into the solution, then the total resistance of the transmission line would be expected to increase, as predicted by equation (6.41). The impedance plots for these experiments are shown in Figure 6.17, demonstrating that the limiting impedance does indeed vary with immersion depth.

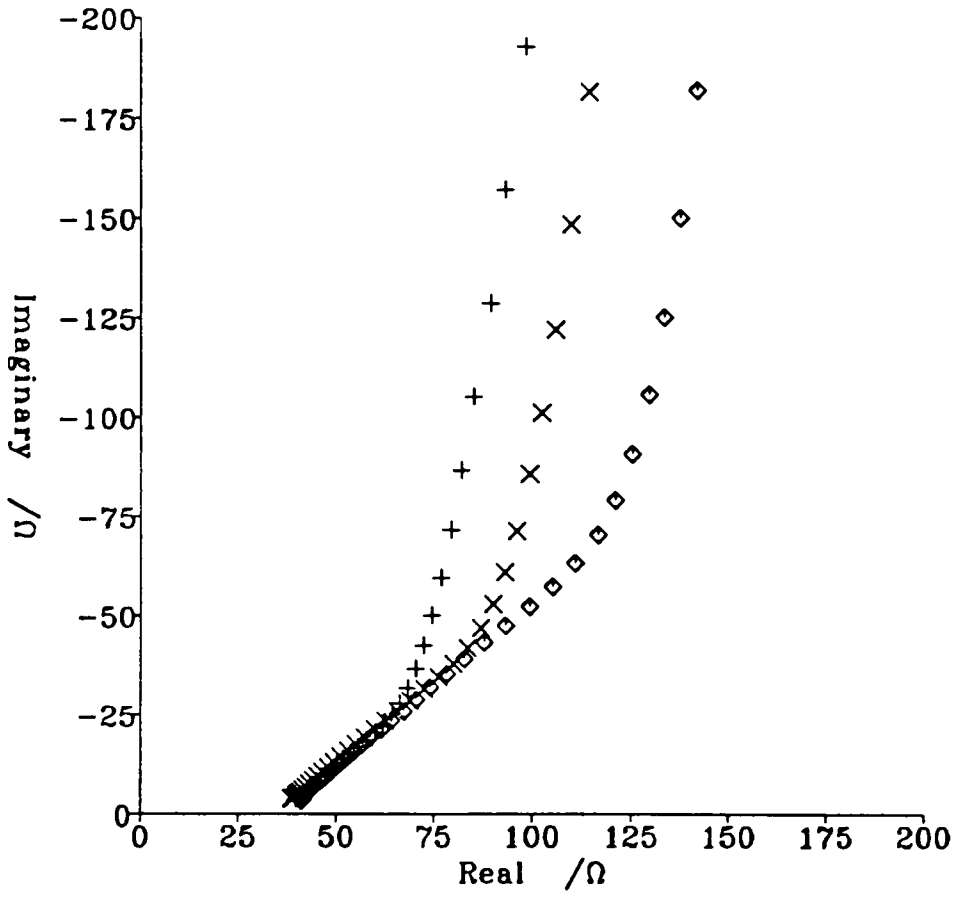

Figure 6.17. Impedance plot showing the response of the unscaled tube immersed to depths of 1 cm (+), 2 cm (×) *and* 3 cm (◇).

Figure 6.18 plots the fit of equation (6.33) to these results, with $R^{\dagger}$ = 95 Ω cm^{-1} and $C^{\dagger}$ = 24 μF cm^{-1} (equivalent to 14 μF cm^{-2}). Hence the simple RC transmission line provides an accurate equivalent circuit for the unscaled tube in this electrode configuration.

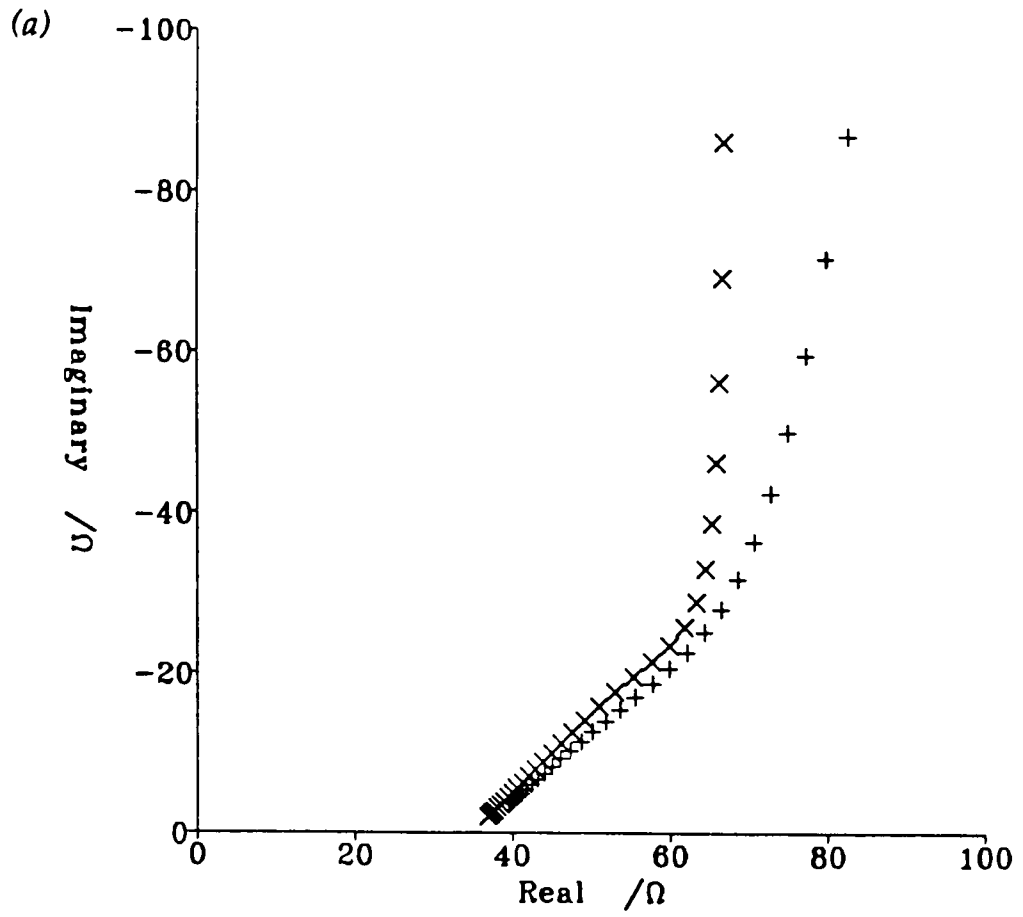

Figure 6.18. Impedance plot showing the agreement between the experimental response (+) of the unscaled tube immersed to depths of (a) 1 cm *and (b)* 3 cm *and the simple transmission line model* (×) *with* $R^{\dagger}$ = 95 Ω cm^{-1} *and* $C^{\dagger}$ = 24 μF cm^{-1}.

6.5.2 Scaled Tube

Similar experiments were carried out on another section of the same tube used in Section 6.5.1, but with scale present. This tube was 14.5 cm long and had a scale layer of mean thickness varying from 0.134 cm at the bottom to 0.064 cm

at the top of the tube (see Table 6.1). Figure 6.19 shows impedance plots for a range of immersion depths varying from completely immersed, where the solution meniscus was just below the top of the tube (to prevent current flow through both ends), to only 1 cm immersed.

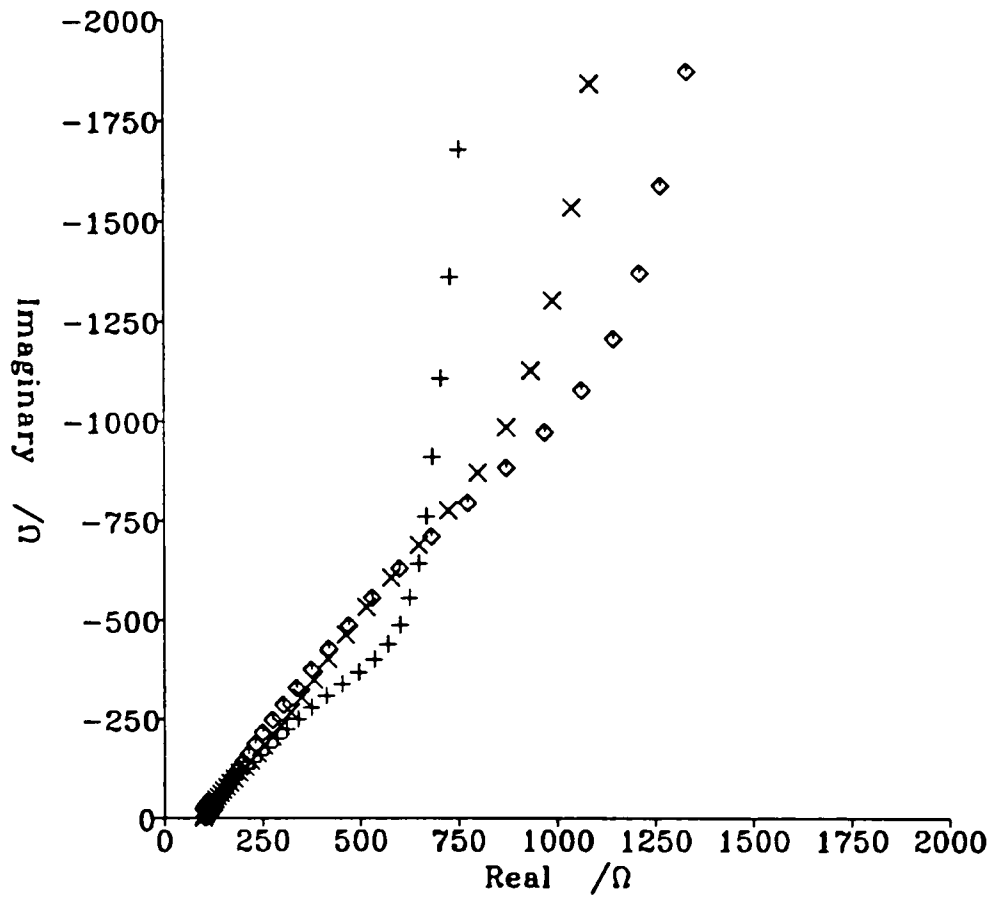

Figure 6.19. Impedance plot of scaled tube immersed to a depth of 1 cm (◇), 4 cm (×) *and fully immersed* (+).

Three equivalent circuits were identified as candidates to represent the behaviour of the scaled tube and these will be discussed in turn.

6.5.2.1 *Non-distributed circuit*

The impedance of the non-distributed circuit, shown in Figure 6.20, is given by the following expression, which was derived from equations (6.7), (6.13) and (6.21),

$$Z = R_u + \frac{R_s - j\omega R_s^2 C_s}{1 + (\omega R_s C_s)^2} - \frac{j}{\omega C_i} \qquad (6.42)$$

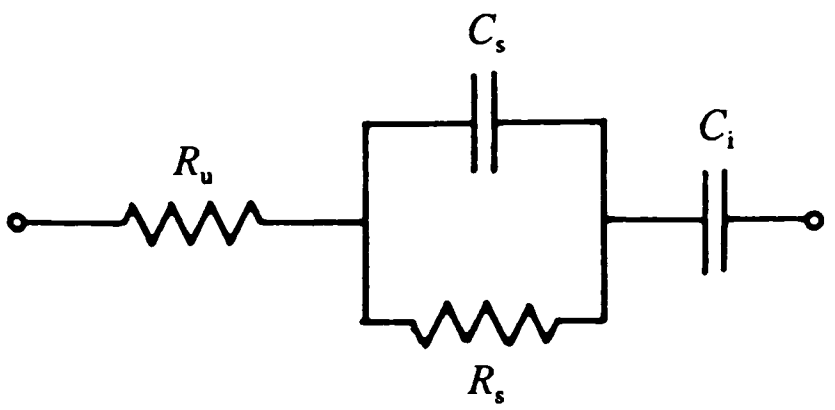

Figure 6.20. Non-distributed circuit.

where R_s and C_s represent the scale resistance and capacitance, and C_i represents the capacitance of the electrode-electrolyte interface. The low frequency limit of equation (6.42) is $R_u + R_s$. The fitting of this circuit to the scaled tube for immersion depths of 1 cm and 4 cm is shown in Figure 6.21. Reasonable fits were obtained at intermediate frequencies but at high frequencies marked deviation was observed.

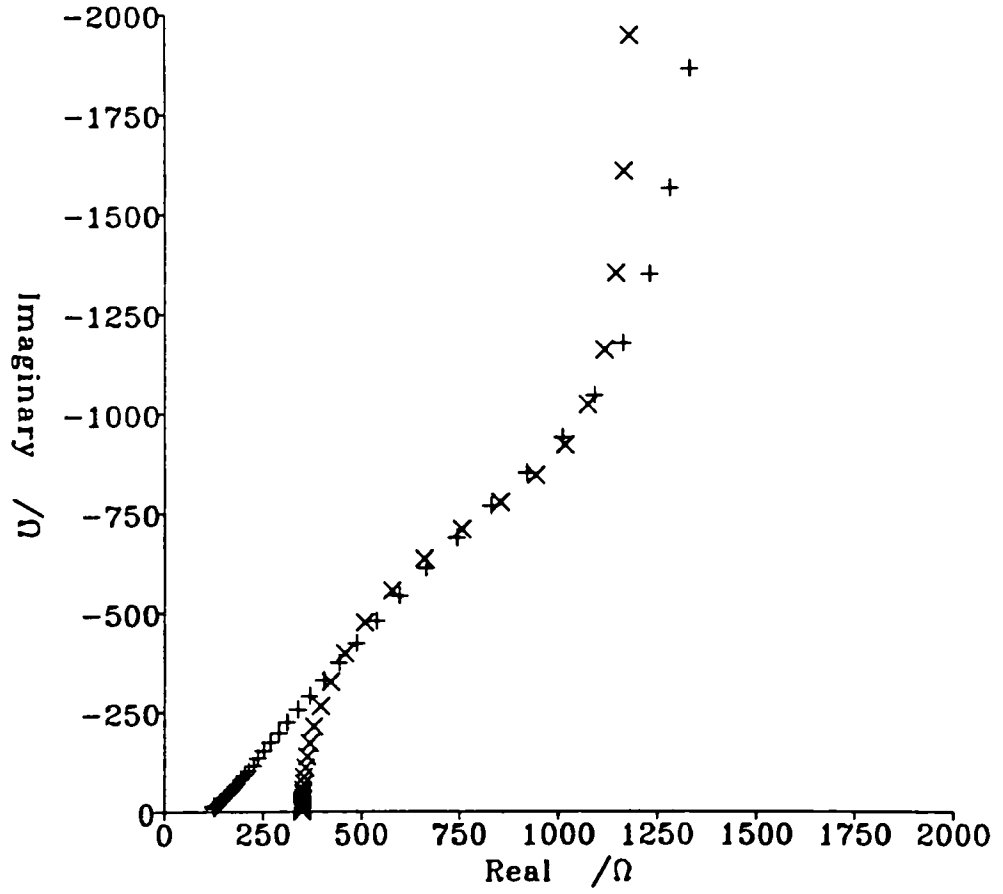

Figure 6.21a. Impedance plot showing the poor agreement between the impedance response of the scaled tube immersed 1 cm (+) *and the non-distributed circuit* (×), *shown in Figure 6.20, with* R_u = 350 Ω, R_s = 850 Ω, C_s = 98 μF *and* C_i = 277 μF.

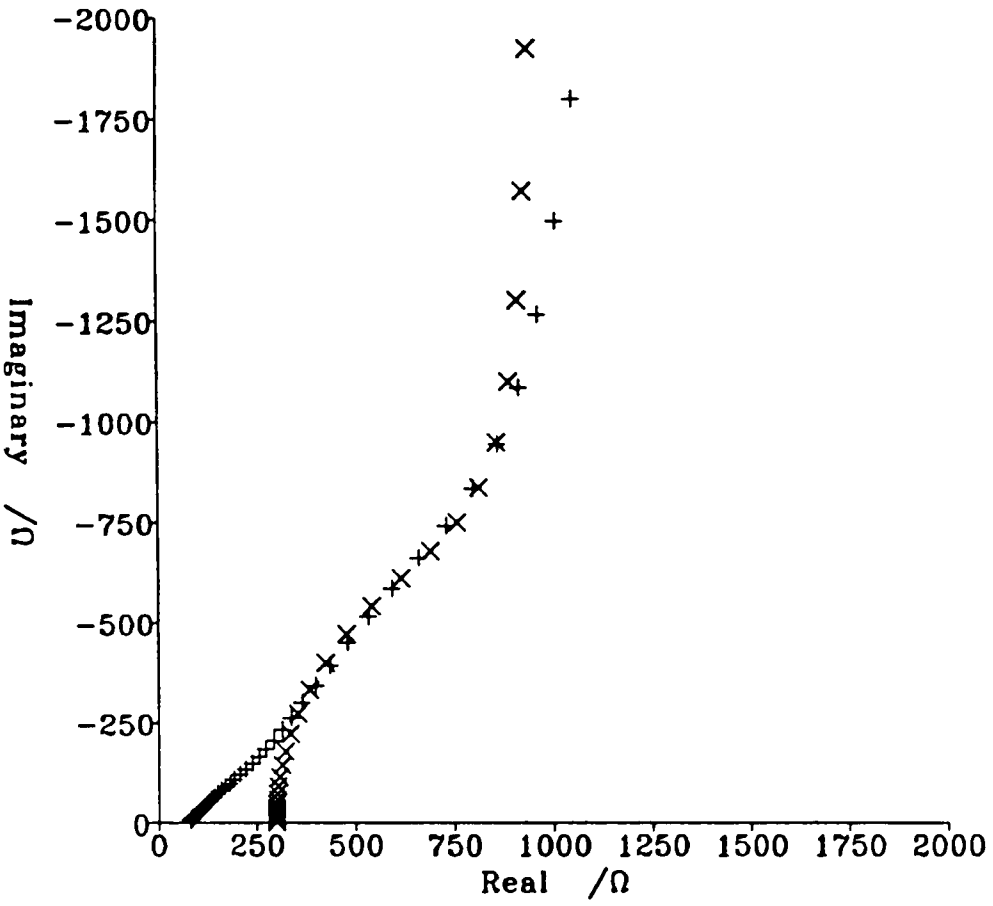

Figure 6.21b. Impedance plot showing the poor agreement between the impedance response of the scaled tube immersed 4 cm (+) *and the non-distributed circuit* (×), *shown in Figure 6.20, with* R_u = 300 Ω, R_s = 650 Ω, C_s = 126 μF *and* C_i = 277 μF.

6.5.2.2 *Terminated transmission line*

To obtain better agreement at high frequency, the equivalent circuit was arbitrarily modified so that the circuit in Section 6.5.2.1 was at the end of a transmission line. This was done to obtain a 45° response at high frequency, yet unchanged behaviour at lower frequencies. This circuit is shown in Figure 6.22, together with fits to the two experiments in Figure 6.21. Agreement was better than before, but in both cases it was difficult to rationalise the significance of the values obtained. The "scale capacitance", C_s, should be proportional to immersion depth, since the capacitance should be proportional to the electrode area ($C = \varepsilon A/d$). This was found to be the case. However, the value of the scale resistance, R_s, should be inversely proportional to immersion depth, since this should be inversely proportional to the immersed electrode area ($R = \rho l/A$), but this was not found with this model.

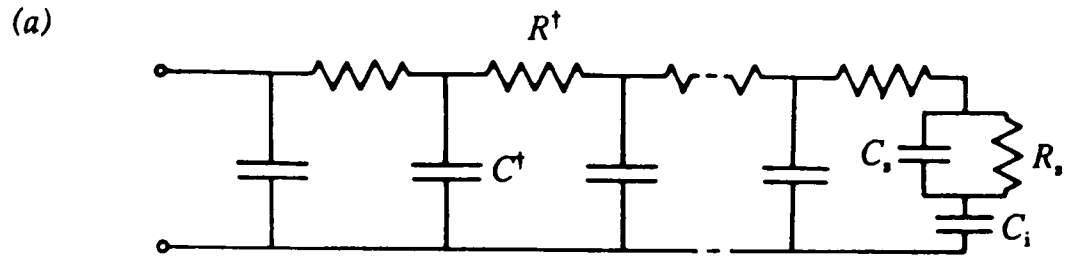

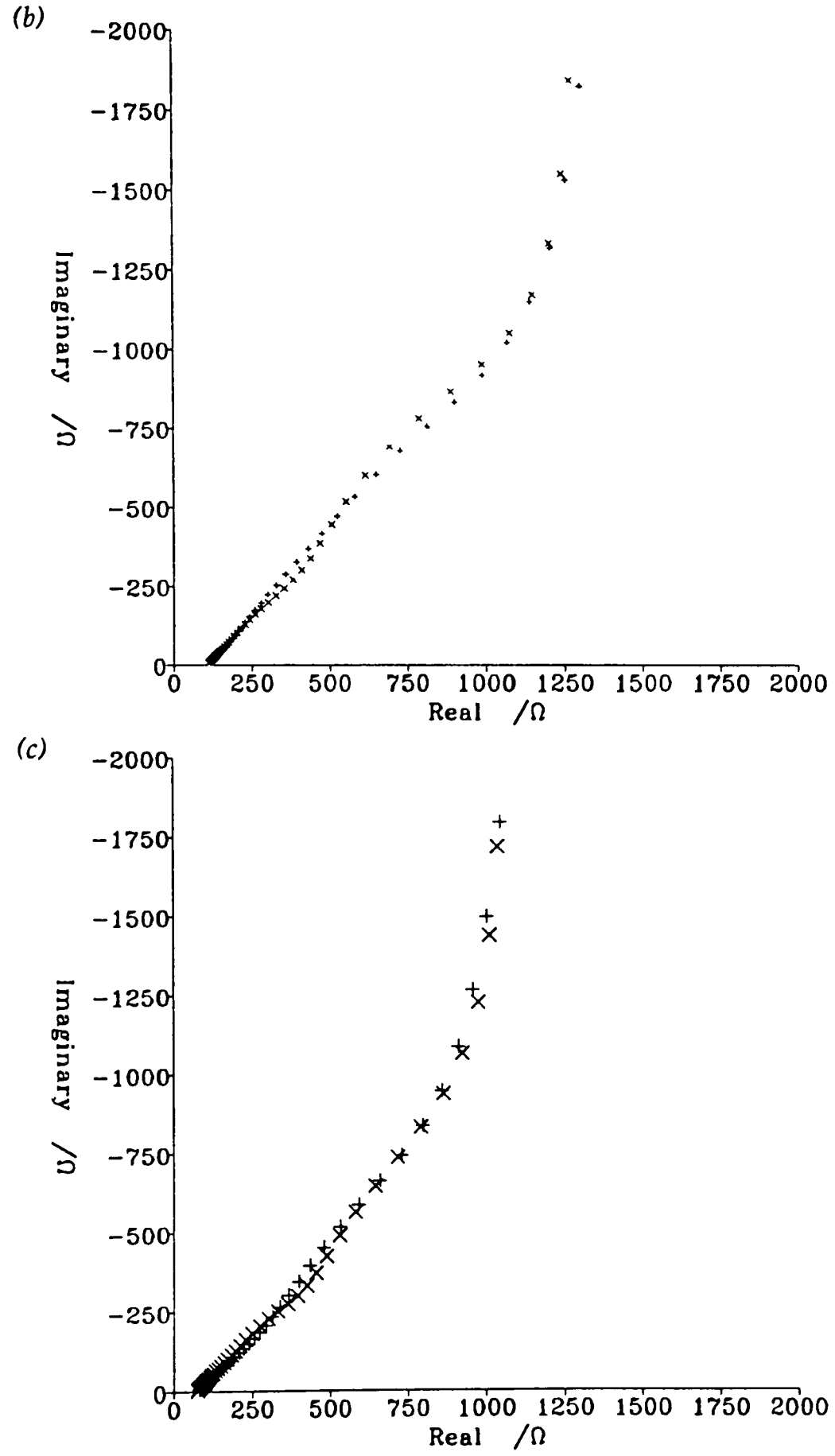

Figure 6.22. Terminated transmission line circuit (a) and impedance plots showing its agreement with the impedance response of the scaled tube immersed at (b) 1 cm (+) *fitted with* (×) R_u = 118 Ω, R_s = 1.2 kΩ, C_s = 20 μF, C_i = 200 μF, $R^\dagger$ = 990 Ω cm^{-1}, $C^\dagger$ = 100 μF cm^{-1}; *and at (c)* 4 cm (+) *fitted with* (×) R_u = 75 Ω, R_s = 900 Ω, C_s = 80 μF, C_i = 227 μF, $R^\dagger$ = 800 Ω cm^{-1}, $C^\dagger$ = 100 μF cm^{-1}.

6.5.2.3 *Simple transmission line*

An alternative approach was to use the simple RC transmission line to model the scaled tube. With this model excellent agreement was obtained with the fully immersed case (see Figure 6.23).

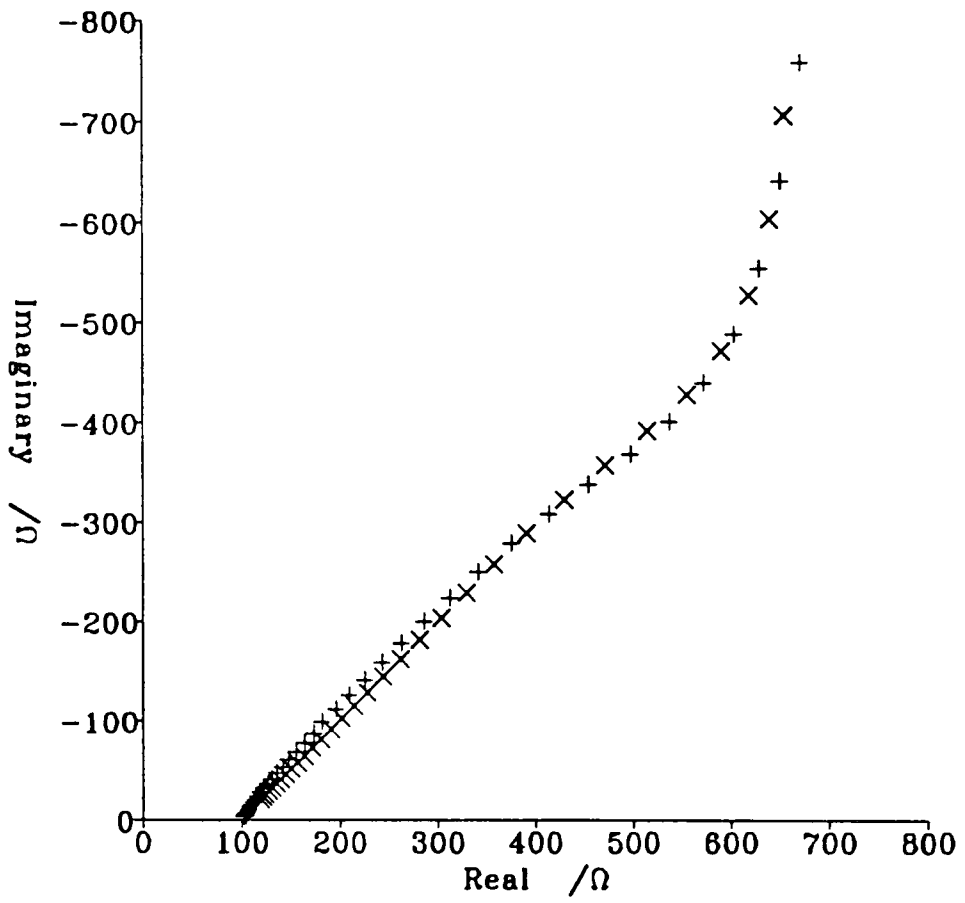

Figure 6.23. Impedance plot showing agreement between data from the fully immersed scaled tube (+) and the simple transmission line model (×) with R_u = 99 Ω, $R^\dagger$ = 120 Ω cm^{-1} *and* $C^\dagger$ = 22.8 μF cm^{-1}. *(Experiment 1 in Table 6.2).*

Partial immersion gave reasonable qualitative agreement with the model but did not produce the expected variation with immersion, namely the total transmission line resistance, $R_{tml} = R^\dagger l$, should have been proportional to the immersion depth. Instead, as can be seen from the low frequency limit in Figure 6.19, there is only a slight increase in R_{tml} with a decrease in immersion depth. A capacitance plot (Figure 6.24) of the experimental data in Figure 6.19 demonstrated that the low frequency (0.1 - 1.0 Hz) capacitance was approximately independent of immersion depth. This suggested that all the scale up the tube was wetted, not just that which was immersed in the solution. If this were the case then

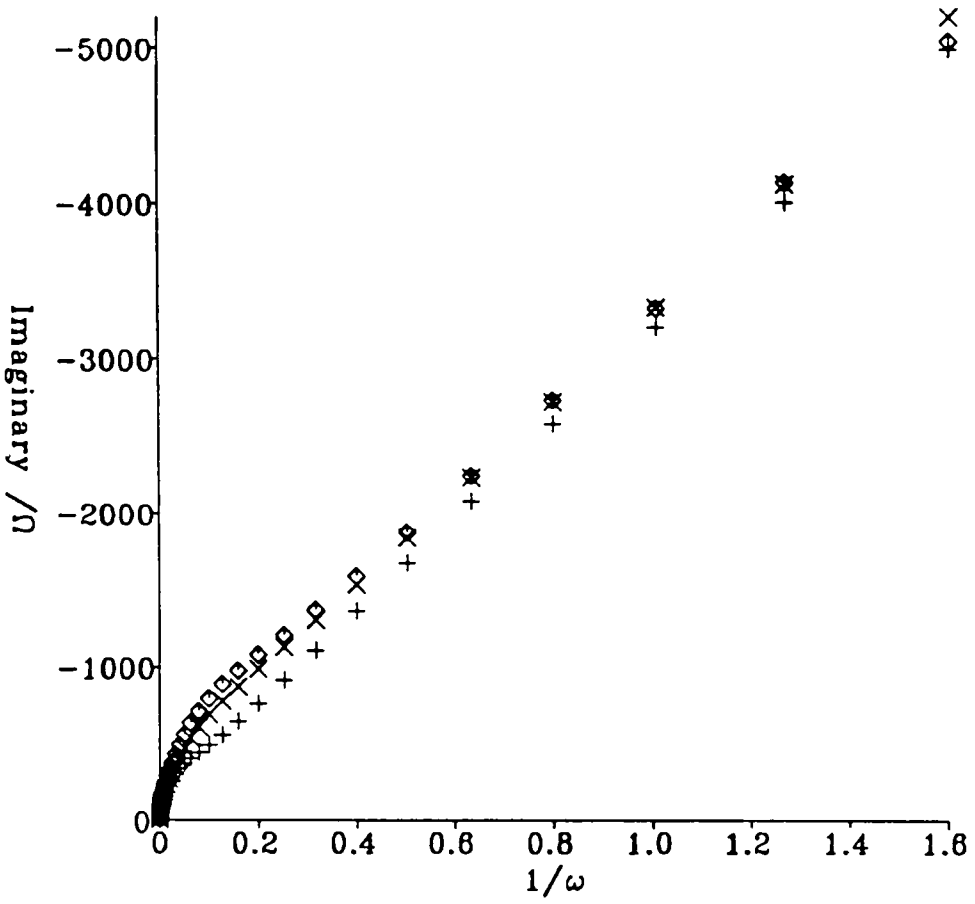

Figure 6.24. Capacitance plot of the impedance data obtained for the scaled tube (length 14.5 cm*) immersed at* 14.5 cm *(i.e. fully immersed)* (+), 4 cm (×) *and* 1 cm (◇). *This shows that the capacitance is independent of the immersion depth.*

the metal-solution interfacial capacitance would be 13.8 μF cm^{-2}, which is in close agreement to that obtained for the unscaled tube.

To test this hypothesis further, the length of the scaled tube was shortened to 7 cm and the a.c. response measured with the tube completely immersed. The procedure was repeated, with the tube shortened further to 3.5 cm. The impedance behaviour in the three cases is given in Figure 6.25. From inspection it can be seen that the real impedance of the low frequency limit is proportional to the tube length in these experiments. The associated capacitance plot is shown in Figure 6.26, from which it is clear that the capacitance is also proportional to the length and has an average value of 15.0 μF cm^{-2} (or 25.4 μF cm^{-1}). This variation of capacitance with length is consistent with all the models but the variation of resisitance is completely inconsistent with the circuits in Sections 6.5.2.1 & 6.5.2.2.

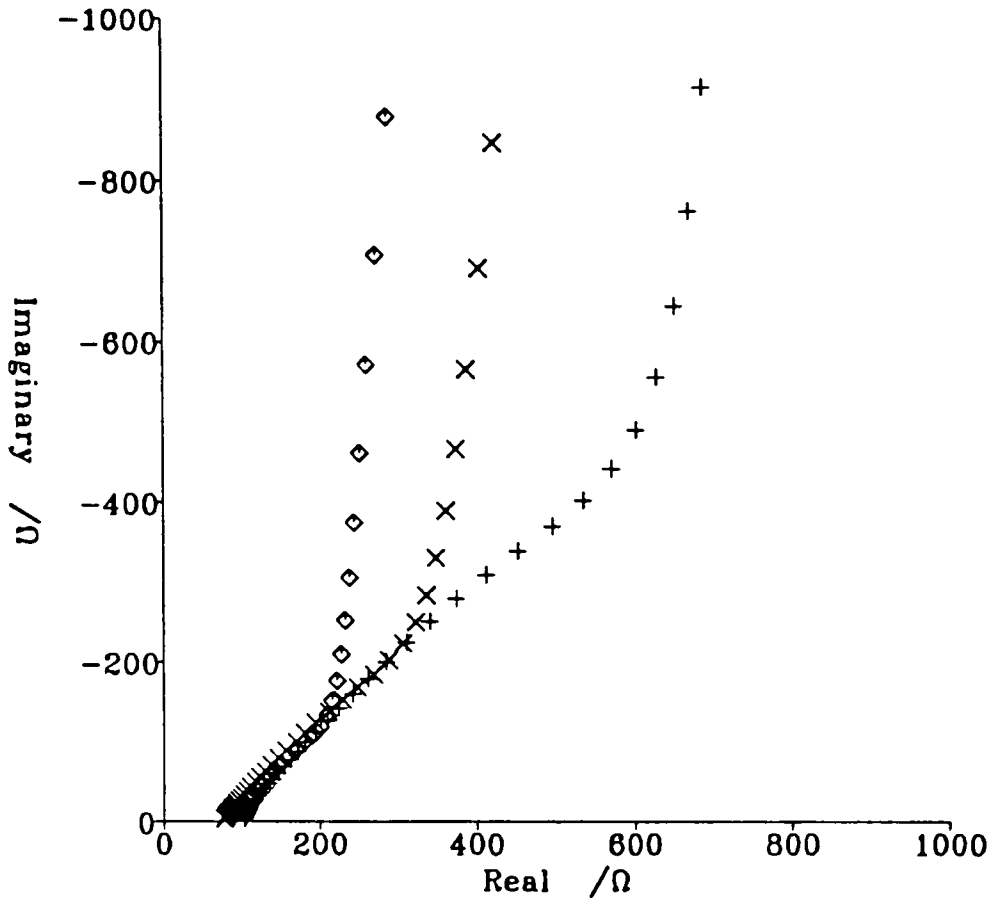

Figure 6.25. Impedance plot for the fully immersed scaled tubes of length 14.5 cm (+), 7 cm (×) *and* 3.5 cm (◇).

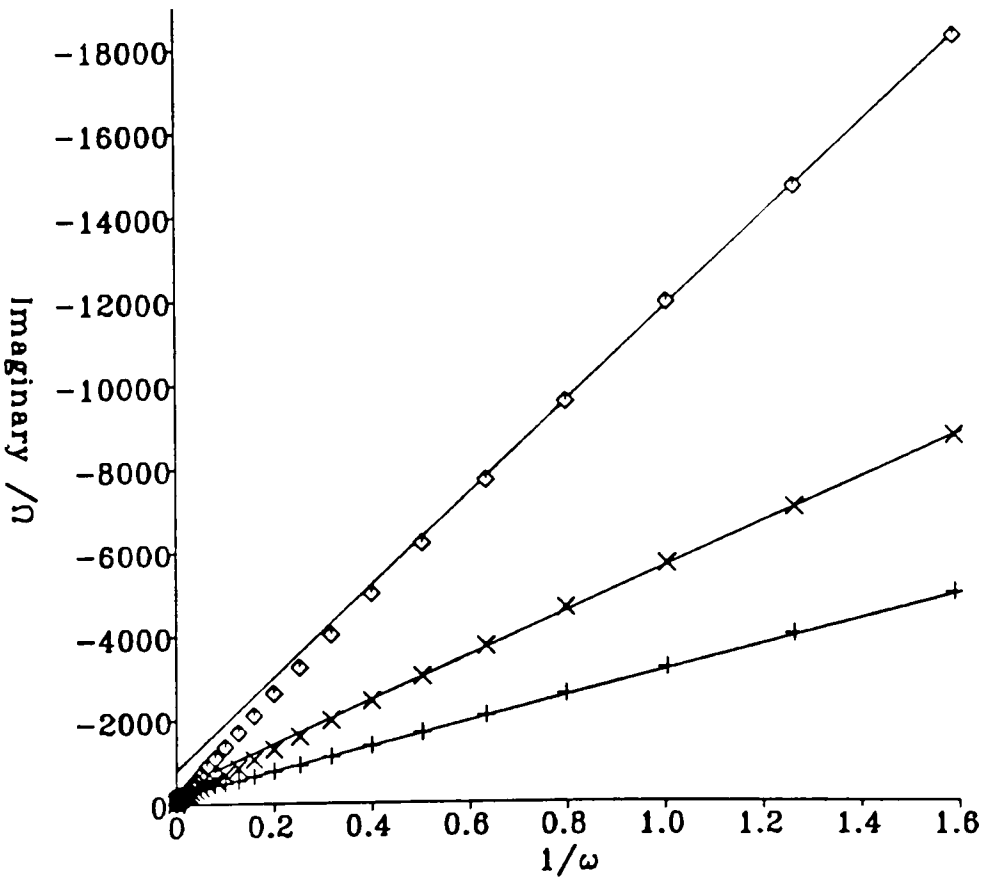

Figure 6.26. Capacitance plot of the impedance data obtained for the fully immersed scaled tubes of length 14.5 cm (+), 7 cm (×) *and* 3.5 cm (◇). *This shows that the capacitance is dependent on the immersion depth, with values of* 331 μF, 192 μF *and* 91 μF *respectively.*

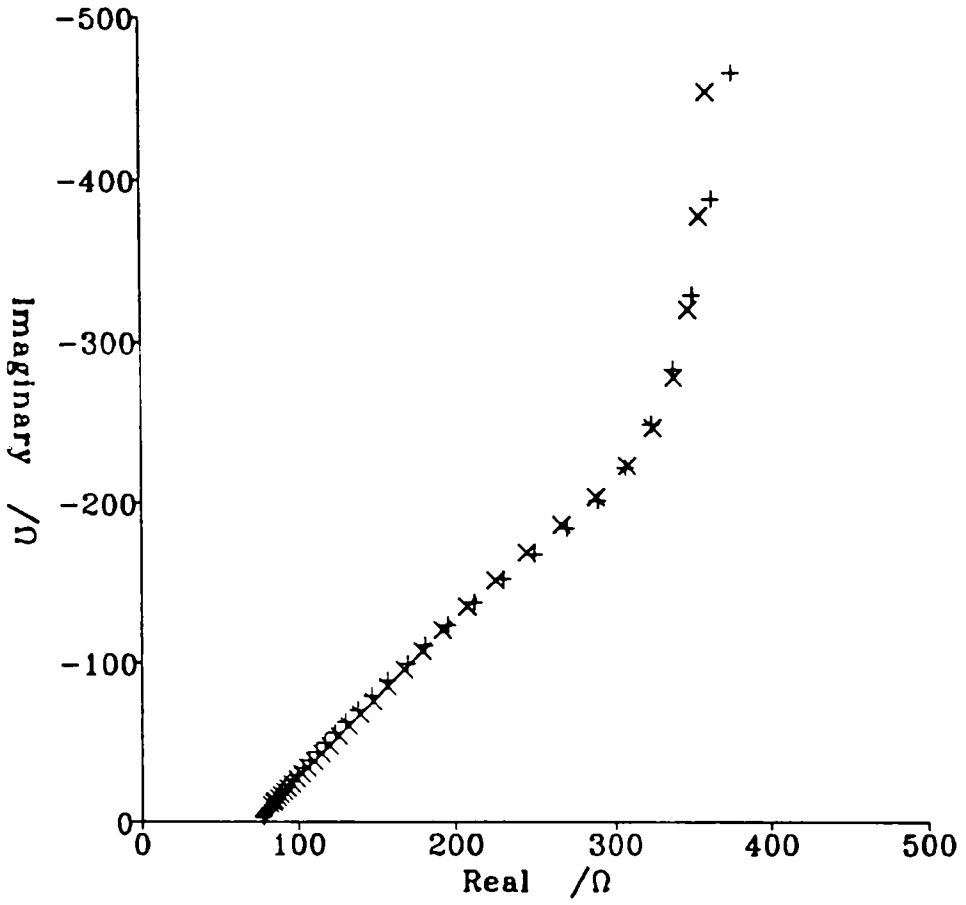

Figure 6.27a. Impedance plot showing the excellent agreement between data from the fully immersed scaled tube of length 7 cm (+) *and the simple transmission line model* (×) *with* $R^{\dagger}$ = 125.7 Ω cm^{-1} *and* $C^{\dagger}$ = 27.4 μF cm^{-1}. *(Experiment 4 in Table 6.2).*

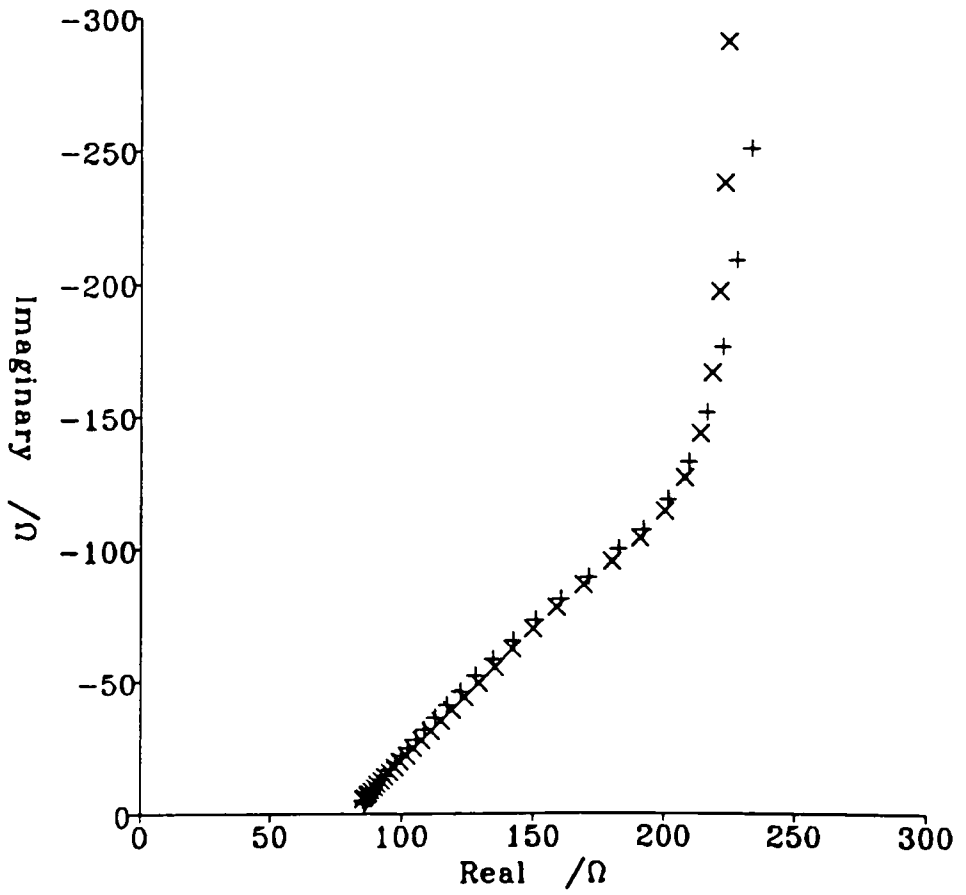

Figure 6.27b. Impedance plot showing the excellent agreement between data from the fully immersed scaled tube of length 3.5 cm (+) *and the simple transmission line model* (×) *with* $R^{\dagger}$ = 125.7 Ω cm^{-1} *and* $C^{\dagger}$ = 26.0 μF cm^{-1}. *(Experiment 7 in Table 6.2).*

Only for the simple RC transmission line is $Z'_{\lim \omega \to 0}$ and C proportional to the tube length. Equation (6.33) was found to give excellent agreement with these experiments, as shown in Figure 6.27, where l was equal to the tube length, $R^\dagger$ = 124 Ω cm^{-1} and $C^\dagger$ = 25.4 μF cm^{-1}. Here $R^\dagger$ represents the resistance of scale and solution together, per unit length of the tube.

It has been shown above that the a.c. response of a fully immersed scaled tube can be modelled by a simple RC transmission line. This model will now be extended to rationalise the behaviour of the partially immersed tube.

6.5.2.4 *Bipartite transmission line*

The data shown in Figure 6.19 demonstrated that the total transmission line resistance, R_{tml}, increased slightly as the immersion depth decreased. This is to be expected since the resistance of the wetted scale alone, R_{so}, is greater than that for solution and scale "in parallel", R_{ss}. This was modelled using the SPICE program

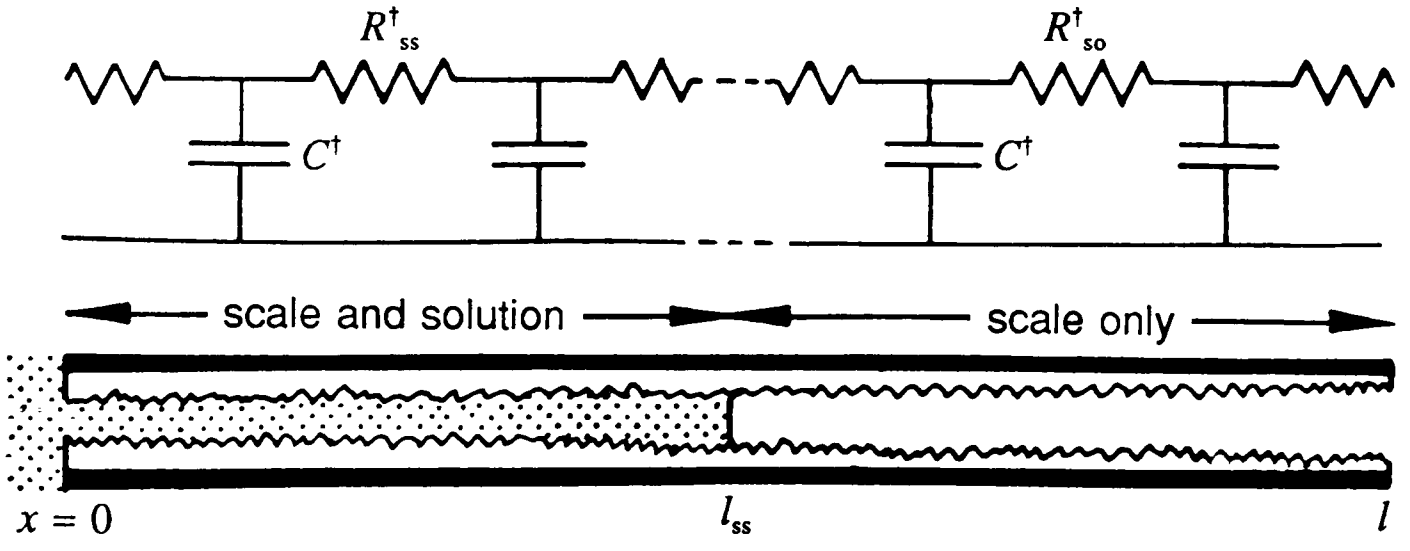

Figure 6.28. Bipartite transmission line circuit.

with a transmission line, but instead of a constant resistance per unit length, the value of $R^\dagger$ altered after a distance corresponding to the immersion depth (see Figure 6.28). The model transmission line was constructed using 100 resistors and capacitors per centimetre. An analytical expression for the impedance of this

circuit was also derived (see Appendix 6) and this gave perfect agreement with the SPICE program.

A mean value of $R^{\dagger}_{ss}$ = 124 Ω cm^{-1} was obtained from the fully immersed experimental data, as was $C^{\dagger}$ = 25.4 μF cm^{-1}. The value of $R^{\dagger}_{so}$ found to fit the experimental data is shown in Table 6.2 and it gave excellent fits with the impedance curves, as shown in Figure 6.29, thus validating the bipartite transmission line model.

Table 6.2. Experimental Parameters from Transmission Line Models

Expt.	Immersion	Transmission Line	R_u /Ω	$R^{\dagger}_{ss}$ /Ωcm^{-1}	l_{ss} /cm	$R^{\dagger}_{so}$ /Ωcm^{-1}	l_{so} /cm	$C^{\dagger}$ /μFcm^{-1}
1	full	simple	99	120	14.5	-	-	22.8
2	partial	bipartite	91	124	4.0	300	10.5	25.4
3	partial	bipartite	96	124	1.0	300	13.5	25.4
4	full	simple	72	125.7	7.0	-	-	27.4
5	partial	bipartite	75	124	4.0	250	3.0	25.4
6	partial	bipartite	77	124	1.0	250	6	25.4
7	full	simple	80	125.7	3.5	-	-	26.0

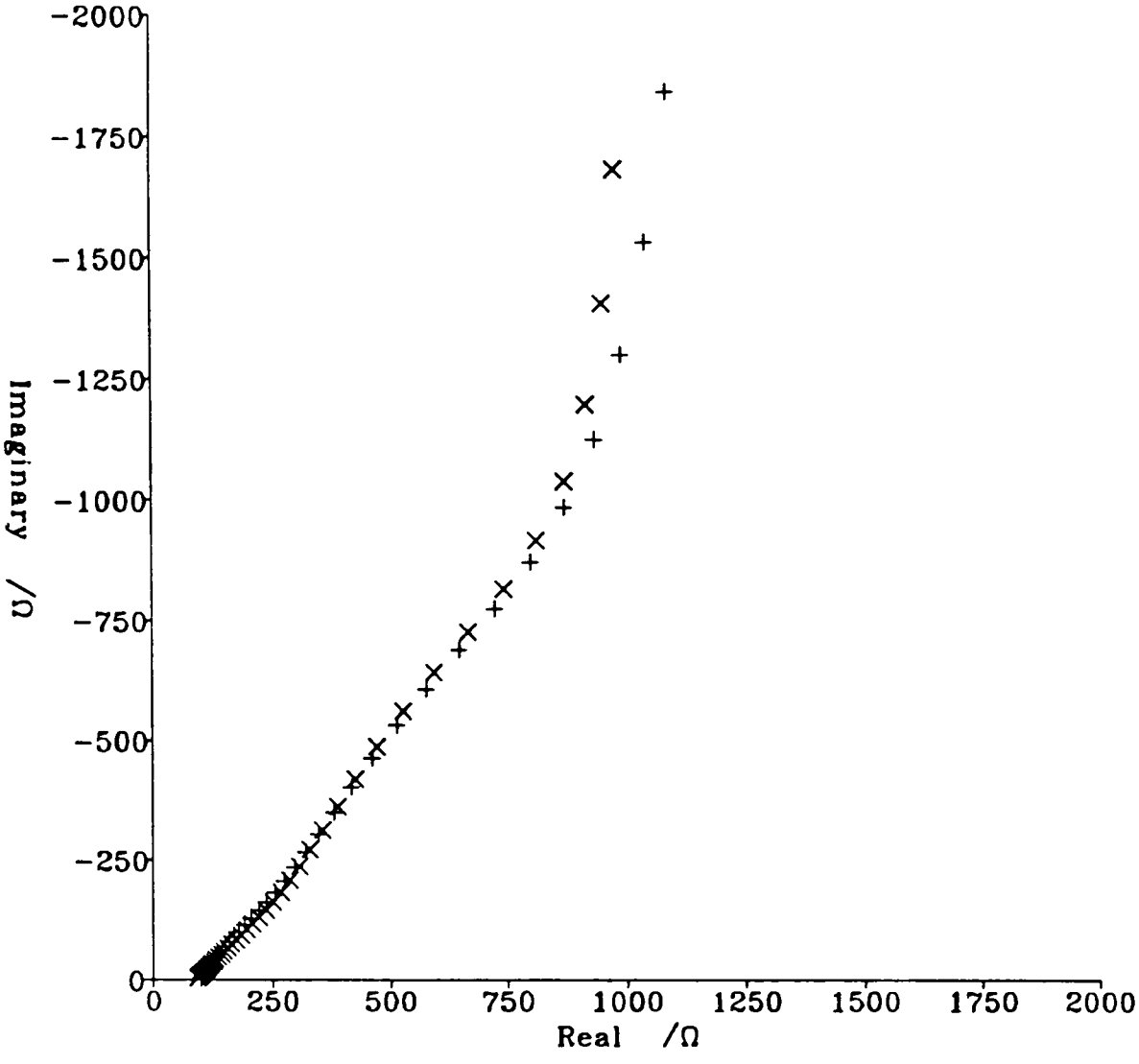

Figure 6.29a. Impedance plot showing the excellent agreement between data from the scaled tube of length 14.5 cm *immersed to a depth of* 4 cm (+) *and the bipartite transmission line model* (×) *with* $R^{\dagger}_{ss}$ = 124 Ω cm^{-1}, $R^{\dagger}_{\infty}$ = 300 Ω cm^{-1} *and* $C^{\dagger}$ = 25.4 μF cm^{-1}. *(Experiment 2 in Table 6.2).*

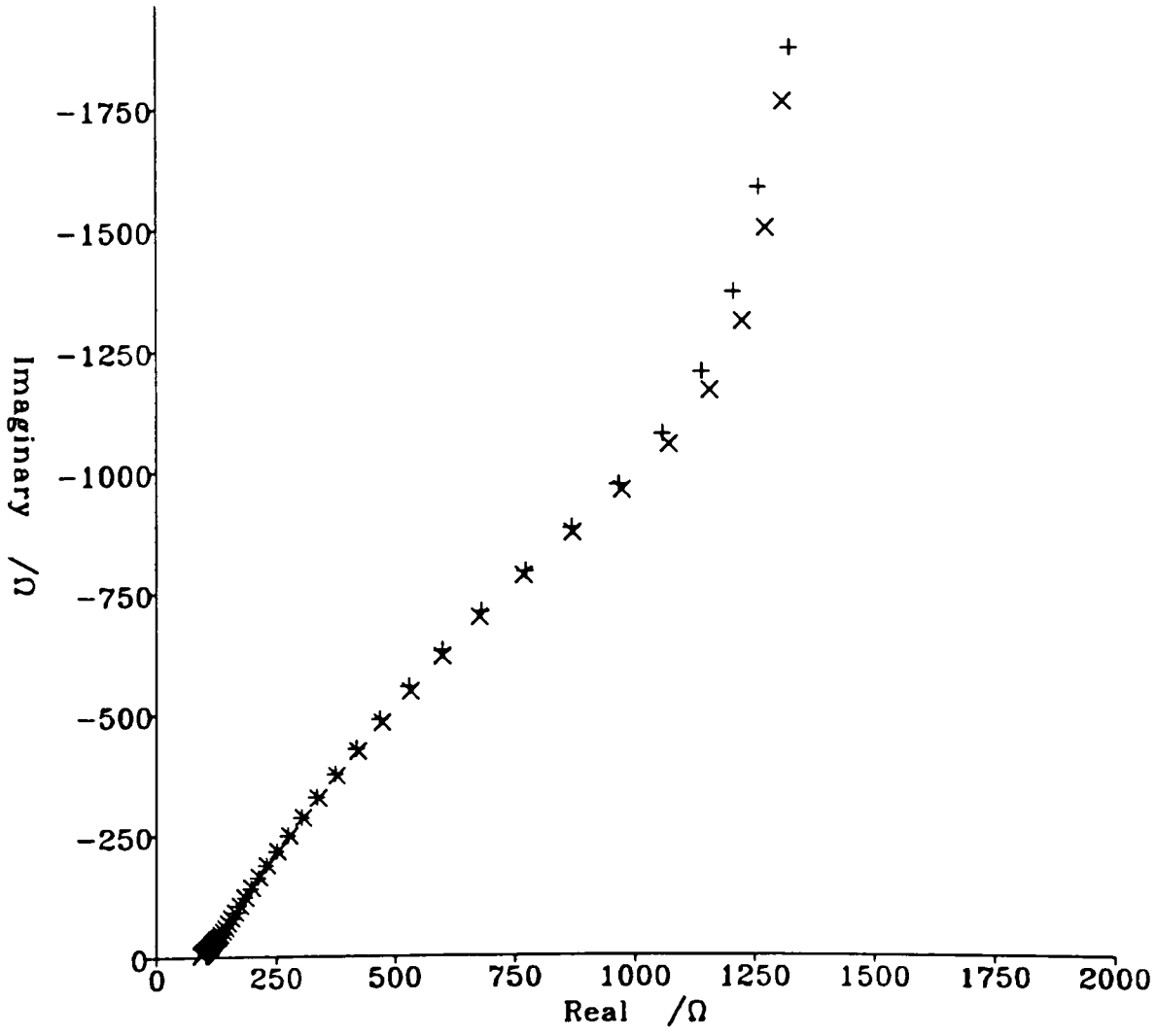

Figure 6.29b. Impedance plot showing the excellent agreement between data from the scaled tube of length 14.5 cm *immersed to a depth of* 1 cm (+) *and the bipartite transmission line model* (×) *with* $R^{\dagger}_{ss}$ = 124 Ω cm^{-1}, $R^{\dagger}_{\infty}$ = 300 Ω cm^{-1} *and* $C^{\dagger}$ = 25.4 μF cm^{-1}. *(Experiment 3 in Table 6.2).*

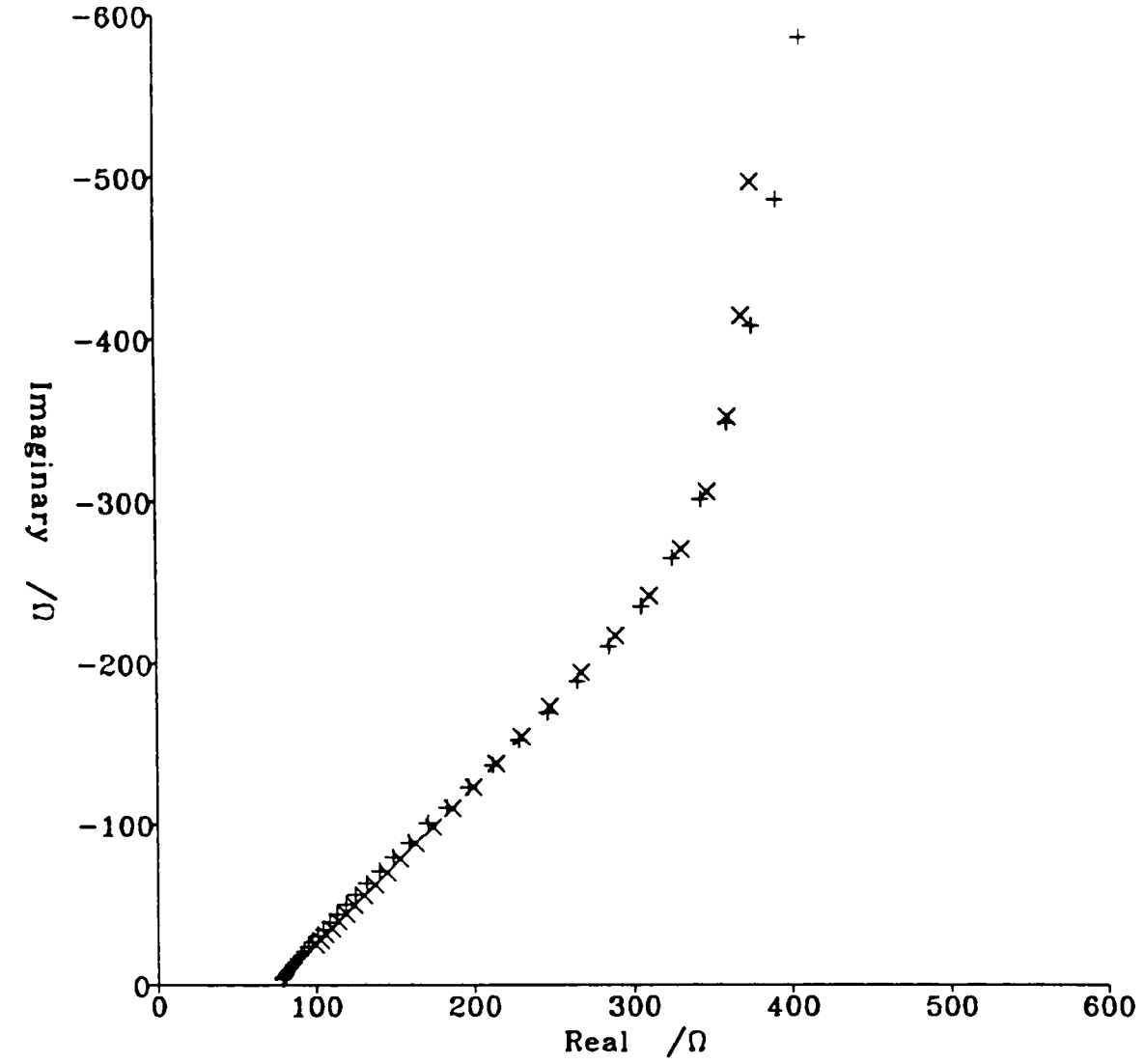

Figure 6.29c. Impedance plot showing the excellent agreement between data from the scaled tube of length 7 cm immersed to a depth of 4 cm (+) and the bipartite transmission line model (×) with $R^{\dagger}_{ss} = 124\ \Omega\ cm^{-1}$, $R^{\dagger}_{\infty} = 250\ \Omega\ cm^{-1}$ *and* $C^{\dagger} = 25.4\ \mu F\ cm^{-1}$. *(Experiment 5 in Table 6.2).*

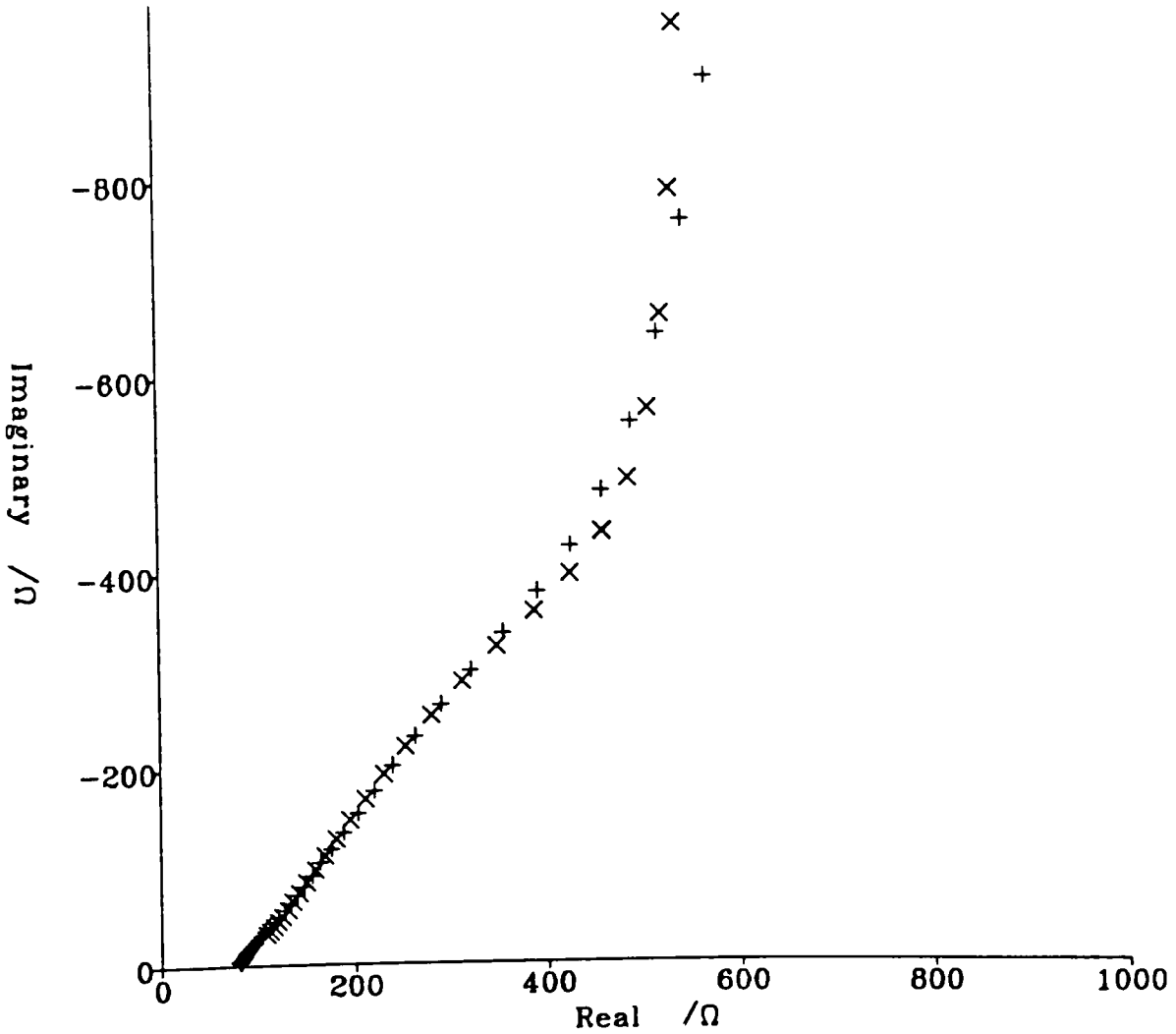

Figure 6.29d. Impedance plot showing the excellent agreement between data from the scaled tube of length 7 cm immersed to a depth of 1 cm (+) and the bipartite transmission line model (×) with $R^{\dagger}_{ss} = 124\ \Omega\ cm^{-1}$, $R^{\dagger}_{\infty} = 250\ \Omega\ cm^{-1}$ *and* $C^{\dagger} = 25.4\ \mu F\ cm^{-1}$. *(Experiment 6 in Table 6.2).*

The scale resistance $R^{\dagger}_{so}$ obtained from the partial immersion experiments was compared to that estimated from the complete immersion data as follows. The thickness of the scale layer was measured at the mouth of each section of tube using a travelling microscope and hence, a mean scale thickness was calculated for each tube length used (Table 6.1). Given the conductivity of the electrolyte [180], the resistance per unit length of the solution was calculated (198 Ω cm^{-1} for the 14.5 cm tube and 237 Ω cm^{-1} for the 7 cm tube). Assuming the resistance of the solution and that of the scale can be treated as parallel resistors (to give the measured value of $R^{\dagger}_{ss}$), the resistance of the "scale only resistor" was estimated to be 305 Ω cm^{-1} for the 14.5 cm tube and 268 Ω cm^{-1} for the 7 cm tube. This is in excellent agreement with the $R^{\dagger}_{so}$ values from the bipartite transmission line model, which are 300 Ω cm^{-1} and 250 Ω cm^{-1}, respectively. This difference in the mean scale thickness explains the difference in $R^{\dagger}_{so}$ for the two lengths of tube.

Further evidence to confirm this model was obtained by altering the electrode configuration. The reference electrode, a silver wire electro-coated in AgBr, was sited inside the scaled tube to negate any transmission line effects. Both this and the scaled electrode were 3.5 cm long and were immersed in a solution containing 3 mM $Ca(NO_3)_2$, 3 mM K_2CO_3, $\approx$1 mM KBr and 0.513 M KNO_3. The electrodes were used in a 2-electrode configuration so that both the current and potential applied did not experience a transmission line. The impedance plot from this experiment was capacitative (though slightly curved) with a series resistance of 9 Ω . Calculation using the resistivities of the solution and of the scale gave an expected resistance of about 2 Ω.

6.6 Conclusions

The equivalent circuit for the unscaled tube is a simple open-ended (reflective) transmission line where the resistors correspond to the solution resistance inside the tube and the capacitors correspond to the double-layer capacitance at the solution-metal interface.

It has been shown that the impedance of a heavily scaled tube can also be modelled by a transmission line, the resistance of which being a combination of the electrolyte resistance in free solution and that in the pores of the calcium carbonate scale. The molar conductivity of 0.5 M KNO_3 in the scale pores (Λ = 55.7 ± 1.2 S cm^2 mol^{-1}) is much less than that in free solution (Λ = 89.24 S cm^2 mol^{-1} [180]). A.c. impedance techniques could therefore be used in control systems to monitor *in-situ* the build up of calcium carbonate scales in pipework and if necessary shut down the process on attainment of critical scale levels.

CHAPTER 7

DISSOLUTION KINETICS VIA THE ELECTROCHEMICAL PARTICLE SIZING OF CALCIUM CARBONATE

7.1 Introduction

The presence of suspended non-conducting particles in a solution may cause increased mass transfer to a hydrodynamic electrode [186-197]. It has been proposed [186-192] that this increase in mass transfer is due to a decrease in the diffusion layer thickness, caused by a rotation of the particles in this layer. The increased mass transport has been shown to be proportional to the volume fraction of the suspended particles [186,194].

In this chapter, this phenomenon has been utilised as a novel technique for monitoring the change in particle size as a suspension of calcium carbonate powder dissolves. The rotating disc electrode (RDE) and its hydrodynamics will be discussed. An expression, proposed by Sonneveld *et al.* [186], will be derived for the increased limiting current due to the particles. This will be developed further to enable the effective particle size to be calculated from current measurements and hence, permit changes in particle size to be monitored. Results from experiments using calcium carbonate particles will be reported and the application of this technique to extracting kinetic information on the dissolution process will be discussed.

The enhancement of mass transfer by solid particles has been studied using a variety of hydrodynamic techniques, though mainly rotating disc electrodes [186,193-195] (see Section 7.2.1) and tubular electrodes [188-191,196, 197]. The variety of particles used has been extensive, though none have used this technique

to monitor the change of particle size. The only study using $CaCO_3$ particles was by Zeilmaker and Barendrecht [193], who simply demonstrated that the particles increased the limiting currents at an RDE. An RDE was also used to investigate this effect with suspensions of Al_2O_3, boron carbide, SiC [194] and glass spheres [195]. Tubular laminar flow cells have been used to study red blood cell suspensions [188-190], glass spheres [196] and sand suspensions [191,197]. Sonneveld *et al.* [186] investigated the effect of carborundum particles on the mass transport to the RDE. SiC particles have also been used to study the enhanced mass transfer at a rotating cylinder electrode [192].

Threshold or critical values for the volume fraction and rotation speed (of an RDE) were observed in certain cases [186,194], below these values the particles had no effect on the rate of mass transport. It has been concluded [186] that the critical volume fraction was an effect of gravity and particle size. Below this volume fraction the upward forces acting on the particles were not sufficient to overcome gravity to bring the particles within the diffusion layer. The critical rotation speed was found to be inversely proportional to the particle radius, which was thought to imply a certain critical velocity required at the particle edge [186].

7.2 Theory

7.2.1 The Rotating Disc Electrode

The rotating disc electrode (RDE) is a very widely used hydrodynamic electrode. It consists of a disc of metal, whose face is the electrode surface, surrounded by a flush insulating sheath. The electrode is rotated about the axis perpendicular to the surface. This motion sets up forced convection; solution is

drawn up towards the electrode surface, then spun round and thrown out laterally, see Figure 7.1.

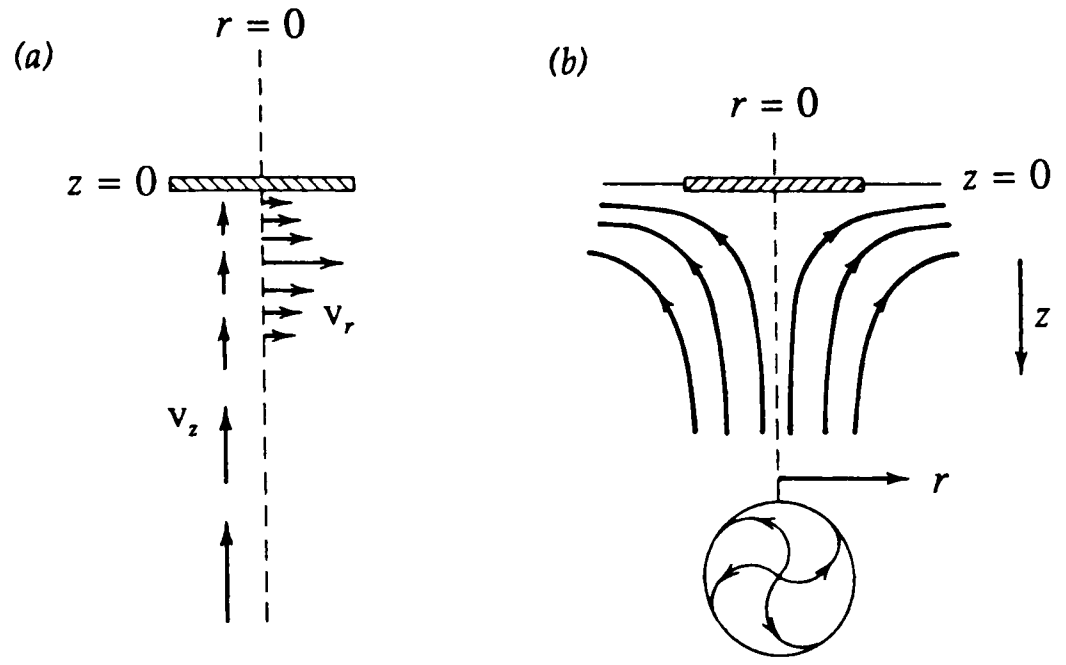

Figure 7.1. Schematic diagram showing the flow of solution at the rotating disc electrode, (a) in vector form showing the solution velocities and (b) as streamlines [175].

The expression for the mass transport limited current at the RDE will be discussed next.

7.2.1.1 *The Levich Equation*

The mass transport equation for the RDE was solved by Levich [198], who rewrote the convective-diffusion equation (1.13) in cylindrical polar co-ordinates (Figure 7.2) because of the symmetry of the problem. Thus

$$\frac{\partial c}{\partial t} = D\left(\frac{\partial^2 c}{\partial z^2} + \frac{\partial^2 c}{\partial r^2} + \frac{1}{r}\frac{\partial c}{\partial r} + \frac{1}{r^2}\frac{\partial^2 c}{\partial \theta^2}\right) - \left(v_r\frac{\partial c}{\partial r} + \frac{v_\theta}{r}\frac{\partial c}{\partial \theta} + v_z\frac{\partial c}{\partial z}\right) \qquad (7.1)$$

This can be simplified considerably. Due to the symmetry of the system, c is independent of θ so

$$\frac{\partial c}{\partial \theta} = \frac{\partial^2 c}{\partial \theta^2} = 0 \qquad (7.2)$$

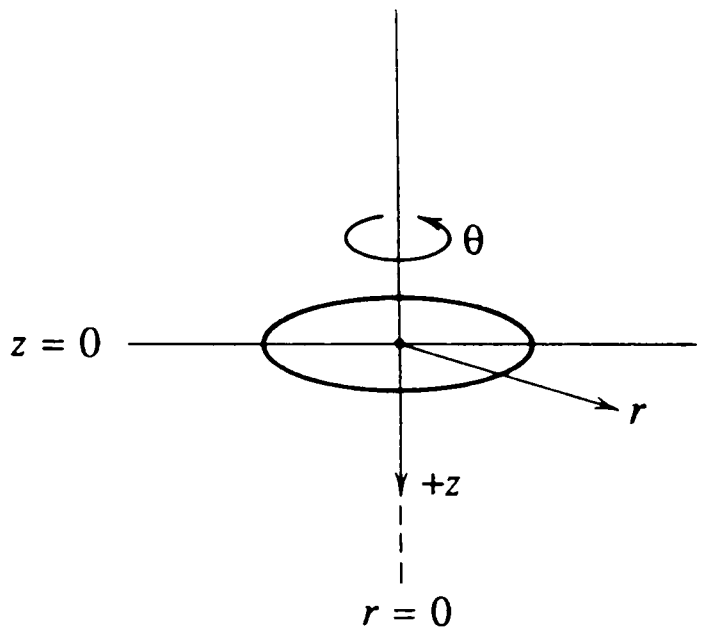

Figure 7.2. Cylindrical coordinates used for solving the convective-diffusion equation at the rotating disc electrode.

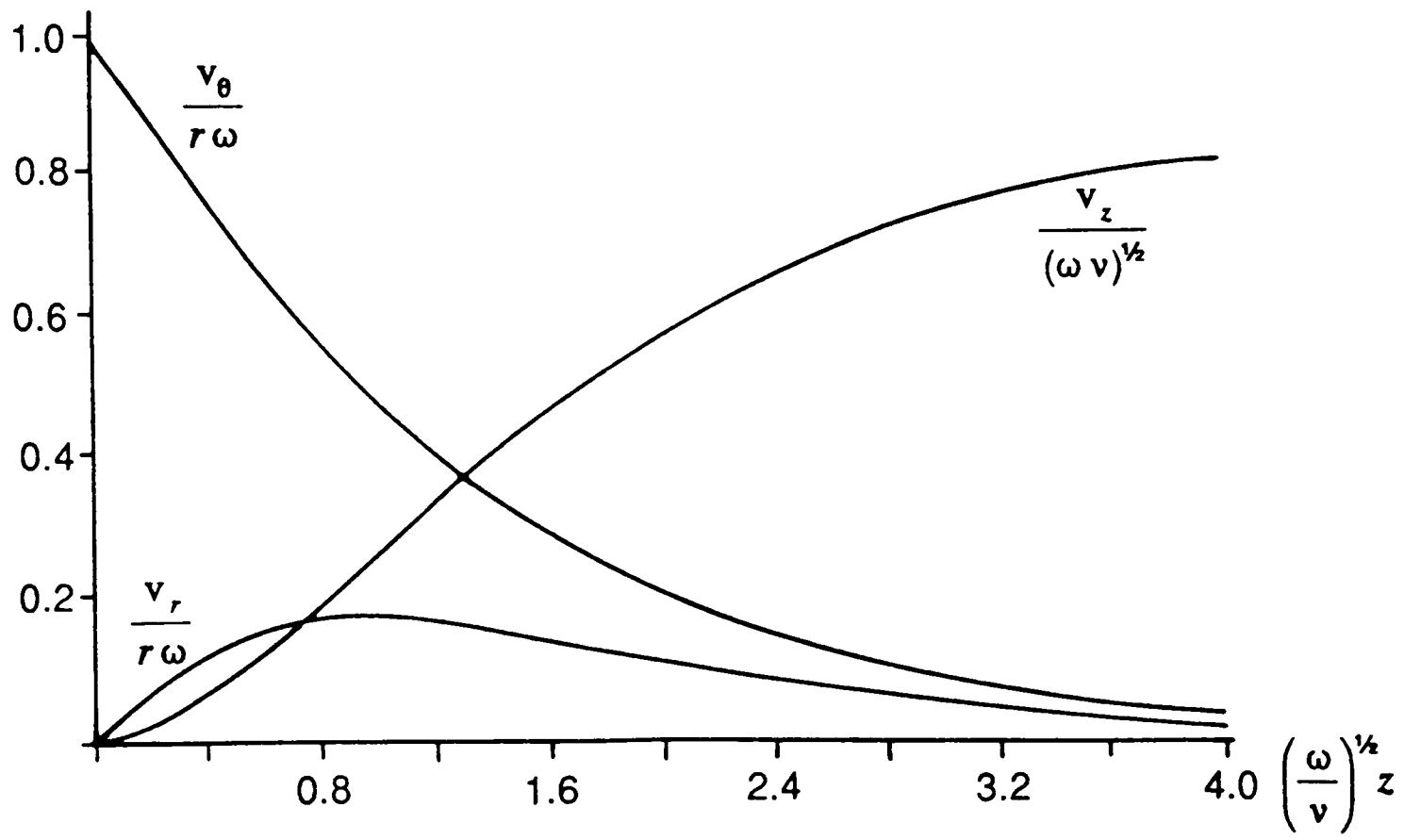

Figure 7.3. Velocity profiles along the three cylindrical coordinates for the rotating disc electrode. The functions plotted are dimensionless.

Provided the radius of the sheath is much greater than that of the electrode, v_z will be independent of r, and at $z = 0$ $(\partial c/\partial r) = 0$, hence across the electrode face

$$\frac{\partial c}{\partial r} - \frac{\partial^2 c}{\partial r^2} - 0 \qquad (7.3)$$

Applying these simplifications at steady state, equation (7.1) becomes

$$v_z \frac{\partial c}{\partial z} = D \frac{\partial^2 c}{\partial z^2} \tag{7.4}$$

The velocity profile for the RDE as a function of z is shown in Figure 7.3. Using an expression for v_z [198] and applying the appropriate boundary conditions, equation (7.4) can be solved [198,199] to give the Levich equation;

$$I_{lim}/A = 0.62048 nFA c_{bulk} D^{\frac{2}{3}} \nu^{-\frac{1}{6}} \omega^{\frac{1}{2}} \tag{7.5}$$

or

$$I_{lim}/A = 1.5553 nFA c_{bulk} D^{\frac{2}{3}} \nu^{-\frac{1}{6}} f^{\frac{1}{2}} \tag{7.6}$$

where A is the electrode area (cm^2), c_{bulk} the bulk concentration (mol cm^{-3}) of the electroactive species, ω is the angular velocity (rad s^{-1}) and f is the frequency of rotation (rev s^{-1} or Hz) of the RDE.

7.2.2 Explanation for Enhanced Mass Transport due to Particles

On adding particles to the rotating disc system, the mass transport to the electrode is enhanced. This effect is not due to the onset of turbulence, as can be shown by the value of the Reynolds number. For an RDE with radius r_E this is given by

$$Re = \frac{2\omega r_E^2}{\nu} \tag{7.7}$$

For r_E = 0.35 cm and a rotation frequency f = 36 Hz, Re is 6200, which is well within the laminar flow region ($Re < 10^5$) [200]. The addition of particles to the system will increase the viscosity and hence only reduce the Reynolds number. The fluid flow round a particle is given by another Reynolds number

$$Re = \frac{2\omega_p a^2}{\nu} \tag{7.8}$$

where ω_p is the angular velocity of the particle with radius a. This has the order of unity for a 4 μm radius particle and so Stokes flow applies around the particles.

A few explanations for this enhanced mass transfer have been proposed. One suggests a blockage of the electrode by the particles, such that the electrode surface is roughened, thus affecting the mass transport [195]. Now, however, the most widely accepted model used to explain this phenomenon involves the rotation of the particles in the diffusion layer. The rotation of the particles arises from the shear forces at the viscous boundary layer. The increased mass transport has been expressed in terms of an effective diffusion coefficient [187-190,201], which is the sum of the normal molecular diffusion coefficient and a term which originates from the stirring effect of the rotating particles. Caprani *et al.* [187] predicted a linear I_{lim} versus ω^n response for the RDE, where n = 7/6 at high rotation speeds and n = 1/2 at low rotation speeds. However they [187] found n to be 0.5 experimentally at low and at high rotation rates. Sonneveld *et al.* [186] also found n to be 0.5 with SiC particles at the RDE and developed a model predicting this I_{lim} - $\omega^{1/2}$ response. This is outlined below.

Figure 7.1a shows the flow pattern perpendicular to the electrode axis (z-axis). Close to the electrode there is a shear rate (dv_r/dz) which, due to viscous forces, induces rotation of the particles in this region. For particles of radius smaller than 20 μm, particle densities of 3 g cm^{-3} and dynamic viscosity of 0.012 g s^{-1} cm^{-1}, it can be shown [186] that the particles accelerate up to the angular rotation frequency of the solution in less than 10 μs after entry. This rotation of the

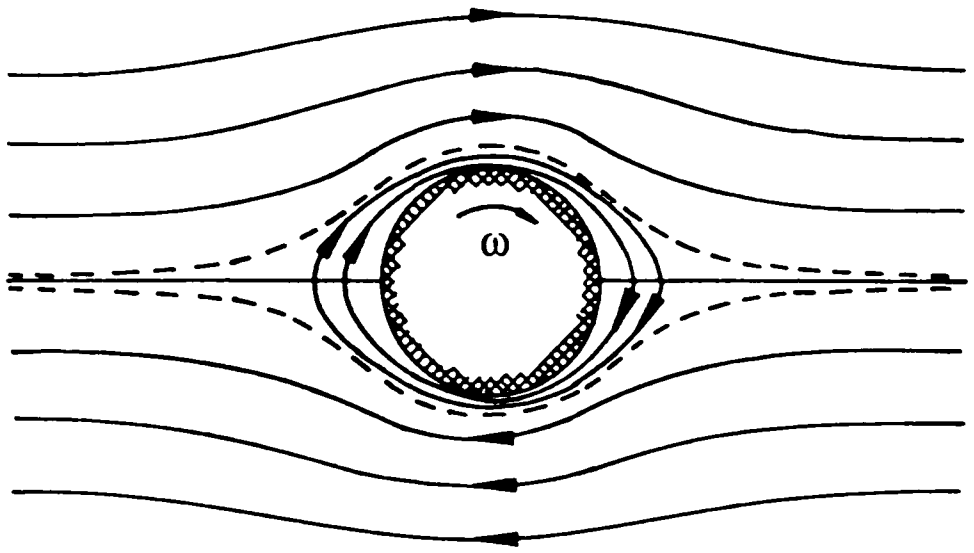

Figure 7.4. Schematic diagram of the flow pattern around a particle close to the RDE. The flow directions are shown relative to the particle. The dashed lines depict the boundary of the domain of closed streamlines, where the solution is well mixed.

particles produces an additional solution velocity component, which contributes to extra mass transport to the electrode. This results in the flow pattern [202] around the particles as depicted in Figure 7.4. Surrounding the particle is a region of closed streamlines, where the solution is well mixed. The volume of this closed region will be small, since this rotational velocity decreases as $1/r^5$ [186]. In the electrode diffusion layer (where a concentration gradient exists) an average reactant concentration is assumed within this closed streamline zone. This therefore gives rise to a local decrease in the diffusion layer thickness.

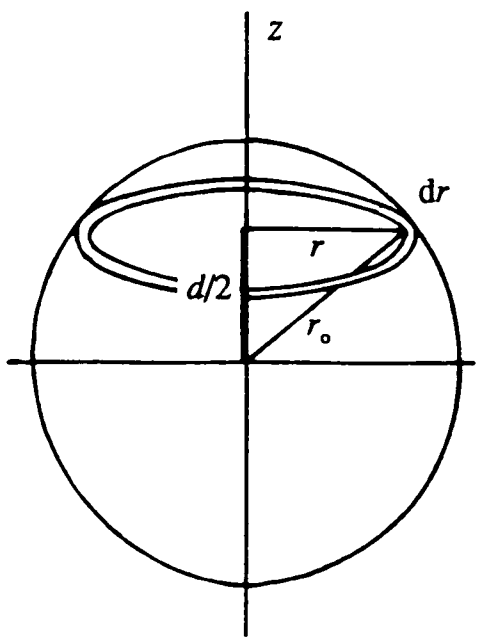

Figure 7.5. Diagram depicting the sphere of solution of radius r_0 around a particle which is well mixed. This gives rise to a local decrease, d, in the diffusion layer thickness.

The magnitude of this reduction, d, depends on the distance, r, away from the z-axis of the particle, shown in Figure 7.5. The distance r_o represents the distance from the centre of the particle to the boundary of the closed streamlines. At distances greater than r_o there is no enhancement of mass transport. Thus the average reduction, $\langle d \rangle$, of the diffusion layer by this film around a particle is given by

$$\langle d \rangle = \frac{\int_0^{r_o} d 2\pi r dr}{\int_0^{r_o} 2\pi r dr} = \frac{4\pi \int_0^{r_o} \left(r_0^2 - r^2\right)^{1/2} r dr}{2\pi \int_0^{r_o} r dr} = \frac{4r_o}{3} \tag{7.9}$$

The average reduction in the diffusion layer thickness for N_δ particles in this layer is

$$\Delta\delta = \frac{4r_o}{3}\frac{A_p N_\delta}{A} = \frac{4r_o^3 N_\delta}{3r_E^2} \tag{7.10}$$

where the area of the electrode $A = \pi r_E^2$ and the effective cross sectional area of a particle $A_p = \pi r_o^2$. The volume fraction of the particles is defined by

$$\phi = \frac{V_p}{V_p + V_s} \tag{7.11}$$

where V_p is the total particle volume and V_s is the solution volume. The number of particles in the diffusion layer, N_δ, is therefore given by

$$N_\delta = \frac{m_\delta}{m_p} = \frac{V_\delta V_p / V_s}{\frac{4}{3}\pi a^3} = \frac{V_\delta \phi}{\frac{4}{3}\pi a^3 (1 - \phi)} \tag{7.12}$$

where m_δ is the total mass of all the particles in the diffusion layer and m_p the mass of one particle. The volume of the diffusion layer, V_δ, is

$$V_\delta = \pi r_E^2 \delta (1 - \phi) \tag{7.13}$$

thus

$$N_\delta = \frac{3\phi r_E^2 \delta}{4a^3} \tag{7.14}$$

Substituting equation (7.14) into equation (7.10) gives the relative decrease in the diffusion layer thickness

$$\frac{\Delta\delta}{\delta} = \left(\frac{r_o}{a}\right)^3 \phi \tag{7.15}$$

The limiting current at an electrode is

$$I_{lim} = nFAJ_{lim} \tag{7.16}$$

The limiting flux, J_{lim}, expressed in terms of diffusion layer thickness, is given by equation (2.2), so

$$I_{lim} = \frac{nFADc_{bulk}}{\delta} \tag{7.17}$$

Thus the limiting current is inversely proportional to the diffusion layer thickness.

Equation (7.5) for the limiting current at an RDE can be abbreviated for clarity as

$$I_{lim} = B\omega^{1/2} \tag{7.18}$$

where

$$B = 0.62nFAc_{bulk}D^{\frac{2}{3}}\nu^{-\frac{1}{6}} \tag{7.19}$$

The enhanced mass transport due to the particles' rotation will now be introduced. The particles reduce the diffusion layer thickness to $\delta - \Delta\delta$, thus from equations (7.17) and (7.18)

$$I_{lim} = \frac{B\omega^{1/2}}{1 - \frac{\Delta\delta}{\delta}} \tag{7.20}$$

Substituting equation (7.15) yields

$$I_{lim} = \frac{B\omega^{1/2}}{\left\{1 - \left(\frac{r_o}{a}\right)^3 \phi\right\}} \tag{7.21}$$

For small values of ϕ this can be expanded in a Taylor series (neglecting higher terms) to give

$$I_{lim} = B\omega^{1/2}\left\{1 + \left(\frac{r_o}{a}\right)^3 \phi\right\} \tag{7.22}$$

Thus the effect of the particles is to add an extra term to the Levich equation which depends on the volume fraction of the particles and the r_o/a ratio.

7.2.3 Dissolution of Particles

According to the model of Sonneveld *et al.* [186] given above, if the particles were to dissolve then their volume fraction would decrease, causing a reduction in the limiting current with time. The rate at which this reduction occurs would thus yield information on the dissolution kinetics of the particles.

If the particles dissolve with a flux J, then for N particles the rate at which they dissolve is given by

$$\frac{dn}{dt} \text{ /mol s}^{-1} = 4\pi a^2 N J \tag{7.23}$$

assuming spherical particles of uniform radius a. The amount (i.e. "moles") of particulate substance present, n, is

$$n = \frac{\frac{4}{3}\pi a^3 \rho N}{M} \tag{7.24}$$

where ρ is the density of the particulate material and M the molar mass. Differentiating equation (7.24) gives

$$\frac{dn}{da} = \frac{4\pi a^2 \rho N}{M} \tag{7.25}$$

Combining equations (7.23) and (7.25) yields

$$\frac{da}{dt} = \frac{JM}{\rho} \tag{7.26}$$

Thus the rate of change of the particle radius is directly proportional to the dissolution flux.

The total volume occupied by the particles is

$$V_p = \frac{4}{3}\pi a^3 N \tag{7.27}$$

which on combination with equation (7.11) gives

$$\left(\frac{r_o}{a}\right)^3 \phi = \frac{4N\pi r_o^3}{3(V_s + V_p)} \tag{7.28}$$

Substituting this into equation (7.22) yields

$$I_{lim} = B\omega^{1/2}\left(1 + \frac{4N\pi r_o^3}{3(V_s + V_p)}\right) \tag{7.29}$$

As the particles dissolve, both r_o and V_p will decrease. However for the small amounts of calcium carbonate used, neglecting V_p only introduces a 5% error. Thus for small values of ϕ

$$I_{lim} = B\omega^{1/2}\left(1 + \frac{4N\pi r_o^3}{3V_s}\right) \tag{7.30}$$

This equation enables the estimation of r_o from the limiting current measurements. As the particles dissolve, equation (7.30) allows the calculation of the rate of change of r_o. Assuming a constant ratio of r_o/a, this can be directly compared to the dissolution rate constant via equation (7.26).

7.2.4 Modelling

Equation (7.26) was used to calculate the rate at which the radius of the particles decreased, using the appropriate dissolution rate law. A FORTRAN 77 program, listed in Appendix 4, was used to simulate the dissolution of the particles. Account was made of the build up of the calcium carbonate dissolution products in solution and hence any reduction in the rate of reaction. Complete mixing was assumed throughout the solution.

7.3 Experimental

7.3.1 Rotating Disc Electrode Apparatus

The working electrode used was a platinum RDE (Oxford Electrodes) of diameter 0.703 cm, the potential of which was controlled, using an Oxford Electrodes potentiostat, relative to a saturated calomel reference electrode (Radiometer). A graphite rod, sited behind a glass sinter, acted as the counter electrode. Rotation speeds of 0 - 40 Hz were achieved using an Oxford Electrode motor and motor controller. Dissolved gases were removed by passing argon (BOC) through the solution, which was thermostatted at 25°C by means of a water jacket.

7.3.2 Choice of Electroactive Species

An electroactive species had to be chosen which gave good well defined reduction or oxidation waves but also did not adsorb on calcium carbonate or react with the Ca^{2+}, CO_3^{2-} or HCO_3^- ions produced. To test the suitability of possible electroactive species, visible absorption spectroscopy was used. Using a solution of the species under investigation, the magnitude of the absorption peaks were measured on a Perkin Elmer Lambda UV/VIS spectrometer. A check was made to

ensure that none of the species was lost due to adsorption onto the glassware or filter paper, before calcium carbonate powder (BDH, AnalaR) was added to the solution and the suspension stirred for an hour. After this time the undissolved calcium carbonate was removed by filtration (Whatman 42 ashless filter paper) and the absorption spectrum of the filtrate measured. If the magnitude of the absorption peaks were unchanged, no adsorption was deemed to have occurred. In this way both potassium ferricyanide and N,N,N',N'-tetramethyl-p-phenylenediamine (TMPD) were found to be suitable electroactive species. In the case of the former, a one electron reduction wave was obtained with an $E_{1/2}$ of +0.2 V (relative to SCE). For TMPD the first oxidation wave, whose $E_{1/2}$ = 0.0 V (relative to SCE), was used.

7.3.3 Particle Sizing

A particle size distribution of the calcium carbonate powder (AnalaR, BDH, Poole) used, was obtained using a laser light scattering technique, courtesy of Cookson Technology Centre, Yarnton, Oxon.

7.3.4 pH-Stat Apparatus

In order to maintain the solution at constant pH as the calcium carbonate dissolved, a "pH-stat" apparatus was used. A glass pH electrode monitored the pH of the bulk solution in the reaction vessel. The pH meter (Jenway 3030) was interfaced with a BBC Master microcomputer, using a purpose built circuit to adjust the output voltage range of the pH meter to between 0 and 1.8V, as required by the microcomputer's analogue to digital converter (ADC). The ADC output was calibrated using buffer solutions of known pH. A BASIC program was executed on the microcomputer which monitored the solution pH. If the pH rose above a

predetermined value, the microcomputer operated a compressed air valve, which injected a known volume of acid into the reaction vessel, and recorded the time at which the addition was made. In the experiments detailed below, the acid used was 1.00 M hydrochloric acid, together with the electroactive species at the same concentration as that in the reaction vessel (so as not to alter the latter's concentration).

7.3.5 Experimental Procedure

A 100 cm^3 solution of the appropriate electroactive species was prepared containing potassium chloride (0.5 M) as background electrolyte and the pH adjusted to the required pH using hydrochloric acid or potassium hydroxide, as appropriate. The solution was degassed for 30 minutes and allowed to reach thermal equilibrium at 25°C. Current-voltage curves were recorded on a chart recorder for various rotation rates, from which the transport limited currents were extracted as a function of rotation speed. These were analysed according to the Levich equation (7.5) by plotting I_{lim} versus $\sqrt{f}$.

A known mass of calcium carbonate powder was then added to the reaction vessel and current-voltage curves were recorded at high rotation speeds as a function of time. In "pH-stat" experiments the volume of acid added was also monitored, whereas in "free-drift" experiments the pH was monitored with time. A magnetic stirrer was also used where necessary to prevent any settling of the calcium carbonate powder.

7.4 Results

The particle size distribution for the batch of calcium carbonate powder used is shown in Figure 7.6. The surface area of the powder was 0.66 $m^2\ g^{-1}$ and the

Plate 11. Scanning electron micrograph of calcium carbonate powder. Magnification x628. *(Courtesy of Cookson Technology Centre).*

Plate 12. Scanning electron micrograph of calcium carbonate powder. Magnification x2040. *(Courtesy of Cookson Technology Centre).*

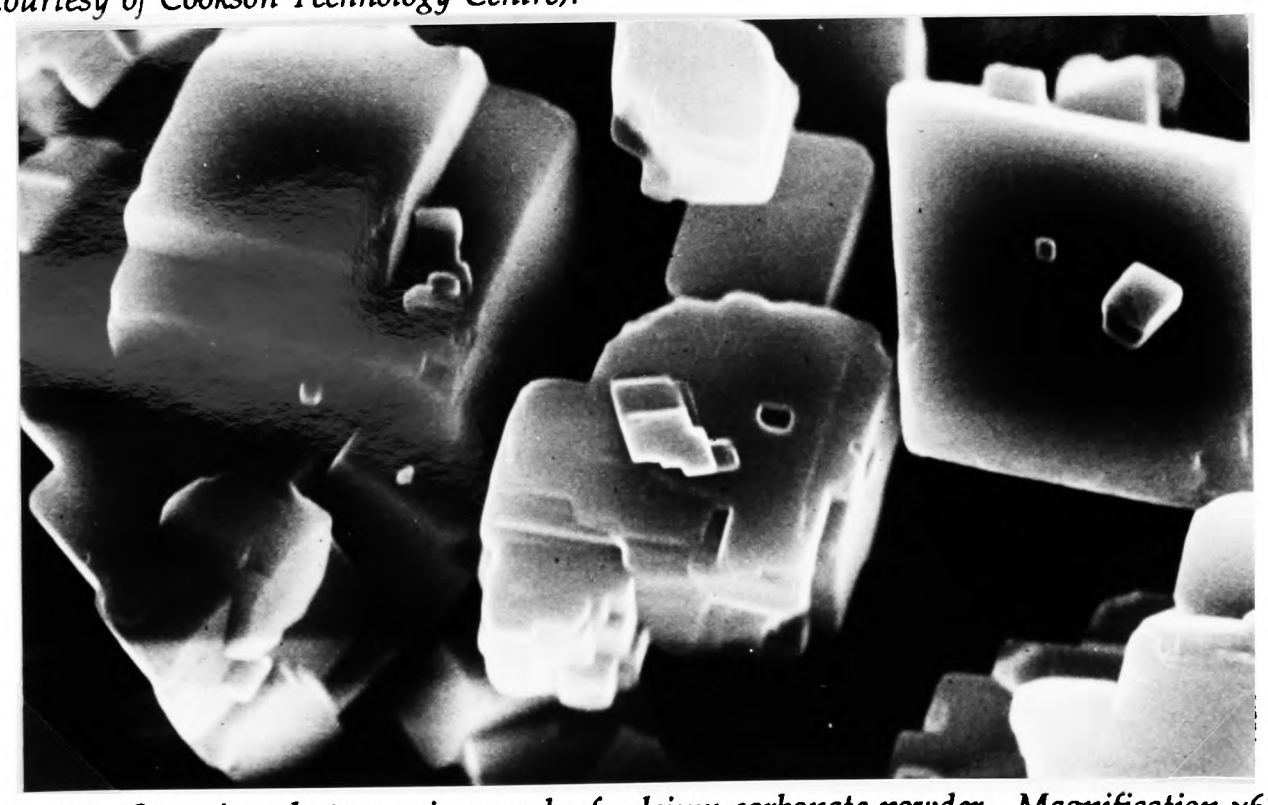

Plate 13. Scanning electron micrograph of calcium carbonate powder. Magnification x6370. *(Courtesy of Cookson Technology Centre).*

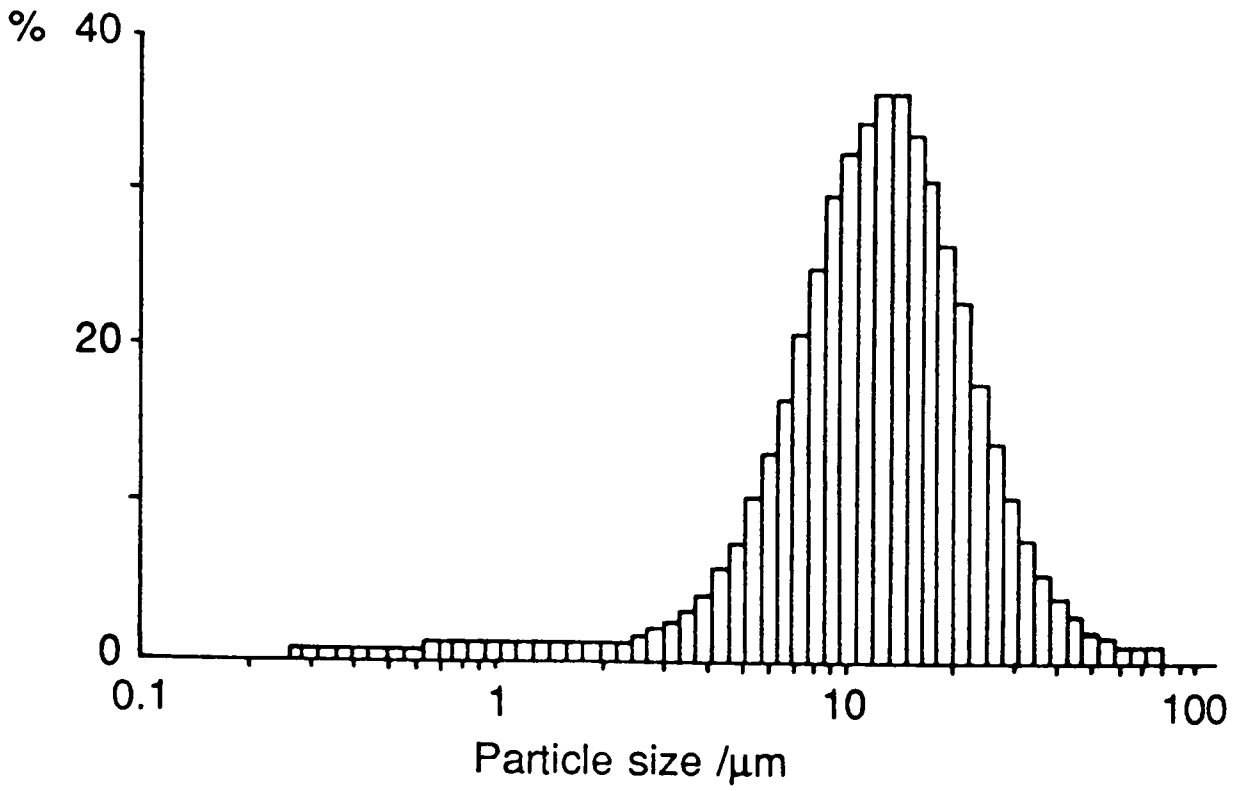

Figure 7.6. Size distribution of the calcium carbonate particles used. (Courtesy of Cookson Technology Centre, Yarnton, Oxon.).

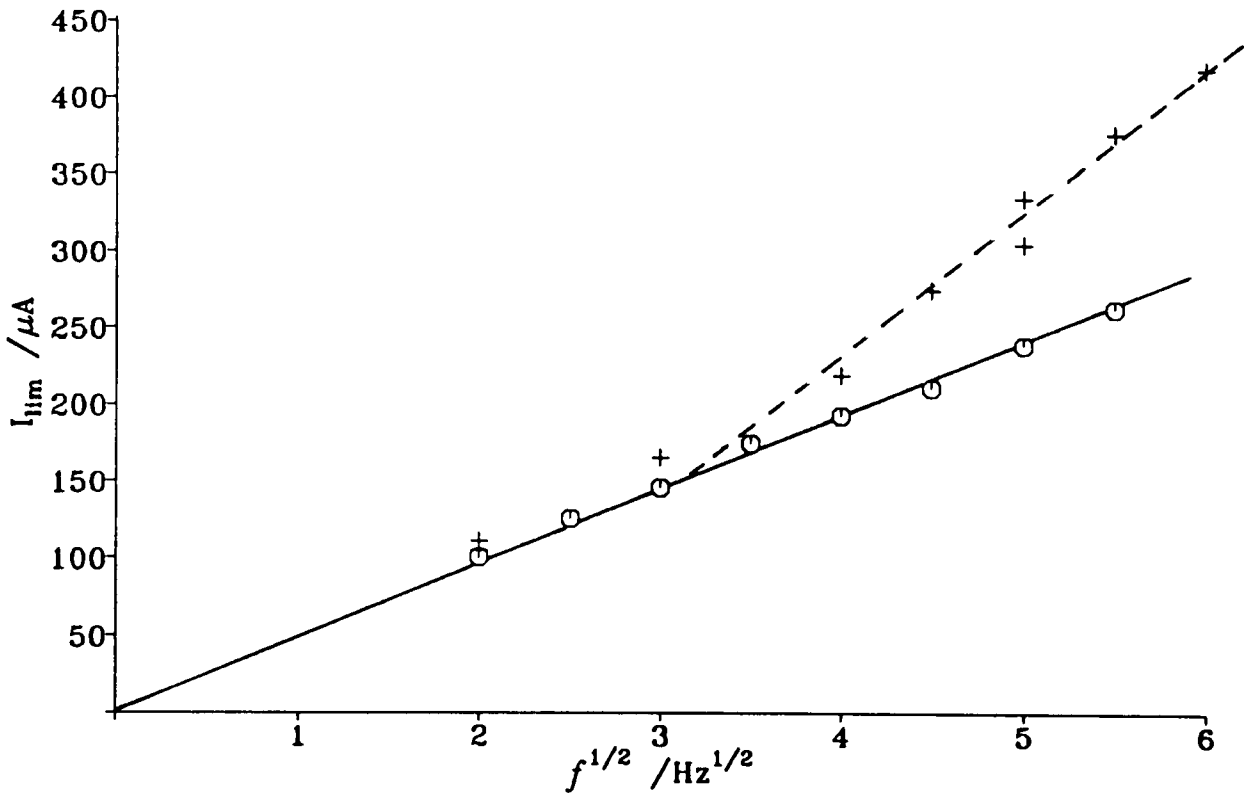

Figure 7.7. Plot of the limiting current at the RDE as a function of $\sqrt{f}$ with (+) and without (o) calcium carbonate particles present.

mean particle diameter was 12.17 μm. Scanning electron microscope photographs of the powder are shown in Plates 11-13.

The results from a preliminary experiment, using potassium ferricyanide as the electroactive species, are shown in Figure 7.7, in which the limiting current is plotted against $\sqrt{f}$ before and after the addition of calcium carbonate particles.

Without the particles the expected linear Levich behaviour (equation (7.6)) was obtained with a diffusion coefficient of 7.3×10^{-6} cm^2 s^{-1}, which was in excellent agreement with the literature value of 7.6×10^{-6} cm^2 s^{-1} [95]. After the addition of calcium carbonate, the values of I_{lim} verified the enhanced mass transport to the RDE due to the particles, and also showed the existence of a critical RDE rotation speed (in this case approximately 9 Hz) below which the enhanced transport was not seen, in agreement with Sonneveld *et al.* [186].

Particle dissolution experiments were carried out under three sets of conditions: pH 6, high pH and in the presence of maleic acid. These cases will be examined in turn.

7.4.1 Dissolution at pH 6

These experiments were carried out at the constant pH of 6.04 ± 0.05 using the pH-stat apparatus. The electroactive species used was N,N,N',N'-tetramethyl-p-phenylenediamine (TMPD) at a concentration of 5.01 mM. After the addition of

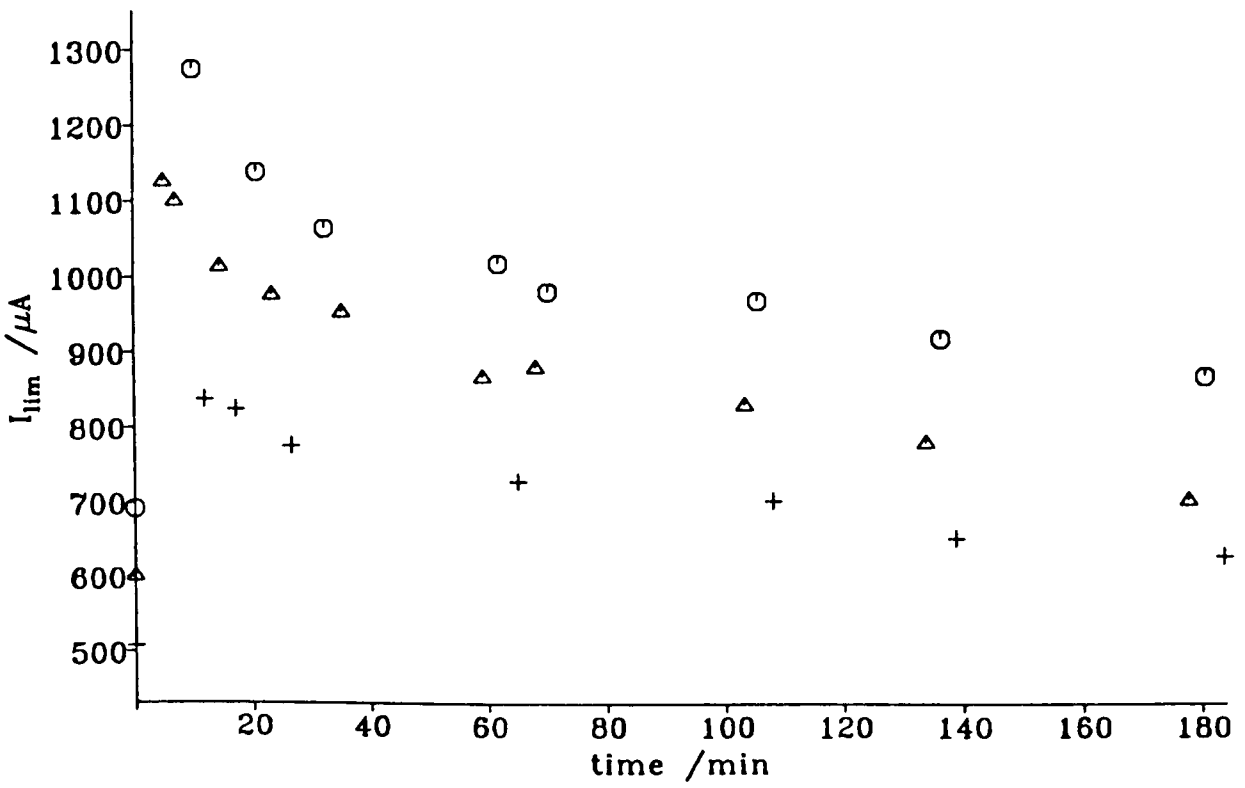

Figure 7.8. Plot of I_{lim} as a function of time at rotation rates of 36 Hz (o), 25 Hz (Δ) *and* 16 Hz (+) *for* 5.01 mM TMPD *in* 0.5 M KCl *at constant* pH = 6.04 ± 0.05, *initially with* 3.8 vol % $CaCO_3$ *particles present. The points at* $t = 0$ *are before the addition of* $CaCO_3$.

11.71 g of calcium carbonate, corresponding to ϕ = 3.8 vol %, the change in I_{lim} was monitored at 16, 25 and 36 Hz. The variation of I_{lim} with time is shown in Figure 7.8. This demonstrated the enhanced mass transport to the RDE by the particles and this decreased as the volume fraction of the particles decreased, due to dissolution. Taking into account the increase in solution volume with the addition of acid, the effective particle radius, r_o, was calculated using equation (7.30) and its variation with time plotted in Figure 7.9. This plot displayed two rates of change in r_o; initially 2.0×10^{-7} cm s^{-1}, then subsequently 3.1×10^{-8} cm s^{-1}.

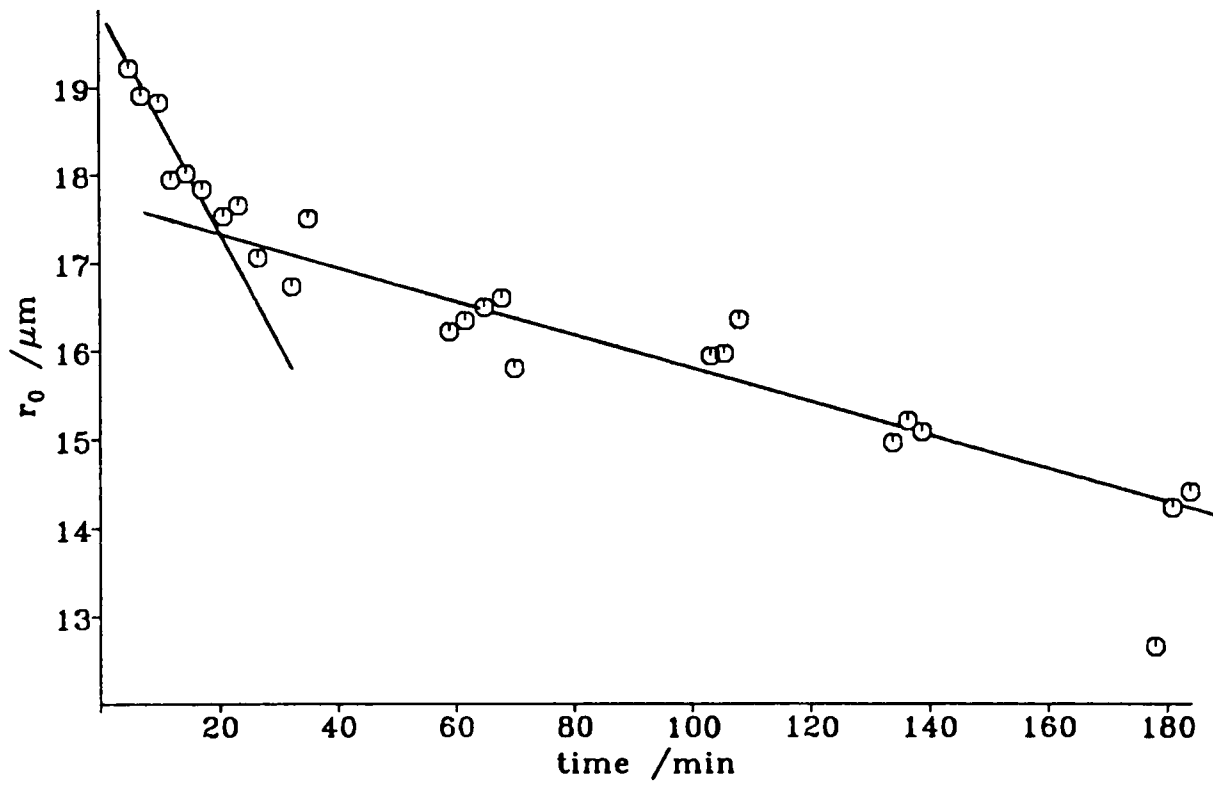

Figure 7.9. Plot of the effective particle radius, r_o, as a function of time for 5.01 mM TMPD *in* 0.5 M KCl *at constant* pH = 6.04 ± 0.05, *initially with* 3.8 vol % $CaCO_3$ *particles present.*

Converting this to the flux of dissolving calcium carbonate, using equation (7.26), yielded 5.9×10^{-9} mol cm^{-2} s^{-1} and 9.1×10^{-10} mol cm^{-2} s^{-1} respectively. Comparing this to the rate obtained from the single crystal calcite dissolution experiments in the channel (and to other particle dissolution/precipitation experiments [36,65]) showed that this value is some 7 - 15 times larger than expected. This discrepancy is likely to be due to the non-instantaneous mixing of the molar acid into the bulk solution, resulting in a localised region of low pH. In

such a region (pH < 4.5), the dissolution would be enhanced by a contribution from the heterogeneous reaction between H^+ and $CaCO_3$ [15].

7.4.2 Dissolution at High pH

To avoid the possibility of any contribution from the direct H^+ reaction, the experiments were repeated at higher pHs (i.e. greater than 7) and without the addition of any acid (i.e. "free drift" experiments). Monitoring the limiting current of the ferricyanide ion reduction over a long period of time (≈ 1 day) showed a slight increase in I_{lim} with time. This was due to the slight evaporation of water from the solution, therefore the experiments were repeated but with the suspension stirred inside a stoppered flask. At intervals, 100 cm^3 portions of the suspension were removed from the flask and transferred to the RDE apparatus, where the limiting current was measured as before. These experiments showed that there was no observable dissolution over a period of 24 hours.

Modelling of the system predicted that, for the amount of calcium carbonate used, the change in particle radius would be unobservable before saturation of the solution occurred. Further modelling indicated that in order to obtain a marked change in the particle radius before saturation occurred, a much smaller initial volume fraction of $CaCO_3$ particles would be required. However, this volume fraction would have to be so small that the mass transport enhancement would be undetectable, even if it were above the critical volume fraction, ϕ_c.

7.4.3 Dissolution in the Presence of Mono- and Di-anions of Maleic Acid

The above experiments and modelling demonstrated that at high pH the dissolution of $CaCO_3$ would be unobservable by this method, due to saturation. In contrast dissolution in the low pH regime where the reaction is with H^+ would occur

at too fast a rate to be measurable. A system is therefore required where the rate of dissolution is intermediate between these two cases.

Compton *et al.* [131] using the channel flow cell showed that the dissolution of calcite in the presence of both $HMal^-$ and Mal^{2-} (where H_2Mal represents maleic acid) proceeded according to the following kinetics

$$J_{Ca^{2+}}/\text{mol cm}^{-2}\,\text{s}^{-1} = 0.043[HMal^-]_o(1 - \theta_{Mal^{2-}}) \tag{7.31}$$

where

$$\theta_{Mal^{2-}} = \frac{K_{Mal}[Mal^{2-}]}{1 + K_{Mal}[Mal^{2-}]} \tag{7.32}$$

and the Langmuirian adsorption equilibrium constant for Mal^{2-}, $K_{Mal} = 4.8\text{x}10^3$ $dm^3\ mol^{-1}$. For maleic acid $pK_1 = 1.83$ and $pK_2 = 6.07$ [93]. By carefully controlling the pH, the speciation of the maleic acid system can be fixed and by suitable choice of overall maleic species concentration and pH, a measurable dissolution rate could be obtained. The presence of both the $HMal^-$ and Mal^{2-} ions also provided buffering action, which would counteract any localised drop in pH on adding acid in the "pH-stat" experiments.

These particle dissolution experiments were carried out in the "pH-stat" mode with 10.05 mM maleic acid, in addition to the 5.01 mM TMPD, in 100 cm^3 of 0.5 M KCl at a pH of 7.0. The variation of the limiting current as a function of time is shown in Figure 7.10. Again taking into account the change in volume on the addition of acid (which also contained TMPD and maleic acid), the effective particle radius r_o was calculated, according to equation (7.30), as a function of time. This is plotted in Figure 7.11. The gradient of this graph gave the rate of change of particle radius of $4.25\text{x}10^{-8}$ cm s^{-1}, which corresponded to a flux of

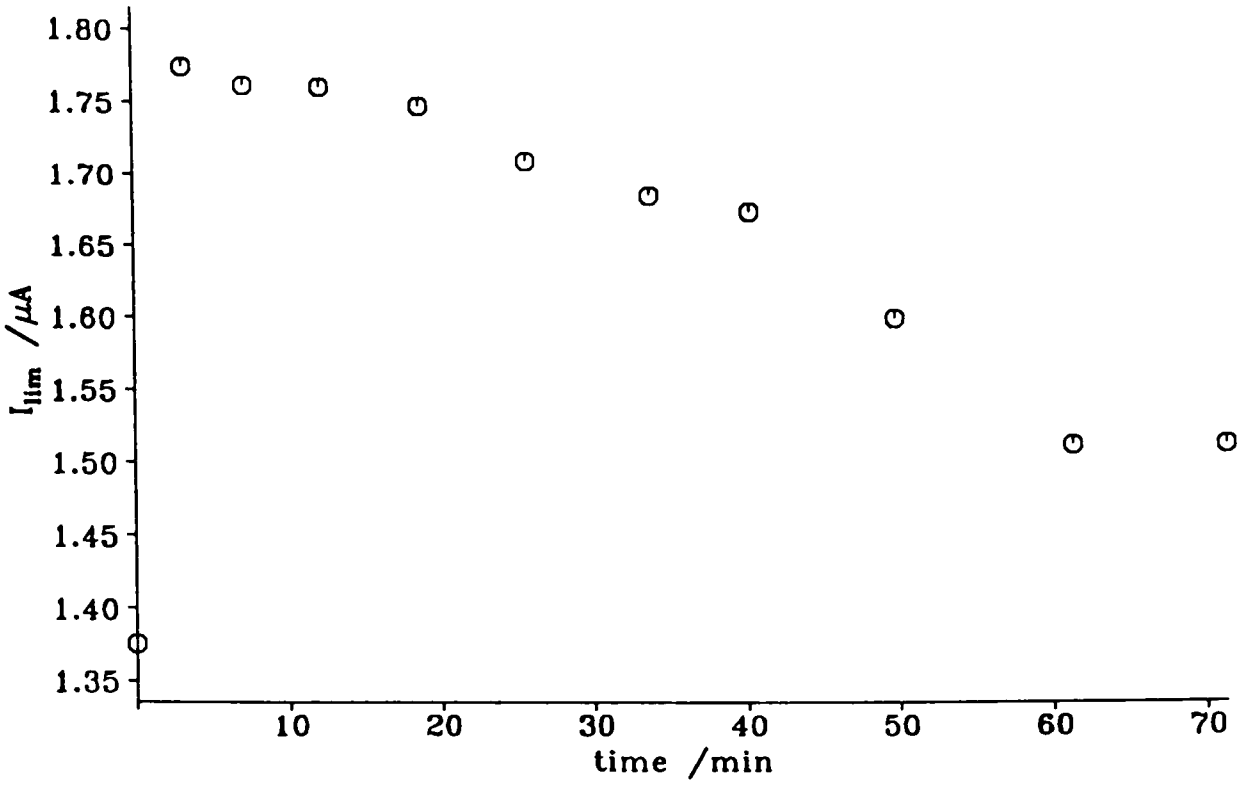

Figure 7.10. Plot of I_{lim} as a function of time at f = 36 Hz *for* 5.01 mM TMPD *in* 0.5 M KCl *with* 10.05 mM *maleic acid present, at constant* pH = 7.00 ± 0.05, *initially with* 5.6 vol % $CaCO_3$ *particles present.*

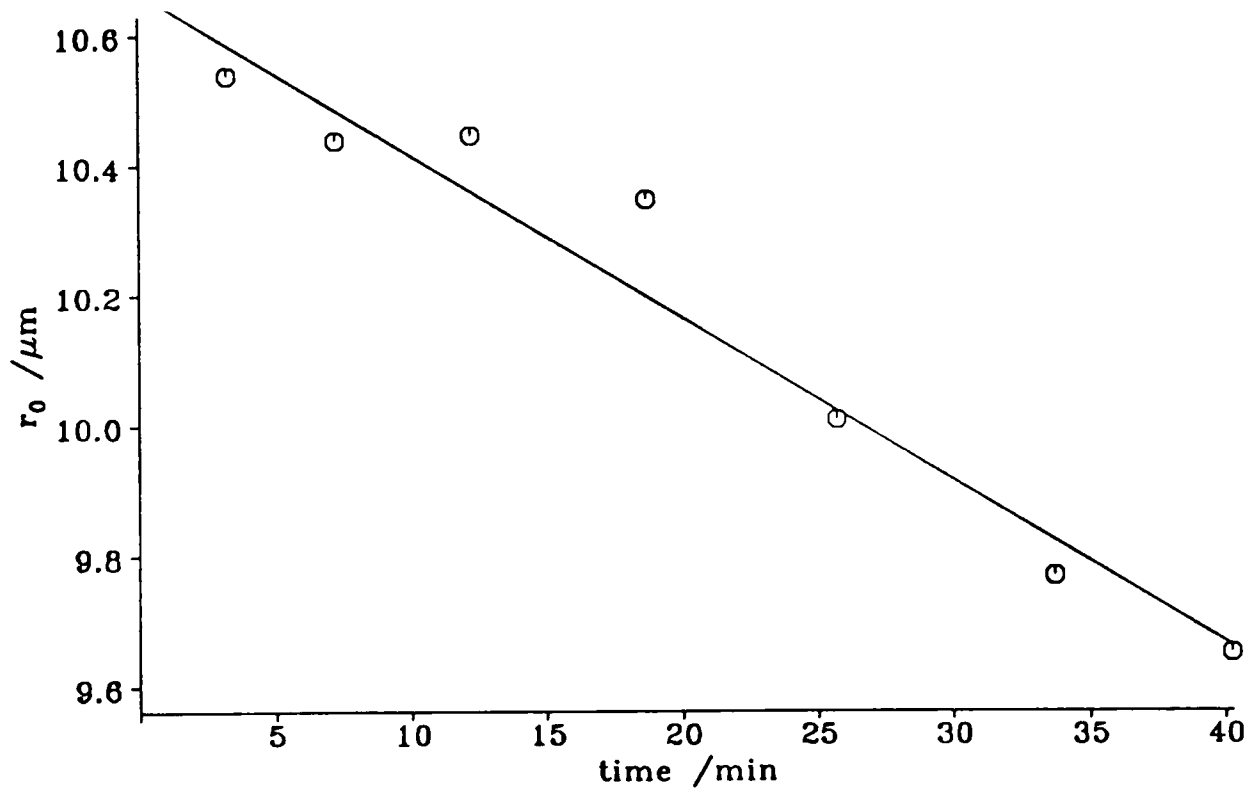

Figure 7.11. Plot of the effective particle radius, r_0, as a function of time for 5.01 mM TMPD *in* 0.5 M KCl *with* 10.05 mM *maleic acid present, at constant* pH = 7.00 ± 0.05, *initially with* 5.6 vol % $CaCO_3$ *particles present.*

1.2×10^{-9} mol cm^{-2} s^{-1} (equation (7.26)). Calculating the speciation present at pH 7.0, the predicted flux from the rate equation (7.31) was 1.0×10^{-9} mol cm^{-2} s^{-1}. Thus there is excellent agreement between the flux determined by this particle

sizing technique and that determined from the dissolution of single crystals in the channel flow cell.

7.5 Conclusions

The enhancement of the mass transport to the RDE by suspended particles has proved to be a novel method in determining their rate of change in size due to dissolution. Clearly this approach could be extended away from that of calcium carbonate dissolution to the dissolution (or precipitation) of other systems, provided the rate of the process is suitable. There must, however, be a significant detectable change in the volume fraction of the particles over the course of the experiment before saturation of the solution occurs, in the case of dissolution processes. In addition, the absolute value of the volume fraction must be greater than the critical value, below which the mass transfer enhancement is not seen.

APPENDIX 1

ADSORPTION OF FOREIGN SPECIES ON CALCITE

The table below lists many of the literature reports on the effect of various species on calcite dissolution/precipitation kinetics, their adsorption on, and coprecipitation with, calcite and distribution coefficients, etc.

Table A1.1. The Adsorption of Various Species on Calcite

Inhibitor	Technique	Conclusions	Reference
Am	equil^{m}, powder, radio-tracer	Am rapidly & strongly adsorbed.	[203]
various cations	diss, powder, P_{CO_2}≈1, titration	Effectiveness of inhibitor $Pb^{2+}>La^{3+}>Y^{3+}>Sc^{3+}>Cd^{2+}>Cu^{2+}>Au^{3+}>Zn^{2+}>Ge^{4+}>Mn^{2+}>Ni^{2+}=Ba^{2+}=Mg^{2+}=Co^{2+}$	[204]
Ba^{2+}, Sr^{2+}, Cd^{2+}, Mn^{2+}, Zn^{2+}, Co^{2+}, Ni^{2+}	equil^{m}	M^{2+}-Ca^{2+} exchange on cation specific surface sites. Sorption was in sequence Cd>Zn≥Mn>Co>Ni»Ba=Sr.	[123]
Ba^{2+}	ppt, seeded growth	Partition coefficient independent of ppt^{n} rate.	[205]
Ba^{2+}	single crystal & powder	Atomic absorption & ESCA study of Ba^{2+} sorption; conclude Ca^{2+}-Ba^{2+} exchange & Langmuirian adsorption.	[206]
Be^{2+}, Mg^{2+}, Sr^{2+}, Ba^{2+}	powder	Kinetics of aragonite to calcite transformation - inhibited by $Be^{2+}>Mg^{2+}>Sr^{2+}>Ba^{2+}$.	[156]
Cd^{2+}	equil^{m}, powder, atomic adsorption	< 1 μmol g^{-1}, linear adsorption isotherm; higher [Cd^{2+}] gave $CdCO_3$ ppt.	[207]
Co^{2+}	powder, radio-tracer	Co^{2+} adsorption occurred but no $CoCO_3$ surface phase formed. Ca^{2+} & Mg^{2+} compete with Co^{2+} for adsorption sites.	[173]

Inhibitor	Technique	Conclusions	Reference
Cu^{2+}	equilibration in distilled & sea water, powder, atomic spect^{y}	Conclude that a coppt. is formed in distilled water, but surface ppt^{n} of $CuCO_3$ occurred in seawater.	[208]
Cu^{2+}	Cu^{2+} detection in calcite	VIS & IR reflectance spectroscopy.	[209]
Cu^{2+}	diss, powder, free drift, conductivity	Cu^{2+} strongly inhibits.	[210]
Cu^{2+}, Pb^{2+}, Zn^{2+}, Cd^{2+}	-	extraction	[211]
Mg^{2+}, SO_4^{2-}	ppt, powder	Enhanced solubility. Langmuirian adsorption.	[106]
Mg^{2+}	ppt, chemo-stat, $P_{CO2}=10^{-2.5}$	Amount of Mg^{2+} incorporated into overgrowth independent of ppt^{n}. rate.	[54]
Mg^{2+}	diss, single crystal, free-drift, conductivity	Inhibition by Mg^{2+}, due to surface adsorption.	[134]
Mg^{2+}, Ba^{2+}, Zn^{2+}	diss, free-drift, atomic abs^{n}	Adsorption occurred. New phases found with Ba & Zn. No new phase with Mg.	[135]
Mg^{2+}, PO_4^{3-}	diss, powder & single crystal, free-drift & pH-stat	Mg^{2+} exhibited Langmuirian adsorption. Phosphate inhibits at very low concentrations.	[29]
Mg^{2+}, Sr^{2+}	ppt, seeded growth, pH-stat	Incorporation of M^{2+} independent of precipitation rate.	[55]
Mg^{2+},	ppt, single crystal, Auger	Langmuirian adsorption of Mg^{2+}. Surface $[Mg^{2+}]/[Ca^{2+}]$ determined.	[136-138]

Inhibitor	Technique	Conclusions	Reference
Mg^{2+}	powder & single crystal, radio-tracer	Adsorption of Mg^{2+}. Surface $[Mg^{2+}]/[Ca^{2+}]$ determined.	[124,139-143]
Mg^{2+}, Co^{2+}, Ni^{2+}, Fe^{2+}	equil^{m}, powder, radio-tracer	Adsorption of M^{2+}. Surface $[M^{2+}]/[Ca^{2+}]$ determined.	[159]
Mg^{2+}	powder, streaming potentials	Adsorption of Mg^{2+}.	[144]
Mg^{2+}, Sr^{2+}	ppt, free-drift, atomic abs^{n}	With Mg^{2+}, $CaCO_3$ precipitated as spherulites, which aged to aragonite and distorted magnesian calcite. Sr^{2+} produced no change of habit.	[154]
Mg^{2+}	ppt, seeded growth, free drift, atomic abs^{n} & titration	Inhibition due to Langmuirian adsorption of Mg^{2+}.	[160]
Mg^{2+}	equil^{m}, X-ray diffraction	Kinetics of aragonite to calcite transformation, inhibited by Mg^{2+}.	[157]
Mg^{2+}	ppt, seeded growth, chemo-stat	Strong inhibition at sea water concentrations.	[147]
Mg^{2+}	ppt, atomic abs^{n}	Distribution coefficient of Mg^{2+} in calcite.	[212]
Mg^{2+}	ppt, seeded growth, chemo-stat	P_{CO2} has significant effect on $MgCO_3$ incorporation.	[153]
Mg^{2+}	ppt, seeded growth, chemo-stat	Distribution coefficient of Mg^{2+} in calcite overgrowths.	[213]

Inhibitor	Technique	Conclusions	Reference
Mg^{2+}, Mn^{2+}, Ni^{2+}, Cr^{3+}, F^-	ppt, free-drift	Only Mg^{2+} & Mn^{2+} showed substantial inhibition.	[214]
Mn^{2+}, Fe^{2+}	ppt, seeded-growth, chemo-stat	Distribution coefficients.	[215]
Mn^{2+}	ppt, seede-growth, chemo-stat	Increased inhibition as $[Mn^{2+}]/[Ca^{2+}]$ increased and Ω decreased.	[58]
Mn^{2+}	equil^m, powder, radio-tracer	Mn^{2+} exchanges with 1 - 2 layers of Ca^{2+}.	[216]
Na^+, K^+	ppt	$[Na^+]/[Ca^{2+}]$ and $[K^+]/[Ca^{2+}]$ ratios in calcite independent of pH & solution $[Ca^{2+}]$. Na^+ & K^+ thought to be incorporated at interstitial sites.	[217]
Sc^{3+}	diss, radio-tracer	Adsorption at active sites.	[218]
Sr^{2+}	ppt, seeded growth, free-drift, AA	Distribution coefficients.	[219]
Zn^{2+}	ppt, free-drift, titration	Inhibition and partial coppt^n.	[220]
Zn^{2+}	ppt, free-drift, titration & radio-tracer	Distribution coefficients.	[221]
Zn^{2+}	equil^m	Zn^{2+}-Ca^{2+} exchange in surface adsorption layer. Freundlich, Lanmuir-Freundlich, 2 part Langmuir isotherms.	[172]

Inhibitor	Technique	Conclusions	Reference
uranyl, UO_2^{2+}	equil^m	Uranyl ion found to adsorb due to formation of hydroxy-carbonato species. Maximum extent of adsorption dependent on $[UO_2^{2+}]$.	[222]
various	ppt, pH-stat	Inhibition $Fe^{2+}>ATP>P_3O_7^{5-}>P_2O_7^{4-}>(PO_3)_6^{6-}>Zn^{2+}>$ $ADP>Ce^{3+}>Pb^{2+}>$carbamyl phosphate$>$ $Fe^{3+}>PO_4^{3-}>Co^{2+}>Mn^{2+}>Be^{2+}>$ β-glycerophosphate$>Ni^{2+}>Cd^{2+}>$ phenylphosphate$>Ba^{2+}>$citrate$>$AMP$>$ $Sr^{2+}>SO_4^{2-}>Mg^{2+}$	[155]
phosphate, silica, NO_3^-, organics	diss, powder, pH-stat	Significant inhibition by PO_4^{3-}. Little or no effect by NO_3^-, silica or organics at sea water concentrations.	[22]
phosphate	ppt, seeded growth, pH-stat	Inhibition dependent on $[HPO_4^{2-}]$ & $[PO_4^{3-}]$.	[57]
phosphate	ppt, free-drift, seeded growth	Inhibition found to be dependent on Ω.	[223]
orthophosphate	equil^m, free-drift & chemo-stat	Phosphate uptake not affected by $[Mg^{2+}]$. or $[F^-]$. Elovichian chemisorption theory used.	[224]
phosphate & glycerophosphate	ppt, seeded growth	50% inhibition at 16 μM & 2 μM for glycero- and ortho-phosphate. Langmuirian adsorption observed.	[51]
orthophosphate	ppt, seeded growth, chemo-stat	Inhibition determined by $[PO_4^{3-}]$.	[56]
phosphate	diss, pH-stat	Phosphate ions strongly adsorbed.	[21]

Inhibitor	Technique	Conclusions	Reference
phosphate	equil^{m}	At low phosphate concentration PO_4^{3-} exchanged with surface CO_3^{2-}. At higher concentration, HPO_4^{2-} is adsorbed with accompanying counterion(s) as neutral species following Freundlich isotherm.	[225]
phosphonates	ppt, seeded growth, free-drift	Inhibition at μM levels. Langmuirian adsorption observed.	[52]
diphosphonates	ppt, pH-stat	Powerful inhibitors at 10^{-7} mol dm^{-3}. Langmuirian adsorption found.	[226]
SeO_3^{2-}	equil^{m}, isotope tracer method, pH7.0-9.5	SeO_3^{2-} exchanged with CO_3^{2-}; SO_4^{2-} & PO_4^{2-} decreased SeO_3^{2-} adsorption but was unaffected by Mg^{2+}, implying anion specific adsorption sites.	[171]
benzenehexacarboxylic and benzene-1.3.5-tricarboxylic acids	ppt, chemo-stat, pH8.50	Benzenehexacarboxylic acid follows Langmuirian adsorption isotherm; benzene-1,3,5-tricarboxylic acid - little effect.	[130]
stearic acid, octadecylamine, octdecanol, cholesterol	ppt, Langmuir trough	Crystallisation of $CaCO_3$ under compressed Langmuir monolayers of organic species.	[227-229]
stearic acid & albumin	powder, free-drift	Stearic acid and albumen form monolayers on surface.	[230]
amino acids, sugars, proteins, acetate, malate, pyruvate, citrate, succinate	ppt	Ppt^{n} greatly inhibited by citrate, malate, pyruvate, glycylglycine and glycogen. Some of the others affect $CaCO_3$ crystal type formed.	[231]
palmitic acid	diss, powder, free drift	S-shape adsorption isotherms. Mg^{2+} ions greatly decreased fatty acid adsorption.	[232]

Inhibitor	Technique	Conclusions	Reference
maleic acid	diss, channel	Langmuirian adsorption of maleic acid dianion.	[131]
tartaric acid	diss, channel	Langmuirian adsorption of tartaric acid dianion. Meso-tartarate more potent isomer.	[132]
α,ω-dicarboxylates	ppt	Effect of species on calcite morphology.	[129]
polyvinyl sulponate (PVS) & polyglutamic acid (PGA)	ppt	PVS no effect. PGA slight effect.	[233]
polymaleic acid	diss, channel	Dissolution rate slowly decreased with time as PMA adsorbed.	[133]

ppt - precipitation; diss - dissolution; equil^{m} - equilibrium;
AA - atomic absorption spectroscopy.

APPENDIX 2

THE THOMAS ALGORITHM

The Thomas algorithm [91], is a simplified form of Gaussian elimination and is an efficient method for the solution of tridiagonal matrix systems. The matrix equation to be solved is written as

$$\{d\} = [T]\{u\} \tag{A2.1}$$

The algorithm operates by factorising the tridiagonal matrix $[T]$ into two bidiagonal matrices $[T_L]$ and $[T_U]$

$$[T] = [T_L][T_U] \tag{A2.2}$$

A solution is then found for the vector $\{f\}$ in

$$[T_L]\{f\} = \{d\} \tag{A2.3}$$

and $\{f\}$ is used to give a final solution

$$[T_U]\{u\} = \{f\} \tag{A2.4}$$

Since

$$[T_L]^{-1}\{d\} = \{f\} \qquad [T_U]\{u\} = [T_L]^{-1}\{d\} \tag{A2.5}$$

thus

$$([T_L][T_U])\{u\} = \{d\} \tag{A2.6}$$

The matrix $[T]$ of $(J\text{-}1)$x$(J\text{-}1)$ elements can be written as

$$[T] = \begin{bmatrix} b_1 & c_1 & 0 & & & & & \\ a_2 & b_2 & c_2 & 0 & & & & \\ & \ddots & \ddots & \ddots & & & & \\ & & \ddots & \ddots & \ddots & & & \\ & & 0 & a_j & b_j & c_j & 0 & \\ & & & & \ddots & \ddots & \ddots & \\ & & & & & \ddots & \ddots & \ddots \\ & & & & & 0 & a_{J-2} & b_{J-2} & c_{J-2} \\ & & & & & & 0 & a_{J-1} & b_{J-1} \end{bmatrix} \tag{A2.7}$$

On factorisation $[T]$ takes the form

$$[T] = [T_L][T_U] = \begin{bmatrix} \alpha_1 & & & & & & 0 \\ \alpha_2 & \alpha_2 & & & & & \\ & \ddots & \ddots & & & & \\ & & \ddots & \ddots & & & \\ & & & & \alpha_{J-2} & \alpha_{J-2} & \\ 0 & & & & & \alpha_{J-1} & \alpha_{J-1} \end{bmatrix} \begin{bmatrix} 1 & \beta_1 & & & & 0 \\ & 1 & \beta_2 & & & \\ & & \ddots & \ddots & & \\ & & & \ddots & \ddots & \\ & & & & 1 & \beta_{J-2} \\ 0 & & & & & 1 \end{bmatrix} \tag{A2.8}$$

where α_j and β_j are to be determined.

By equating the left- and right-hand sides of the equation $[T] = [T_L]\,[T_U]$, the the following relations are obtained

$$\alpha_1 = b_1 \tag{A2.9}$$

$$\beta_1 = \frac{c_1}{\alpha_1} \tag{A2.10}$$

$$\alpha_j = b_j - a_j\beta_{j-1} \qquad j = 2,3\ldots J\text{-}1 \tag{A2.11}$$

$$\beta_j = \frac{c_j}{\alpha_j} \qquad j = 2,3\ldots J\text{-}2 \quad (a_j \neq 0) \tag{A2.12}$$

After obtaining α_j and β_j, the equation for $\{f\}$ is solved

$$[T_L]\{f\} = \{d\} \tag{A2.13}$$

where the elements f_j of $\{f\}$ are given by

$$f_1 = \frac{d_1}{\alpha_1} \tag{A2.14}$$

$$f_j = \frac{(d_j - a_j f_{j-1})}{\alpha_j} \qquad j = 2,3...J\text{-}1 \tag{A2.15}$$

$\{f\}$ is then used to determine the elements u_j of $\{u\}$

$$u_{J-1} = f_{J-1} \tag{A2.16}$$

$$u_j = f_j - \beta_j u_{j+1} \qquad j = 1,2...J\text{-}2 \tag{A2.17}$$

By this procedure the matrix equation $[T]\{u\} = \{d\}$ is solved for $\{u\}$.

APPENDIX 3

THE POTENTIOSTAT

The potentiostat is a device which actively maintains the potential difference between the working (WE) and reference (RE) electrodes at a given value by altering the voltage between the working and counter (CE) electrodes, as necessary. In other words, it forces whatever current is necessary through the WE so that the required potential is achieved. The potentiostat's design is based on the operational amplifier. The ideal operational amplifier has several useful features

(a) Infinite input impedance, i.e. the inverting (-) and non-inverting (+) inputs draw no current from the voltage sources (can be 10^5 - 10^{14} Ω).

(b) Zero output impedance, i.e. the output voltage remains constant irrespective of the current drawn (limits typically 5 - 100 mA).

(c) Infinite gain, A, i.e. any voltage difference between the inputs, drives the output to the limit deliverable by the power supply. (Typically $A = 10^4$ - 10^8 for d.c. signals).

$$E_{out} = -A(E_- - E_+) \qquad \text{(A3.1)}$$

(d) Infinite bandwidth, i.e. it can respond to a change in voltage with infinite speed or respond to a signal of any frequency. (Typical unity-gain bandwidths, 100 Hz - 100 MHz).

In most applications the operational amplifier is stabilised by feeding back part of its output to the inverting input (negative feedback). In this mode of operation the two inputs are forced to have the same potential. A typical (schematic) potentiostat circuit is shown in Figure A3.1. Amplifier 1 keeps point S at virtual earth, therefore

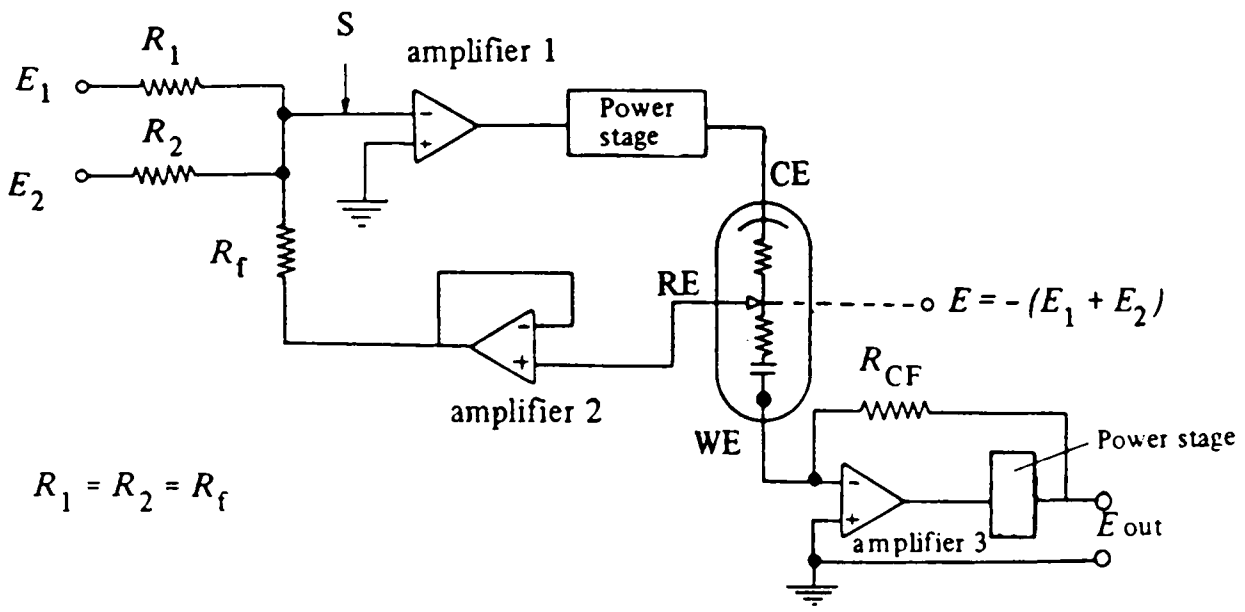

Figure A3.1. Simple potentiostat circuit diagram.

the RE must be at $-(E_1 + E_2)$, in order for the voltages to sum to zero at S. Amplifier 3 maintains the WE at virtual earth, thus the potential of the WE is $+(E_1 + E_2)$ relative to the RE. Amplifier 2 acts as a "voltage follower" to prevent the RE being polarised by the current required to keep S at virtual earth. It also means that its output can be used externally without affecting the system. Amplifier 3 acts as a "current follower", since its voltage output ($= -IR_{CF}$) is proportional to the current flowing between the WE and CE. Booster amplifiers (non-inverting, usually low gain) are included, permitting the attainment of larger currents and voltages than would have otherwise been accessible. The significance of having two voltage inputs is that one can be used to set a d.c. potential, which may or may not be ramped, and the other can be an alternating signal so that the resulting sum is a given potential with an a.c. perturbation, as used for a.c. impedance spectroscopy (see Chapter 6).

The circuit diagrams for the actual potentiostats used are given in Figure A3.2.

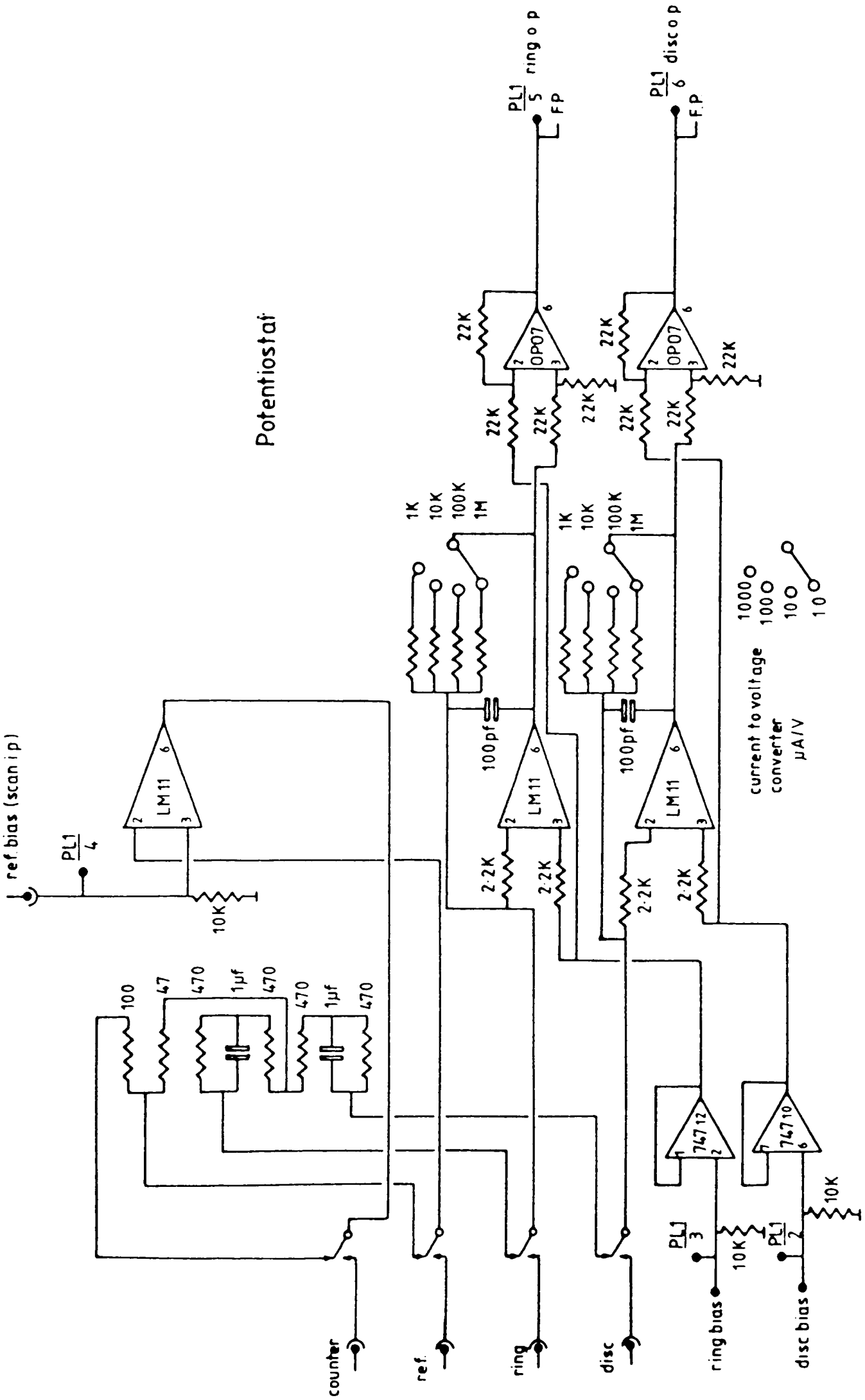

Figure A3.2a. Oxford Electrodes potentiostat circuit diagram.

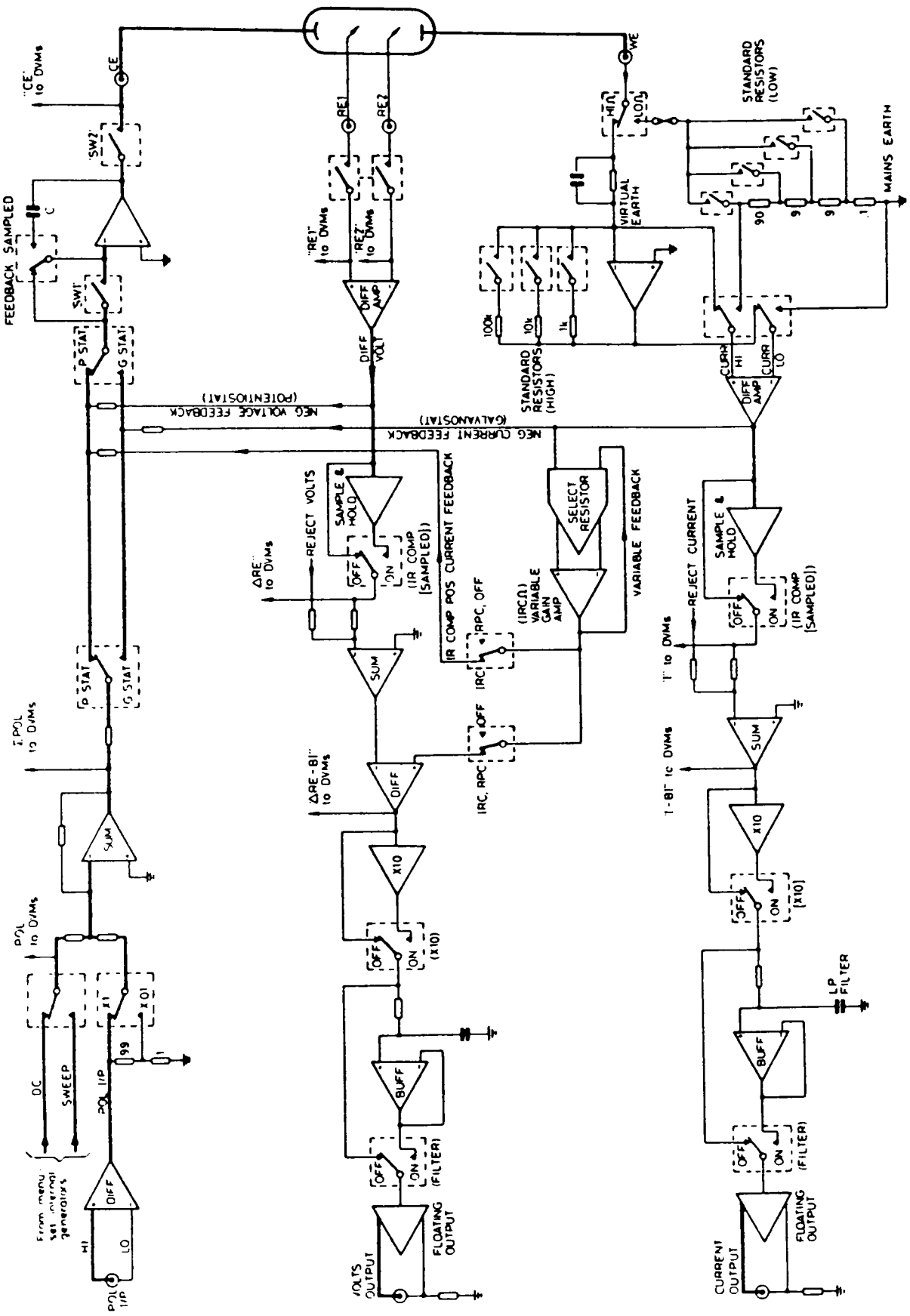

Figure A3.2b. Schlumberger Solartron 1286 Electrochemical Interface circuit diagram.

APPENDIX 4

COMPUTER PROGRAMS

A4.1 BIBCN

This section lists the computer program which uses the Backwards Implicit Finite Difference method to model the dissolution of $CaCO_3$ in the channel cell. This program has the surface kinetics defined by the rate equation (4.43) and the surface boundary matrix elements as given in Table 4.5 (Approach 1).

```
C   DISSOLUTION OF CaCO3 - BCN EQUATION
C   ***********************************************
C   EQUILIBRIUM ASSUMED AT EACH POINT
C   FOR HIGH pH (pH>8) ONLY

      IMPLICIT DOUBLE PRECISION (A-H,O-Z)
      DOUBLE PRECISION LA(0:3000),LB(0:3000),GA(0:3000,2),
     +GB(0:3000,2),GC(0:3000,2),H(0:3000,2),D(0:3000),
     +B(0:3000),GAOLD,GHOLD,GCOLD,SUM,SENH,AVG,
     +BCA,SUMCA
      DOUBLE PRECISION KG,K1,KA1,KA2,KW,KSP,KCA,KCO3
      LOGICAL CONV(4)
      CHARACTER DATFILE*28,HDAT*10,DF*1
      COMMON /BLOCKA/B,D,NX,NY /BLOCKB/KG,K1,DELY
     +/BLOCKC/GA,H,KA1,KA2,KW,BOH,BCA,KSP
     +/BLOCKD/K,IT,NIT,CONV,PPM


C   FIXED VALUES
C   TWOH = 2h   DD = d   DA = D_Ca   XE = length of xtal
C   KA2 - 2nd H2CO3 dissociation consts.
C   GA=[Ca2+], GB=[HCO3-], GC=[CO3 2-]


      DA=7.93E-6
      KA2=1.409E-13
      KW=1.45E-20
      KSP=6.26E-14

      PRINT*,'All dimensions of length in cm'

      PRINT*,'Value of kKK?'
      READ*,KG
      PRINT*,'Value of K_Ca?'
      READ*,KCA
      PRINT*,'Value of K_CO3?'
      READ*,KCO3
      PRINT*,'Size of Grid X'
      READ*,NX
      PRINT*,'Size of Grid Y'
      READ*,NY
      PRINT*,'Volume flow rate'
      READ*,V
      PRINT*,'Bulk pH'
      READ*,BPH
      PRINT*,'Bulk [Ca2+] /mM'
      READ*,BCA
      BCA=BCA*1.0E-6
      PRINT*,'Number of iterations'
      READ*,NIT
      PRINT*,'Convergence of surface [Ca2+] /ppm'
      READ*,PPM
      PRINT*,'Height of channel (2h)'
      READ*,TWOH
      PRINT*,'Width of channel (d)'
      READ*,DD
      PRINT*,'Length of crystal'
      READ*,XE
      PRINT*,'Distance from xtal to edge of sensor'
      READ*,GAP
      PRINT*,'Diameter of sensor'
      READ*,DIA
      PRINT*,'Datafile output of [H+]sensor? Y/N'
      READ'(A1)',DF


C   BULK [OH-]
      BOH=KW*(10**(BPH))*1.E3

C   DELTA X,  DELTA Y
      DELX=XE/DBLE(NX)
      DELY=TWOH/DBLE(NY)

C   NDSTR is value of k at downstream limit

      NDSTR=INT((GAP+DIA)/DELX)+NX
      IGAP=INT(GAP/DELX)

C   CALCULATION OF LAMBDA(j) for Ca

      DO 10 J=1,NY-1
        LA(J)=DA*DELX*(TWOH**3)*DD/
     +        (6.0*V*(DELY**3)*DBLE(J)*(TWOH-DBLE(J)*DELY))
10    CONTINUE


C   SET GA(j,k&k+1)=bulk [Ca2+], GB(j,k&k+1)=0 GC(j,k&k+1)=0

      DO 17 K=1,2
        DO 15 J=0,NY-1
          GA(J,K)=BCA
          GB(J,K)=0.0
          GC(J,K)=0.0
15      CONTINUE
17    CONTINUE

      SUMCA=BCA
      GAOLD=1.
      GHOLD=1.
      GCOLD=1.

C   Loop to increment to successive vectors over crystal

      DO 30 K=0,NX-1
```

```
C       reset convergence flags

        CONV(1)=.FALSE.
        CONV(2)=.FALSE.
        CONV(3)=.FALSE.

C       Iterative loop until convergence is reached

        DO 20 IT=1,NIT


C *****  Set initial/final parameters for Ca & Calc GA(j,k+1)
C        followed by BI calc & surface [Ca2+] calc

        D(1)=GA(1,1)+(LA(1)*DELY*KG/DA)
     +        *(KSP-GA(0,2)*GC(0,2))
     +        /((1+KCA*GA(0,2))*(1+KCO3*GC(0,2)))
        B(1)=LA(1)+1.
        B(NY-1)=LA(NY-1)+1.
        CALL BI(GA,LA)
        GA(0,2)=GA(1,2)+(DELY*KG/DA)
     +   *(KSP-GA(0,2)*GC(0,2))
     +   /((1+KCA*GA(0,2))*(1+KCO3*GC(0,2)))

C       Calc Surface [H+]
        CALL QUAD(0)

C       Calc Surface [CO3 2-]
        GC(0,2)=(GA(0,2)-BCA)/(1.0+H(0,2)/KA2)


C       Check convergence on surface data for Ca,H & CO3

        CALL CONVCHK(1,GA,GAOLD)
        CALL CONVCHK(2,H,GHOLD)
        CALL CONVCHK(3,GC,GCOLD)
        IF(CONV(1).AND.CONV(2).AND.CONV(3))THEN
          IF(MOD(K,200).EQ.0.0)THEN
            PRINT*,'K=',K,'  IT=',IT
          ENDIF
          GOTO21
        ENDIF

C       Put surface conc equal to old values
C         for convergence check
        GAOLD=GA(0,2)
        GHOLD=H(0,2)
        GCOLD=GC(0,2)


C       End of iterative loop
20      CONTINUE

C       Pick out mid-xtal [Ca2+] & [CO3 2-] values

21      IF(K.EQ.INT(NX/2)-1)THEN
          CAHALF=GA(0,2)
          CO3HALF=GC(0,2)
        ENDIF


C ****** Put G(k+1) values as new G(k) values

        DO 27 J=0,NY-1
          GA(J,1)=GA(J,2)
          GC(J,1)=GC(J,2)
          H(J,1)= H(J,2)
27      CONTINUE

C       Running total of surface [Ca] over xtal (K=0-NX)
        SUMCA=SUMCA+GA(0,2)

C   End of main K loop
30  CONTINUE

C   Get values at end of xtal

    CAEND=GA(0,2)
    CO3END=GC(0,2)

C ******************
C *** DOWNSTREAM ***
C ******************

C   Sensor calcs in integer units of delx
C   IGAP calculated earlier

    IDIA=INT(DIA/DELX)
    IRAD=IDIA/2
    SUM=0.0
    AREA=0.0

    DO 100 K=NX,NX+IGAP+IDIA

C     CALC [Ca] downstream

      D(1)=GA(1,1)
      B(1)=LA(1)+1.0
      B(NY-1)=LA(NY-1)+1.0
      CALL BI(GA,LA)
      GA(0,2)=GA(1,2)



C     Downstream sensor ave [H+] calc

C     Calc [H+] at upstream edge of sensor for next loop
      IF (K.EQ.NX+IGAP-1) THEN
        CALL QUAD(0)
        H(0,1)=H(0,2)
      ENDIF

C     FOR K OVER SENSOR
      IF (K.GE.NX+IGAP.AND.K.LE.NX+IGAP+IDIA) THEN
        W=DBLE(IRAD**2-(NX+IGAP+IRAD-K)**2)
        IF (W.LT.0.0) THEN
          W=0.0
        ENDIF
        W=2.0*SQRT(W)
        AREA=AREA+W
C       Calc [H+] for next (ie k+1) value of K
        CALL QUAD(0)
        SUM=SUM+W*LOG10(H(0,1))
        H(0,1)=H(0,2)
      ENDIF


C     PUT [Ca](k+1) VALUES AS NEW [Ca](k) VALUES

      DO 50 J=0,NY-1
        GA(J,1)=GA(J,2)
50    CONTINUE

100 CONTINUE

    PRINT103,NX,NY,NIT
    PRINT104,PPM
    PRINT*,'Using Brown-Compton-Narramore equation'
    PRINT105,V,BPH
    PRINT106,KG,KCA,KCO3,KSP,BCA*1.0E6
    PRINT107,K1,KA1,KA2
    PRINT108,CAHALF,CO3HALF,CAEND,CO3END
    PRINT109,SUMCA/(DBLE(NX)+1)
103 FORMAT(1X,'Grid Size: x ',I7,',  y ',I7,'  Max no item ',I3)
104 FORMAT (1X,'Convergence of surface [Ca2+],[H+] &
   + [CO3)2-]to ',F5.2,'ppm')
105 FORMAT (1X,'Vf=',F5.3,'  Bulk pH=',F5.2)
106 FORMAT (1X,'kKK=',1PE9.3,'  K(Ca,L)=',E9.3,'
```

```
     +K(CO3,L)=',E9.3/1X,'Ksp=',E9.3,'  [Ca2+]b=',0PF6.3,'mM')
107  FORMAT (1X,'K1=',1PE9.3,'  KA1=',E9.3,'  KA2=',E9.3)
108  FORMAT (1X,'Mid Crystal [Ca]o=',1PE9.3,'  [CO3]o=',
     +E9.3/1X, 'End of Crystal [Ca]o=',E9.3,'  [CO3]o=',E9.3)
109  FORMAT (1X,'Average surface [Ca2+] over xtal =',1PE9.3)

C    AVERAGE [H+] OVER SENSOR
     AVG=SUM/AREA
     SENH=10**AVG
     PRINT120,NX+IGAP,NX+IGAP+IDIA
     PRINT*,'Average sensor [H+]=',SENH

C    write SENH to datafile
     IF(ICHAR(DF).EQ.89)THEN
       CALL NAME(HDAT,V)
       OPEN(3,FILE=HDAT,STATUS='NEW')
       WRITE(3,130)V,SENH
       CLOSE(3)
     ENDIF

     CLOSE(2)
     STOP
110  FORMAT(30(1X),E23.16)
120  FORMAT(1X,'Sensor between K=',I4,' and K=',I4)
130  FORMAT(F5.3,2X,1PE9.3)
     END

     SUBROUTINE BI(G,L)
C    To calculate concentrations of one vector using the
C      Backward Implicit Finite Difference Method
     DOUBLE PRECISION L(0:3000),G(0:3000,2),U(0:3000),
    +D(0:3000),A(0:3000),B(0:3000),C(0:3000),
    +AL(0:3000),BE(0:3000)F(0:3000)
     COMMON /BLOCKA/B,D,NX,NY

C       SET VALUES OF D(ie d(j)), A, B, C

     DO 200 J=1,NY-1
       A(J)=-L(J)
       C(J)=-L(J)
200  CONTINUE
     DO 220 J=2,NY-1
       D(J)=G(J,1)
220  CONTINUE
     DO 240 J=2,NY-2
       B(J)=2*L(J)+1.
240  CONTINUE

C       CALCULATE ALPHA AND BETA

     AL(1)=B(1)
     BE(1)=C(1)/AL(1)
     DO 400 J=2,NY-1
       AL(J)=B(J)-A(J)*BE(J-1)
       BE(J)=C(J)/AL(J)
400  CONTINUE

C       CALCULATE f(j) VALUES

     F(1)=D(1)/AL(1)
     DO 500 J=2,NY-1
       F(J)=(D(J)-A(J)*F(J-1))/AL(J)
500  CONTINUE

C       CALCULATE u(j) VALUES

     U(NY-1)=F(NY-1)
     DO 600 J=NY-2,1,-1
       U(J)=F(J)-BE(J)*U(J+1)
600  CONTINUE

C       u(j) values are new G(j,k+1) values

     DO 650 J=1,NY-1
       G(J,2)=U(J)
650  CONTINUE

700  RETURN
     END

     SUBROUTINE QUAD(J)
C    To solve quadratic equation for [H+]
     IMPLICIT DOUBLE PRECISION (A-H,O-Z)
     DOUBLE PRECISION GA(0:3000,2),H(0:3000,2),
    + A,B,C,ROOT(2),BCA
     DOUBLE PRECISION KA1,KA2,KW,KSP
     COMMON /BLOCKC/GA,H,KA1,KA2,KW,BOH,BCA,KSP

C    SOLVE QUADRATIC FOR [H+]

     A=(GA(J,2)-BCA+BOH)/KA2
     B=BOH-KW/KA2
     C=-KW
     ROOT(1)=SQRT(B*B-4.0*A*C)
     ROOT(2)=(-B-ROOT(1))/(2.0*A)
     ROOT(1)=(-B+ROOT(1))/(2.0*A)

C    FIND POSITIVE ROOT

     IF(ROOT(1).GE.0.0.AND.ROOT(2).GE.0.0)PRINT*,'2 +ve
    +ROOTS',ROOT
     IF(ROOT(1).LT.0.0.AND.ROOT(2).LT.0.0)PRINT*,'2 -ve
    +ROOTS',ROOT
     H(J,2)=MAX(ROOT(1),ROOT(2))

     RETURN
     END

     SUBROUTINE CONVCHK(I,G,GOLD)
C    To check for convergence in iterative loop
     DOUBLE PRECISION G(0:3000,2),GOLD
     LOGICAL CONV(4)
     COMMON /BLOCKD/K,IT,NIT,CONV,PPM
     CHARACTER*5 ION(4)
     DATA ION/'Ca2+','H+','CO3--','HCO3-'/

     IF(GOLD.EQ.0.0.AND.G(0,2).EQ.0.0)THEN
       PRINT*,'ZERO CHECK CONV K=',K,ION(I)
     ELSE
     P=1000000.0*(MAX(GOLD,G(0,2))-MIN(GOLD,G(0,2)))/
    +          MAX(GOLD,G(0,2))
     IF (P.LT.PPM) CONV(I)=.TRUE.
     IF (P.GE.PPM.AND.IT.EQ.NIT) THEN
       PRINT100,ION(I),P,K
     ENDIF
     ENDIF
     RETURN
100  FORMAT(1X,'SURFACE [',A5,'] converged to ',F12.3,'ppm'
    +,3(1X),'K=',I4)
     END

     SUBROUTINE NAME(HDAT,V)
C    To provide name for output file relating to flow rate
     IMPLICIT DOUBLE PRECISION(A-H,O-Z)
     CHARACTER*1 DGT1,DGT2,HDAT*10

     IV=INT(V*100.)
     ITENS=INT(V*10)
     DGT1=CHAR(ITENS+48)
     IUNITS=MOD(IV,10)
     DGT2=CHAR(IUNITS+48)
     HDAT='TEMP'//DGT1//DGT2//'.DAT'

     RETURN
     END
```

A4.2 PARTPH

Computer program used to simulate the dissolution of calcium carbonate particles, assuming complete mixing. In this case, the program modelled the "pH-stat" mode of operation.

```
c     Particle Dissolution

      real kKK,KCa,KCO3,Ksp,Ka1,Ka2,Kw,m,N
      double precision Vs,Vsi
      COMMON Ca,H,dmKa1,DMKA2,DMKW,Vs,Vsi,X

      print*,'Solution volume Vs?'
      read*,Vs
      print*,'Mass of CaCO3?'
      read*,m
      print*,'Particle radius a? /um'
      read*,a
      a=a*1.E-4
      print*,'Constant pH'
      read*,pH
      print*,'Max time'
      read*,tmax
      print*,'Time intervals'
      read*,tint

C     Constants (rho = density of CaCO3)
      kKK=950.
      KCa=1.E6
      KCO3=3.E7
      Ksp=6.26E-14
      Ka1=1.E-9
      Ka2=1.409E-13
      Kw=1.45E-20
      dmKa1=Ka1*1.E9
      dmKa2=Ka2*1.E9
      dmKw=Kw*1.E18
      rho=2.930


      y=(10.**-pH)-sqrt(Kw)
      X=(y*y+2.*y*sqrt(Kw))/(y+sqrt(Kw))
      Vsi=Vs
      Vc=m/rho
      N=3.*Vc/(4.*3.141592654*a*a*a)
      Ca=0.
      CO3=0.
      HCO3=0.
      H2CO3s=0.
      H=10.**(-pH-3.)
      OHi=Kw/H

c     Calc mol fractions
      xCO3=1./(1.+(H/Ka2)*(1.+H/Ka1))
      xHCO3=H*xCO3/Ka2
      xH2CO3s=H*xHCO3/Ka1

C     fluxpua = flux per unit area
C     a = particle radius
C     adot = da/dt

      print1001
      do 100 i=0,int(tmax)
        fluxpua=kKK*(Ksp-Ca*CO3)/
     /     ((1.+KCa*Ca)*(1.+KCO3*CO3))
        adot=fluxpua*100.09/rho
        if(mod(i,int(tint)).eq.0)then
          print1000,i,Ca,CO3,HCO3,H2CO3s,Vs,a,adot
        endif
        flux=fluxpua*4.*3.141592654*a*a*N
        Ca=Ca+flux/Vs
        CO3=Ca*xCO3
        HCO3=Ca*xHCO3
        H2CO3s=Ca*xH2CO3s
        Camol=Ca*Vs
        call quart
        Ca=Camol/Vs
        CO3=Ca*xCO3
        HCO3=Ca*xHCO3
        H2CO3s=Ca*xH2CO3s
        a=a-adot
        if(a.le.0.0)a=0.0
100   continue
      phi=Vc/(Vc+Vs)
      Vcf=4.*3.141592654*a*a*a*N/3.
      phif=Vcf/(Vcf+Vs)
      print*,'m=',m,' N=',N,' Vc=',Vc
      print*,' phi=',phi,' phif=',phif
      stop
1000  format(1x,i7,1x,1pe11.5,1x,e8.2,1x,e8.2,1x,e8.2,
     &1x,0pf4.0,1x,1pd8.2,1x,e8.2)
1001  format(1x,4x,'t/s',6x,'Ca',8x
     &,'CO3',5x,'HCO3',4x,'H2CO3*',2x,'Vs',5x,'a',7x,'da/dt')
      end

      SUBROUTINE quart
      real COEFF(5),REZ(5),IMZ(5)
      double precision Vs,Vsi
      COMMON Ca,H,dmKa1,DMKA2,DMKW,Vs,Vsi,X

C     CONVERT VOLS TO dam3

      Ca=Ca*1.0E9
      X=X+(Vs-Vsi)*0.001/Vs
      X=X*1.0E9

      print*,Ca,H,dmKa1,dmKa2,dmKw,Vs,Vsi,X
C     SOLVE QUARTIC FOR [H]

      COEFF(1)=1
      COEFF(2)=dmKa1+2.*Ca-X
      COEFF(3)=dmKa1*Ca-dmKa1*X-dmKw+dmKa1*dmKa2
      COEFF(4)=(-dmKa2*X-dmKw)*dmKa1
      coeff(5)=-dmKa1*dmKa2*dmKw
      N=5
      TOL=X02AJF()
      IFAIL=0
      CALL C02AEF(COEFF,N,REZ,IMZ,TOL,IFAIL)
      IF (IFAIL.NE.0) THEN
        PRINT*,'FAIL',IFAIL
      ENDIF
      do 10 i=1,5
      print*,rez(i),imz(i)
10    continue

C     FIND CORRECT ROOT
      I=1
800   IF (REZ(I).LE.0.0.OR.IMZ(I).NE.0.0) THEN
        I=I+1
        IF (I.EQ.5) THEN
```

```
        PRINT*,'H+ ROOTS NOT POSITIVE REAL'
        I=1
      ELSE
      GOTO 800
      ENDIF
    ENDIF
    hh=REZ(I)

C   RECONVERT VOLS TO cm3
    Ca=Ca*1.0E-9
    hh=hh*1.0E-9
    X=X*1.E-9
    Vs=Vs+(H-hh)*Vs/1.E-3

    RETURN
    END
```

APPENDIX 5

CRYSTALLOGRAPHY OF CALCITE

A5.1 Notation

A cleaved calcite crystal is rhombohedral in shape and as such can be described using rhombohedral axes of equal length and interaxial angle α ($\neq 90°$), see Figure A5.1.

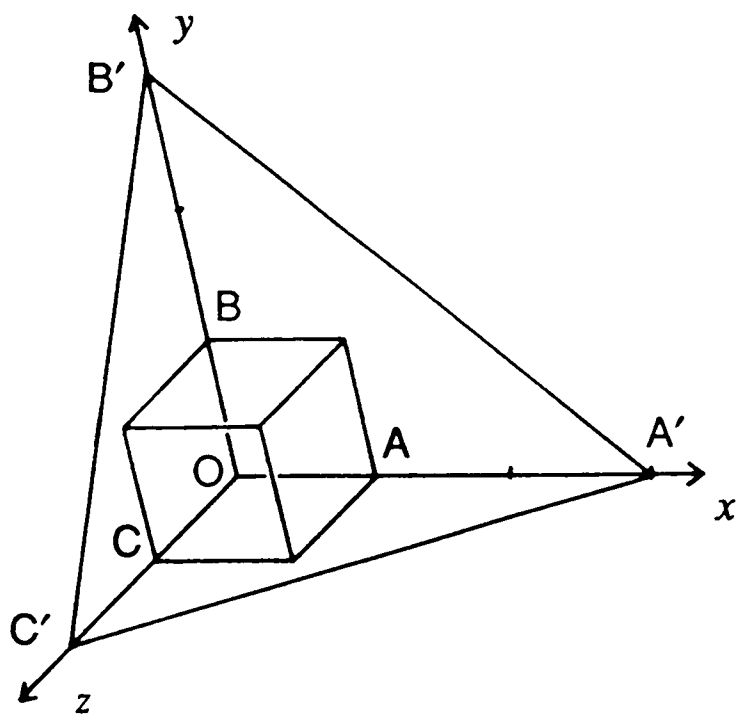

Figure A5.1. Rhombohedral axes, together with the unit cell and the (223) *plane.*

The position of planes, directions and point sites in a lattice are described by reference to the unit cell and the three principal axes, x, y and z. Planes in the crystal structure are referred to using the Miller indices (*hkl*). These are calculated from the values of the intercepts, OA′, OB′ and OC′ in Figure A5.1, where the plane in question crosses the three axes. The Miller indices are the reciprocals of the ratios of the intercepts to the corrresponding unit cell dimensions. Thus the plane A′B′C′ is expressed as

$$\left(\frac{OA}{OA'}, \frac{OB}{OB'}, \frac{OC}{OC'}\right)$$

with the ratios written in the smallest integer form. It should be noted that the Miller indices (111) represent all planes parallel to ABC.

Examining the rhombohedral cell, the Miller indices for all the faces of the unit cell are (100), (010) and (001). In the crystal structure these planes make up a group of the same crystallographic type and are given the collective symbol {100}.

Any direction can be described by the three smallest integers in the ratios of the distance travelled along the three principal axes as a fraction of the unit cell dimensions. In Figure A5.1 the direction OD is defined as [111]. The directions [111], [11$\bar{1}$], [$\bar{1}$1$\bar{1}$] and [$\bar{1}\bar{1}\bar{1}$] are of the same crystallographic type and are collectively described as <111>. Thus the brackets [ ] and ( ) imply specific directions and planes respectively, and the brackets < > and { } refer respectively to directions and planes of the same type.

A5.2 Calcite Structure

The structure of calcite is based on that of NaCl [234] but with the cubic unit cell of halite distorted in order to accommodate the large CO_3 groups, see Figure A5.2a. This results [235] in a face-centred rhombohedral pseudo-cell containing 4 $CaCO_3$. However, this is not a true rhombohedral unit cell because of the orientation of the CO_3 triangles. The rhombohedral unit cell therefore contains 32 $CaCO_3$ with a_r = 12.85 Å and α = 101°55′. The faces of this rhombohedron correspond to the cleavage planes of calcite, which are usually described in

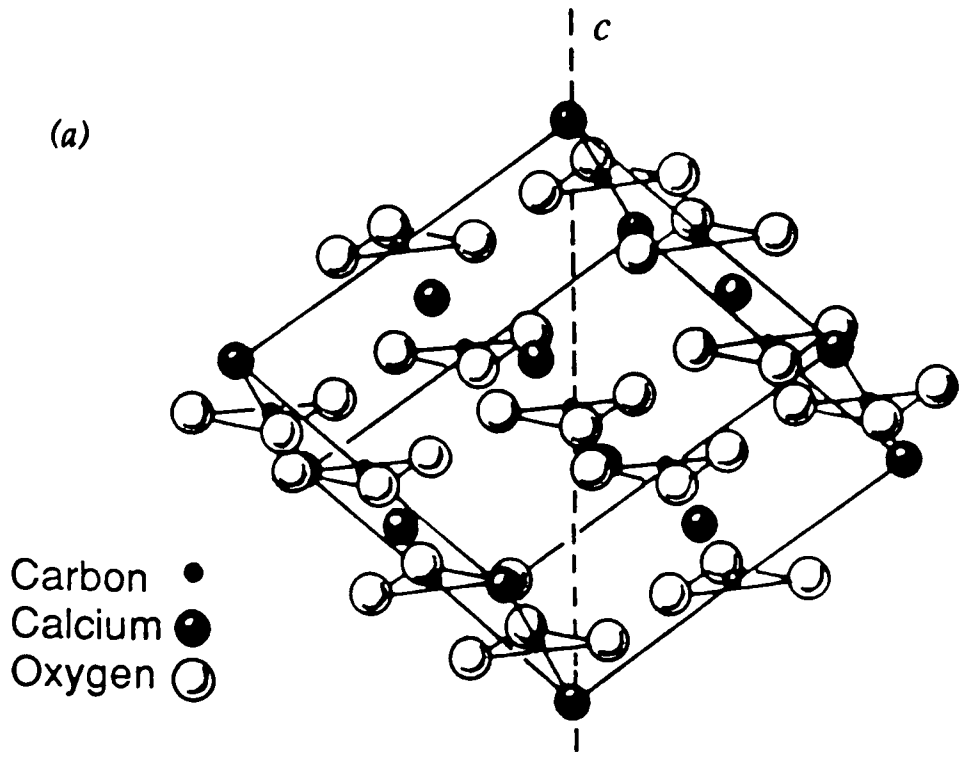

Figure A5.2. (a) Stucture of calcite, shown as the cleavage rhomb. (b) Relationship of the steep, true unit cell to the cleavage rhombohedron. The hexagonal cell is also shown.

morphological studies as {100}, using Miller indicies, or {10$\bar{1}$1} in Miller-Bravais notation. The true unit cell, however, as shown by X-ray crystallography, is a much steeper rhombohedral cell with a_r = 6.37 Å and α = 46°05′ [235]. This is a primitive cell containing 2 $CaCO_3$ with faces {211} (or {40$\bar{4}$4} in Miller-Bravais notation), if the cleavage planes are assumed to be {100}. If the faces of the true unit cell are defined as {100} instead, then the cleavage planes become {211} (Miller-Bravais {10$\bar{1}$4}). Figure A5.2b shows the relationship between the true unit cell and the

cleavage rhombohedron. In addition the alternative hexagonal axes are shown with the associated hexagonal cell.

In this thesis the cleavage planes of calcite have been referred to using the Miller notation and assigning them as the {100} planes.

APPENDIX 6

ANALYTICAL SOLUTION FOR THE IMPEDANCE OF THE BIPARTITE TRANSMISSION LINE

In Chapter 6 a bipartite transmission line equivalent circuit was used to explain the impedance response of a scaled tube partially immersed in electrolyte. The circuit consists of an RC transmission line whose resistance per unit length, $R^{\dagger}$, changes at a point, $x = l_{ss}$, corresponding to the solution meniscus. The impedance of this circuit will be solved analytically below.

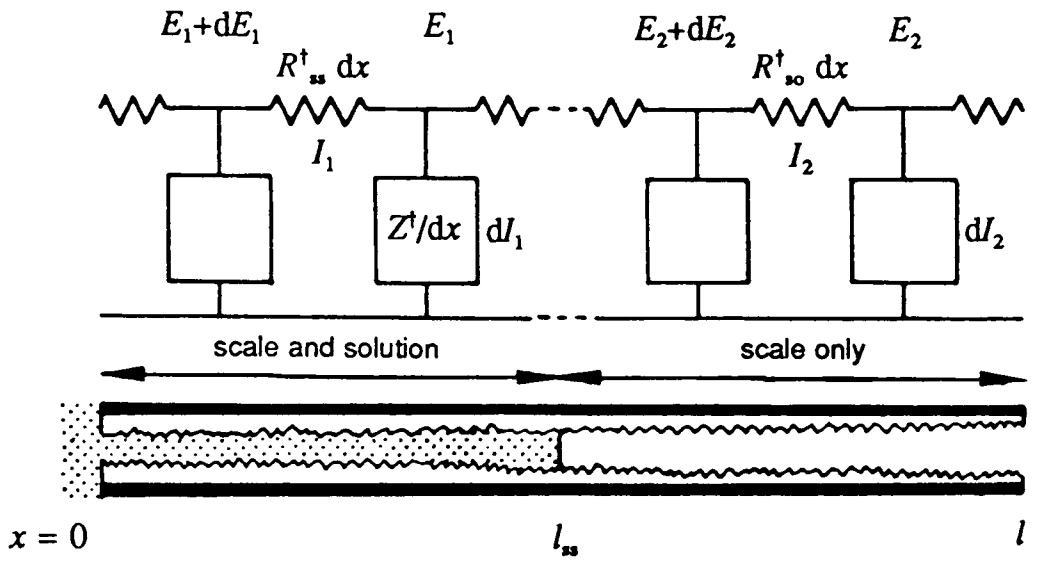

Figure A6.1. Two infinitely small sections of the bipartite transmission line circuit, one either side of $x = l_{ss}$, which is the point corresponding to the solution meniscus.

Consider two infinitesimally small sections dx in the transmission line either side of the meniscus, as shown in Figure A6.1. Provided small amplitude alternating voltages are used, the current response is linear and the impedance is only dependent on the frequency ω. Thus

$$0 \le x \le l_{ss}\ ; \quad dE_1 = -I_1 R^{\dagger}_{ss} dx \quad \Rightarrow \frac{dE_1}{dx} + I_1 R^{\dagger}_{ss} = 0 \tag{A6.1}$$

$$0 \le x \le l_{ss}\ ; \quad dI_1 = -\frac{E_1}{Z^{\dagger}} dx \quad \Rightarrow \frac{dI_1}{dx} + \frac{E_1}{Z^{\dagger}} = 0 \tag{A6.2}$$

and

$$l_{ss} \le x \le l\ ; \quad dE_2 = -I_2 R^{\dagger}_{so} dx \quad \Rightarrow \frac{dE_2}{dx} + I_1 R^{\dagger}_{so} = 0 \tag{A6.3}$$

$$l_{ss} \le x \le l\ ; \quad dI_2 = -\frac{E_2}{Z^{\dagger}} dx \quad \Rightarrow \frac{dI_2}{dx} + \frac{E_2}{Z^{\dagger}} = 0 \tag{A6.4}$$

where x is the direction along the transmission line, $R^{\dagger}_{ss}$ is the resistance per unit length of the first section of the transmission line (representing scale and soloution), $R^{\dagger}_{so}$ is the resistance per unit length of the second section (scale only) and $Z^{\dagger}$ the impedance per unit length of the electrolyte-electrode interface.

Combining equations (A6.1), (A6.2) and (A6.3), (A6.4) gives the following differential equations

$$0 \le x \le l_{ss}\ ; \quad \frac{d^2 I_1}{dx^2} - \frac{R^{\dagger}_{ss}}{Z^{\dagger}} I_1 = 0 \tag{A6.5}$$

$$0 \le x \le l_{ss}\ ; \quad \frac{d^2 E_1}{dx^2} - \frac{R^{\dagger}_{ss}}{Z^{\dagger}} E_1 = 0 \tag{A6.6}$$

and

$$l_{ss} \le x \le l\ ; \quad \frac{d^2 I_2}{dx^2} - \frac{R^{\dagger}_{so}}{Z^{\dagger}} I_2 = 0 \tag{A6.7}$$

$$l_{ss} \le x \le l\ ; \quad \frac{d^2 E_2}{dx^2} - \frac{R^{\dagger}_{so}}{Z^{\dagger}} E_2 = 0 \tag{A6.8}$$

Solving the differential equation (A6.6) yields

$$0 \le x \le l_{ss}\ ; \quad E_1(x) = A\exp\left(-x\sqrt{\frac{R^{\dagger}_{ss}}{Z^{\dagger}}}\right) + B\exp\left(+x\sqrt{\frac{R^{\dagger}_{ss}}{Z^{\dagger}}}\right) \tag{A6.9}$$

where A and B are defined by the following boundary condition

$$x = 0\ ; \quad A + B = E_o \tag{A6.10}$$

Similarly solving equation (A6.8) gives

$$l_{ss} \le x \le l \; ; \quad E_2(x) = A' \exp\left(-x\sqrt{\frac{R_{so}^{\dagger}}{Z^{\dagger}}}\right) + B' \exp\left(+x\sqrt{\frac{R_{so}^{\dagger}}{Z^{\dagger}}}\right) \tag{A6.11}$$

Applying the boundary condition at the other end of the transmission line

$$\left.\frac{dE_2}{dx}\right|_{x=0} = 0 \tag{A6.12}$$

together with the differential of equation (A6.11) yields

$$A' = B' \exp\left(2l\sqrt{\frac{R_{so}}{Z^{\dagger}}}\right) \tag{A6.13}$$

At the boundary $x = l_{ss}$ the potentials must be identical, thus

$$E_1(l_{ss}) = E_2(l_{ss}) \tag{A6.14}$$

as must be the current

$$\frac{1}{R_{ss}}\left.\frac{dE_1}{dx}\right|_{x=l_{ss}} = \frac{1}{R_{so}}\left.\frac{dE_2}{dx}\right|_{x=l_{ss}} \tag{A6.15}$$

Substituting the terms for E_1 and E_2 into these boundary conditions and solving the simultaneous equations yields the pre-exponential factor

$$B = E_o \exp\left(-l_{ss}\sqrt{\frac{R_{ss}^{\dagger}}{Z^{\dagger}}}\right) \frac{\left\{\begin{array}{l}\left(\sqrt{R_{so}^{\dagger}} - \sqrt{R_{ss}^{\dagger}}\right)\exp\left[(2l - l_{ss})\sqrt{\frac{R_{so}^{\dagger}}{Z^{\dagger}}} - 2l_{ss}\sqrt{\frac{R_{ss}^{\dagger}}{Z^{\dagger}}}\right] + \\ \left(\sqrt{R_{so}^{\dagger}} + \sqrt{R_{ss}^{\dagger}}\right)\exp\left[l_{ss}\sqrt{\frac{R_{so}^{\dagger}}{Z^{\dagger}}} - l_{ss}\sqrt{\frac{R_{ss}^{\dagger}}{Z^{\dagger}}}\right]\end{array}\right\}}{\left\{\begin{array}{l}\left(\sqrt{R_{so}^{\dagger}} - \sqrt{R_{ss}^{\dagger}}\right)\exp\left[(2l - l_{ss})\sqrt{\frac{R_{so}^{\dagger}}{Z^{\dagger}}} - 2l_{ss}\sqrt{\frac{R_{ss}^{\dagger}}{Z^{\dagger}}}\right] + \\ \left(\sqrt{R_{so}^{\dagger}} + \sqrt{R_{ss}^{\dagger}}\right)\exp\left[l_{ss}\sqrt{\frac{R_{so}^{\dagger}}{Z^{\dagger}}} - 2l_{ss}\sqrt{\frac{R_{ss}^{\dagger}}{Z^{\dagger}}}\right] + \\ \left(\sqrt{R_{so}^{\dagger}} + \sqrt{R_{ss}^{\dagger}}\right)\exp\left[(2l - l_{ss})\sqrt{\frac{R_{so}^{\dagger}}{Z^{\dagger}}}\right] + \\ \left(\sqrt{R_{so}^{\dagger}} - \sqrt{R_{ss}^{\dagger}}\right)\exp\left[l_{ss}\sqrt{\frac{R_{so}^{\dagger}}{Z^{\dagger}}}\right]\end{array}\right\}} \qquad \text{(A6.16)}$$

The current in the first section of the transmission line is described by equation (A6.1), which, on substituting the differential of equation (A6.9), can be rewritten as

$$0 \le x \le l_{ss}\ ; \quad I(x) = -\frac{1}{\sqrt{Z^{\dagger}R_{ss}^{\dagger}}}\left\{(B - E)\exp\left(-x\sqrt{\frac{R_{ss}^{\dagger}}{Z^{\dagger}}}\right) + B\exp\left(x\sqrt{\frac{R_{ss}^{\dagger}}{Z^{\dagger}}}\right)\right\} \qquad \text{(A6.17)}$$

At the mouth of the tube the current is given by

$$I(0) = -\frac{1}{\sqrt{Z^{\dagger}R_{ss}^{\dagger}}}(2B - E_o) \qquad \text{(A6.18)}$$

which on substituting equation (A6.16) yields

$$I(0) = \left(\frac{E_o}{\sqrt{Z^\dagger R_{ss}^\dagger}}\right) \frac{\left\{ \begin{array}{l} -\left(\sqrt{R_{so}^\dagger} - \sqrt{R_{ss}^\dagger}\right)\exp\left[\left(2l - l_{ss}\right)\sqrt{\frac{R_{so}^\dagger}{Z^\dagger}} - 2l_{ss}\sqrt{\frac{R_{ss}^\dagger}{Z^\dagger}}\right] - \\ \left(\sqrt{R_{so}^\dagger} + \sqrt{R_{ss}^\dagger}\right)\exp\left[l_{ss}\sqrt{\frac{R_{so}^\dagger}{Z^\dagger}} - 2l_{ss}\sqrt{\frac{R_{ss}^\dagger}{Z^\dagger}}\right] + \\ \left(\sqrt{R_{so}^\dagger} + \sqrt{R_{ss}^\dagger}\right)\exp\left[\left(2l - l_{ss}\right)\sqrt{\frac{R_{so}^\dagger}{Z^\dagger}}\right] + \\ \left(\sqrt{R_{so}^\dagger} - \sqrt{R_{ss}^\dagger}\right)\exp\left[l_{ss}\sqrt{\frac{R_{so}^\dagger}{Z^\dagger}}\right] \end{array} \right\}}{\left\{ \begin{array}{l} \left(\sqrt{R_{so}^\dagger} - \sqrt{R_{ss}^\dagger}\right)\exp\left[\left(2l - l_{ss}\right)\sqrt{\frac{R_{so}^\dagger}{Z^\dagger}} - 2l_{ss}\sqrt{\frac{R_{ss}^\dagger}{Z^\dagger}}\right] + \\ \left(\sqrt{R_{so}^\dagger} + \sqrt{R_{ss}^\dagger}\right)\exp\left[l_{ss}\sqrt{\frac{R_{so}^\dagger}{Z^\dagger}} - 2l_{ss}\sqrt{\frac{R_{ss}^\dagger}{Z^\dagger}}\right] + \\ \left(\sqrt{R_{so}^\dagger} + \sqrt{R_{ss}^\dagger}\right)\exp\left[\left(2l - l_{ss}\right)\sqrt{\frac{R_{so}^\dagger}{Z^\dagger}}\right] + \\ \left(\sqrt{R_{so}^\dagger} - \sqrt{R_{ss}^\dagger}\right)\exp\left[l_{ss}\sqrt{\frac{R_{so}^\dagger}{Z^\dagger}}\right] \end{array} \right\}} \qquad \text{(A6.19)}$$

Hence the impedance of the bipartite transmission line is given by

$$Z_{2tml} = \sqrt{Z^{\dagger}R_{ss}^{\dagger}}\,\frac{\left\{\begin{array}{l}\left(\sqrt{R_{so}^{\dagger}}-\sqrt{R_{ss}^{\dagger}}\right)\exp\left[(2l-l_{ss})\sqrt{\frac{R_{so}^{\dagger}}{Z^{\dagger}}}-2l_{ss}\sqrt{\frac{R_{ss}^{\dagger}}{Z^{\dagger}}}\right]+\\ \left(\sqrt{R_{so}^{\dagger}}+\sqrt{R_{ss}^{\dagger}}\right)\exp\left[l_{ss}\sqrt{\frac{R_{so}^{\dagger}}{Z^{\dagger}}}-2l_{ss}\sqrt{\frac{R_{ss}^{\dagger}}{Z^{\dagger}}}\right]+\\ \left(\sqrt{R_{so}^{\dagger}}+\sqrt{R_{ss}^{\dagger}}\right)\exp\left[(2l-l_{ss})\sqrt{\frac{R_{so}^{\dagger}}{Z^{\dagger}}}\right]+\\ \left(\sqrt{R_{so}^{\dagger}}-\sqrt{R_{ss}^{\dagger}}\right)\exp\left[l_{ss}\sqrt{\frac{R_{so}^{\dagger}}{Z^{\dagger}}}\right]\end{array}\right\}}{\left\{\begin{array}{l}-\left(\sqrt{R_{so}^{\dagger}}-\sqrt{R_{ss}^{\dagger}}\right)\exp\left[(2l-l_{ss})\sqrt{\frac{R_{so}^{\dagger}}{Z^{\dagger}}}-2l_{ss}\sqrt{\frac{R_{ss}^{\dagger}}{Z^{\dagger}}}\right]-\\ \left(\sqrt{R_{so}^{\dagger}}+\sqrt{R_{ss}^{\dagger}}\right)\exp\left[l_{ss}\sqrt{\frac{R_{so}^{\dagger}}{Z^{\dagger}}}-2l_{ss}\sqrt{\frac{R_{ss}^{\dagger}}{Z^{\dagger}}}\right]+\\ \left(\sqrt{R_{so}^{\dagger}}+\sqrt{R_{ss}^{\dagger}}\right)\exp\left[(2l-l_{ss})\sqrt{\frac{R_{so}^{\dagger}}{Z^{\dagger}}}\right]+\\ \left(\sqrt{R_{so}^{\dagger}}-\sqrt{R_{ss}^{\dagger}}\right)\exp\left[l_{ss}\sqrt{\frac{R_{so}^{\dagger}}{Z^{\dagger}}}\right]\end{array}\right\}} \qquad \text{(A6.20)}$$

A6.1 Bipartite Transmission Line with Purely Capacitative Interfacial Impedance

If the impedance $Z^{\dagger}$ in Figure A6.1 is replaced by a pure capacitance $C^{\dagger}$ then the following substitution can be made

$$Z^{\dagger} = +\frac{1}{j\omega C^{\dagger}} \qquad \text{(A6.21)}$$

Also given that

$$\sqrt{j} = \frac{1}{\sqrt{2}}(1+j) \qquad \text{(A6.22)}$$

and

$$\sqrt{-j} = \frac{1}{\sqrt{2}}(1-j) \qquad \text{(A6.23)}$$

and making the following abbreviations

$$\alpha = \left(\frac{R_{ss}^{\dagger}}{2\omega C^{\dagger}}\right)^{1/2}\left\{(2l - l_{ss})\sqrt{\frac{R_{so}^{\dagger}}{Z^{\dagger}}} - 2l_{ss}\sqrt{\frac{R_{ss}^{\dagger}}{Z^{\dagger}}}\right\} \tag{A6.24}$$

$$\beta = \left(\frac{R_{ss}^{\dagger}}{2\omega C^{\dagger}}\right)^{1/2}\left\{l_{ss}\sqrt{\frac{R_{so}^{\dagger}}{Z^{\dagger}}} - 2l_{ss}\sqrt{\frac{R_{ss}^{\dagger}}{Z^{\dagger}}}\right\} \tag{A6.25}$$

$$\gamma = \left(\frac{R_{ss}^{\dagger}}{2\omega C^{\dagger}}\right)^{1/2}(2l - l_{ss})\sqrt{\frac{R_{so}^{\dagger}}{Z^{\dagger}}} \tag{A6.26}$$

$$\delta = \left(\frac{R_{ss}^{\dagger}}{2\omega C^{\dagger}}\right)^{1/2} l_{ss}\sqrt{\frac{R_{so}^{\dagger}}{Z^{\dagger}}} \tag{A6.27}$$

equation (A6.20) becomes

$$Z_{2tml} = (1 - j)\left(\frac{R_{ss}^{\dagger}}{2\omega C^{\dagger}}\right)\frac{\left\{\begin{array}{l}\left(\sqrt{R_{so}^{\dagger}} - \sqrt{R_{ss}^{\dagger}}\right)\exp[(1+j)\alpha] \\ + \left(\sqrt{R_{so}^{\dagger}} + \sqrt{R_{ss}^{\dagger}}\right)\exp[(1+j)\beta] \\ + \left(\sqrt{R_{so}^{\dagger}} + \sqrt{R_{ss}^{\dagger}}\right)\exp[(1+j)\gamma] \\ + \left(\sqrt{R_{so}^{\dagger}} - \sqrt{R_{ss}^{\dagger}}\right)\exp[(1+j)\delta]\end{array}\right\}}{\left\{\begin{array}{l}-\left(\sqrt{R_{so}^{\dagger}} - \sqrt{R_{ss}^{\dagger}}\right)\exp[(1+j)\alpha] \\ -\left(\sqrt{R_{so}^{\dagger}} + \sqrt{R_{ss}^{\dagger}}\right)\exp[(1+j)\beta] \\ + \left(\sqrt{R_{so}^{\dagger}} + \sqrt{R_{ss}^{\dagger}}\right)\exp[(1+j)\gamma] \\ + \left(\sqrt{R_{so}^{\dagger}} - \sqrt{R_{ss}^{\dagger}}\right)\exp[(1+j)\delta]\end{array}\right\}} \tag{A6.28}$$

Rewriting in trigonometric form gives

$$Z_{2tml} = (1-j)\left(\frac{R_{ss}^{\dagger}}{2\omega C^{\dagger}}\right)^{1/2} \frac{\left\{\begin{array}{l}\left(\sqrt{R_{so}^{\dagger}}-\sqrt{R_{ss}^{\dagger}}\right)e^{\alpha}\cos\alpha+\left(\sqrt{R_{so}^{\dagger}}+\sqrt{R_{ss}^{\dagger}}\right)e^{\beta}\cos\beta \\ +\left(\sqrt{R_{so}^{\dagger}}+\sqrt{R_{ss}^{\dagger}}\right)e^{\gamma}\cos\gamma+\left(\sqrt{R_{so}^{\dagger}}-\sqrt{R_{ss}^{\dagger}}\right)e^{\delta}\cos\delta \\ +j\left[\begin{array}{l}\left(\sqrt{R_{so}^{\dagger}}-\sqrt{R_{ss}^{\dagger}}\right)e^{\alpha}\sin\alpha+\left(\sqrt{R_{so}^{\dagger}}+\sqrt{R_{ss}^{\dagger}}\right)e^{\beta}\sin\beta \\ +\left(\sqrt{R_{so}^{\dagger}}+\sqrt{R_{ss}^{\dagger}}\right)e^{\gamma}\sin\gamma+\left(\sqrt{R_{so}^{\dagger}}-\sqrt{R_{ss}^{\dagger}}\right)e^{\delta}\sin\delta\end{array}\right]\end{array}\right\}}{\left\{\begin{array}{l}-\left(\sqrt{R_{so}^{\dagger}}-\sqrt{R_{ss}^{\dagger}}\right)e^{\alpha}\cos\alpha-\left(\sqrt{R_{so}^{\dagger}}+\sqrt{R_{ss}^{\dagger}}\right)e^{\beta}\cos\beta \\ +\left(\sqrt{R_{so}^{\dagger}}+\sqrt{R_{ss}^{\dagger}}\right)e^{\gamma}\cos\gamma+\left(\sqrt{R_{so}^{\dagger}}-\sqrt{R_{ss}^{\dagger}}\right)e^{\delta}\cos\delta \\ +j\left[\begin{array}{l}-\left(\sqrt{R_{so}^{\dagger}}-\sqrt{R_{ss}^{\dagger}}\right)e^{\alpha}\sin\alpha-\left(\sqrt{R_{so}^{\dagger}}+\sqrt{R_{ss}^{\dagger}}\right)e^{\beta}\sin\beta \\ +\left(\sqrt{R_{so}^{\dagger}}+\sqrt{R_{ss}^{\dagger}}\right)e^{\gamma}\sin\gamma+\left(\sqrt{R_{so}^{\dagger}}-\sqrt{R_{ss}^{\dagger}}\right)e^{\delta}\sin\delta\end{array}\right]\end{array}\right\}} \quad \text{(A6.29)}$$

Multiplying the numerator and denominator by the complex conjugate of the latter and making the following abbreviations

$$\zeta_{cos1} = \left(\sqrt{R_{so}^{\dagger}}-\sqrt{R_{ss}^{\dagger}}\right)e^{\alpha}\cos\alpha+\left(\sqrt{R_{so}^{\dagger}}+\sqrt{R_{ss}^{\dagger}}\right)e^{\beta}\cos\beta +\left(\sqrt{R_{so}^{\dagger}}+\sqrt{R_{ss}^{\dagger}}\right)e^{\gamma}\cos\gamma+\left(\sqrt{R_{so}^{\dagger}}-\sqrt{R_{ss}^{\dagger}}\right)e^{\delta}\cos\delta \quad \text{(A6.30)}$$

$$\zeta_{cos2} = -\left(\sqrt{R_{so}^{\dagger}}-\sqrt{R_{ss}^{\dagger}}\right)e^{\alpha}\cos\alpha-\left(\sqrt{R_{so}^{\dagger}}+\sqrt{R_{ss}^{\dagger}}\right)e^{\beta}\cos\beta +\left(\sqrt{R_{so}^{\dagger}}+\sqrt{R_{ss}^{\dagger}}\right)e^{\gamma}\cos\gamma+\left(\sqrt{R_{so}^{\dagger}}-\sqrt{R_{ss}^{\dagger}}\right)e^{\delta}\cos\delta \quad \text{(A6.31)}$$

$$\zeta_{sin1} = \left(\sqrt{R_{so}^{\dagger}}-\sqrt{R_{ss}^{\dagger}}\right)e^{\alpha}\sin\alpha+\left(\sqrt{R_{so}^{\dagger}}+\sqrt{R_{ss}^{\dagger}}\right)e^{\beta}\sin\beta +\left(\sqrt{R_{so}^{\dagger}}+\sqrt{R_{ss}^{\dagger}}\right)e^{\gamma}\sin\gamma+\left(\sqrt{R_{so}^{\dagger}}-\sqrt{R_{ss}^{\dagger}}\right)e^{\delta}\sin\delta \quad \text{(A6.32)}$$

$$\zeta_{sin2} = -\left(\sqrt{R_{so}^{\dagger}}-\sqrt{R_{ss}^{\dagger}}\right)e^{\alpha}\sin\alpha-\left(\sqrt{R_{so}^{\dagger}}+\sqrt{R_{ss}^{\dagger}}\right)e^{\beta}\sin\beta +\left(\sqrt{R_{so}^{\dagger}}+\sqrt{R_{ss}^{\dagger}}\right)e^{\gamma}\sin\gamma+\left(\sqrt{R_{so}^{\dagger}}-\sqrt{R_{ss}^{\dagger}}\right)e^{\delta}\sin\delta \quad \text{(A6.33)}$$

equation (A6.29) becomes

$$Z_{2tml} = \left(\frac{R_{ss}^{\dagger}}{2\omega C^{\dagger}}\right)^{1/2} \frac{\left\{\begin{array}{l}\left(\zeta_{cos1}\zeta_{cos2}+\zeta_{sin1}\zeta_{sin2}+\zeta_{cos2}\zeta_{sin1}-\zeta_{cos1}\zeta_{sin2}\right) \\ +j\left(\zeta_{cos2}\zeta_{sin1}-\zeta_{cos1}\zeta_{sin2}-\zeta_{cos1}\zeta_{cos2}-\zeta_{sin1}\zeta_{sin2}\right)\end{array}\right\}}{\left(\zeta_{cos2}^{2}+\zeta_{sin2}^{2}\right)} \quad \text{(A6.34)}$$

Using equation (A6.34), the real and imaginary components of the bipartite transmission line circuit can be calculated for any given frequency ω. (An uncompensated solution resistance, R_u, was added to the real component to model actual experimental data).

REFERENCES

1. I. Mills, T. Cvitaš, K. Homann, N. Kallay, K. Kuchitsu; "Quantities, Units and Symbols in Physical Chemistry", IUPAC, Blackwell Scientific Publications, Oxford, 1988.
2. K.B. Oldham and C.G. Zoski, in "Comprehensive Chemical Kinetics", Eds. C.H. Bamford and R.G. Compton, Vol. 26, p. 92.
3. A. Fick, *Philosophical Magazine*, 10, 30 (1855).
4. A. Fick, *Poggendorf's Annalen der Physik und Chemie*, 94, 59 (1855).
5. C.M.A. Brett and A.M.C.F. Oliveira Brett, in "Comprehensive Chemical Kinetics", Eds. C.H. Bamford and R.G. Compton, Vol. 26, p. 356.
6. K.B. Oldham and C.G. Zoski, in "Comprehensive Chemical Kinetics", Eds. C.H. Bamford and R.G. Compton, Vol. 26, p. 113.
7. K.B. Oldham and C.G. Zoski, in "Comprehensive Chemical Kinetics", Eds. C.H. Bamford and R.G. Compton, Vol. 26, p. 122.
8. Southampton Electrochemistry Group, "Instrumental Methods in Electrochemistry", Ellis Horwood, Chichester, 1985, p. 26.
9. H.J.M. Hanley (ed.), "Transport Phenomena in Fluids", Dekker, New York, 1969.
10. J.G. Boguski, *Chem. Ber.*, 9, 1442, 1599, 1646 (1876).
11. J.G. Boguski and N. Kajander, *Chem. Ber.*, 10, 34 (1877).
12. W. Spring, *Z. Phys. Chem. (Leipzig)*, 1, 209 (1887).
13. W. Spring, *Z. Phys. Chem. (Leipzig)*, 2, 13 (1888).
14. P.R. Unwin, D. Phil. Thesis, Oxford University, 1989.
15. R.G. Compton and P.R. Unwin, *Phil. Trans. R. Soc. Lond. A*, 330, 1 (1990).
16. L.N. Plummer, D.L. Parkhurst and T.M.L. Wigley, *Am. Chem. Soc. Symp. Ser.*, 93, 537 (1979).
17. J.W. Morse and R.A. Berner, in "Chemical Modelling in Aqueous Systems", Ed. E.A. Jenne, *Am. Chem. Soc. Symp. Ser.*, 93, 499 (1979).
18. J.W. Morse, *Rev. Mineral.*, 11, 227 (1983).
19. G. Dorange and A. Guetchidjian, *Comptes Rendu Acad. Sc. Paris Ser. C*, 286, 159 (1978).
20. J.W. Morse, *Am. J. Sci.*, 274, 97 (1974).
21. R.A. Berner and J.W. Morse, *Am. J. Sci.*, 274, 108 (1974).
22. J.W. Morse, *Am. J. Sci.*, 274, 638 (1974).
23. J.W. Morse, *Am. J. Sci.*, 278, 344 (1978).
24. J.W. Morse, J. de Kanel and K. Harris, *Am. J. Sci.*, 279, 488 (1979).
25. L.N. Plummer and T.M.L. Wigley, *Geochim. Cosmochim. Acta*, 40, 191 (1976).
26. L.N. Plummer, T.M.L. Wigley and D.L. Parkhurst, *Am. J. Sci.*, 278, 179 (1978).
27. J.W. Mullin, "Crystallisation", Chemical Rubber Company Press, Cleveland, 1972, p. 480.
28. E.L. Sjöberg, *Geochim. Cosmochim. Acta*, 40, 441 (1976).
29. E.L. Sjöberg, *Stockholm Contrib. Geol.*, 32, 1 (1978).
30. E.L. Sjöberg and D. Rickard, *Geochim. Cosmochim. Acta*, 47, 2281 (1983).
31. D. Rickard and E.L. Sjöberg, *Am. J. Sci.*, 283, 815 (1983).
32. E.L. Sjöberg and D. Rickard, *Chem. Geol.*, 42, 119 (1984).

33. E.L. Sjöberg and D. Rickard, *Chem. Geol.*, 49, 405 (1985).
34. E.L. Sjöberg and D. Rickard, *Geochim. Cosmochim. Acta*, 48, 485 (1984).
35. R.G. Compton and P.J. Daly, *J. Colloid Interface Sci.*, 101, 159 (1984).
36. R.G. Compton, P.J. Daly and W.A. House, *J. Colloid Interface Sci.*, 113, 12 (1986).
37. R.G. Compton and P.J. Daly, *J. Colloid Interface Sci.*, 115, 493 (1987).
38. J. Schott, S. Brantley, D. Crerar, C. Guy, M. Borcsik and C. Willaime, *Geochim. Cosmochim. Acta*, 53, 373 (1989).
39. D. Buhmann and W. Dreybrodt, *Chem. Geol.*, 48, 189 (1985).
40. D. Buhmann and W. Dreybrodt, *Chem. Geol.*, 53, 109 (1985).
41. J. Baumann, D. Buhmann, W. Dreybrodt and H.D. Schulz, *Chem. Geol.*, 53, 219 (1985).
42. W. Dreybrodt and D. Buhmann, *Chem. Geol.*, 90, 107 (1991).
43. L. Chou, R.M. Garrels and R. Wollast, *Chem. Geol.*, 78, 269 (1989).
44. L. Chou and R. Wollast, *Geochim. Cosmochim. Acta*, 48, 2205 (1984).
45. M.M. Reddy and G.H. Nancollas, *J. Colloid Interface Sci.*, 36, 166 (1971).
46. G.H. Nancollas and M.M. Reddy, *J. Colloid Interface Sci.*, 37, 824 (1971).
47. H.N.S. Wiechers, P. Sturrock and G.V.R. Marais, *Water Res.*, 9, 835 (1975).
48. T.F. Kazmierczak, M.B. Tomson and G.H. Nancollas, *J. Phys. Chem.*, 86, 103 (1982).
49. W.P. Inskeep and P.R. Bloom, *Geochim. Cosmochim. Acta*, 49, 2165 (1985).
50. M.M. Reddy, *Verh. Internat. Verein. Limnol.*, 19, 429 (1975).
51. M.M. Reddy, *J. Crystal Growth*, 41, 287 (1977).
52. M.M. Reddy and G.H. Nancollas, *Desalination*, 12, 61 (1973).
53. M.M. Reddy, L.N. Plummer and E. Busenburg, *Geochim. Cosmochim. Acta*, 45,1281 (1981).
54. S. Zhong and A. Mucci, *Chem. Geol.*, 78, 283 (1989).
55. A. Mucci and J.W. Morse, *Geochim. Cosmochim. Acta*, 47, 217 (1983).
56. A. Mucci, *Geochim. Cosmochim. Acta*, 50, 2255 (1986).
57. E.A. Burton and L.M. Walter, *Geochim. Cosmochim. Acta*, 54, 797 (1990).
58. E.L. Dromgoole and L.M. Walter, *Geochim. Cosmochim. Acta*, 54, 2991 (1990).
59. C.W. Davies and A.L. Jones, *Discuss. Faraday Soc.*, 5, 103 (1949).
60. C.W. Davies and A.L. Jones, *Trans. Faraday Soc.*, 51, 812 (1955).
61. T. Foxall, G.C. Peterson, H.M. Rendall and A.L. Smith, *J. Chem. Soc., Faraday Trans. I*, 75, 1034 (1979).
62. D.W. Thompson and P.G. Pownall, *J. Colloid Interface Sci.*, 131, 74 (1989).
63. W.A. House, *J. Chem. Soc., Faraday Trans. I*, 77, 341 (1981).
64. A.E. Nielsen, "Kinetics of Precipitation", Pergamon, Oxford, 1964.
65. G.E. Cassford, W.A. House and A.D. Pethybridge, *J. Chem. Soc., Faraday Trans. I*, 79, 1617 (1983).
66. J. Christoffersen and M.R. Christoffersen, *J. Crystal Growth*, 100, 203 (1990).
67. A.E. Nielsen, *J. Crystal Growth*, 67, 289 (1984).
68. W.A. House, in "Comprehensive Chemical Kinetics", Ed. R.G. Compton, Vol. 28, Chap. 3.

69. W.K. Burton, N. Cabrera and F.C. Frank, *Phil. Trans. R. Soc. Lond. Ser. A*, 243, 299 (1951).
70. R.B. Bird, W.E. Stewart and E.N. Lightfoot, "Transport Phenomena", Wiley, New York, 1960, p. 47.
71. V.G. Levich, "Physicochemical Hydrodynamics", Prentice-Hall, Englewood Cliffs, 1962, p. 32.
72. J.S. Newman, "Electrochemical Systems", Prentice-Hall, Englewood Cliffs, 1962.
73. B.A. Coles and R.G. Compton, *J. Electroanal. Chem.*, 144, 87 (1983).
74. V.G. Levich, "Physicochemical Hydrodynamics", Prentice-Hall, Englewood Cliffs, 1962, pp. 112-116.
75. M.A. Lévêque, *Ann. Mines Mem. Ser. 12*, 13, 201 (1928).
76. P.R. Unwin and R.G. Compton, *J. Electroanal. Chem.*, 245, 287 (1988).
77. J.L. Anderson and S. Moldoveanu, *J. Electroanal. Chem.*, 179, 107 (1984).
78. J.B. Flanagan and L. Marcoux, *J. Phys. Chem.*, 78, 718 (1974).
79. K.B. Oldham, *J. Electroanal. Chem.*, 122, 1 (1981).
80. P. Pastore, F. Magno, I. Lavagnini and C. Amatore, *J. Electroanal. Chem.*, 301, 1 (1991).
81. M.R. Goldman and L.R. Barrett, *Trans. Inst. Chem. Eng.*, 47, T29 (1969).
82. A.A. Wragg, *Electrochim. Acta*, 16, 373 (1971).
83. R. Alkire and A.A. Mirarefi, *J. Electrochem. Soc.*, 124, 1043 (1977).
84. D. Britz, "Digital Simulation in Electrochemistry", 2nd Edition, Springer-Verlag, Berlin Heidelburg, 1988.
85. J. Crank & P. Nicolson, *Proc. Cambridge Phil. Soc.*, 43, 50 (1947).
86. S. Moldoveanu and J.L. Anderson, *J. Electroanal. Chem.*, 175, 67 (1984).
87. S.G. Weber and W.C. Purdy, *Anal. Chim. Acta*, 100, 531 (1978).
88. P. Laasonen, *Acta Math.*, 81, 309 (1949).
89. R.G. Compton, M.B.G. Pilkington and G.M. Stearn, *J. Chem. Soc., Faraday Trans. I*, 84, 2155 (1988).
90. R.G. Compton, A.C. Fisher, R.G. Wellington, D. Bethell and P. Lederer, *J. Phys. Chem.*, 95, 4749 (1991).
91. L. Lapidus and G.F. Pinder, "Numerical Solution of Partial Differential Equations in Science and Engineering", Wiley, New York, 1982.
92. W. Lang, *Zeiss Information*, 70, 114 (1964).
93. R.C. Weast, "Handbook of Chemistry and Physics", 55th Edition, Chemical Rubber Company, Cleveland, 1975.
94. G.J. Janz, in "Reference Electrodes", Eds. D.J.G. Ives & G.J. Janz, Academic Press, 1961, p. 205.
95. M. Stackelburg, M. Pilgram and V. Toome, *Z. Elektrochem.*, 57, 342 (1953).
96. W. Stumm and J.J. Morgan, "Aquatic Chemistry", 2nd Edition, Wiley, New York, 1981.
97. D.N. Hague, "Fast Reactions", Wiley-Interscience, London, 1971, p. 84.
98. D.D. Perrin, "Dissociation Constants of Inorganic Acids and Bases in Aqueous Solution", IUPAC, Butterworths, London, 1969, p. 213.
99. H.S. Harned and S.R. Scholes, *J. Am. Chem. Soc.*, 63, 1706 (1941).
100. A.C. Walker, U.B. Brar and J. Johnston, *J. Am. Chem. Soc.*, 49, 1235 (1929).

101. K.B. Krauskopf, "Introduction to Geochemistry", McGraw-Hill, New York, 1967, p. 74.
102. R.L. Jacobson and D. Langmuir, *Geochim. Cosmochim. Acta*, 38, 301 (1974).
103. L.N. Plummer and E. Busenberg, *Geochim. Cosmochim. Acta*, 46, 1011 (1982).
104. O.I. Martinova, L.G. Vasina and S.A. Pozdnyakova, *Dokl. Akad. Nauk SSSR*, 205, 1110 (1971).
105. L. Ghiringhelli and G. Bianucci, *Ann. Idrol.*, 1, 36 (1963).
106. G.W. Akin and J.V. Lagerwerff, *Geochim. Cosmochim. Acta*, 29, 353 (1965).
107. G. Grèzes and M. Basset, *C.R. Hebd. Seances Acad. Sci.*, 260, 869 (1965).
108. T.E. Larson and A.M. Buswell, *J. Am. Water Works Ass.*, 34, 1667 (1942).
109. F.J. Millero, P.J. Milne and V.L. Thurmond, *Geochim. Cosmochim. Acta*, 48, 1141 (1984).
110. G.L. Frear and J. Johnston, *J. Am. Chem. Soc.*, 51, 1082 (1929).
111. M. Wolf, O. Breitkopf and R. Puk, *Chem. Geol.*, 76, 291 (1989).
112. D. Langmuir, *Geochim. Cosmochim. Acta*, 32, 835 (1968).
113. J.P. Miller, *Am. J. Sci.*, 250, 161 (1952).
114. C.L. Christ, P.B. Hostetler and R.M. Siebert, *J. Res. U.S. Geol. Surv.*, 2, 175 (1974).
115. G.W.C. Kaye and T.H. Laby, "Tables of Physical and Chemical Constants", Longmans.
116. P.W. Atkins, "Physical Chemistry", 2nd Edition, Oxford Unviersity Press, Oxford, 1982.
117. P-P. Chiang and M.D. Donohue, *J. Colloid Interface Sci.*, 122, 230 (1988).
118. J.M. Thomas and G.D. Renshaw, *Trans. Faraday Soc.*, 61, 791 (1965).
119. K. Sangwall, "Etching of Crystals: Theory, Experiment and Application", Defects in Solids series, Vol. 15, Eds. S. Amelinckx and J. Nihoul, North-Holland, Amsterdam, 1987, p. 310.
120. N. Cabrera, in "Reactivity of Solids", Proc. 4th Int. Symp., Ed. J.H. de Boer, North-Holland, Amsterdam, 1960, p. 345.
121. A.L. Smith, *J. Colloid Interface Sci.*, 55, 525 (1976).
122. Y.C. Huang, F.M. Fowkes, T.B. Lloyd and N.D. Sanders, *Langmuir*, 7, 1742 (1991).
123. J.M. Zachara, C.E. Cowan and C.T. Resch, *Geochim. Cosmochim. Acta*, 55, 1549 (1991).
124. P. Brättler, P. Möller and U. Rösick, *Earth Planetary Sci. Lett.*, 14, 50 (1972).
125. P. Möller and C.S. Sastri, *Z. Phys. Chem., Neue Folge*, 89, 80 (1974).
126. R.E. Keith and J.J. Gilman, *Acta Metall.*, 8, 1 (1960).
127. V.Z. Bengus, F.F. Lavrent, L.M. Soifer and V.I. Startsev, *Soviet Physics. Cryst.*, 5, 418 (1960).
128. A.R. Patel and K.N. Goswami, *Physica*, 29, 33 (1963).
129. S. Mann, J.M. Didymus, N.P. Sanderson, B.R. Heywood and E.J.A. Samper, *J. Chem. Soc., Faraday Trans.*, 86, 1873 (1990).
130. Z. Amjad, *Langmuir*, 3, 224 (1987).
131. R.G. Compton, K.L. Pritchard, P.R. Unwin, G. Grigg, P. Silvester, M. Lees and W.A. House, *J. Chem. Soc., Faraday Trans. I*, 85, 4335 (1989).

132. A.J. Barwise, R.G. Compton and P.R. Unwin, *J. Chem. Soc., Faraday Trans.*, 86, 137 (1990).
133. P.R. Unwin and R.G. Compton, *J. Chem. Soc., Faraday Trans.*, 86, 1517 (1990).
134. D. Buhmann and W. Dreybrodt, *Chem. Geol.*, 64, 89 (1987).
135. P. Kaushansky and S. Yariv, *Appl. Geochem.*, 1, 607 (1986).
136. J.W. Morse, A. Mucci, L.M. Walter and M.S. Kaminsky, *Science*, 205, 904 (1979).
137. A. Mucci, J.W. Morse and M.S. Kaminsky, *Am. J. Sci.*, 285, 289 (1985).
138. A. Mucci and J.W. Morse, *Am. J. Sci.*, 285, 306 (1985).
139. P. Möller and G. Werr, *Radiochimica Acta*, 18, 144 (1972).
140. P. Möller, *J. Inorg. Nucl. Chem.*, 35, 395 (1973).
141. P. Möller and P.P. Parekh, *Marine Chem.*, 3, 63 (1975).
142. C.S. Sastri and P. Möller, *Chem. Phys. Lett.*, 26, 116 (1974).
143. P. Möller and G. Rajagopalan, *Z. Phys. Chem., Neue Folge*, 94, 297 (1975).
144. K. de Groot and E.M. Duyvis, *Nature*, 212, 183 (1966).
145. G.M. Lafon, *Am. J. Sci.*, 278, 1455 (1978).
146. R. Garrels and R. Wollast, *Am. J. Sci.*, 278, 1469 (1978).
147. R.A. Berner, *Geochim. Cosmochim. Acta*, 39, 489 (1975).
148. R.A. Berner, *Am. J. Sci.*, 278, 1475 (1978).
149. D.C. Thorstenson and L.N. Plummer, *Am. J. Sci.*, 277, 1203 (1977).
150. D.C. Thorstenson and L.N. Plummer, *Am. J. Sci.*, 278, 1478 (1978).
151. J.W. Morse and M.L. Bender, *Chem. Geol.*, 82, 265 (1990).
152. F.T. Mackenzie, W.B. Bischoff, F.C. Bishop, M. Loijens, J. Schoonmaker and R. Wollast, in [151].
153. E.A. Burton and L.M. Walter, *Geochim. Cosmochim. Acta*, 55, 777 (1991).
154. M.M. Reddy and G.H. Nancollas, *J. Crystal Growth*, 35, 33 (1976).
155. H.J. Meyer, *J. Crystal Growth*, 66, 639 (1984).
156. M.E. McLester, D.F. Martin and W.H. Taft, *J. Inorg. Nucl. Chem.*, 32, 391 (1970).
157. J.L. Bischoff and W.S. Fyfe, *Am. J. Sci.*, 266, 65 (1968).
158. R.M. Pytkowicz, *J. Geol.*, 73, 196 (1965).
159. V. Koß and P. Möller, *Z. Anorg. Allg. Chem.*, 410, 165 (1974).
160. M.M. Reddy and K.K. Wang, *J. Crystal Growth*, 50, 470 (1980).
161. W.J. Hamer, G.D. Pinching and S.F. Acree, *J. Research Nat. Bur. Standards*, 35, 539 (1945) & W.J. Hamer and S.F. Acree, *ibid.*, 35, 381 (1945), in G. Kortüm, W. Vogel and K. Andrussow, "Dissociation Constants of Organic Acids in Aqueous Solution", IUPAC, Butterworths, London, 1961.
162. G.D. Pinching and R.G. Bates, *J. Research Nat. Bur. Standards*, 45, 444 (1950), in G. Kortüm, W. Vogel and K. Andrussow, "Dissociation Constants of Organic Acids in Aqueous Solution", IUPAC, Butterworths, London, 1961.
163. G.D. Pinching and R.G. Bates, *J. Research Nat. Bur. Standards*, 45, 322 (1950), in G. Kortüm, W. Vogel and K. Andrussow, "Dissociation Constants of Organic Acids in Aqueous Solution", IUPAC, Butterworths, London, 1961.
164. J.D. Morrison and J.M. Robertson, *J. Chem. Soc.* 17, 987 in "Tables of Interatomic Distances and Configuration in Molecules and Ions", Ed. L.E. Sutton, The Chemical Society, Special Publication Nº11, London, 1958.
165. O. Ermer, *Helv. Chim. Acta*, 64, 1902 (1981).

166. J. Bjerrum, G. Schwarzenbach and L.G. Sillén, "Stability Constants; Part I: Organic Ligands", IUPAC, The Chemical Society, Special Publication Nº6, London, 1957.
167. L.B. Yeatts and W.L. Marshall, *J. Phys. Chem.*, 73, 81 (1969).
168. R.M. Garrels & M.E. Thompson, *Am. J. Sci.*, 260, 57 (1962).
169. E.J. Reardon and D. Langmuir, *Am. J. Sci.*, 274, 599 (1974).
170. C. Klein and C.S. Hurlbut Jr., 20th Ed., "Manual of Mineralogy", Wiley, New York, 1985, p. 329.
171. C.E. Cowan, J.M. Zahara and C.T. Resch, *Geochim. Cosmochim. Acta*, 54, 2223 (1990).
172. J.M. Zachara, J.A. Kittrick and J.B. Harsh, *Geochim. Cosmochim. Acta*, 52, 2281 (1988).
173. W.A. Kornicker, J.W. Morse and R.N. Damasceno, *Chem. Geol.*, 53, 229 (1985).
174. J.R. MacDonald, "Impedance Spectroscopy;- Emphasizing Solid Materials and Systems", Wiley, New York, 1987.
175. A.J. Bard and L.R. Faulkner, "Electrochemical Methods", Wiley, New York, 1980.
176. R. de Levie, *Electrochim. Acta*, 9, 1231 (1964).
177. R. de Levie, *Electrochim. Acta*, 10, 113 (1965).
178. J.C. Scully, "The Fundamentals of Corrosion", 3rd Edition, Pergamon Press, Oxford, 1990, p. 167.
179. F.J. Graham, H.C. Brookes and J.W. Bayles, *J. Appl. Electrochem.*, 20, 45 (1990).
180. H. Falkenhagen, "Electrolytes", Oxford University Press, Oxford, 1943, p. 73.
181. R.G. Compton, A.M. Waller, H. Block and J. Chapples, *J. Appl. Electrochem.*, 20, 23 (1990).
182. L. Nyikos and T. Pajkossy, *Electrochim. Acta*, 30, 1533 (1985).
183. T. Pajkossy and L. Nyikos, *J. Electrochem. Soc.*, 133, 2061 (1986).
184. W.H. Mulder and J.H. Sluyters,*Electrochim. Acta*, 33, 303 (1988).
185. M. Keddam and H. Takenouti, *Electrochim. Acta*, 33, 445 (1988).
186. P.J. Sonneveld, W. Visscher and E. Barendrecht, *J. Appl. Electrochem.*, 20, 563 (1990).
187. A. Caprani, M.M. de Ficquelmont-Loizos, L. Tamisier and P. Peronneau, *J. Electrochem. Soc.*, 135, 635 (1988).
188. G. Antonini, G. Guiffant and D. Quemada, *J. Chim. Phys.*, 71, 1123 (1974).
189. G. Antonini, G. Guiffant, D. Quemada and A.M. Dosne, *Biorheology*, 15, 111 (1978).
190. K.H. Keller, *Federation Proceedings*, 30, 1591 (1971).
191. J. Postlethwaite and D.N. Holdner, *Can. J. Chem. Eng.*, 54, 255 (1976).
192. G.C. Pini and P.L. DeAnna, *Electrochim. Acta*, 22, 1423 (1977).
193. H. Zeilmaker and E. Barendrecht, *Ext. Abstr. Int. Soc. Electrochem.*, 31st Meeting, Venice, 1980, p. 911.
194. M.M. de Ficquelmont-Loizos, L. Tamisier and A. Caprani, *J. Electrochem. Soc.*, 135, 626 (1988).
195. E. Leitel, A. Pinkowski and K.P. Thiessen, *Z. Phys. Chem. (Leipzig)*, 260, 448, (1979).
196. J.W. Smith and D.H. King, *Can. J. Chem. Eng.*, 53, 41 (1975).

197. J. Postlethwaite and D.N. Holdner, *Can. J. Chem. Eng.*, 53, 31 (1975).
198. V.G. Levich, "Physicochemical Hydrodynamics", Prentice-Hall, Englewood Cliffs, 1962, pp. 60-78.
199. C.M.A. Brett and A.M.C.F. Oliveira Brett, in "Comprehensive Chemical Kinetics", Eds. C.H. Bamford and R.G. Compton, Vol.26, pp. 361-364.
200. V.Yu. Filanovski & V.Yu. Pleskov, *Prog. in Surf. Membrane Sci.*, 10, 27 (1976).
201. G. Bugliarello and J. Sevilla, *J. Biorheol.*, 7, 85 (1970).
202. G.K. Batchelor and J.T. Green, *J. Fluid Mech.*, 56, 375 (1972).
203. P.M. Shanbhag and J.W. Morse, *Geochim. Cosmochim. Acta*, 46, 241 (1982).
204. S.G. Terjesen, O. Erga and S.G. Thorsen, *Chem. Eng. Sci.*, 14, 277 (1961).
205. N.E. Pingatore and M.P. Eastman, *Chem. Geol.*, 45, 113 (1984).
206. G.M. Bancroft, J.R. Brown and W.S. Fyfe, *Chem. Geol.*, 19, 131 (1977).
207. P. Papadopoulos and D.L. Rowell, *J. Soil Sci.*, 39, 23 (1988).
208. M.L. Franklin and J.W. Morse, *Ocean Sci. Eng.*, 7, 147 (1982).
209. S.J. Gaffey and K.L. Reed, *Econ. Geol.*, 82, 195 (1987).
210. O. Erga and S. Terjesen, *Acta Chem. Scand.*, 10, 872 (1956).
211. W.F. Pickering, *Water Air Soil Poll.*, 20, 299 (1983).
212. A. Katz, *Geochim. Cosmochim. Acta*, 37, 1563 (1973).
213. A. Mucci, R. Canuel and S. Zhong, *Chem. Geol.*, 74, 309 (1989).
214. O. Söhnel and J.W. Mullin, *J. Crystal Growth*, 60, 239 (1982).
215. E.L. Dromgoole and L.M. Walter, *Chem. Geol.*, 81, 311 (1990).
216. V. Koß and P. Möller, *Inorg. Nucl. Chem. Lett.*, 10, 849 (1974).
217. M. Ishikawa and M. Ichikuni, *Chem. Geol.*, 42, 137 (1984).
218. I. Nestaas and S.G. Terjesen, *Acta Chem. Scand.*, 23, 2519 (1969).
219. N.E. Pingatore and M.P. Eastman, *Geochim. Cosmochim. Acta*, 50, 2195 (1986).
220. A. Glasner and D. Weiss, *J. Inorg. Nucl. Chem.*, 42, 655 (1980).
221. A. Tsutsu and H.D. Holland, *Geochim. Cosmochim. Acta*, 30, 439 (1966).
222. J.W. Morse, P.M. Shanbhag, A. Saito and G.R. Choppin, *Chem. Geol.*, 42, 85 (1984).
223. W.A. House, *J. Colloid Interface Sci.*, 119, 505 (1987).
224. J. de Kanel and J.W. Morse, *Geochim. Cosmochim. Acta*, 42, 1335 (1978).
225. T. Suzuki, S. Inomata and K. Sawada, *J. Chem. Soc., Faraday Trans. I*, 82, 1733 (1986).
226. A.G. Xyla and P.G. Koutsoukos, *J. Chem. Soc., Faraday Trans. I*, 83, 1477 (1987).
227. S. Mann, B.R. Heywood, S. Rajam and J.D. Birchall, *Proc. R. Soc. Lond. A*, 423, 457 (1989).
228. S. Rajam, B.R. Heywood, J.B.A. Walker, S. Mann, R.J. Davey and J.D. Birchall, *J. Chem. Soc., Faraday Trans.*, 87, 727 (1991).
229. B.R. Heywood, S. Rajam and S. Mann, *J. Chem. Soc., Faraday Trans.*, 87, 735 (1991).
230. E. Suess, *Geochim. Cosmochim. Acta*, 34, 157 (1970).
231. Y. Kitano and D.W. Hood, *Geochim. Cosmochim. Acta*, 29, 29 (1965).
232. R.W. Lahann and R.C. Campbell, *Geochim. Cosmochim. Acta*, 44, 629 (1980).

233. S. Sarig and F. Kahana, *J. Crystal Growth*, 35, 145 (1976).
234. W.H. Bragg, *Phil. Trans. Roy. Soc. Lond. A*, 89, 468 (1914).
235. W.A. Deer, R.A. Howie and J. Zussman, "Rock-Forming Minerals", Vol. 5, Longmans, London, 1962.